

## Micro-Scale Experiments and Models for Composite Materials with Materials Research

**Zike, Sanita; Mikkelsen, Lars Pilgaard; Sørensen, Bent F.; Tvergaard, Viggo**

*Publication date:*  
2015

*Document Version*  
Publisher's PDF, also known as Version of record

[Link back to DTU Orbit](#)

*Citation (APA):*  
Zike, S., Mikkelsen, L. P., Sørensen, B. F., & Tvergaard, V. (2015). Micro-Scale Experiments and Models for Composite Materials with Materials Research. DTU Wind Energy. (DTU Wind Energy PhD; No. 0050(EN)).

## DTU Library

Technical Information Center of Denmark

---

### General rights

Copyright and moral rights for the publications made accessible in the public portal are retained by the authors and/or other copyright owners and it is a condition of accessing publications that users recognise and abide by the legal requirements associated with these rights.

- Users may download and print one copy of any publication from the public portal for the purpose of private study or research.
- You may not further distribute the material or use it for any profit-making activity or commercial gain
- You may freely distribute the URL identifying the publication in the public portal

If you believe that this document breaches copyright please contact us providing details, and we will remove access to the work immediately and investigate your claim.

# Micro-Scale Experiments and Models for Composite Materials with Materials Research

DTU Wind Energy  
PhD Thesis 2015

Sanita Zike

DTU Wind Energy PhD-0050 (EN)  
ISBN: 978-87-93278-39-4

June 2015

DTU Vindenergi  
Institut for Vindenergi

---



**Authors:** Sanita Zike

**Title:** Micro-Scale Experiments and Models for Composite Materials with Materials Research

**Department:** DTU Wind Energy

**Summary:**

Numerical models are frequently implemented to study micro-mechanical processes in polymer/fibre composites. To ensure that these models are accurate, the length scale dependent properties of the fibre and polymer matrix have to be taken into account. Most often this is not the case, and material properties acquired at macro-scale are used for micro-mechanical models. This is because material properties at the macro-scale are much more available and the test procedures to obtain them are well defined. The aim of this research was to find methods to extract the micro-mechanical properties of the epoxy resin used in polymer/fibre composites for wind turbine blades combining experimental, numerical, and analytical approaches.

Experimentally, in order to mimic the stress state created by a void in a bulk material, test samples with finite root radii were made and subjected to a double cantilever beam test in an environmental scanning electron microscope. Deformation around the notches was measured using a digital image correlation method. Analytically, the experimental results were related to the HRR theory, and the concept of strain energy density was used to find the micro-scale stress-strain relationship and failure strength. In the numerical approach, the experimentally measured strain fields were matched with the numerically predicted strain fields for different power law hardening material models.

In addition, this study includes evaluation of the strain gauge accuracy, when devices are applied on polymer and polymer/composite materials.

**June 2015**

**Project period:**

2012-2015

**Education:**

Doctor of Philosophy (PhD)

**Supervisors:**

Lars P. Mikkelsen

Bent F. Sørensen

Viggo Tvergaard

**Contact No.:**

+45 26564635

**Report No.:**

DTU Wind Energy PhD-0050 (EN)

ISBN: 978-87-93278-39-4

**Sponsorship:**

Danish Centre for Composite Structures and Materials for Wind Turbines (DCCSM), grant no. 09-067212

**Pages:** 74

**Tables:** 6

**Figures:** 61

**References:** 92

**Technical University of Denmark**

Department of Wind Energy

Frederiksborgvej 399

Building 118

4000 Roskilde

Denmark

Phone 46 77 50 24

zike@dtu.dk

www.vindenergi.dtu.dk

## Preface

Ph.D. thesis was carried out during the period January 1<sup>st</sup> 2012 – June 30<sup>th</sup> 2015 at the Section of Composites and Materials Mechanics, Department of Wind Energy, Technical University of Denmark (DTU). The Ph.D project was funded by the Danish Centre for Composite Structures and Materials for Wind Turbines (DCCSM), grant no. 09-067212, from the Danish Strategic Research Council (DSF).

The study has been supervised by:

Associate Professor Ph.D. *Lars P. Mikkelsen* (Section of Composites and Materials Mechanics, Department of Wind Energy, DTU),

Professor dr.techn. *Bent F. Sørensen* (Section of Composites and Materials Mechanics, Department of Wind Energy, DTU), and

Professor Emeritus dr.techn. *Viggo Tvergaard* (Section of Solid Mechanics, Department of Mechanical Engineering, DTU).

I am very grateful to my supervisors for giving me an opportunity to work on this project, also for their time and guidance. I would also like to thank the colleagues Christian H. Madsen, Erik Vogeley, and Troels Hoff for their assistance in the experimental part of my study.

Roskilde, June 30<sup>th</sup> 2015

Sanita Zike



## Abstract

Numerical models are frequently implemented to study micro-mechanical processes in polymer/fibre composites. To ensure that these models are accurate, the length scale dependent properties of the fibre and polymer matrix have to be taken into account. During macro-scale tests, the acquired properties are often affected by unavoidable flaws and present somewhat an averaged response of the material. These averaged properties are sufficient for macro-mechanical models, but are inappropriate for micro-scale models. Microscopically, e.g. around a flaw, the behaviour of the material is expected to vary from the averaged response. Nevertheless, the averaged properties are often used in micro-mechanical models due to lack of properties at the micro-scale. The aim of this research was to find methods to extract the micro-mechanical properties of the epoxy resin used in polymer/fibre composites for wind turbine blades.

In this study, test samples were manufactured with finite root radii to mimic the stress state created by a void in a bulk material. The test samples were subjected to a double cantilever beam test in an environmental scanning electron microscope, and strains around the notch were measured using a digital image correlation method. To relate the experimentally measured strains with the corresponding stresses, analytical and numerical approaches were employed. Analytically, the concept of strain energy density was used to find the micro-scale stress-strain relationship. In the numerical approach, the experimentally measured strain fields were matched with the numerically predicted strain fields for different power law hardening material models. Experimental results show that at the micro-scale the failure strain reaches 20% at the notch edge, and the corresponding failure stresses were estimated of approximately 250 MPa. Profoundly different mechanical properties were measured during the macro-scale tests for the same epoxy polymer. Macroscopically, the failure strains of 5-6% and failure stresses of 70-86 MPa were measured in simple tension and compression.

Moreover, the matrix in the polymer/fibre composite is subjected to various stress states, which affect its mechanical behaviour. In order to predict failure in the polymer/fibre composites, it is important that the applied material models can capture these variations. Two plasticity laws, based on the von Mises and Drucker-Prager yield criteria, were used to predict the behaviour of the epoxy resin in tension, compression, and shear. The response in tension and shear was equally well predicted by both criteria, whereas in compression the Drucker-Prager criterion gave a better fit with the experiments.

Furthermore, in polymer/composite tests, strain gauge devices are often employed. Experimentally, it was observed that the measurements using strain gauge devices differ from those obtained by clip-on and laser extensometers when applied on the same test samples. To understand what is causing these discrepancies, a numerical study was conducted. Numerically, the accuracy of different types of strain gauge device was studied, when they were applied on materials with stiffness in the range of 1-200 GPa. It was found that the strain gauge measurements were mainly affected by the test sample stiffness and thickness, as well by the strain gauge length.

## Abstrakt

Numeriske og analytiske modeller er ofte implementeret for at studere den micro-mekaniske opførsel af fiberforstærkede polymer matrix kompositter. For at sikre at disse modeller er nøjagtige, længdeskala afhængige egenskaber af fiber og matrix materialet er ofte nødvendige at inkludere. Under udførelse af makroskopiske test, er de målte egenskaber ofte påvirket af initialt forekommende skader i materialet og vil samtidig kun give gennemsnitslige værdier for materialet. Gennemsnitslige værdier som er tilstrækkelige til de makro-mekaniske modeller, men som ofte er helt uegnede til at modellere micro-mekaniske mekanismer. Alligevel anvendes disse ofte i micro-mekaniske modeller grundet manglen på materialeegenskaberne på micro-skala. Formålet med ph.d. projektet er at finde metoder til at fastlægge de micro-mekaniske egenskaber af et specifikt epoxy materiale der ofte anvendes som matrix materiale i kompositmaterialet i vindmøllevinger.

I dette studie er undersøgt testemner med en kærnv med en endelig kærnradius med det formål at efterligne spændingstilstanden omkring voids i et matrix materialet. Testemnerne testes ved hjælp af en såkaldt dobbelt cantilever bjælke test metode under et environmental scanningselektronmikroskop. Tøjningstilstanden rundt om kærven måles ved anvendelse af digitalt image korrelation. Analytiske og numeriske metoder anvendes for at kunne relatere de eksperimentelt målte tøjningstilstande med de tilsvarende spændingstilstande. Analytisk bruges tøjningsenergien til at finde stress-strain relation for epoxy materialet under antagelse af et potenshærdende materiale. Den numeriske metode baserer sig på at de eksperimentelt målte tøjningsfelter bliver sammenlignet med de tilsvarende numerisk forudsagte tøjningsfelter under anvendelse af forskellige materialemodeller. Resultaterne viser, at der opnås en deformation på 20% tøjning ved kærvoverflade og at de tilsvarende spændinger er estimeret til omkring 250 MPa. Makroskopisk, under en simpel tryk og træk-test findes en brudtøjning på 5-6%, ved tilsvarende brudspænding på 70-86 MPa.

Yderligere er matrixen i kompositmaterialet belastet i forskellige spændingstilstande. Noget der påvirker dets mekaniske opførsel. Det er væsentligt at de anvendte materialemodeller kan fange disse variationer for korrekt at kunne forudsige brud i fiberkompositter. To forskellige plasticitet love, baseret på henholdsvis von Mises og Drucker-Prager flydekriteriet anvendes til at forudsige opførelsen af epoxy materialet udsat for henholdsvis træk, tryk, og forskydning. Træk og forskydning er lige godt forudsagt af begge flydekriterier, mens Drucker-Prager kriteriet giver en bedre forudsigelse af trykopførslen.

Strain gauges bruges ofte ved test af polymer matrix kompositter. Eksperimentelt er målingerne baseret på strain gauge observeret at afvige betydeligt fra de tilsvarende værdier fundet ved clip-on eller laser extensometer. I første omgang blev det antaget, at testemnets generelle stivhed blev påvirket af strain gauge, der, som et resultat, overestimerede materialestivheden. Et intensivt finite element studie blev udført for at få en mere detaljeret forståelse af, hvad der påvirker strain gaugens nøjagtighed. Numerisk blev nøjagtigheden af forskellige typer af strain gauges undersøgt anvendt på materialer med en stivhed i intervallet 1-200 GPa. Det konstateres, at strain gauge fejlmåling hovedsagelig påvirkes af prøven stivhed og tykkelse samt af strain gauges længde.

## Author papers

[P1] ZIKE, Sanita; MIKKELSEN, Lars Pilgaard. Mechanical material characterization of an epoxy regarding hydrostatic pressure sensitivity (submitted)

[P2] ZIKE, Sanita; MIKKELSEN, Lars Pilgaard. Correction of Gauge Factor for Strain Gauges Used in Polymer Composite Testing. *Experimental Mechanics*, 2014, 54.3: 393-403.

[P3] ZIKE, Sanita; SØRENSEN, Bent F.; MIKKELSEN, Lars Pilgaard. Experimental determination of the micro-scale strength and stress-strain relation for an epoxy resin (submitted)

[P4] ZIKE, Sanita; MIKKELSEN, Lars Pilgaard; SØRENSEN, Bent F. DCB Test Sample Design for Micro-Mechanical Testing. In: *19th International Conference on Composite Materials (ICCM 2013)*.

## Contents

<b>Preface.....</b>	<b>i</b>
<b>Abstract.....</b>	<b>ii</b>
<b>Abstrakt .....</b>	<b>iii</b>
<b>Author papers.....</b>	<b>iv</b>
<b>1 Introduction.....</b>	<b>1</b>
1.1 Composite materials .....	1
1.2 From macro to micro scale .....	2
1.3 Concluding remarks.....	4
1.4 Outline of the thesis.....	4
<b>2 Theoretical framework.....</b>	<b>5</b>
2.1 Non-linear fracture mechanics.....	5
2.2 Blunting crack tips and notches.....	8
2.3 Cohesive law .....	8
2.4 Pressure independent and pressure dependent material models .....	9
2.5 Digital image correlation method .....	12
<b>3 Macro-scale tests.....</b>	<b>15</b>
3.1 Mechanical characterization of an epoxy resin [P1].....	15
3.2 Application of pressure independent and dependent material models [P1].....	19
3.3 Errors of strain gauge devices used on compliant materials [P2].....	21
<b>4 Micro-scale tests.....</b>	<b>29</b>
4.1 Methods [P3, P4].....	30
4.2 Extraction of the micro-scale stress-strain relation [P3].....	39
4.3 Numerically estimated strain fields .....	43
4.4 Strain field characterization [P3].....	57
4.5 Error estimation of the experimental strain measurements [P3].....	62
<b>5 Discussion .....</b>	<b>65</b>
<b>6 Conclusions.....</b>	<b>69</b>
<b>References .....</b>	<b>70</b>

# 1 Introduction

## 1.1 Composite materials

Polymer/fibre composite materials are often used in structural load carrying components. In the wind energy industry, polymer/fibre composites are particularly important due to their high stiffness (aerodynamic performance), low density (weight), and good fatigue performance (material degradation) [1,2]. Polymer/fibre composites consist of two main components: polymer-based resin as matrix and fibres as reinforcement. The fibres are usually designed to carry the main load of the composite structure. They possess high strength and stiffness, and lower density compared to metals. The fibres are usually made of glass and carbon. To make the fibres meaningful in the structural components, a binding agent or matrix is needed. The role of the matrix in the composites is to maintain structural integrity by having sufficient strength and stiffness to support the fibres and bind them in multiple variations to ensure the structural performance needed. The matrix often possesses less strength and stiffness than the fibres, but has greater toughness. Usually, the matrix is a thermoset polymer (epoxies, polyesters, and vinyl esters) with a stiffness of 3-4 GPa, a failure strain of about 5–8%, and a density of 1.1–1.3 g/cm<sup>3</sup> [2].

### 1.1.1 *The role of the matrix in composite material failure*

Although, the design of the composite structural material mostly suggests that load will be carried by the fibres, a lot of microscopic processes actually depend on the matrix properties and the fibre-matrix interface. This is true loading both parallel and transverse to the fibres. For instance, when composite structures are loaded in line with the fibres in compression, strength is influenced by fibre resistance to buckling and kinking [3–5]. Strength in compression therefore depends on how well the fibres are supported by the matrix, which will improve with greater shear stiffness and strength of the matrix. When composite structures are loaded transverse to the fibres whether in tension or compression, the main failure modes are related to fibre/matrix debonding, matrix yielding, and cavitation (in tension) of the matrix [6–10]. Moreover, several failure modes can be presented in the same material due to the inhomogeneous nature of the composite (e.g. clusters of fibres and resin rich areas), which causes local stress state variations [7]. Therefore, the matrix could yield in some regions, while in the other regions it could fail due to cavitation-induced cracking or fibre/matrix debonding.

### 1.1.2 *The mechanical behaviour of the matrix versus bulk polymer*

When composites are loaded transverse to the fibres, failure is dominated by the properties of the matrix, so one might expect that the failure of the composite would be similar to that of pure polymers. But in fact composites possess rather low strains to failure with transverse loading, e.g. composites tend to fail at strains below 1%, whereas the failure strains exceed 5% in a pure polymer, i.e. in the absence of fibres [11]. In composites, the lower strains to failure can be expected to be enhanced by:

- Fibres giving rise to local stresses;
- Residual stresses because the fibres and matrix have different thermal expansion coefficients [12];
- Incomplete adhesion at the fibre-matrix interface;
- Reduced plasticity of the matrix due to the reinforcement by much stiffer fibres; and
- A multi-axial stress state in the matrix inside the composite.

For instance, Asp et al. [11] have tried to mimic matrix behaviour in the composite by studying pure polymer behaviour under high pressure, i.e. the pressure which the matrix could be subjected to inside the composite. They attained that, under high pressure, the strains to failure of the epoxy polymer are significantly lower and suggested that the multi-axial stress state of the matrix by itself can explain the differences between the behaviour of pure polymer and the behaviour of the composite matrix. Furthermore, voids, flaws, and incomplete adhesion at the matrix-fibre interface would limit the composite behaviour with the transverse loading even more.

### 1.1.3 Pressure sensitivity of polymers

Polymer materials, in general, are considered pressure sensitive [13–17], i.e. the yield strength of a polymer material improves under hydrostatic pressure. Under moderate pressures, the polymer can display both higher yield strength and strain, e.g. brittle polymers can become ductile [15,18]. Moderate pressures suppress crazing and post-pone cracking, allowing the material to approach stresses needed for yielding [18]. The yield strength continues to increase with external pressure, because the molecular movements responsible for shear deformation are restricted in polymer. With high pressure, the stress required to induce shear deformation becomes greater than the stress needed for fracture [14], and the transition from ductile to brittle behaviour can occur [15].

## 1.2 From macro to micro scale

The strength of materials when measured empirically is usually lower than their theoretical strength, which is related to cohesion forces within the material [19]. For instance, the theoretical strength of polymer materials is assumed to be about 10% of the elastic modulus,  $E$  [20]. Therefore, for epoxy resin with  $E = 3$  GPa, the strength should be approximately 300 MPa. Nevertheless, the macroscopic strength of epoxy resin is experimentally measured in the range of 50-80 MPa [12,21]. The common explanation of this phenomenon is that materials have flaws, which cause a non-uniform stress distribution in a volume, as first explained by Griffith [22]. The flaws (also voids and other inclusions) increase stresses locally, and this means that an externally applied stress,  $\sigma_\infty$ , is not equal to an internal stress,  $\sigma_l$ . As a result, a material failure is initiated under external loads lower than the cohesive strength of the material. For example, for the elliptical holes in flat plates under tensile loading, the stress concentration at the tip of the major axis is given as [23]

$$\sigma_l = \sigma_\infty \left(1 + \frac{2a}{b}\right), \quad (1.1)$$

where  $a$  is the major axis and  $b$  the minor axis of the elliptical hole. For voids and spherical inclusions, the local stress will be approximately three times greater than the stress applied externally,  $\sigma_l = 3\sigma_\infty$ . As the elliptical hole takes on the appearance of a sharp crack,  $b \ll a$ , the local stress will increase, and the external load required to initiate material failure will decrease.

Along with sensitivity to flaws, the mechanical behaviour of brittle and quasi-brittle materials is reported to be size-dependent [21,24–26]. Size-dependent behaviour is partly explained by Weibull statistical theory. According to the Weibull theory, the probability of a weak point (largest flaw) decreases with a smaller volume. A reduced flaw size postpones failure, which allows the measurement of higher strength values [21,26]. For example, if we reduce the dimensions of an object made of the epoxy resin from macroscopic to microscopic, its strength at failure is reported to increase from 50 MPa to 165 MPa [21]. Variations in mechanical behaviour at different length scales cannot always be explained by the size of the flaws. For example, smaller material dimensions can lead to a different stress state, such as the transition from a plane strain to a plane stress. This would be particularly relevant for materials with one of the geometrical dimensions similar to a flaw size. In this case, the material would experience improved toughness, which would allow more effective dissipation of the local stresses.

Another concept that may explain the length-scale effect is strain gradient plasticity [27,28]. This means that for relatively small deformation regions, plastic flow depends on the strain gradients within the material, which appear either because of the geometry of loading or because the material itself is plastically inhomogeneous. For instance, Fleck et al. [27] have conducted experimental tests with copper wires under both tension and torsion. They showed that copper wires with a diameter within the range of 12-170  $\mu\text{m}$  have rather small variations of strength in tension, while strength in torsion is significantly improved in thinner wires. The minor differences of strength in tension are related to the lack of strain gradients because the material is experiencing uniform deformation. In torsion, however, strain gradients are present because shear strain depends on the distance from the rotational axis. Similarly, the effect of strain gradients can be expected in matrices filled with fine particles [29], in nano- and macro- indentation tests [30], and around cracks [31,32].

Around cracks and notches, stresses and strains can be expected to be modified by strain gradients, which cannot be predicted by conventional plasticity or elasticity theory [31,32]. The plastic strain gradient in front of a notch can be expected to limit the plastic flow resulting in a lower amount of plastic deformation and higher stresses at the tip [32]. The effect of the strain gradient becomes more significant as the material deformation scales with a material length scale. For instance, Mikkelsen and Goutianos [32] conducted a numerical analysis in order to study the dependency of the blunted crack tip fields on material length scale. They found that if the size of the plastic zone is 1000 times larger than the material length scale, a conventional plasticity theory is sufficient, and that if it is less than the material length scale, elastic solutions

can be used. For the intermediate sizes, they recommend that the solutions should include the dependency of the yield on the plastic strain gradient. These findings are reported to be independent of the hardening exponent and yield strain ( $\sigma_o/E$ ). For the epoxy resin, the material length scale parameter from the indentation test is estimated within the range of 0.1-0.15  $\mu\text{m}$  [33]. According to the numerical analysis by Mikkelsen and Goutianos [32], the yield of the epoxy resin in front of the notch is affected by the plastic strain gradient if the region of the plastic zone is larger than 0.1-0.15  $\mu\text{m}$  and smaller than 100-150  $\mu\text{m}$ .

### 1.3 Concluding remarks

The mechanical properties of the composite structure strongly depend on the behaviour of its components, as well as on the proportion, distribution, and interaction between the fibres and the matrix. Understanding the interaction between the components inside the composite (and other microscopic defects and voids [34]), generally requires going down scales from the macro- to the micro- scale. The easiest and possibly the cheapest way is to employ analytical and/or numerical methods, e.g. finite element methods (FEM). To acquire accurate numerical predictions, it is often assumed that the material properties have to be defined with respect to the desired length scale, i.e. micro-scale models should use microscopic fibre and matrix properties. Usually, this is not the case, because macroscopic properties are much more available, and the test procedures to obtain them are well defined.

### 1.4 Outline of the thesis

Thesis consists of two main parts: macro-scale and micro-scale tests. At the macro-scale, standardized methods are applied to study the epoxy resin behaviour under different stress states. The material behaviour under various stress states is predicted with two plasticity laws based on the pressure dependent Drucker-Prager yield criterion and the pressure independent von Mises yield criterion. In addition, errors of strain measurement device, strain gauge, are evaluated when applied on compliant materials. Results at the macro-scale are given in the papers [P1] and [P2]. In the second part, an approach of extracting the micro-scale properties is presented. Instead of going down scales by reducing the test sample geometry equivalent to the micro-scale, the strain-to-failure measurements are done in the region of high stress localization, i.e. around notches with finite root radii. The double cantilever beam (DCB) tests are performed in a vacuum chamber of an environmental scanning electron microscope (ESEM). From the images captured in the ESEM, strains are measured implementing a 2D digital image correlation method (DIC). Analytical, experimental, and numerical approaches are used to extract the stress-strain relation at the micro-scale. The DCB test design and micro-scale experiments are presented in the papers [P4] and [P3], respectively.



## 2 Theoretical framework

### 2.1 Non-linear fracture mechanics

#### 2.1.1 General principles

During the micro-scale study, it is assumed that the stress and strain fields around the notch can be characterized by the concepts of non-linear fracture mechanics by Hutchinson [35], as well as Rice and Rosengren [36] (further denoted as the HRR theory). The HRR theory assumes that the behaviour of an elastic-plastic material can be described by the  $J_2$  deformation theory. According to the  $J_2$  deformation theory, the total strains are uniquely related to the stresses during deformation, and the material can be seen as nonlinearly elastic [37,38]. The behaviour of elastic-plastic and nonlinearly elastic material agrees as far as loading is monotonic, i.e. without unloading. Moreover, in order to estimate the stress-strain relation accurately, loading needs to be proportional [37]. Proportionality means that during loading the principal stresses maintain constant direction and their values change with some constant ratio. If the proportional or nearly proportional loading is maintained, then solutions by the  $J_2$  deformation theory and the  $J_2$  flow theory will agree [37,39]. For both theories, the yield surface is defined accordingly to the von Mises yield criterion, thus deformation is independent of hydrostatic pressure.

Furthermore, to apply the concepts of the HRR theory, it is important that the  $J$ -dominance prevails, i.e. the region, where the HRR theory is applicable, is sufficiently large, and the fracture process zone, including finite strains, is confined to the notch edge or the crack tip (Fig. 1). In the case of extensive yielding around the notch/crack and small dimensions of the test sample, both intensity and angular variations of the stress and strain around the notch/crack will be affected by boundaries of the test sample [40,41]. The  $J$ -dominance can be controlled with an applied load and/or geometry of the test sample. Moreover, the size of the HRR region depends on the intrinsic properties of the material as a hardening exponent and loading conditions (tension or bending) [40]. For samples under pure moment loading, the minimum size requirement is that the geometrical dimensions (half of the width of the test sample and length of un-cracked ligament) are at least 25 to 50 times larger than  $J/\sigma_o$  [40–42], where  $J$  is the loading parameter (description is given below) and  $\sigma_o$  is the yield stress in tension.

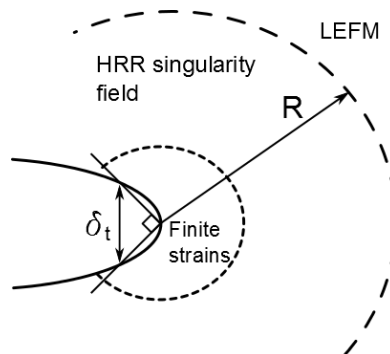


Fig. 1 The region of  $J$ -dominance

If the requirements given above are satisfied, the conditions of the crack can be characterized with a single parameter J-integral. The J-integral can be used both to present the energy released during the fracture and the state of stresses and strains around the crack. According to Rice [43], the J-integral is equal to the energy release rate,  $G$ , in a linear elastic material, i.e.  $G = J$ , which is given within the context of LEFM. Therefore, similarly to  $G$  the J-integral describes the change in potential energy with a crack advance. In the elastic-plastic materials, use of the J-integral as an energy release rate can be limited, because the strain energy is not fully recovered during crack growth [19].

Commonly, the J-integral is estimated around any contour encircling the tip of the crack or notch,  $\Gamma$ , in a counter clockwise direction [43]

$$J = \int_{\Gamma} W dx_2 - T \frac{\partial u}{\partial x_1} ds, \quad (2.1)$$

where  $T$  is the traction vector acting on the contour  $\Gamma$ ,  $u$  is the displacement vector,  $s$  is the arc length along  $\Gamma$ ,  $x_1 = x$ , and  $x_2 = y$  (see Fig. 2). The parameter  $W$  is the strain energy density given as a function of the stress and strain increment

$$W = \int_0^\varepsilon \sigma_{ij} d\varepsilon_{ij}. \quad (2.2)$$

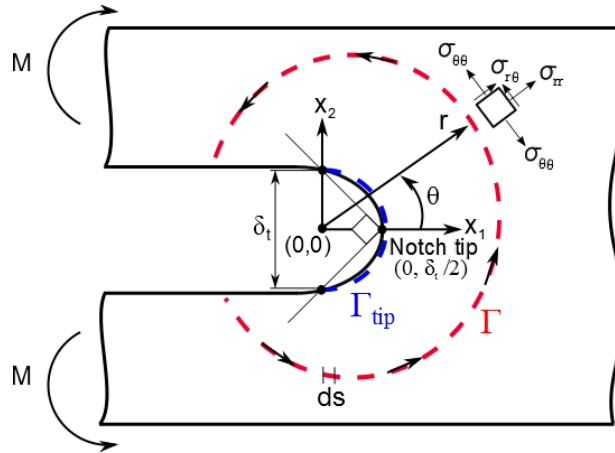


Fig. 2 Contours used for the J-integral determination

### 2.1.2 Determination of the micro-scale stress-strain relation

In this study, the strain energy density is used to extract the micro-scale stress-strain relation and failure stress of the epoxy resin (analytical approach). When  $\Gamma$  is taken around the semi-circular notch edge ( $\Gamma = \Gamma_{tip}$ ) as the blue dashed line in Fig. 2, then there is no traction acting on the contour and  $T = 0$  [43]. According to Eq. 2.1, now the J-integral is only a function of the strain energy density,  $W$ , around the contour and is given as

$$J = \int_{\Gamma_{tip}} W dx_2, \quad (2.3)$$

where  $dx_2 = r \cos\theta d\theta$ ,  $r = \delta_t/2$  (distance to the notch edge), and  $\theta$  is an angle around the notch (Fig. 2). This gives that  $J = 1/2 \int W \delta_t \cos\theta d\theta$ . Integrating Eq. 2.3 from  $-\pi/2$  to  $\pi/2$  follows that the mean strain energy density around the notch edge is

$$\bar{W} = J/\delta_t. \quad (2.4)$$

From Eq. 2.2 and Eq. 2.4, it can be seen that  $W$  can be obtained with two independent approaches. These two approaches are applied here to relate the experimentally measured strains around the notch with the stress-strain relations of power law hardening materials. The power law hardening materials are defined by a Ramberg-Osgood relation [44]

$$\frac{\varepsilon}{\varepsilon_o} = \frac{\sigma}{\sigma_o} + \alpha \left( \frac{\sigma}{\sigma_o} \right)^n, \quad (2.5)$$

where  $\sigma_o$  is the yield stress in tension,  $\varepsilon_o = \sigma_o/E$  is the elastic strain,  $\alpha$  is a parameter, and  $n$  is the hardening exponent.

The micro-scale stress-strain relation is analytically extracted by, first, determining  $\bar{W}$  around the notch considering the path independence of the J-integral [43], i.e. the J-integral evaluated around the notch is the same as around the external boundaries. Second,  $\bar{W}$  is matched with  $W$ , which is gained from the stress-strain relations of power law hardening materials with various hardening exponents. In this case,  $W$  denotes the area below the stress-strain curve (Eq. 2.2), and the strain limit of the stress-strain curves is taken from the experimental strain measurements around the notch. The resultant micro-scale stress-strain relation is found when condition  $\bar{W} = W$  is satisfied.

### 2.1.3 Strain field characterization

According to the HRR theory, the strains around the crack tip within the  $J$ -dominance region have a unique character and are given as

$$\varepsilon_{ij} = \alpha \varepsilon_o \left( \frac{J}{\alpha \sigma_o \varepsilon_o I_n r} \right)^{\frac{n}{n+1}} \bar{\varepsilon}_{ij}(\theta, n), \quad (2.6)$$

where the dimensionless function  $\bar{\varepsilon}_{ij}$  and normalizing constant  $I_n$  is dependent on the crack loading mode, on  $n$ , and on whether plane strain or plane stress state prevails [39]. The dimensionless function  $\bar{\varepsilon}_{ij}$  is expected to be independent of  $J$  and  $r$  in the  $J$ -dominance region. Thus, the strain distribution around the crack can be divided into two components. The first shows the magnitude, and the second component shows angular variations of the strain around the crack. Both components are expected to depend on the intrinsic properties of material. These assumptions are considered here, when the strain fields around the notches are characterized.

## 2.2 Blunting crack tips and notches

The HRR theory describes the stress and strain fields (singularity fields) around initially sharp cracks. According to McMeeking's [45] numerical study, the stress and strain fields around the blunting notch can be described in the same way as far as the shape of a blunted notch agrees with the shape of a blunted crack. Moreover, the singularity fields are independent of the notch size if all length parameters are normalized with the current notch width,  $b$ . McMeeking defined the initial notch width,  $b_o$ , at the point, where lines drawn back at  $45^\circ$  from the notch tip intersect the notch edge in the undeformed state. The same point he used to measure  $b$  in the deformed state. Nevertheless, he mentions that the width variations between his chosen point and the elastic-plastic boundary are minor. Assuming that the variations are small, in this study, the notch width is defined at the point, where lines drawn back at  $45^\circ$  from the notch tip intersect the notch edge both in the undeformed and deformed state, i.e.  $\delta_{to} = b_o$  and  $\delta_t \neq b$ , respectively. The opening displacement,  $\delta_t$ , is commonly used to measure the width of blunted cracks [39].

Furthermore, the stress in front of the notch is assumed to depend on the ratio between the current and initial notch width,  $b/b_o$  (in this study  $\delta_{to}/\delta_t$ ). McMeeking [45] showed that there is unique relationship between the notch width and externally applied load,  $J$ , if both sides are normalized with the initial notch width

$$\delta_t/\delta_{to} = d_n(\alpha\varepsilon_o, n)J/\sigma_o\delta_{to}, \quad (2.7)$$

where  $d_n$  is the parameter. Eq. 2.7 is similar to the one given for initially sharp cracks, which, accordingly to the HRR theory, is unique relationship between the crack opening displacement and  $J$  and is given as

$$\delta_t = d_n(\alpha\varepsilon_o, n)J/\sigma_o, \quad (2.8)$$

where  $d_n$  depends on the intrinsic material properties ranging from 0.8 for large  $n$  values to 0.3 for  $n = 3$  ( $\alpha = 1$ ), with a weak dependence on  $\alpha\varepsilon_o$  [39,46]. In this study, McMeeking's numerical approach is used to characterize the strain fields around notches with different initial notch root radii.

## 2.3 Cohesive law

Alternatively to the analytical approach, where two different methods to determine the strain energy density are used, the failure stress at the micro-scale is found employing a cohesive law [47]. Fig. 3 illustrates the main concept of this theory [48,49], i.e. the failure initiates not at the real crack tip, but in the fracture process zone where microscopic failure processes (e.g. void formation, micro-cracks, etc.) take place. Therefore, the length of fictitious crack is the sum of the actual crack length and fracture process zone. As the material strength in tension,  $\sigma_t$ , is reached in the fracture process zone, the material between the actual and fictitious crack tip will start to weaken, and the actual crack will start to propagate. The amount of energy absorbed per crack area for the propagating crack is given as [48]

$$G = \int_0^{\delta_n^*} \sigma(\delta) d\delta_n^*, \quad (2.9)$$

where stresses,  $\sigma$ , depend on the opening between fictitious crack faces,  $\delta$ , and  $\delta_n^*$  is the opening of newly developed crack. Alternatively, the work done during the separation can be evaluated by means of the J-integral, i.e. the J-integral evaluated around the crack tip equals the crack tip fracture energy,  $G$  [47]. And, the  $J$  value during crack propagation,  $J_R$ , is expressed as [47]

$$J_R = \int_0^{\delta_n^*} \sigma(\delta_n^*) d\delta_n^* + J_o, \quad (2.10)$$

where  $J_o$  is the stress intensity, at which the crack has initiated.

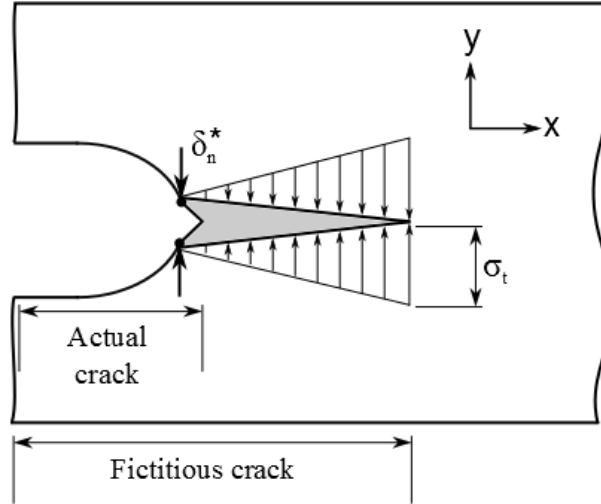


Fig. 3 A cohesive law model

## 2.4 Pressure independent and pressure dependent material models

### 2.4.1 The von Mises yield criterion

At the macro-scale, behaviour of the epoxy resin under different loadings is predicted employing two plasticity laws. The first is  $J_2$  flow theory. According to the  $J_2$  flow theory, a yield surface of material is shaped correspondingly to the von Mises yield criterion, and deformation during yielding can be described with an isotropic hardening, i.e. the yield surface expands with the same ratio for all strain components [37]. The von Mises yield criterion considers that yield will occur as an elastic shear strain-energy density reaches a critical value and is given as [50]

$$F = \sigma_e - \sigma_o, \quad (2.11)$$

where  $F$  is the plastic flow potential,  $\sigma_e = \sqrt{3J_2}$  is the effective stress,  $J_2$  is the second deviatoric stress invariant (given in [50]), and  $\sigma_o$  is the yield stress in simple tension. According to the von Mises yield criterion, the effective stress can be related to the stress in uniaxial tension,  $\sigma_t$ , compression,  $\sigma_c$ , and pure shear,  $\tau$ , as follows  $\sigma_e = \sigma_t = \sigma_c = \tau\sqrt{3}$ . The corresponding effective strain is given as  $\varepsilon_e = \sqrt{4/3J_2'}$ , where  $J_2'$  is the second deviatoric strain invariant (given in [50]). The effective strain in the uniaxial tension,  $\varepsilon_t$ , compression,  $\varepsilon_c$ , and pure shear,  $\gamma$ , can be obtained as  $\varepsilon_e = \varepsilon_t = \varepsilon_c = \gamma/\sqrt{3}$  if a constant volume during

deformation is assumed. From the effective stresses and strains, it can be concluded that the stress-strain relations in uniaxial tension and uniaxial compression will agree.

#### 2.4.2 The Drucker-Prager yield criterion

Another model used to describe a plastic deformation of the epoxy resin during the macro-scale tests is based on a Drucker-Prager yield criterion. The Drucker-Prager criterion can be seen as a modified von Mises yield criterion, where an additional term dependent on the hydrostatic stress component and intrinsic properties of material [50] is included. The flow rule in the Drucker-Prager material model is given as

$$F = \sigma_e - \sigma_o - \mu \sigma_m, \quad (2.12)$$

where  $\sigma_m$  is a hydrostatic component of the stress and  $\mu$  is a pressure sensitivity parameter.

In the FEM model, the extended linear Drucker-Prager criterion is used. According to it, the yield strength of a material (in Fig. 4 denoted as  $q$ ) increases linearly with a hydrostatic pressure,  $p$ , as shown in Fig. 4. The strength variations with a pressure are expected to be different in tri-axial compression and tri-axial tension [51].

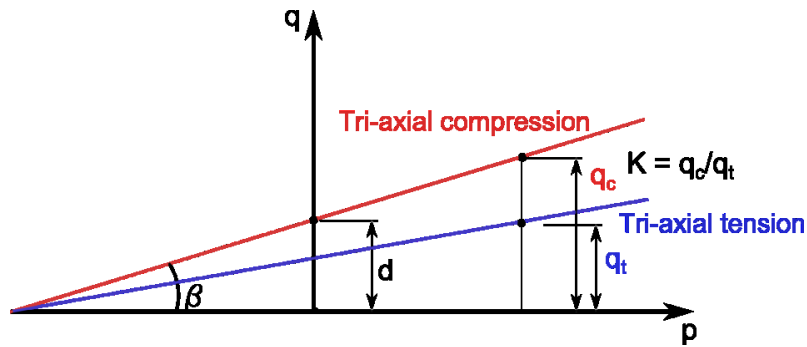


Fig. 4 The linear Drucker-Prager criterion [51]

The flow rule in the extended Drucker-Prager model is given as [51]

$$F = t - p \tan \beta - d. \quad (2.13)$$

In Eq. 2.13 the parameter  $t$  is given as  $t = \frac{1}{2} q \left[ 1 + \frac{1}{K} - \left( 1 - \frac{1}{K} \right) \left( \frac{r}{q} \right)^3 \right]$ , where  $q$  is equal to  $\sigma_e$  as  $q = \sqrt{3 \cdot J_2}$ , and  $r$  depends on the third deviatoric stress invariant,  $J_3$ , i.e.  $r^3 = \frac{27}{2} J_3$ . Moreover,  $K$  is the ratio between the yield stress in tri-axial compression and tri-axial tension (in Fig. 4  $K = q_c/q_t$ ). If the yield stress in tri-axial tension and tri-axial compression is equal, i.e.  $K = 1$ , then  $t = q = \sigma_e$ . Further, in Eq. 2.13 the hydrostatic pressure is denoted as  $p$ , i.e.  $p = -\sigma_m = -1/3(\sigma_1 + \sigma_2 + \sigma_3)$ ,  $d$  is the material cohesion, and  $\tan \beta$  can be related to  $\mu$  given in Eq. 2.12, where  $\beta$  is the friction angle [51].

In the extended Drucker-Prager model parameters  $K$  and  $\beta$  have to be taken from the tri-axial test results, which were not available in this study. Following the reference [51], the parameters given in Eq. 2.13 are

found by matching the Drucker-Prager criterion with the Mohr-Coulomb criterion. From the Mohr-Coulomb yield criterion, a material strength in uniaxial tension and uniaxial compression can be directly related to a pressure sensitivity of the material.

#### 2.4.3 The Mohr-Coulomb criterion

According to the Mohr-Coulomb criterion, the failure occurs when the material reaches the maximum shear stress, which is a function of the normal stress [52]

$$|\tau| = c - \sigma \tan \varphi. \quad (2.14)$$

In Eq. 2.14 the parameter  $c$  denotes cohesion, and  $\varphi$  is the angle of an internal friction. In Fig. 5 the stress state under pure shear (the smallest circle) and compression (the largest circle) is presented. If the yield stress is pressure independent, then both circles shown in Fig. 5 will have the same radius, whereas for the pressure dependent material the radii will differ. Moreover, for the pressure sensitive materials, the envelope curve connecting the failure stresses in pure shear and compression will appear inclined with respect to the  $\sigma$  axis [52]. The angle of inclination is denoted as friction angle  $\varphi$ .

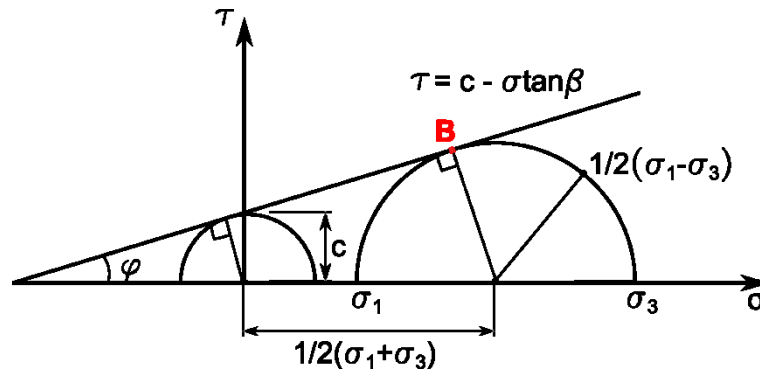


Fig. 5 The Mohr-Coulomb criterion (inclined line indicates the failure envelope)

In the Mohr-Coulomb criterion the strength in simple compression,  $\sigma_c$ , and simple tension,  $\sigma_t$ , is defined as [52]

$$\sigma_t = \frac{2c \cos \varphi}{1 + \sin \varphi} \text{ and} \quad (2.15)$$

$$\sigma_c = \frac{2c \cos \varphi}{1 - \sin \varphi}. \quad (2.16)$$

The friction parameter  $\varphi$  can be extracted from Eq. 2.15 and Eq. 2.16, relating the material behaviour in simple compression and tension

$$\lambda_{ct} = \frac{\sigma_c}{\sigma_t} = \frac{1 + \sin \varphi}{1 - \sin \varphi} \rightarrow \sin \varphi = \frac{\lambda_{ct} - 1}{\lambda_{ct} + 1}. \quad (2.17)$$

According to the reference [51], the pressure sensitivity parameters for the Mohr-Coulomb criterion can be related to those in the Drucker-Prager criterion expressing the flow rules, Eq. 2.13 and Eq. 2.14, with the principal stresses in tri-axial compression. As a result, following relations are given

$$\tan \beta = \frac{6 \sin \varphi}{3 - \sin \varphi} \text{ and} \quad (2.18)$$

$$K = \frac{3 - \sin \varphi}{3 + \sin \varphi}. \quad (2.19)$$

Using Eq. 2.17, the Drucker-Prager parameters can be related to the material strength in uniaxial tension and compression as

$$K = \frac{\lambda_{ct} + 2}{2\lambda_{ct} + 1} \text{ and} \quad (2.20)$$

$$\tan \beta = \frac{3(\lambda_{ct} - 1)}{\lambda_{ct} + 2}. \quad (2.21)$$

## 2.5 Digital image correlation method

### 2.5.1 Basic principles

The digital image correlation (DIC) method is a computational technique, which is capable of measuring displacements and strains by matching a grayscale intensity pattern between the initial undeformed and deformed sample surface [53–55]. Therefore, two main steps can be distinguished: 1) recording images of the test sample surface in an initial undeformed state and in the deformed or loaded state; and 2) processing of acquired images using software. At the initial state, the computational tool divides the measurement area into evenly spaced squares (facets) with their own specific grayscale pattern. When the test sample is deformed, the grayscale pattern is displaced. For instance, the grayscale pattern of the facet in the initial undeformed state is shown in Fig. 6a, and the same facet in the deformed state is shown in Fig. 6b. It can be seen that the DIC technique tries to track the initial grayscale pattern of the facet on the deformed surface allowing its displacements and transformations.

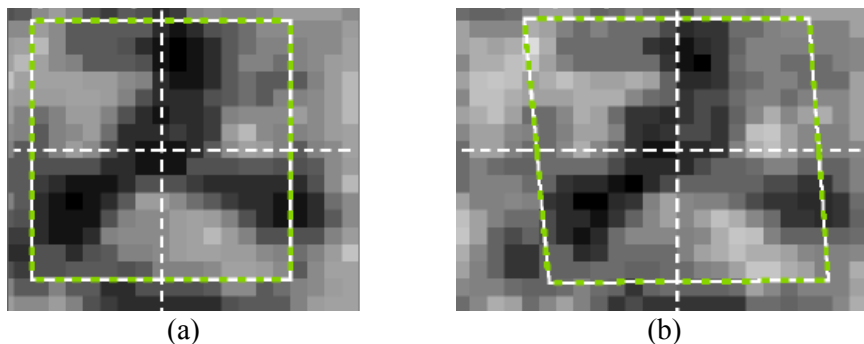


Fig. 6 The grayscale pattern of the facet in the initial (a) and deformed (b) state [55]

Schematically, the facet in the initial and deformed state is illustrated in Fig. 7. Fig. 7b shows that the facet in the deformed state is displaced by rotations and translations with respect to the global coordinate system



(x-y), and the local coordinate system of the facet (x'-y') will differ from the one in the deformed state (x''-y''). In order to find the point,  $P''$ , in the deformed state following expression is used [55]

$$P'' = u + P'F \quad (2.22)$$

where  $P'$  presents the coordinates of the point in the initial state,  $u$  is the rigid body translation, and  $F$  is the deformation gradient tensor. The deformation gradient tensor,  $F = UR^*$ , is split into the rotation matrix,  $R^*$ , and the stretch tensor,  $U$ . Point directions and rotations are described by  $R^*$ , whereas  $U$  describes the facet deformation. Concluding, the resultant strain measurements are dependent only on  $U$ , and are independent of rotations and rigid body translations.

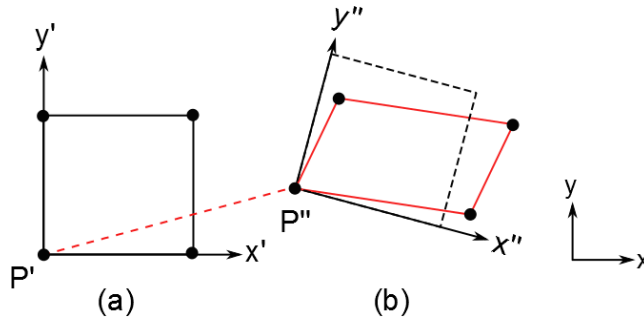


Fig. 7 Coordinates of the facet in the initial (a) and deformed (b) state

### 2.5.2 Surface pattern

Surface pattern is highly important to perform accurate strain measurements with the DIC method and has to meet a number of requirements [53–56].

- 1) High contrast in order to clearly allocate the pixels in the initial and deformed image.
- 2) Random distribution in order to distinguish the facet greyscale pattern from the neighbouring facets [57].
- 3) Appropriate size of speckles (neither too large nor too small). In the recorded images the speckle size should be sufficiently large so that it can be recognized by the computational tool. At the same time, the speckles should be sufficiently small in order to get larger variety of the greyscale values and to have an increased spatial resolution. According to the reference [53], the optimal size of the speckle should fit to the square with a length of 3 to 6 pixels.
- 4) The pattern must follow the deformation of the test sample, for instance, the pattern must not peel off or fracture before the sample.
- 5) The surface pattern must be dull as reflections can cause computational errors.
- 6) The pattern should lack large areas with bright and dark spots.
- 7) The surface has to be flat for 2D DIC.

### 2.5.3 Microscopic imaging

The DIC is particularly attractive as it can be applied across multiple length scales, thus it can be used from structural to nano scale measurements. For the micro-scale measurements, the DIC can be coupled with an optical, atomic force, and scanning electron microscopy (SEM) [54], i.e. images recorded with the microscope are used to measure a material deformation applying computational tools. Nonetheless, some limitations are reported. In the case of coupling with the SEM, the recorded image may be contaminated by distortions. Distortions are caused by electromagnetic field fluctuations, time shift between scan lines, heating, charging of the SEM stage or sample, and environmental factors (e.g. thermal fluctuations, mechanical vibrations, air currents, etc.) [58–60]. Besides contrast and lightning changes, these distortions can cause pixel movements which create non-uniform (“artificial”) displacement fields. Distortions can be recognized by baseline tests [53], which are performed either by recording images of the stationary test sample after certain time intervals or by conducting a rigid body in-plane translational test.

Moreover, the DIC measurements are reported to be affected by large deformation [54] and out-of-plane displacements [53]. In the case of large deformations, some pixels of the reference facet run out of the area of the assumed facet within the deformed image. Consequently, the similarity between the initial facet and the facet in the deformed image will decrease [54]. Due to the out-of-plane displacement, the distance between particles in the recorded image will change, which, consequently, will affect the measured strain values [53].

### 3 Macro-scale tests

#### 3.1 Mechanical characterization of an epoxy resin [P1]

Macro-mechanical properties of the epoxy polymer *Airstone 760E* typically used as a matrix in polymer/fibre composites were studied in the room temperature under different loadings as uniaxial tension, uniaxial compression, and pure shear. Material behaviour in simple tests was acquired following the standard testing procedures [61–63] (for more details see [P1]). Along with extraction of the macro-mechanical properties of the epoxy resin, the validity of the compression and shear test was evaluated. In compression, the load eccentricity and friction between the test sample and compression plate was studied. In shear, twisting and a non-uniform strain distribution along the test sample surface was discussed.

##### 3.1.1 An overview of mechanical behaviour in tension, compression, and shear

The experimental results in tension, compression, and shear are summarized in Table 1. It can be seen that the epoxy resin possesses rather ductile behaviour approaching the failure strains,  $\epsilon_u$ , of 4.8%, 10%, and 6% in tension, shear, and compression, respectively. Corresponding true strength,  $\sigma_u$ , is 72 MPa in tension, 86.5 MPa in compression, and 43 MPa in shear. The elastic modulus,  $E$ , slightly varies with a type of loading, and the mean value is approximately 3 GPa. Results are presented for the tests having a strain rate of 0.05%/s-0.08%/s in the elastic region.

**Table 1 Mechanical properties of the epoxy resin in tension, shear, and compression**

	$E$ [GPa]	$\sigma_u$ [MPa]	$\epsilon_u$ [%]
<i>Compression</i>	$3.43 \pm 0.08$	$86.5 \pm 2.0$	$5.8 \pm 0.1$
<i>Tension</i>	$3.01 \pm 0.03$	$71.8 \pm 0.4$	$4.8 \pm 0.1$
<i>Shear</i> <sup>a</sup>	$0.97 \pm 0.03$	$42.9 \pm 0.4$	$10.0 \pm 1.0$

<sup>a</sup> Values present the shear modulus, shear stress, and shear strain

##### 3.1.2 The effect of strain rate

Fig. 8a shows variations of the mechanical response in tension under the strain rates,  $\dot{\epsilon}$ , in the range of 0.037-0.25%/s. Results demonstrate that the test samples subjected to smaller  $\dot{\epsilon}$  have more gradual failure, and it becomes more abrupt increasing  $\dot{\epsilon}$ . At the same time, the test samples under higher  $\dot{\epsilon}$  experience slightly larger  $\sigma_u$  and  $\epsilon_u$  values. The true values of  $\sigma_u$  are within the range of 70-75 MPa, and the corresponding  $\epsilon_u$  is within the range of 4.7-5.1%. In overall, the effect of the strain rate within the given range was found as small.

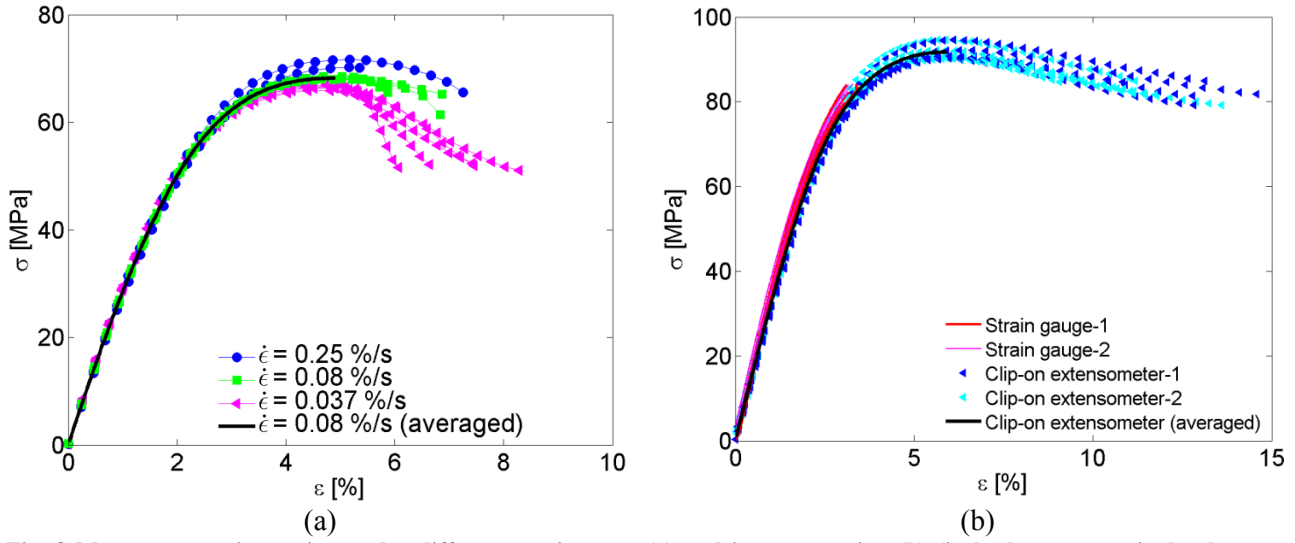


**Fig. 8** Measurements in tension under different strain rates (a) and in compression (b) (in both cases nominal values are presented)

### 3.1.3 Accuracy of the compression test

Some of the common problems related to an accurate compression test are the precise alignment of the test sample and the friction at the contact surface between the test sample and compression plate [62,64].

Experimentally, in order to evaluate a possible misalignment of the test samples, the strain measurement devices were applied on all four prismatic test sample faces. Results show that the load is applied evenly as  $E$  acquired from the measurement devices on the opposite faces show rather small differences. The  $E$  discrepancy of 8% and 12% was attained for the strain gauges and clip-on extensometers within the strain range of 0.25-0.65%, respectively. In Fig. 8b the acquired stress-strain relations from all four faces are presented.

Furthermore, in the experiments it was apparent that the friction at the interface between the test sample surface and compression plate cannot be neglected, because the epoxy resin specimens were prone to non-uniform deformation in the form of barrelling as shown in Fig. 9a. The friction is limiting the contact face deformation resulting in a non-uniform deformation of the test samples [62,64]. In order to study the effect of the friction on the stress-strain relation in compression, finite element methods (FEM) were applied. In the FEM model, the test samples in compression were modelled with unconstrained and constrained loading face. The latter mimics the friction at the interface. Numerical results showed that the model with the constrained faces deforms in the form of barrelling similar to the experiments. In the case of unconstrained loading faces, uniform deformation was predicted. Even though material deformation appeared highly different with and without constraint of the loading faces, the actual effect on the stress-strain relationship up to the maximum strength was negligible as shown in Fig. 9b. Applying the constraint, the stresses in the yield initiation region were slightly increased, which indicates that the experimentally measured stresses are slightly higher than material is actually possessing.

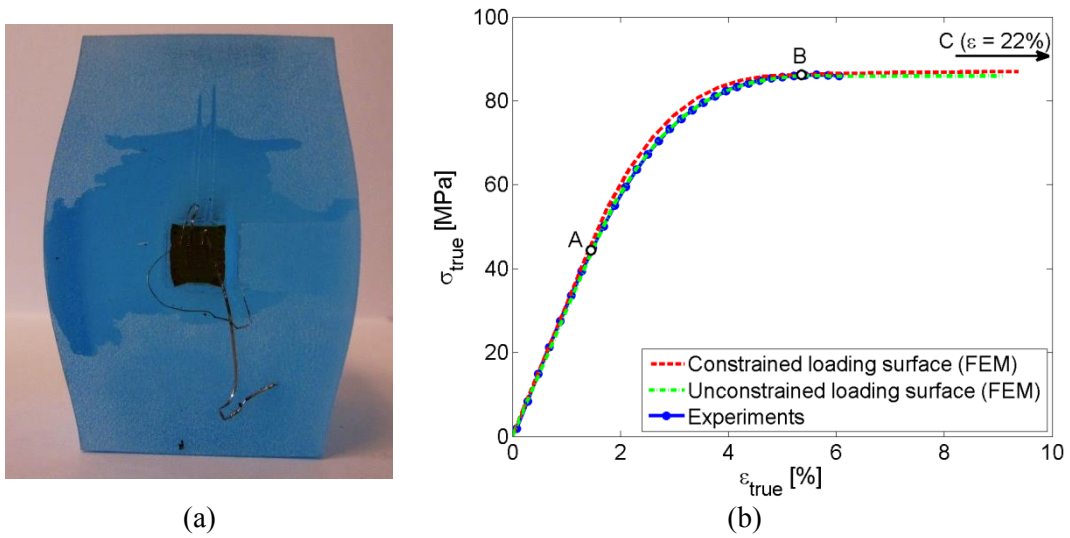


**Fig. 9** The sample tested in compression (a); the effect of friction at the interface between the test sample and the compression plate (b)

#### 3.1.4 Accuracy of the shear test measurements

According to the standard [61], the main difficulty of the accurate shear test for isotropic materials is force eccentricity, i.e. twisting. The main causes of twisting can be listed as a low tolerance to twist of the testing material (e.g. too thin sample), an out-of-tolerance fixture, and improperly installed test sample in the fixture [61]. The standard recommends that the twist of the test samples is evaluated, and the measurements from one surface are applicable if the twist is not exceeding 3%. Experimentally, minor twist of 1.5-4% was measured in the elastic region. The stress-strain curves attained from the strain gauges applied on opposite faces are shown in Fig. 10a (front surface: strain gauge-1 and back surface: strain gauge-2).

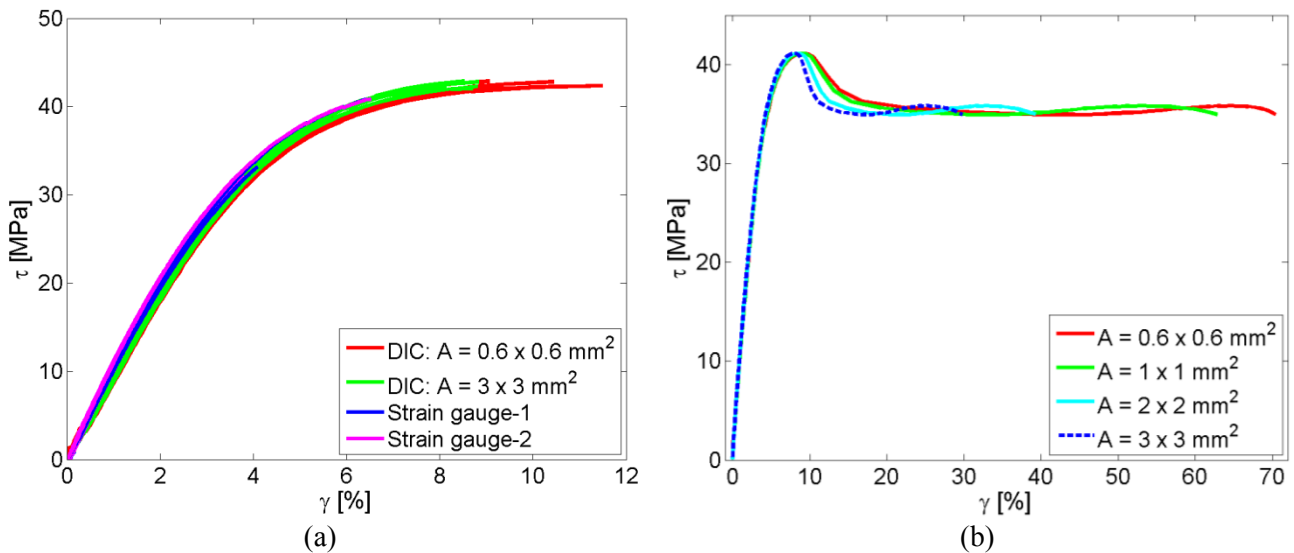


**Fig. 10** The stress-strain relation in shear up to the maximum  $\tau$  (a) and up to complete failure (b)

Considering that twist is small, further the shear strain was attained only from the front surface of the test samples utilizing a digital image correlation method (DIC). Acquiring the strain values with the DIC method, the stress-strain curve in shear was observed to depend on the measurement area,  $A$ , over which the shear strain is averaged as shown in Fig. 10a,b. The variations of the shear test results were studied considering an area to vary from  $A = 0.6 \times 0.6 \text{ mm}^2$  (120 points) to  $A = 3.0 \times 3.0 \text{ mm}^2$  (3000 points). The latter agrees with the measurement area covered by the strain gauge devices commonly used in the shear tests employing the Iosipescu fixture. Results showed that with a smaller  $A$  the steepness of the stress-strain curve in shear was slightly reduced (Fig. 10a), i.e. lower shear modulus was measured. Moreover, the strain at  $\tau_u$  (averaged between different samples) was increased by approximately 1% and strain at complete failure reached 70% (Fig. 10b). It was unclear how precise are these measurements up to failure, but it seemed that the DIC software was able to follow facets, i.e. decorrelation was not observed.

Observing the shear strain distribution along the test sample surface, the variations of the shear strain measurements with  $A$  were attributed to non-uniformities of the strain as shown in Fig. 11. In Fig. 11a the shear strain extracted from several line paths similar to those shown in Fig. 11b are presented. It can be seen that the strain distribution can be considered as uniform along the  $y$ -axis between the notch tips (red curve in Fig. 11), whereas non-uniform in the transverse direction along the  $x$ -axis (blue curve in Fig. 11). The non-uniformities along the  $x$ -axis varied with an applied load, i.e. the width of the strain peaks along the  $x$ -axis became narrower at higher loads. As a result of the strain non-uniformity along the  $x$ -axis, the averaged strain was reduced using larger measurement area.

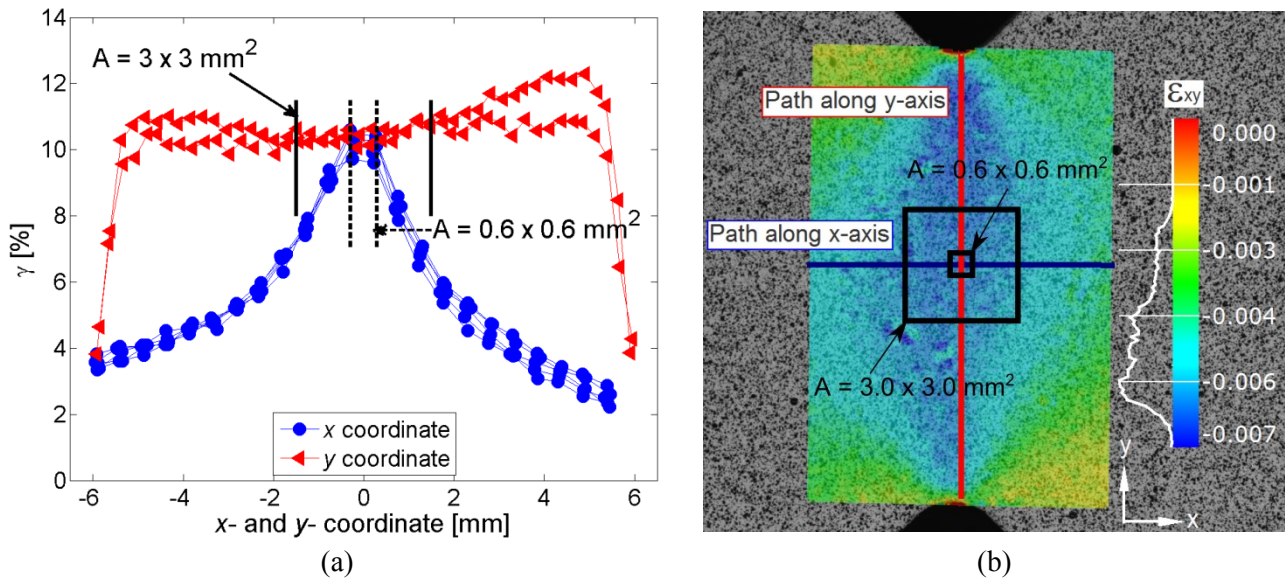


**Fig. 11** The shear strain variations along the  $x$ - and  $y$ - axis (a), and the contour plots showing a non-uniform shear strain distribution (b)

### 3.2 Application of pressure independent and dependent material models [P1]

The epoxy resin behaviour in shear and compression was predicted with two plasticity models. The first was  $J_2$ -flow theory, which considers that yield surfaces can be characterized with a von Mises yield criterion. In the second model, yield surfaces were described with a Drucker-Prager yield criterion. The main difference between two yield criteria is the component of a hydrostatic pressure (subsection 2.4), which is included in the Drucker-Prager criterion, whereas neglected in the von Mises yield criterion. The plasticity models were studied employing finite element methods, and results in tension were used to define initial mechanical properties of the epoxy resin.

#### 3.2.1 Different strength in compression and tension

In section 3.1.1 it was shown that the strength of the epoxy resin in compression is approximately 1.2 times larger than in tension. Possible reasons can be listed as

- 1) Residual stresses or Baushinger effect [65];
- 2) Larger material susceptibility to micro-crack initiation, nucleation, and growth in tension than in compression [15,65];
- 3) Pressure sensitivity of the epoxy resin [13,14,17].

First, the residual stresses or Bauschinger effect [65] originating from manufacturing or multiple loading steps like tension-compression can be expected to be particularly significant for highly anisotropic polymers [15] and less relevant for isotropic materials, where the difference is expected to be limited to a small strain range [65]. Second, the material behaviour in tension can be expected to be more susceptible to micro-cracking than in compression. As a result, failure during tension is initiated earlier. Observing the samples tested in tension, also presented in Fig. 12, the cracks starting from the edges can be indeed visible.

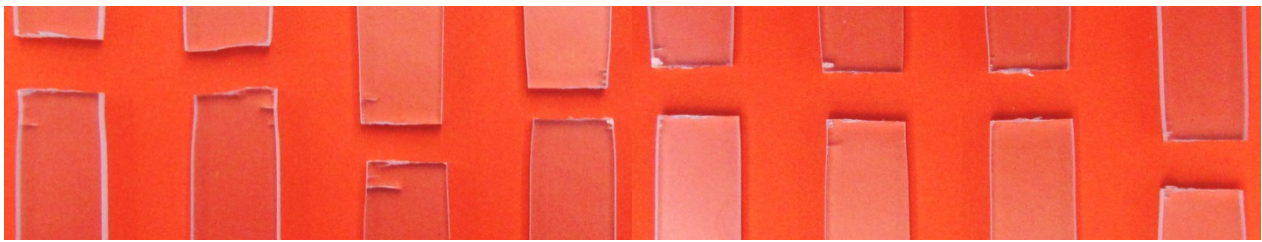


**Fig. 12** Test samples tested in tension with the strain rate of 0.037%/s

Third, in general, polymers are considered to be pressure sensitive materials, including the epoxy resin [66]. In order to estimate either material behaviour is pressure sensitive or not, the von Mises yield criterion was used. According to the von Mises yield criterion, the effective stress can be related to the stress in uniaxial tension,  $\sigma_t$ , compression,  $\sigma_c$ , and pure shear,  $\tau$ , as follows  $\sigma_e = \sigma_t = \sigma_c = \tau\sqrt{3}$ , and the effective strain in the uniaxial tension,  $\varepsilon_t$ , compression,  $\varepsilon_c$ , and pure shear,  $\gamma$ , can be obtained as  $\varepsilon_e = \varepsilon_t = \varepsilon_c = \gamma/\sqrt{3}$  (see subsection 2.4.1). Ideally, the effective stress-strain relations under different loading should overlap. In Fig. 13 the

plastic effective stress-strain relations acquired from the experiments in tension, compression, and shear are presented. Results show that there is a minor difference between the effective stress-strain relation in tension and shear, whereas the effective stress-strain relation in compression neither agrees with the one in tension nor shear. Disagreement between the effective stress-strain relation in compression and shear is suggested to indicate that the epoxy resin is possessing pressure dependent behaviour.

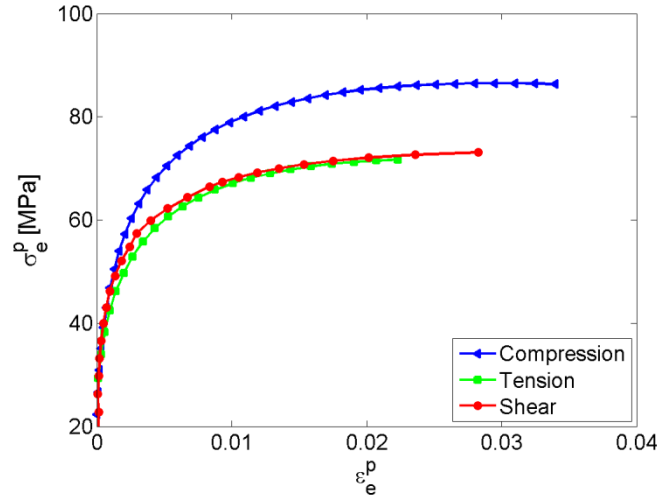


**Fig. 13 The effective plastic stress-strain curve in compression, tension, and shear (experimental results)**

### 3.2.2 Numerical results

Numerical results in Fig. 14a show that the  $J_2$ -flow theory based on the von Mises yield criterion predicts equally well the epoxy resin behaviour in shear and tension. On the other hand, according to this model the material is experiencing the same strength in tension and compression. This disagrees with the experiments. Consequently, the  $J_2$ -flow theory is assumed to be sufficient in numerical models, where the failure is governed by the response of the epoxy resin in shear and tension. For the models where the matrix behaviour under compressive loading is significant, the plasticity law based on the Drucker-Prager yield criterion is suggested. Fig. 14b shows that the mechanical behaviour of the epoxy resin is equally well predicted for all loadings assuming that the yield surface of the epoxy polymer can be described with the Drucker-Prager criterion. Small deviations in the yield initiation region of the stress-strain curve in compression are attributed to slightly larger stresses in the experiments due to the friction at the interface between the test sample and compression plate (see subsection 3.1.3). In the Drucker-Prager model, the friction angle is set to  $11^\circ$  (Eq. 2.21) and parameter  $K$  to 0.94 (Eq. 2.20).



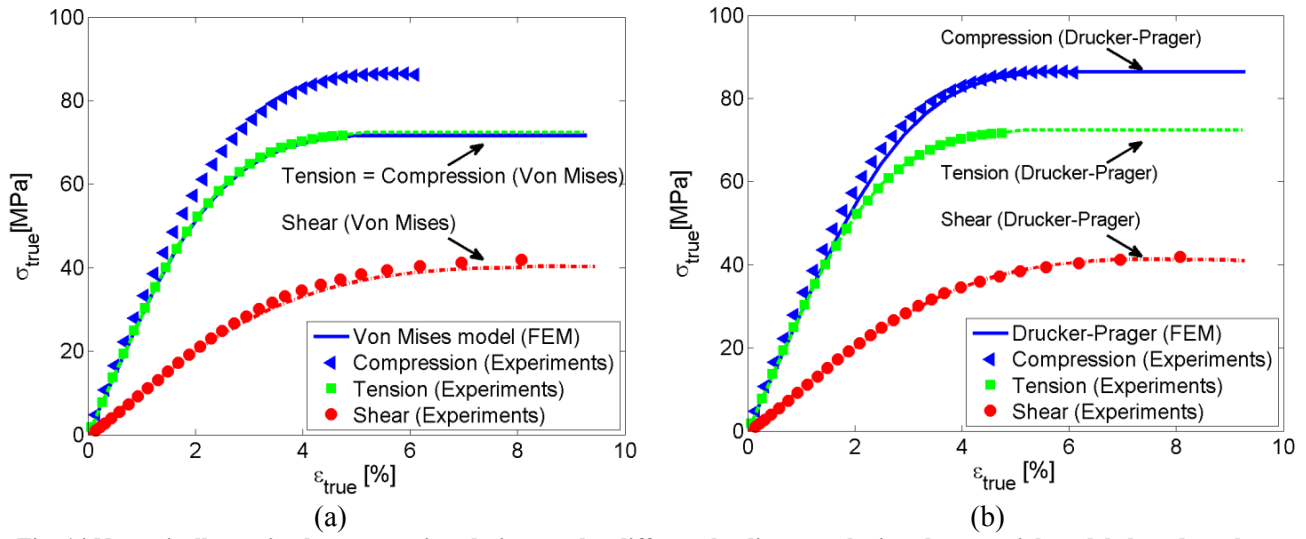


Fig. 14 Numerically attained stress-strain relations under different loadings employing the material models based on the von Mises yield criterion (a) and the linear extended Drucker-Prager yield criterion (b)

### 3.3 Errors of strain gauge devices used on compliant materials [P2]

Study was initiated by experimental observations during which different values of  $E$  were measured for identical polymers and polymer matrix based composites. The difference was observed comparing the measurements attained from the strain gauge with the laser and clip-on extensometers. The strain gauge devices tended to measure lower strains when applied on compliant materials than the alternative devices, which as a result gave higher  $E$  values (also reported elsewhere [67–73]). Similar problems are also reported for fibre Bragg grating sensors when embedded in polymer and polymer/fibre composite materials [74,75].

In this study, first, the strain gauge caused strain disturbances in the test sample were investigated. Second, a numerical parametric study was conducted to attain the most significant strain gauge and test sample properties, which affect measurements of the strain gauge device. Third, possible improvements of a design of the strain gauge devices, which would reduce the measurement errors, were evaluated.

#### 3.3.1 Experimental observations

In order to emphasize the problem, two examples of the measurement errors of strain gauge devices when attached on compliant materials are given below. In the *first case*, the polymer PC/ABS (polycarbonate/acrylonitrile butadiene styrene) was tested under cyclic tension loading within elastic strain region, i.e. the applied displacement was approximately 0.3 mm. The test samples had a dog-bone shape and the gauge dimensions of 40 x 6 x 1 mm<sup>3</sup> as shown in Fig. 15a,b. The strain was measured employing a laser extensometer with a gauge length of 11 mm (Fig. 15d) and strain gauges HBM LY11-3/350 with a gauge length of 3 mm. Fig. 15c shows that  $E$  is about 1.5 times larger implementing the strain gauge devices than the one gained from the laser extensometer.

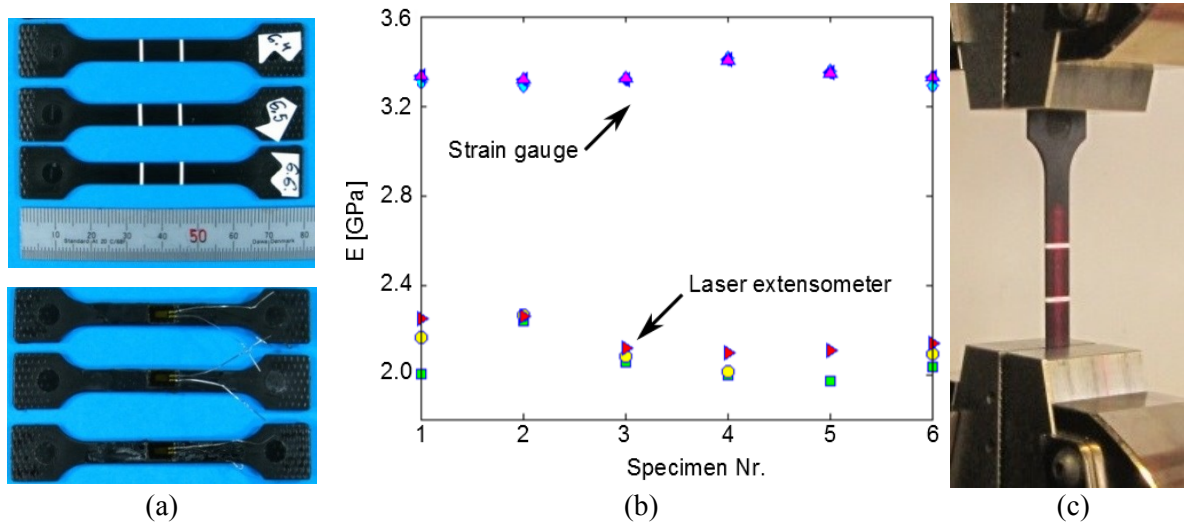


Fig. 15 Samples made of PC/ABS (a) are tested in tension (c) employing the strain gauges and laser extensometer; the extracted  $E$  values are presented in (b) (first case)

In the *second case*, the strain measurements were compared between three different devices, i.e. the strain gauge with a gauge length of 10 mm (*HBM LY11-10/350*), clip-on extensometer with a gauge length of 50 mm, and laser extensometer with a gauge length of 11 mm. The clip-on extensometers and strain gauges were used simultaneously, i.e. they were applied on both sides of the test sample as shown in Fig. 16c. The polymer samples were tested under cyclic tension in an elastic region (testing speed was 1 mm/min and the maximum displacement was 0.4 mm) having the gauge dimensions of 85 x 10 x 4 mm<sup>3</sup>, see Fig. 16a. Fig. 16b shows that  $E$  was the lowest ( $E = 2.15$  GPa), when the strain was measured with the laser extensometer, it was slightly increased applying the clip-on extensometers ( $E = 2.22$  GPa), and was the highest using the strain gauge device ( $E = 2.5$  GPa). The measurements by clip-on extensometer were slightly affected by the attached strain gauges.

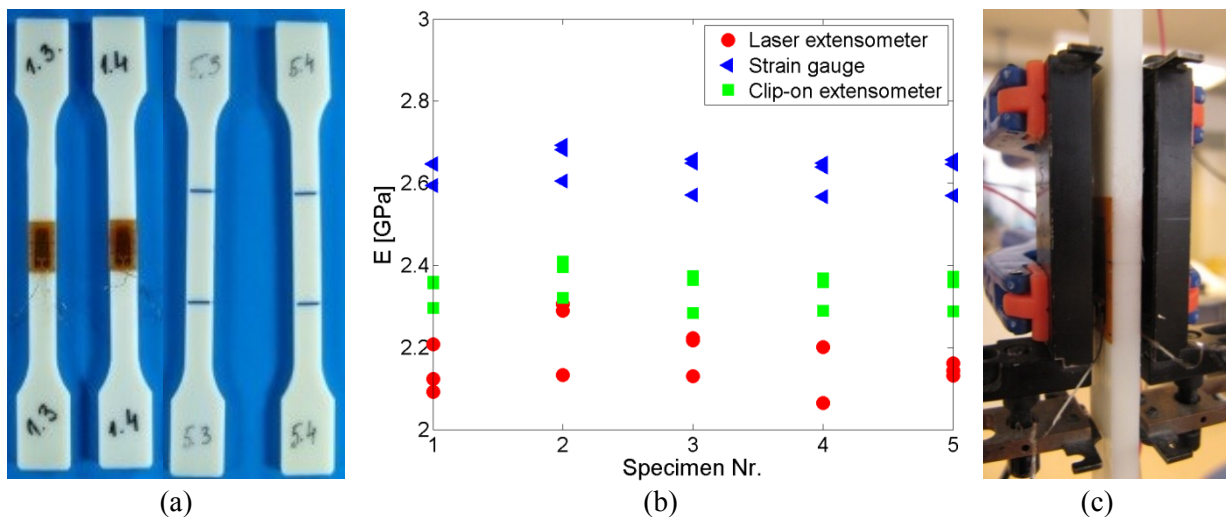


Fig. 16 Polymer samples (a) tested in tension (c) employing different strain measurement devices; the extracted  $E$  values are given in (b) (second case)

In addition, the variations of  $E$  with the measurement device were also observed for the composite materials with  $E > 10$  GPa. The ratio between the strain gauge and clip-on extensometer measurements was gained below 1.05 when both devices applied simultaneously. Some other deviations can be also seen in Fig. 8b and Fig. 10 (during compression and shear tests), where the stress-strain curves appear somewhat steeper, when strain is measured with strain gauge devices.

### 3.3.2 The strain gauge device

A strain gauge is a strain measurement device constructed from a thin metallic grid, which is enclosed between polymer films, as shown in Fig. 17. When the strain gauge is applied on a material undergoing deformation, the thin metallic grid (gauge) is also deformed. As a result of grid deformation, the current flow through the strain gauge [76,77] is changed. Performing experimental tests, the change of the electrical resistance,  $\Delta R/R_o$ , in the gauge is measured and converted into the strain values using the gauge factor,  $GF$ , given as

$$GF = \frac{\Delta R / R_o}{\Delta L / L_o}, \quad (3.1)$$

where  $L_o$  is the initial length and  $\Delta L$  is the displacement of the gauge. Most often,  $GF$  is given by a manufacturer, which is found from the strain gauge calibration on a stiff material like steel [78].

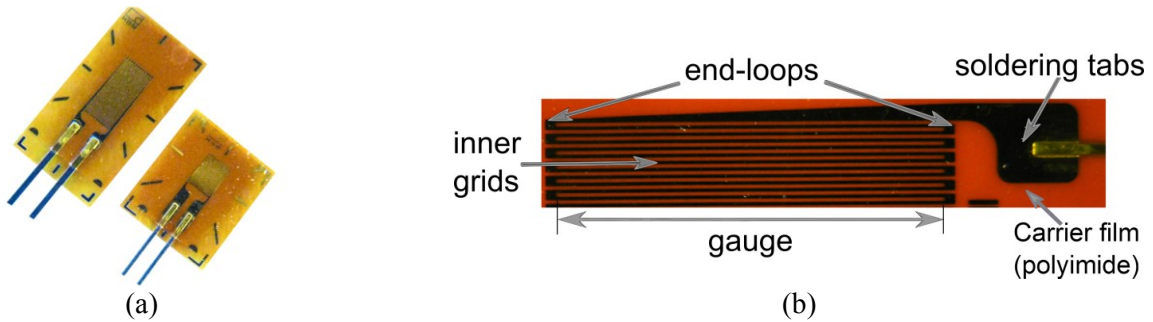


**Fig. 17** The HBM *Y* series strain gauge devices (a) and different parts of the strain gauge pattern (b)

### 3.3.3 Numerical model

Detailed 2D and 3D numerical models were used to simulate the experimental set-up, including an exact distinction of different strain gauge parts. The 2D model was simplified retaining the distinction between the end-loops, gauge, carrier film, and soldering tabs (Fig. 17b); whereas the 3D model included exact copy of the actual strain gauge device and is presented in Fig. 18. In both cases, the strain gauge pattern represented the commercially available *Hottinger Baldwin Messtechnik GmbH* (HBM) *Y* series strain gauges [79] with the gauge length,  $L_{gauge}$ , from 1.5 to 10 mm, similar to those shown in Fig. 17a. In these strain gauges, the metallic grid is made of a constantan with  $E = 180$  GPa [80], and a polymer film is made of polyimide with  $E = 3.1$  GPa [80]. In the numerical models, the test samples were assumed to have  $E$  from 1 GPa to 200 GPa and a thickness,  $t_{spec}$ , within the range of 1-30 mm. Moreover, in order to exclude the effect of strain

transition through a carrier film and adhesive, a numerical calibration was conducted. The numerical calibration involved determination of the strain distortions applying different type of strain gauges on a 200 GPa stiff and 30 mm thick test samples. The observed strain discrepancy of approximately 1% was extracted from all numerical results.

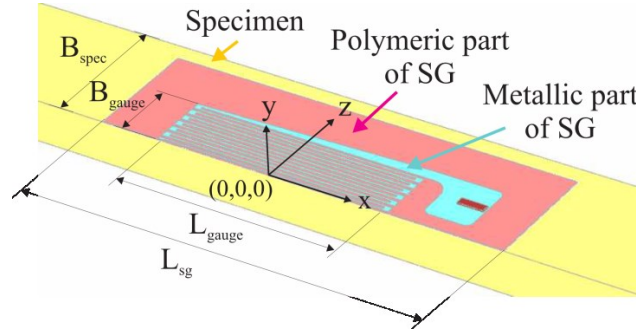


**Fig. 18 A numerical 3D model with an exact pattern of the strain gauge device**

A correction coefficient,  $C$ , was used in order to evaluate the errors of the strain gauge measurements and to provide the gauge factor adjustment values.  $C$  shows the ratio between the elastic modulus extracted from the strain gauge measurements,  $E_{sg}$ , and the one defined in the simulation model,  $E_{spec}$ ,

$$C = \frac{E_{sg}}{E_{spec}}. \quad (3.2)$$

In the experiments  $C$  was expressed as the ratio between  $E_{sg}$  and  $E$  extracted from the clip-on extensometer,  $E_{ext}$ , and laser extensometer,  $E_{laser}$ , measurements. For more details regarding methods, see [P2].

#### 3.3.4 Strain disturbances around the strain gauge

Numerically obtained strain disturbances caused by the attached strain gauge device for material with  $E = 1$  GPa and  $t_{spec} = 30$  mm are presented in Fig. 19. From contour plots, it can be seen that strain is lower below the gauge, and strain is non-uniform along the gauge length ( $x$ -axis) and width ( $z$ -axis). In the thickness direction, the deformation of more compliant material is constrained by the attached strain gauge. Depending on how much the strain gauge affects the strains through the thickness, the reinforcement by the strain gauge can be divided into the local and global reinforcement [77]. The global reinforcement describes the phenomenon, where strains are modified through the whole thickness with the attached strain gauge. In the local reinforcement, the strains are considered to change only close to the attached strain gauge [68].

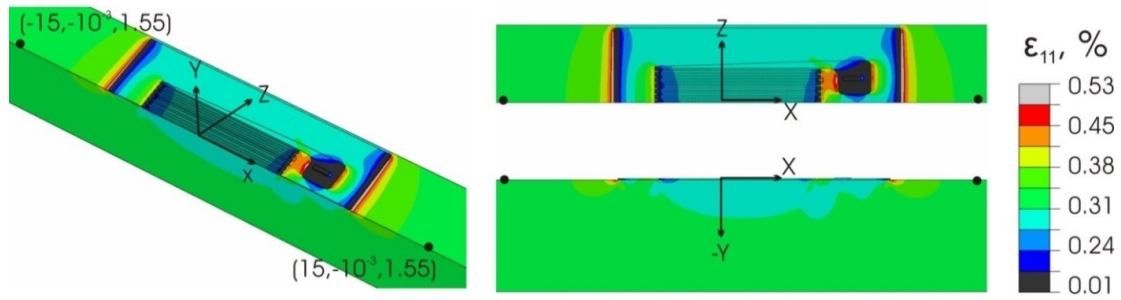


**Fig. 19 Numerically attained strain disturbances around and below the strain gauge device**

Furthermore, the normalized strain variations along the strain gauge length are illustrated in Fig. 20 (for the same sample given in Fig. 19). The normalized strains were obtained dividing strains at the surface of the specimen by the average strain experienced over the whole specimen. Sharp peaks of the normalized strains are related to the edges where strains are transferred between the metal and carrier film, as well as the carrier film and the test sample. Peaks indicate very large and very low strain existence along the edges. Due to the strain distortions along the edges, inside the gauge the normalized strains tend to decrease close to the end-loops, which respectively affect the strain measurement accuracy of strain gauge devices. The strain reduction in the gauge section close to the end-loops can be also seen in the contour plots given in Fig. 19.

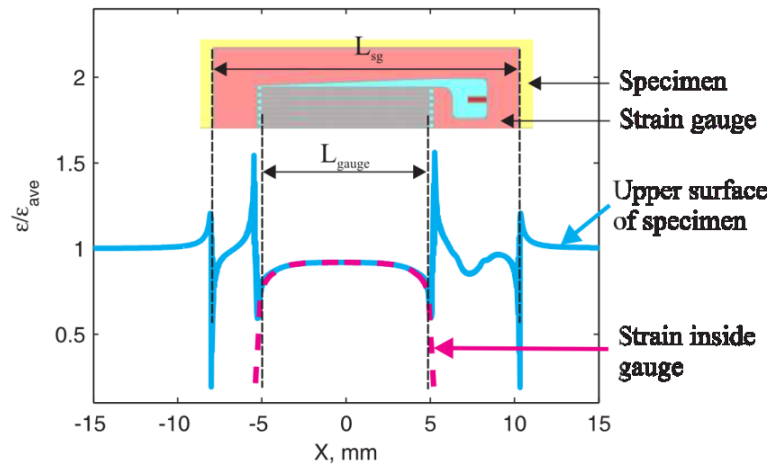


**Fig. 20 Strain distortions on the test sample surface below the attached strain gauge**

In addition to numerical study, the strain disturbances were measured experimentally on the test samples with  $E = 2$  GPa and  $L_{gauge} = 1.5$  mm utilizing the 2D digital image correlation method. The test samples were tested in tension recording images with an optical microscope. Similarly as in the numerical model, the area occupied by the strain gauge showed smaller strain values, i.e. above the strain gauge  $\varepsilon$  was around 0.4% and for rest of the sample  $\varepsilon \approx 0.6\%$ . Larger strain reduction was observed in the soldering tab area having a strain minimum of 0.1%. Applying the DIC method, the strain distortions were observed at the edges separating the test sample and polymeric part of the strain gauge. Unfortunately, the distortion peaks at the edges of the end-loops were not captured.

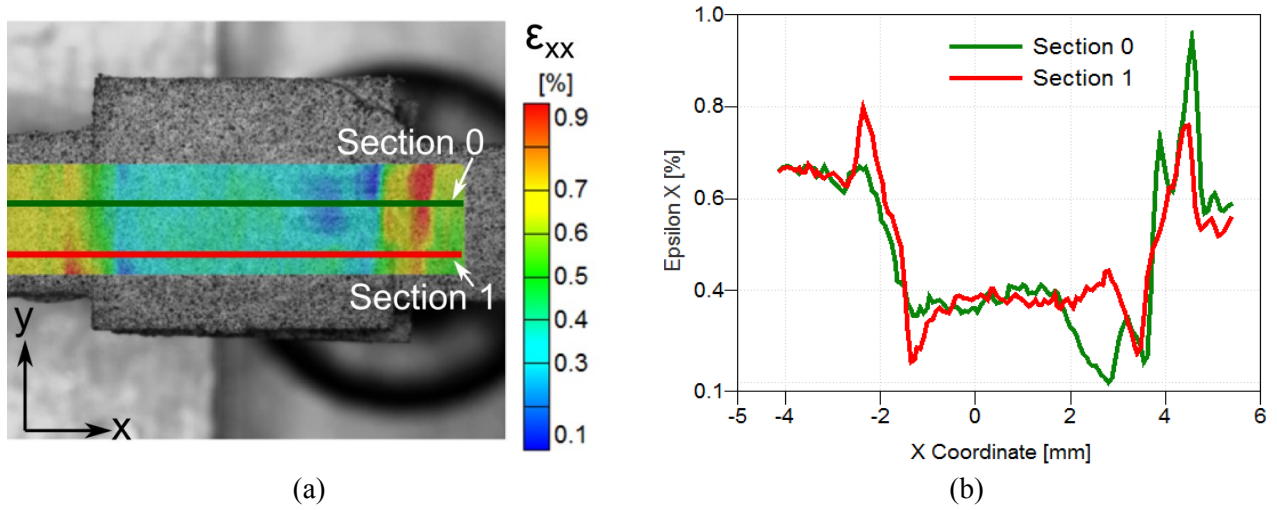


**Fig. 21** Experimentally attained strain contour plots (a) and strains along the line paths (b) for the sample with  $E_{spec} = 2$  GPa with the attached strain gauge device with  $L_{gauge} = 1.5$  mm

### 3.3.5 The effect of gauge length

One of the most important parameters affecting the strain gauge device measurements is the gauge length,  $L_{gauge}$  (Fig. 17b). From the numerical results, it appeared that the strain measurements by shorter strain gauges are more affected by the strain distortions close to the end loops what leads to higher measurement errors, even though the longer strain gauges contribute to a greater volume of total strain field disturbances, i.e. larger surface area of the sample is constrained. For instance, the normalized strain distribution inside the gauge with a different  $L_{gauge}$  is given in Fig. 22. Results show that the shortest strain gauge is giving the lowest strains, and the strain measurements become closer to the actual strains of material as the strain gauge length is increased.

The effect of the gauge length on the correction coefficient,  $C$ , for testing materials with  $E_{spec}$  within the range of 1-200 GPa is presented in Fig. 23. Numerical results show that the strain gauge with  $L_{gauge} = 1.5$  mm applied on the test sample with  $E_{spec} = 1$  GPa will need  $C$  of 1.52, i.e. the strain gauge measurement error is 52 %. The values of  $C$  are significantly reduced with a stiffer material and approach approximately 1.05 if applied on the material with  $E_{spec} = 10$  GPa. Profoundly lower  $C$  values are needed if the longer strain gauges are used. For instance, applying the strain gauge device with  $L_{gauge} = 10$  mm on the material with  $E_{spec} = 1$  GPa, the measurement error is approximately 15% and is reduced to 5% when applied on the material with  $E_{spec} = 3$  GPa. Estimated errors and correction coefficients are provided for the samples with a thickness ( $t_{spec}$ ) of 30 mm.



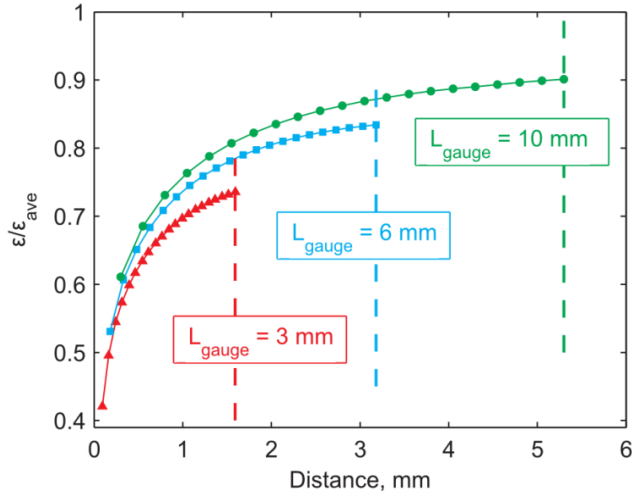


Fig. 22 The strain distribution inside the gauge ( $E_{spec} = 1$  GPa and  $t_{spec} = 30$  mm)

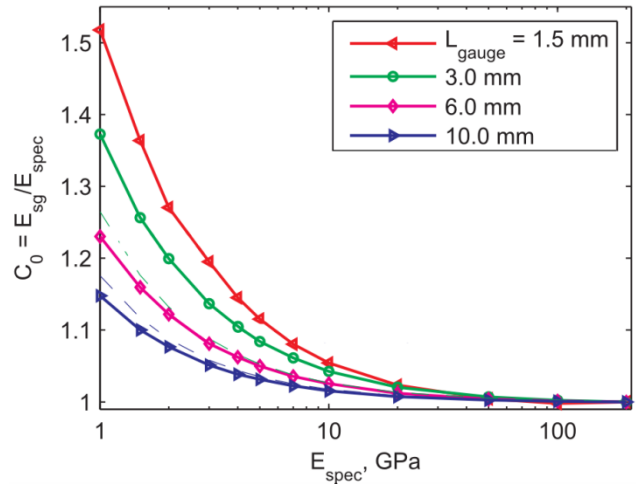


Fig. 23 The correction coefficient variations with the gauge length ( $t_{spec} = 30$  mm)

### 3.3.6 The effect of test sample thickness

Another parameter significantly affecting the accuracy of the strain gauge measurements is the test sample thickness,  $t_{spec}$ . The effect of  $t_{spec}$  on  $C$  using the strain gauges with different  $L_{gauge}$  is shown in Fig. 24 for material with  $E_{spec} = 1$  GPa. Results show that for thin samples,  $t_{spec} = 1$  mm,  $C$  is approaching 2.18 indicating the strain measurement error of 118 % for all strain gauge types. Increasing the test sample thickness up to 5 mm,  $C$  is profoundly reduced up to 1.2-1.55 depending on the length of the gauge. Starting with a certain thickness,  $t_{cr}$ ,  $C$  becomes independent of further increment of  $t_{spec}$  and depends only on the type of the strain gauge device and material stiffness. The existence of  $t_{cr}$  indicates a transition from global to only local reinforcement effect.

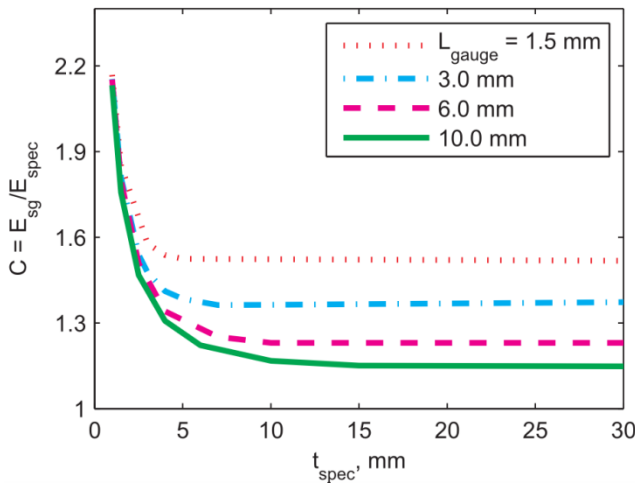


Fig. 24 The effect of the sample thickness ( $E_{spec} = 1$  GPa)

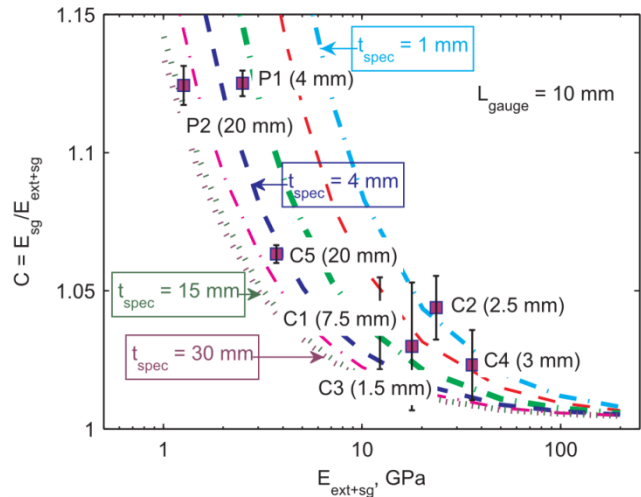


Fig. 25 The numerical results compared to the experiments

### 3.3.7 Correction of experimental measurements

The numerically attained  $C$  values could be used to correct the experimentally attained strains by the strain gauge device. In this relation, the numerically derived  $C$  values were compared to the experiments as shown

in Fig. 25. The experimental data are presented for the test samples with different thicknesses and material stiffness, which are attached to the strain gauges with  $L_{gauge} = 10$  mm. The neat polymer materials, which are denoted as *P1* and *P2* with a thickness of 4 mm and 20 mm, respectively, have the largest values of  $C$  (in this case expressed as the ratio  $E_{sg}/E_{sg+ext}$ ). The thicker sample, *P2*, is found to agree well with the numerical results with  $C = 1.125$ , whereas for *P1* the ratio  $E_{sg}/E_{sg+ext}$  is slightly larger for the experimental results ( $C = 1.125$ ) than predicted numerically ( $C = 1.1$ ). Further, the correction coefficient descends more for multi-axial glass fibre and polymer matrix composites, denoted as *C1*, *C2*, *C3*, *C4*, and *C5*. In overall, the correlation between the experimental correction coefficient and  $E_{spec}$  follows the same tendency as it was numerically predicted. However, the effect of the test sample thickness was not captured for the composite materials. This is suggested to be due to the substantially inhomogeneous structure of composites.

### 3.3.8 Enhanced strain gauge design [81]

The impact of  $L_{gauge}$  has been explained with the strain distortions around the edges separating the gauge from the polymeric film. This observation led to an assumption that longer end-loops of the strain gauge device (Fig. 26) would improve the measurement precision isolating the gauge from the edge induced distortions. Thus, a 3D model was created increasing the length of the end-loops from 0.3 to 2 mm for the strain gauge device *LY11-10/350* ( $L_{gauge} = 10$  mm) attached to 15 mm thick specimen with  $E_{spec} = 1$  GPa. Fig. 26 shows that measurement errors are reduced using longer end-loops, i.e.  $C$  is decreased from 1.138 to 1.078. The effect is expected to be even more profound for shorter strain gauges.

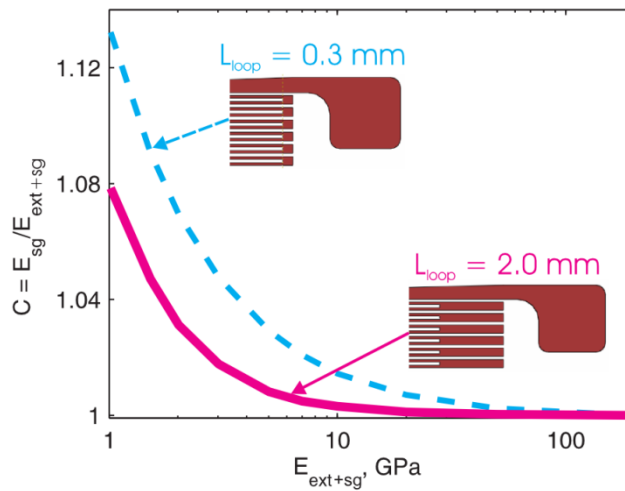


**Fig. 26** Reduced strain measurement errors with improved strain gauge design



#### 4 Micro-scale tests

During macro-scale measurements, the failure strains of the epoxy resin were found within the range of 5-6% and the failure stress within the range of 70-85 MPa. Now, the same epoxy resin is tested at the micro-scale in order to extract the micro-scale stress-strain relation. Strain variations are studied around the notch representing the region with locally magnified stress, similarly as a void in a bulk material. Samples are made with the notches with the initial width,  $\delta_{i0}$ , of 95  $\mu\text{m}$  (Test Series 1) and 245  $\mu\text{m}$  (Test Series 2) as shown in Fig. 27. Double cantilever beam (DCB) tests are performed in a vacuum chamber of an environmental scanning electron microscope (ESEM). From the images captured in the ESEM, strains are measured employing a 2D digital image correlation method. The corresponding stresses are determined applying analytical and numerical approaches. The experimental part of the micro-scale tests is given in paper [P3]. The summary of [P3] includes

- Overview of strains measured both in Cartesian and cylindrical coordinate system;
- Strain field comparison between the notches with different initial width by normalizing all length parameters with the notch opening displacement,  $\delta_i$ ;
- Determination of the micro-scale stress-strain relation by means of the strain energy density.

The micro-scale experiments are supplemented with the FEM modelling results. Applying numerical methods, the strain fields measured experimentally are fitted to power law hardening materials with different  $n$  values. In addition, the significance of the micro-cracks evolving from the notch edge on the resultant strain measurements is evaluated. Furthermore, before actual tests, an optimization of the DCB test sample dimensions was made and published in the paper [P4]. A short summary is given in the part *Methods*.

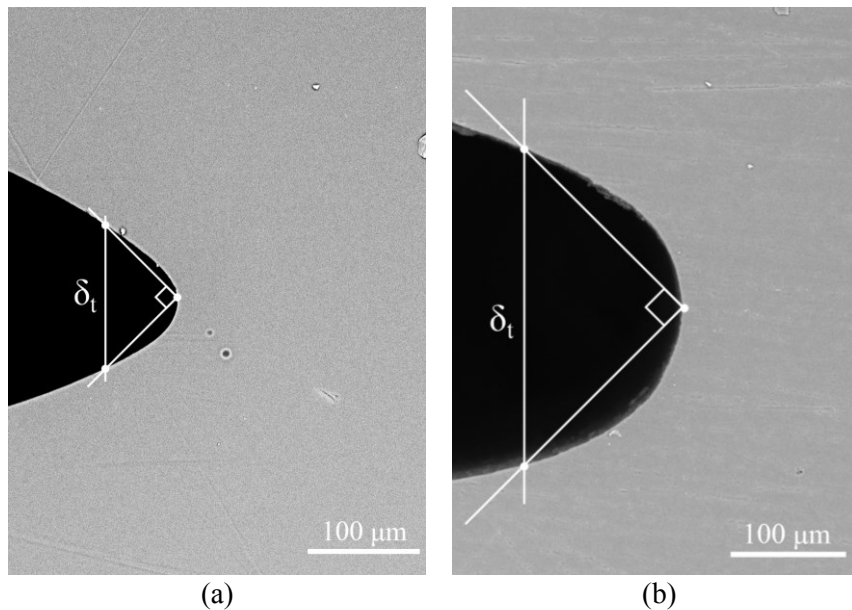


Fig. 27 The notch from the Test Series 1 with  $\delta_{i0} = 95 \mu\text{m}$  (a) and Test Series 2 with  $\delta_{i0} = 245 \mu\text{m}$  (b)

## 4.1 Methods [P3, P4]

### 4.1.1 Optimization of the DCB test sample design [P4]

A pre-study of a DCB test sample design for micro-mechanical testing is done in order to obtain reliable fracture characterizing parameters for thermoplastic and thermoset polymers within the restrictions of the DCB fixture [82]. The thermoplastic sample is assumed to be 0.75 mm thick with  $E = 250$  MPa and critical  $J$  value of  $20 \text{ kJ/m}^2$  [83], whereas the thermoset sample is assumed to be 1 mm thick with  $E = 3$  GPa and  $J_c = 0.1\text{-}1 \text{ kJ/m}^2$  [83]. Fig. 28 shows that the initial test sample, both for thermoplastic and thermoset material, includes reinforcing beams at the side edges in order to control a beam deflection and rotation, as well as to ensure the specimen beam between the load-introduction and the crack tip is under pure bending [84]. The main parameters varied during the numerical study are crack length and stiffness of reinforcing beams.

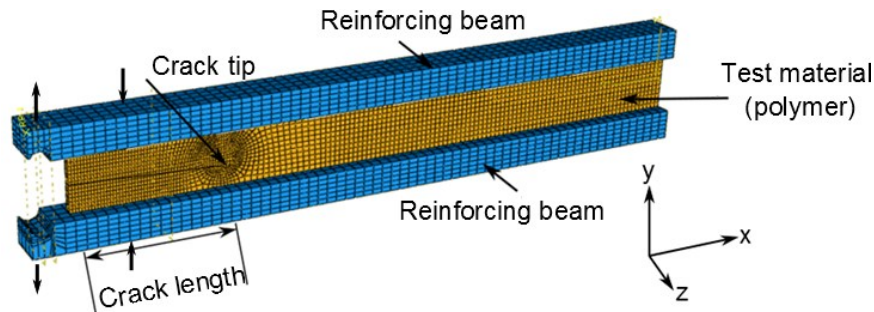


Fig. 28 The DCB test sample

Evaluation of the test sample design adequacy included determination of

- 1) Deflection of the beams, which are supposed to be within the limits of the DCB fixture;
- 2) Stress intensity around the crack to ensure that the material behind the crack tip is loaded under pure bending moments and is not affected by the test sample geometry;
- 3) Studying compression stresses at the rear end, including buckling analysis.

For instance, the deflections of the thermoplastic sample beams without reinforcing beams would reach the DCB fixture limits before fracture. The numerical study showed that using the reinforcing beams with  $E$  within the range of 2.8-4 GPa and dimensions of  $70 \times 4 \times 3 \text{ mm}^3$  the deflections would remain within the limits of the DCB fixture and stress intensity around the crack would be sufficient to initiate fracture. For the epoxy polymer, the reinforcing beam selection is found to be less critical as the epoxy is possessing sufficient stiffness and low  $J_c$ . From the numerical analysis, it appeared that the actual tests could be performed without reinforcing beams. Moreover, the crack length within the range of 19 mm – 34 mm is found to be appropriate to avoid large deflections, ensure that the J-integral is not affected by the sample geometry, and that the beams behind the crack are loaded under pure bending. Furthermore, the compressive stresses at the rear end are not expected to cause buckling, and the yielding zone is predicted to be confined to the crack tip for the epoxy polymer.

#### 4.1.2 Test sample manufacturing

Samples used in macro- and micro- scale tests are made of *Airstone 760E*. The main manufacturing processes are kept the same as mixing with a hardener *Airstone (TM) 766H*, which is 1/3 of the epoxy polymer weight, degassing in a vacuum chamber up to the vacuum of 98%, curing at 50°C for 5 hours, and, after cooling up to the room temperature, post-curing at 80°C for 3 hours.

For the samples used in micro-scale tests, after degassing, the liquid epoxy is poured into the mould consisting of two glass plates positioned parallel to each another with a distance equal to the specimen width as shown in Fig. 29. In order to ensure that the liquid resin does not pour out, a rubber pipe (red line in Fig. 29) between two glass plates is wrapped around three side edges. Clamping holders are used to fix the mould. Furthermore, in order to create notches with different radii a sharp paper knife razor wrapped with an ETFE (ethylene tetrafluoroethylene) film with thickness of 12.7  $\mu\text{m}$  and PTFE (polytetrafluoroethylene) adhesive tape with thickness of 80  $\mu\text{m}$  is immersed into an uncured epoxy. As a result, the test samples have an initial notch width of approximately 95  $\mu\text{m}$  and 245  $\mu\text{m}$ , denoted as Test Series 1 and Test Series 2, respectively.

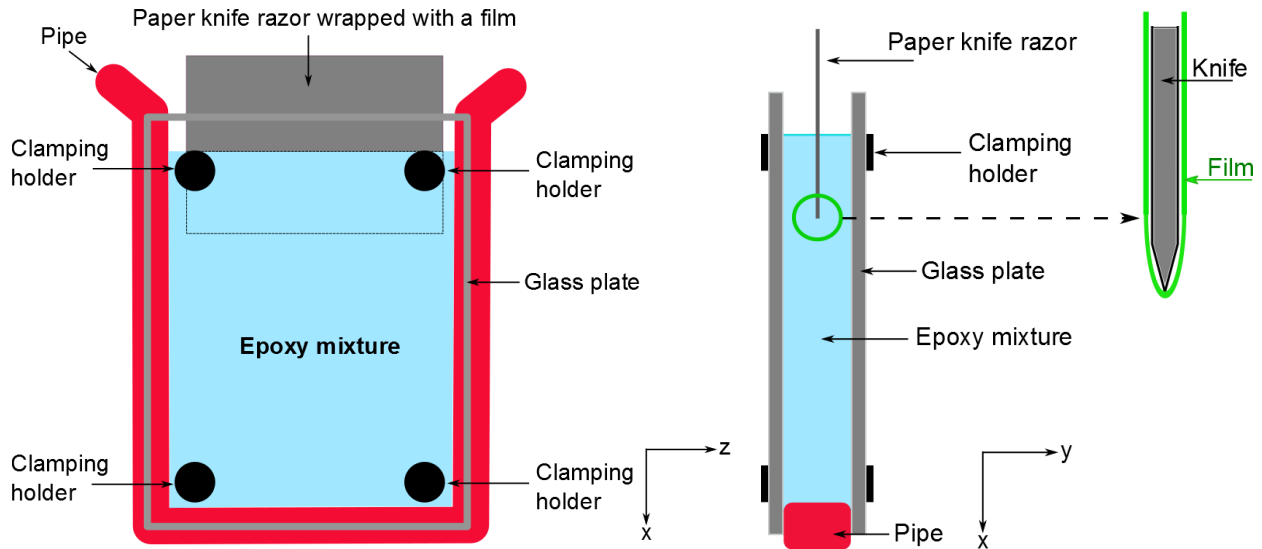
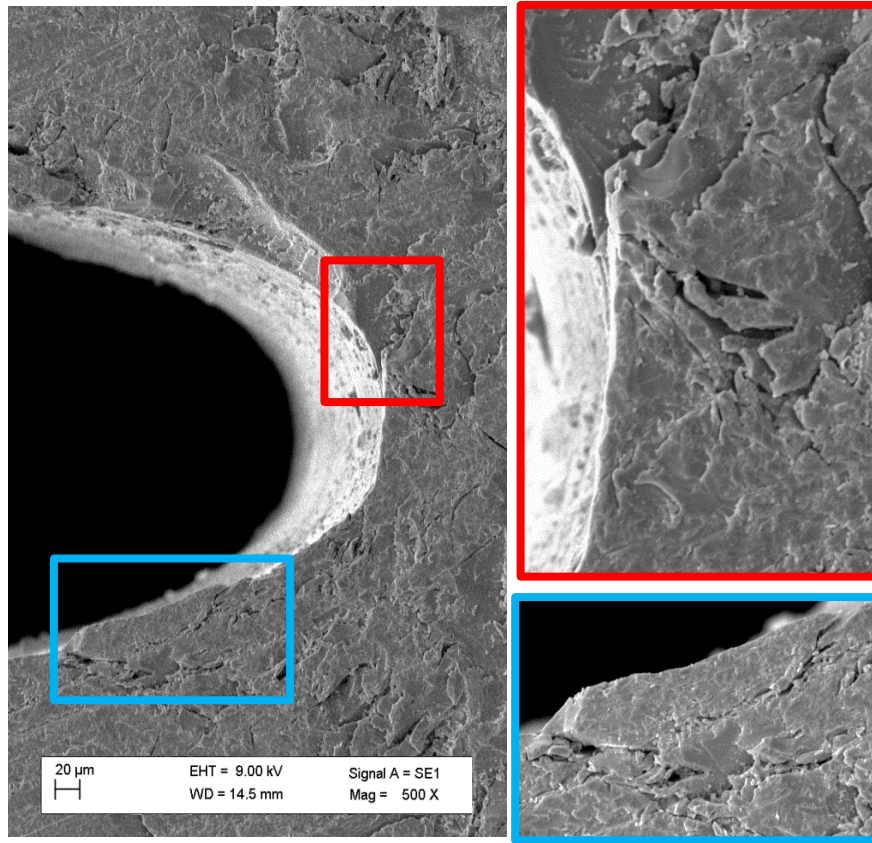


Fig. 29 The DCB test sample manufacturing

#### 4.1.3 Machining

After post-curing, the paper knife razor is removed and the block of epoxy is cut into samples with thickness of 2.5 mm. Further, holes with a radius of 1mm are drilled at the end of the beams to create a “hook” for fixing the test sample within the DCB fixture. After cutting, the sample surface was rather rough and defects around the notch could be observed as shown in Fig. 30. In order to remove cutting defects and deep scratches around the notch, water cooled grinding of the front and back surface of the test samples is done utilizing a machine *Struers LabPol 25*. A sandpaper with a grit 1000 and 4000 is used to grind off approximately 0.4 mm and 0.1 mm, respectively, including the front and back surface.



**Fig. 30 The test sample surface after cutting**

Additional polishing is done with a diamond paste with monocrystalline diameter of  $1\mu\text{m}$  using a silk cloth to remove grinding scratches on the surface used for strain measurements. In total, the polishing time was about 5 to 10 minutes. After machining, the shadings around the notches could be seen in a polariscope, particularly for the notches with a smaller size as shown in Fig. 31a. These shadings are indicating residual stresses around the notch [85]. In order to remove residual stresses, the test samples are heated in an oven at  $80^\circ\text{C}$  for one hour. After heating, shadings either disappeared (Fig. 31b) or became smaller. Heating for a longer time did not show any further reduction of shadings around the notch.

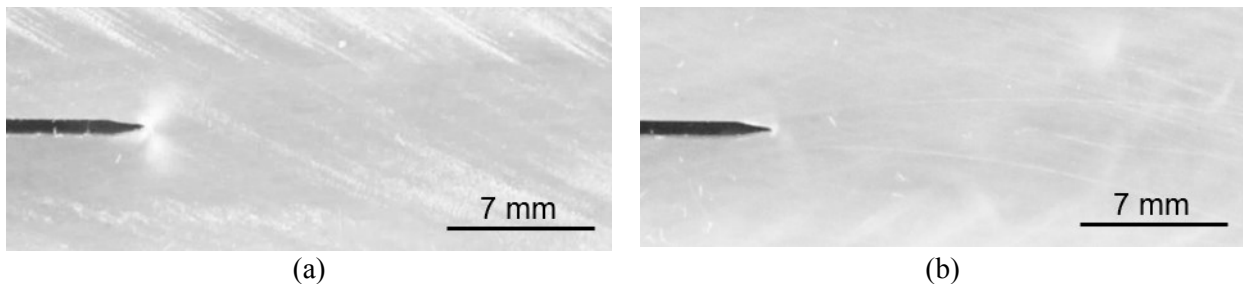


**Fig. 31 Residual stresses around the notch after machining (a) and after heating 1h at  $80^\circ\text{C}$  (b)**

At last, the final test sample dimensions are given in Fig. 32.

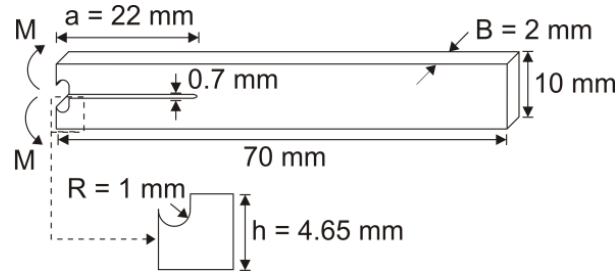


**Fig. 32 Final dimensions of the DCB test sample**

#### 4.1.4 Speckle sputtering

After manufacturing and machining steps, a gold layer with thickness of 15 nm is sputtered onto the surface to be imaged. This made possible to evaluate a surface smoothness before and after the test, since the speckle particles applied afterwards can be easily removed by immersing samples in ethanol and applying ultrasound. Gold layer gives also a higher contrast for ESEM images later used for the digital image correlation method (DIC) analysis. In the next step, speckles are sprayed on the test sample surface in order to utilize the DIC method for strain measurements. Speckles are created by spraying solutions containing 1 w% of Ti- and 5 w% of Fe- oxide particles. The mean diameter of  $\text{TiO}_2$  and FeO particles is 0.5  $\mu\text{m}$  and 1.1  $\mu\text{m}$ , respectively, and the total range of particle size is from 0.05  $\mu\text{m}$  to 3  $\mu\text{m}$  according to the measurements by a laser diffraction particle size analyser *Beckman Coulter LS 13 320* [86]. The spraying is done with an airbrush *BossDye-132* with a nozzle size of 0.3 mm [87].

#### 4.1.5 Loading procedure in the experimental set-up

The test samples are subjected to a double cantilever beam (DCB) test applying symmetric bending moments inside an environmental scanning electron microscope (ESEM) *ZEISS EVO 60* [88]. The experiments are performed using the DCB fixture specially designed by Sørensen et al. [82]). Fig. 33 shows the main parts of the fixture as stage, grips, rollers, brads, and thin steel band, which runs in-between rollers. Before the test, the steel band is fixed and two tensile forces of identical magnitude are applied at the ends of the steel band by the displacement of the stage. The moments in the test sample beam are created by brads separated by the distance of 12 mm. The front brads are transferring the tensile load, whereas the middle brads create the compressive force. The loading fixture is equipped with a load cell with a capacity of 75 N (corresponding to a maximum moment of 6 Nm) and high precision linear displacement transducer *LDI 8/1* for load and opening measurements, respectively.



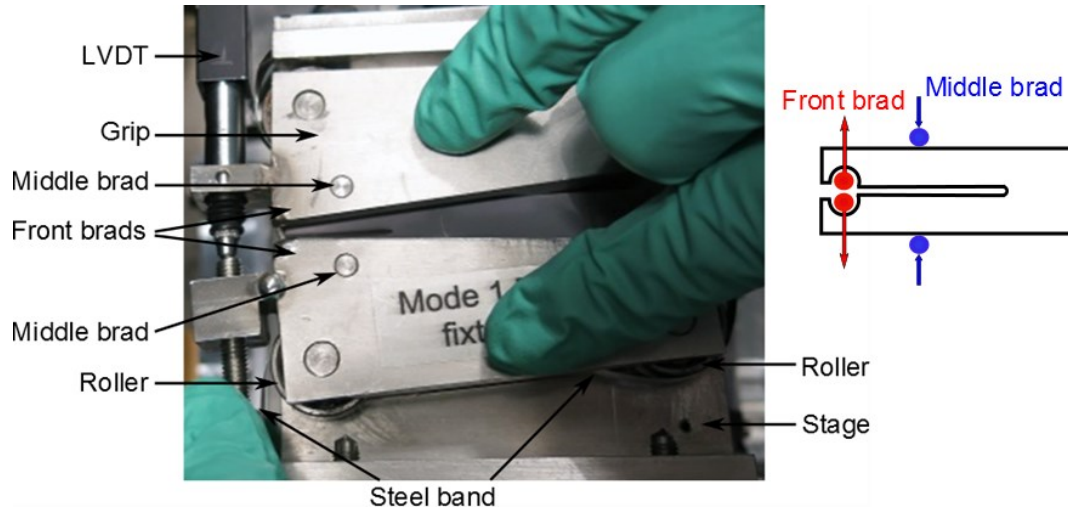


Fig. 33 The DCB test fixture used in the micro-scale tests

Displacement fields indicating symmetric loading are presented in Fig. 34.

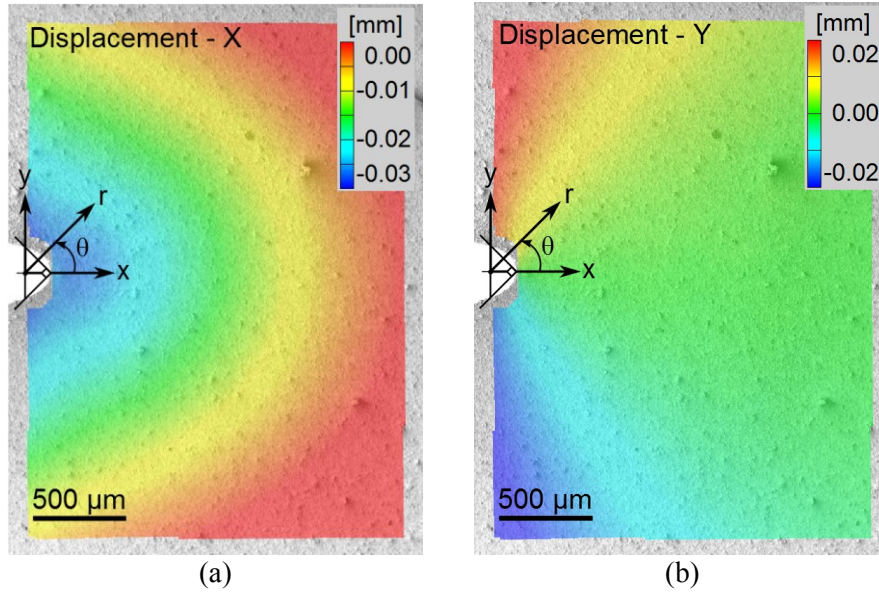


Fig. 34 Displacement fields along the  $x$ - (a) and  $y$ - axis (b) loading with  $J = 5.3 \text{ kJ/m}^2$

During the DCB test, the test samples are loaded step by step including regions of *loading-hold-unloading-hold* as shown in Fig. 35. In this study, results are presented for five steps separated by an applied moment,  $M$ , of 0.40 Nm, 0.56 Nm, 0.80 Nm, 0.96 Nm, and 1.20 Nm. The reason of *unloading* and *hold* steps is to study permanent strains and to capture images at different magnifications as x100, x500, and x1000 (magnification is altered during the test). During *hold* of approximately 4 min, the fixture displacement is fixed, and load drop of 15% is observed for higher loads. The load drop is neglected in a result analysis and is attributed to visco-elastic or visco-plastic deformation of the epoxy polymer.

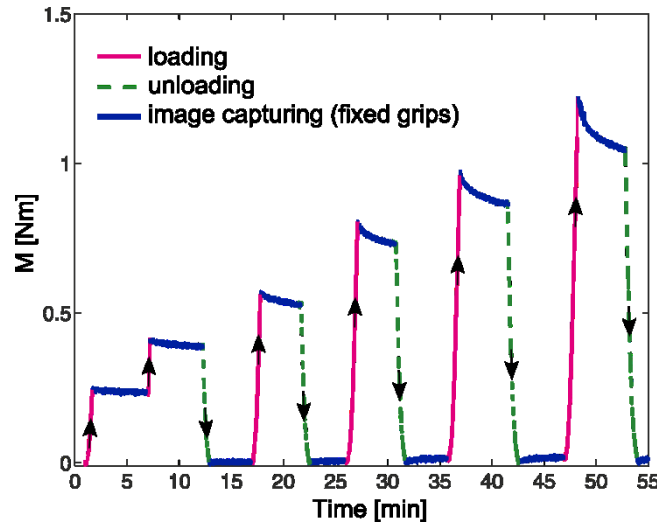


Fig. 35 A typical loading curve during the DCB test, which shows the applied moment versus time

In this study, the  $J$  integral is considered as a loading parameter. Assuming that the loading beams are deforming elastically, the relation between  $J$  and  $M$  for the DCB test samples in plane stress is

$$J_{app} = \frac{12M^2}{B^2h^3E}, \quad (4.1)$$

where  $B$  and  $h$  are the test sample dimensions presented in Fig. 33b,  $\nu$  is Poisson's ratio taken as 0.4, and  $E$  is Young's modulus equal to 2852 MPa. Since the actual test samples have non-uniform loading beams as shown in Fig. 36b, the stress state around the notch is changed, and Eq. 4.1 is not valid. Therefore, numerical tools are employed to estimate the loading state around the notch.

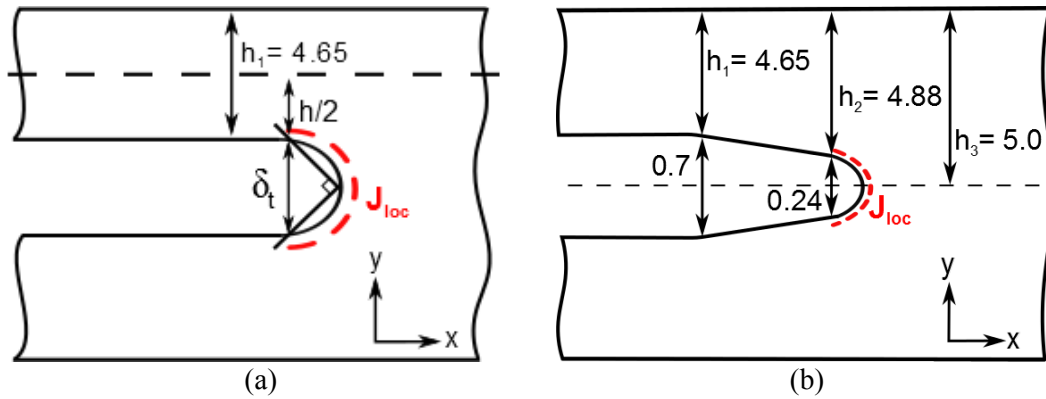


Fig. 36 A shape of uniform notch (a) and actual notch for the Test Series 2 (b)

During numerical analysis, the test sample is assumed to be linear-elastic with  $E = 2852$  MPa and  $\nu = 0.4$ . The  $J$ -integral around the notch edge,  $J_{loc}$ , is assumed to be a function of the strain energy density,  $W$ , as given in Eq. 2.3. For linear-elastic material,  $W = 1/2\sigma\varepsilon$ , which denotes the area below the stress-strain curve, and  $\varepsilon = \sigma/E$ . This gives that  $W = \sigma^2/2E$ , and

$$J_{loc} = \frac{\sigma^2}{2E} \delta_t. \quad (4.2)$$

In order to determine  $J_{loc}$ , the effective stresses around the notch edge are extracted up to the nodes used to measure the notch opening displacement,  $\delta_t$ . This approach is compared with the J-integral calculated by the FEM software and is denoted as  $J_{FEM}$ . First, agreement between different approaches of  $J$  determination is evaluated. For this purpose, the test samples with uniform beam width of 4.65 mm and 4.88 mm as shown in Fig. 36a are considered. In Table 2 it can be seen that the deviations between  $J_{loc}$  and  $J_{FEM}$  are around 1 kJ/m<sup>2</sup> loading with  $M = 1.2$  Nm. Moreover, both values show good agreement with analytically derived  $J_{app}$  (Eq. 4.1). Further, the same approach of  $J_{loc}$  estimation is used for the test samples with non-uniform width of the loading beams (Fig. 36b). Results show that due to the non-uniformities,  $J_{loc}$  around the notch is reduced. The estimated  $J_{loc}$  values for different applied  $M$  are given in Table 3 and show good agreement with  $J_{FEM}$ . In this study, the  $J_{loc}$  values are used to define the loading state of the test samples.

**Table 2  $J$  estimated around the notch for the plane stress state ( $M = 1.2$  Nm)**

	Uniform notch ( $h = 4.65$ mm)	Uniform notch ( $h = 4.88$ mm)	Non-uniform notch (Test Series 2)	Non-uniform notch (Test Series 1)
$J_{loc}$ [kJ/m <sup>2</sup> ]	15.8	13.5	11.7	12.8
$J_{app}$ [kJ/m <sup>2</sup> ]	15.1	13.1	15.1	15.1
$J_{FEM}$ [kJ/m <sup>2</sup> ]	14.6	12.7	11.8	10.9

**Table 3  $J_{loc}$  for different applied  $M$**

$M$ [Nm]	Test Series 1		Test Series 2	
	$J_{loc}$ [kJ/m <sup>2</sup> ]	$J_{FEM}$ [kJ/m <sup>2</sup> ]	$J_{loc}$ [kJ/m <sup>2</sup> ]	$J_{FEM}$ [kJ/m <sup>2</sup> ]
1.20	12.7	10.9	11.7	11.8
0.96	7.2	7.0	7.5	7.5
0.80	4.9	4.8	5.3	5.2
0.56	2.4	2.4	2.5	2.6
0.40	1.1	1.2	1.2	1.3

#### 4.1.6 Strains in the cylindrical coordinate system

Commonly, the strain fields around notches and cracks are presented in cylindrical coordinate system. As actual strains obtained from the ARAMIS software are measured in the Cartesian ( $x$ - $y$ - $z$ ) coordinate system, a strain transformation to the polar coordinate system is done as follows [89]

$$\varepsilon_{rr} = \varepsilon_{xx} \cos^2 \theta + \varepsilon_{yy} \sin^2 \theta + \varepsilon_{xy} \sin 2\theta, \quad (4.3)$$

$$\varepsilon_{\theta\theta} = \varepsilon_{xx} \sin^2 \theta + \varepsilon_{yy} \cos^2 \theta - \varepsilon_{xy} \sin 2\theta, \quad (4.4)$$

$$\varepsilon_{r\theta} = \sin \theta \cos \theta (\varepsilon_{yy} - \varepsilon_{xx}) + \varepsilon_{xy} \cos 2\theta, \quad (4.5)$$

where  $\theta = \tan^{-1}(y/x)$  and  $x, y$  are point coordinates in the deformed state, when the centre point (0,0) is set to  $\delta_t/2$  from the notch tip (Fig. 2). The notch opening displacement,  $\delta_t$ , is used as the opening distance between the intercept of two 45° lines drawn back from the tip as shown in Fig. 2. The same equations are applied to



create user defined visualizations in the DIC software for the strain contour presentation. In addition, the effective von Mises strain,  $\varepsilon_e$ , which is the combination of different strain components,  $\varepsilon_{ij}$ , is also included and is given in subsection 2.4.1.

#### 4.1.7 FEM model

In order to relate the experimentally measured strain fields around the notch with different power law hardening materials, numerical tools are employed. Numerically, the test sample from the Test Series 2 is simulated under moment loading similarly to the experiments. The 3D FEM model considers a half of the DCB test sample with symmetry along the  $y$ -axis (*Face - 2* in Fig. 37). The model dimensions of 70 x 5 x 2 mm<sup>3</sup> are retained the same as in the experiments, including the beam width of 4.65 mm and non-uniform shape of the notch. The initial width,  $w_0$ , of a semi-circular notch is 248  $\mu\text{m}$ .

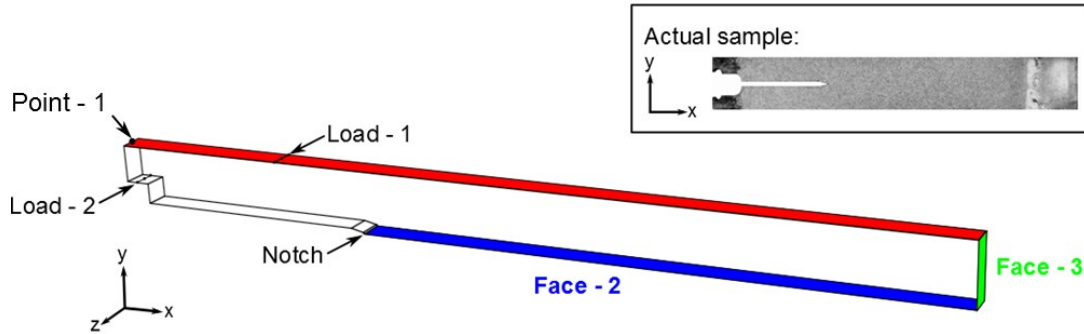
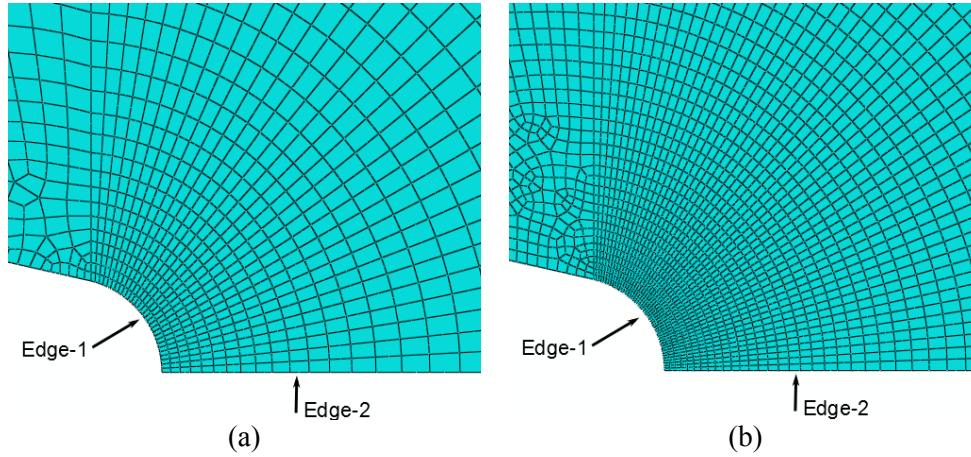


Fig. 37 A FEM model

In order to load the notch with moments, two opposed concentrated loads (in Fig. 37 denoted as *Load-1* and *Load-2*) are applied on nodes separated by a distance of 12 mm along the  $x$ -axis. Equation constraint is used to redistribute the loads equally in line across the width of the sample. Similarly to the experiments, the FEM model includes loading and unloading steps with the maximum applied moment of 1.2 Nm. Amplitude is defined to simulate the loading and unloading steps. During unloading,  $J = 0 \text{ kJ/m}^2$ , i.e. reverse loading is not performed. In addition, to avoid the movements of the model in a space, the rear end of the model (*Face-3* in Fig. 37) and *Point-1* is constrained along the  $x$ -axis and  $z$ -axis, respectively.

Furthermore, quadratic elements (20 nodes per element) with a full integration are used around the notch. For the rest of the part, linear elements (8 nodes per element) with a reduced integration are defined due to instabilities of loaded beam for the materials with  $n > 6$ . A sweep mesh technique is used around the notch with the elements of hexahedral-dominated shape. The rest of the part is having either structured or sweep mesh with elements of hexahedral shape. Along the *Edge-1* and *Edge-2* (Fig. 38), the number of elements is set to 30 with the bias of 10 for the *Edge-2*. This gives an element size of  $5 \times 11 \times 250 \mu\text{m}^3$  around the notch edge and  $14 \times 24 \times 250 \mu\text{m}^3$  further away from the tip at the distance of 160  $\mu\text{m}$ . Mesh is shown in Fig. 38a. In order to evaluate the effect of the element size, the model with a finer mesh (Fig. 38b) is made. The number of elements is increased to 50 along the *Edge-1* and *Edge-2*, and the global element size is reduced

to 150  $\mu\text{m}$ . As a result, the in-plane dimensions of the element are reduced 1.7 times. The element size is evaluated for the linear-elastic model by extracting the strains along the circular and line paths at  $J = 11.7 \text{ kJ/m}^2$ . Results show negligible discrepancies for the strain components  $\varepsilon_{\theta\theta}$  and  $\varepsilon_{r\theta}$ ; whereas for the strain component  $\varepsilon_{rr}$  small decline with a finer mesh is attained, see Fig. 39. In addition, for coarser mesh the element size in thickness direction is reduced to 75  $\mu\text{m}$  and in-plane elements are slightly increased in order to keep the aspect ratio below 1:10 (optimal aspect ratio according to [51]). Results are not found to be affected by larger aspect ratio of 1:50, see Fig. 39.



**Fig. 38 Coarser (a) and finer (b) mesh around the notch**

In addition, to acquire  $J_{FEM}$ , the notch face is defined as a crack front, and the edge corresponding to the notch tip as a crack line. The crack is defined on a symmetry plane with an extension direction (1,0,0) without element degeneracy.

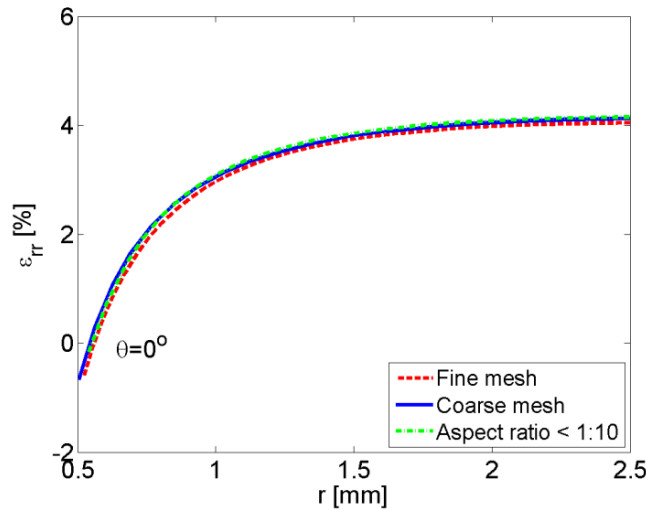


**Fig. 39 The  $\varepsilon_{rr}$  variations along a line path at  $\theta = 0^\circ$**

## 4.2 Extraction of the micro-scale stress-strain relation [P3]

### 4.2.1 Strain energy density around the notch

Following the approach given in subsection 2.1.2, the micro-scale stress-strain relation is found by means of the strain energy density. Experimentally, first,  $\bar{W}$  around the notch is determined at the onset of failure using Eq. 2.4. As the failure strains around the notch will be further needed, the test sample from the Test Series 2 (Fig. 27b) without an extensive amount of micro-cracks around the notch edge is chosen and shown in Fig. 40a. The notch opening displacement of  $346 \mu\text{m}$  is measured when loaded with  $M = 1.2 \text{ Nm}$ , i.e.  $J = 11.7 \text{ kJ/m}^2$ . This gives that  $\bar{W} = 33.8 \text{ MJ/m}^3$ .

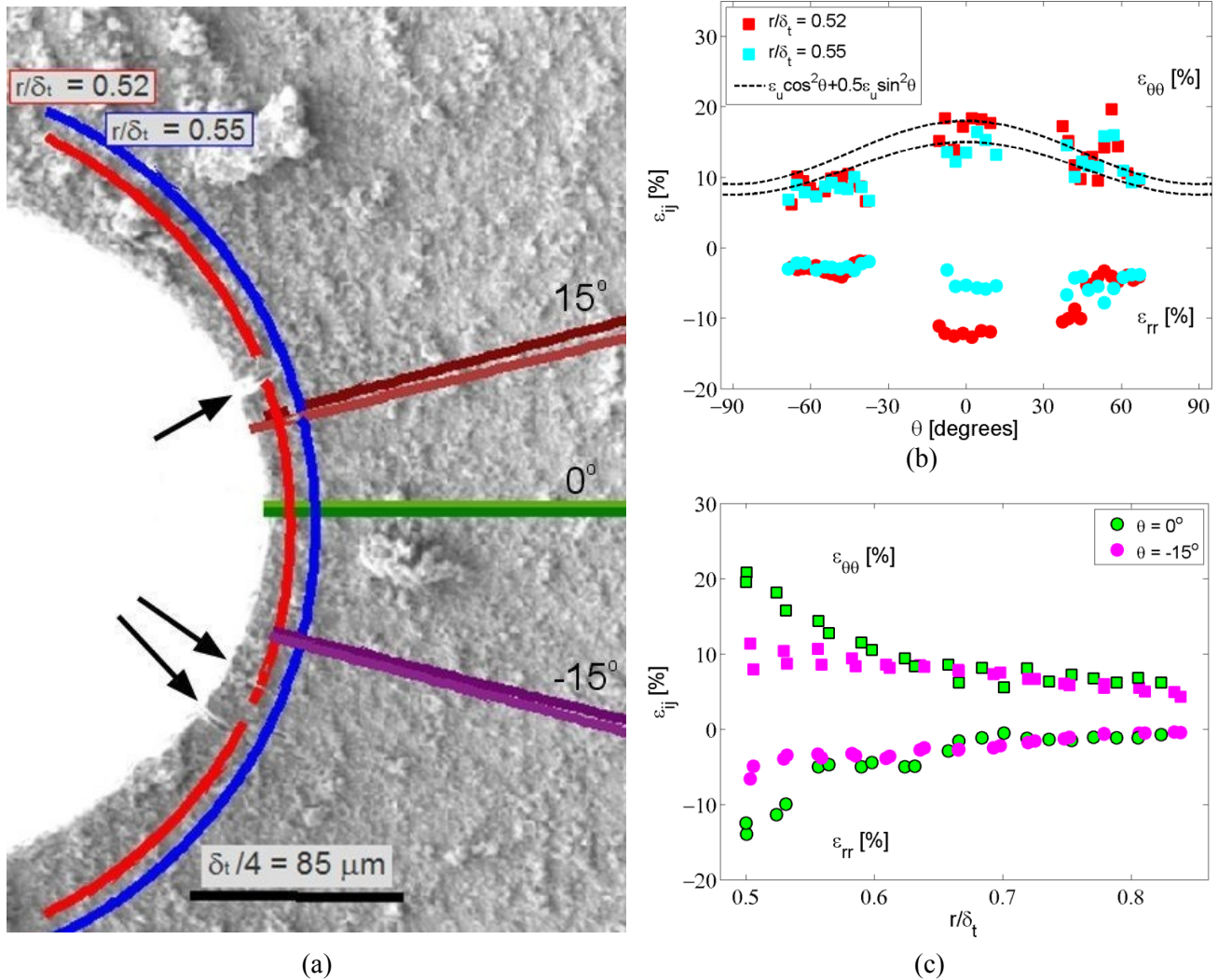


Fig. 40 The notch loaded with  $J = 11.7 \text{ kJ/m}^2$  (a) and the corresponding strains around circular (b) and line paths (c)

### 4.2.2 Failure strain measurements

For the test sample loaded with  $J = 11.7 \text{ kJ/m}^2$  shown in Fig. 40a, the strains around the notch edge and in front of the notch are presented in Fig. 40b,c. The strains are extracted both along circular and line paths in order to avoid biased measurements by larger particles and micro-cracks. The circular paths have a

normalized radius  $r/\delta_t = 0.52$  and  $r/\delta_t = 0.55$ , respectively, the distance from the notch edge is around  $7 \mu\text{m}$  and  $17 \mu\text{m}$ . From Fig. 40b it appears that the extreme values of  $\varepsilon_{rr}$  and  $\varepsilon_{\theta\theta}$  at  $\theta = 0^\circ$  approach -13% and 17%, respectively. Slightly larger the numerical strain values are attained from the line paths starting just at the notch edge without an incline as it is shown in Fig. 40c, where the extreme values of  $\varepsilon_{rr}$  and  $\varepsilon_{\theta\theta}$  reach -15% and 20%, respectively. The maximum value of  $\varepsilon_{\theta\theta}$  is taken as the failure strain,  $\varepsilon_u$ . Moreover, in Fig. 40b it can be seen that the actual strain distribution around the notch is non-uniform and the mean strain,  $\bar{\varepsilon}$ , is  $15\%$ <sup>1</sup>.

#### 4.2.3 Strain energy density attained from the stress-strain relations

Now, the values of  $\varepsilon_u$  and  $\bar{\varepsilon}$  for the strain component  $\varepsilon_{\theta\theta}$  are used to extract  $W$  from the stress-strain relations. The macroscopic tensile stress-strain curve of the epoxy resin is fitted to the Ramberg-Osgood relation (Eq. 2.5) varying the  $n$  values from 1 to 13. The resultant stress-strain curves for power law hardening materials are shown in Fig. 41a. Moreover, the  $W$  values (Eq. 2.2) extracted from the stress-strain curves as a function of  $n$  for the strain limits of 15% and 20% are given in Fig. 41b. In the same figure, previously determined  $\bar{W}$  is given as a black dotted line (Eq. 2.4). In the first approximation,  $W$  is calculated from the stress-strain curves with a strain limit of 20%. It gives that  $\bar{W}$  and  $W$  match, if the material hardening exponent is  $n \approx 6$  (Fig. 41b) with the corresponding microscopic failure stress,  $\hat{\sigma}_u$ , of 220 MPa (Fig. 41a). In the second approximation, since the strain distribution around the notch is non-uniform, the strain limit is set to 15%. In this case,  $\bar{W}$  and  $W$  match, if  $n < 4$  and  $\hat{\sigma}_u$  is above 450 MPa for  $\varepsilon_u = 20\%$ .

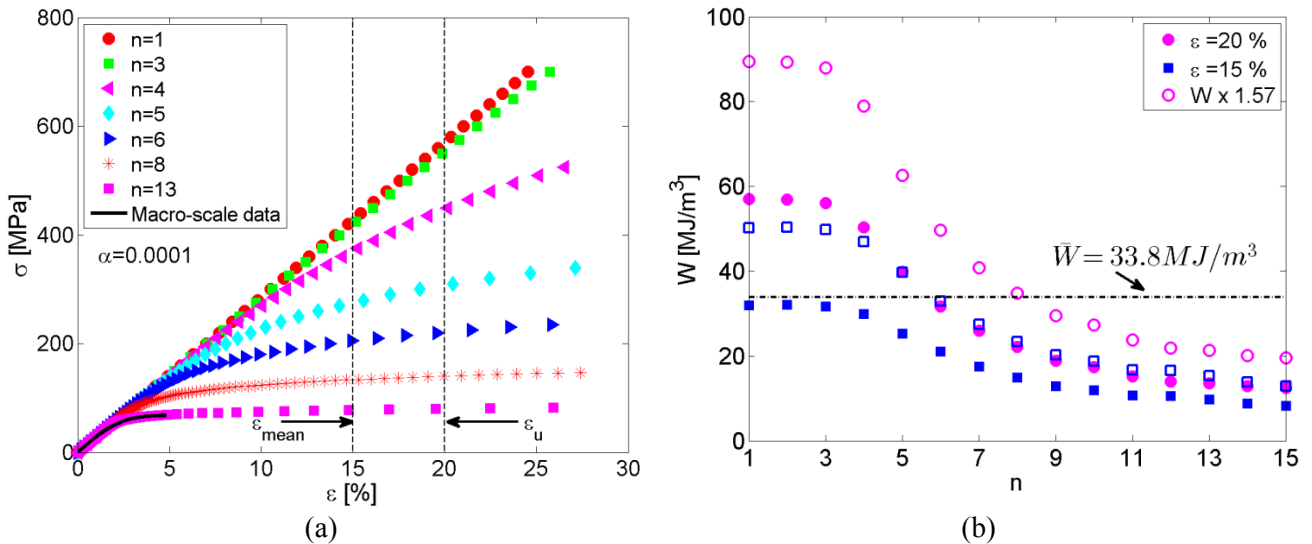


Fig. 41 The stress-strain relations with  $n$  from 1 to 13 (a) and  $W$  as a function of  $n$  for the strain limit of 15% and 20% (b)

<sup>1</sup>  $\bar{\varepsilon} = \varepsilon_u \cos^2 \theta + 0.5 \varepsilon_u \sin^2 \theta = \varepsilon_u \cos^2 \theta + 0.5 \varepsilon_u \sin^2 \theta + 0.5 \varepsilon_u \sin^2 \theta - 0.5 \varepsilon_u \sin^2 \theta = \varepsilon_u - 0.5 \varepsilon_u \sin^2 \theta = \{\sin^2 \theta = 0.5(1 - \cos 2\theta)\} = \varepsilon_u - 0.25 \varepsilon_u + 0.25 \varepsilon_u \cos 2\theta = \{\cos 2\theta = -\int \sin 2\theta d(2\theta)\} = 0.75 \varepsilon_u - 0.25 \int_{-\pi}^{\pi} \sin 2\theta d(2\theta) = \left\{\theta = \pm \frac{\pi}{2}; 2\theta = \pm \pi\right\} = 0.75 \varepsilon_u + 0.25 \varepsilon_u (\cos \pi - \cos(-\pi)) = 0.75 \varepsilon_u$

Furthermore, from the numerical results presented in the subsection 4.3, it appears that the  $W$  values are non-uniform through thickness, i.e.  $W$  measured on the surface is about 1.94, 1.58 and 1.56 times lower than the  $W$  averaged through the thickness for the materials with  $n = 1$ ,  $n = 6$ , and  $n = 8$ , respectively. Therefore,  $W$  attained from the surface strain measurements is multiplied with 1.57. Results are given in Fig. 41b as empty markers. As a result, considering non-uniformities of  $W$  through thickness and the strain distribution around the notch edge, the experiments can be related to the material with  $n \approx 6$ .

#### 4.2.4 Permanent strains

Next, both approximations are verified with the permanent strain,  $\varepsilon^p$ , measurements. Accordingly to Fig. 41a, for the material with  $n = 4$ ,  $\varepsilon^p$  should be approximately 3% for  $\varepsilon$  at the loaded state of 20%. Experimentally,  $\varepsilon^p$  is found to be around half of  $\varepsilon$  at the loaded state, i.e. for  $\varepsilon = 20\%$  the permanent strains slightly exceed 10%. Thus, the first approximation giving  $n \approx 6$  is found to fit the experiments better.

Additionally, the effective strains measured in loaded,  $\varepsilon_e$ , and unloaded state,  $\varepsilon_e^p$ , are used to construct the stress-strain curve. When the test samples are unloaded, it is assumed that the elastic deformation is completely removed, and the steepness of the unloading curve agrees with the steepness of the stress-strain relation during loading in the elastic region as shown in Fig. 42. Moreover, it is assumed that during re-loading the epoxy resin will yield, when the stresses at previous loading are reached. These assumptions are used to construct the stress-strain relation, i.e. knowing the strain values in loaded,  $\varepsilon$ , and unloaded state,  $\varepsilon^p$ , the stress,  $\sigma$ , is found from

$$\sigma = E(\varepsilon - \varepsilon^p). \quad (4.6)$$

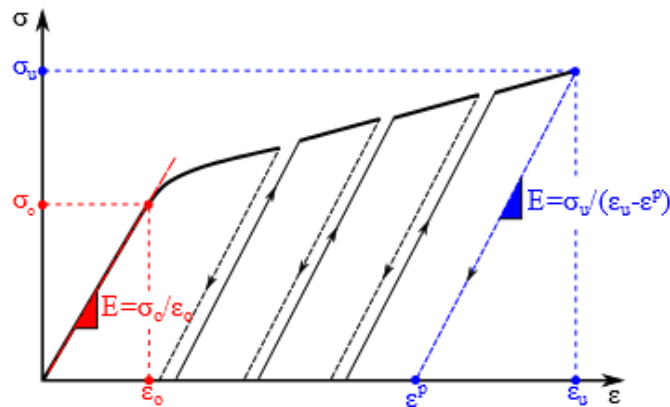
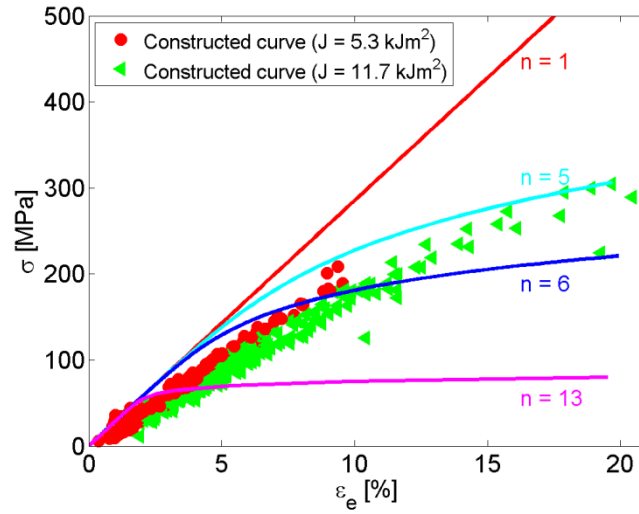


Fig. 42 The sketch of the stress-strain relation during loading and unloading

Experimentally, the strains are extracted from the line paths drawn in front of the notch at  $\theta = 0^\circ$ . For the measurement points with the same index number in the loaded and unloaded state, Eq. 4.6 is used to extract the stress. Results are shown in Fig. 43 for two loading steps, i.e. for the samples first loaded up to  $J = 5.3$

$\text{kJ/m}^2$  and afterwards unloaded then loaded up to  $J = 11.7 \text{ kJ/m}^2$  and afterwards unloaded. In addition, the stress-strain curves with  $n = 1$ ,  $n = 5$ ,  $n = 6$ , and  $n = 13$ , also given in Fig. 41a, are included.



**Fig. 43 The stress-strain curves constructed from the experimentally measured strains in the loaded and unloaded state**

From the results shown in Fig. 43, it appears that the epoxy resin is comparable with the power law hardening material having  $n \approx 5$ . Nevertheless, some deviations are visible. In Fig. 43 it can be seen that the constructed stress-strain curves are somewhat displaced along the  $\varepsilon_e$  axis. Moreover, the constructed stress-strain relations acquired at different loading states are not overlapping (red and green markers in Fig. 43). The possible reasons could be non-linear unloading and the strain measurement errors caused by the test sample movements along the  $z$ -axis. According to the literature [90], the epoxy polymer is possessing non-linear hysteresis loops during cyclic loading, which are load and strain rate dependent. For high strain rates and low loads, the non-linearity is minor and the loading and unloading curves are almost linear with the same stiffness. Increasing the load, the non-linearity becomes more profound, and the steepness of unloading curves is reduced (The steepness in unloading is defined as a line connecting the  $\varepsilon_e$  and  $\varepsilon^p$  values). Lower stiffness during unload would indicate that the steepness and stresses are overestimated in the constructed curves. For instance, if the stiffness during unloading is 1.5 times lower, then according to Eq. 4.6 the failure stress would be around 200 MPa. In order to have more accurate estimates, additional tests would be required, e.g. cyclic tensile tests. The second cause of the deviations could be the strain measurement errors, which are predicted up to 1% for the strain component  $\varepsilon_e$ . If the strain measurements both in the loaded and unloaded state are affected by the  $z$ -axis displacements, then the estimated stress values should remain unchanged (as the difference between  $\varepsilon_e$  and  $\varepsilon^p$  is unaffected), and the stress-strain curve should be translated along the  $\varepsilon_e$  axis. On the other hand, if the strain measurements in the unloaded state are unaffected by the  $z$ -axis displacements, then the stresses in the constructed stress strain curve are overestimated (as the difference between  $\varepsilon_e$  and  $\varepsilon^p$  is increased). According to Eq. 4.6, additional strain of 1% would increase the stress by 30 MPa for  $E = 3 \text{ GPa}$ . Considering all previous assumptions, an approximate estimate is that the



epoxy resin can be fitted to the power law hardening material with  $n$  from 5 to 6 with the corresponding failure stresses in the range of 200-300 MPa. Similar stress-strain curves are also constructed for the strain component  $\epsilon_{\theta\theta}$  with slightly lower stiffness.

### 4.3 Numerically estimated strain fields

The experimentally measured strain fields are compared to different material models applying numerical tools. The FEM models present the sample from the Test Series 2, i.e.  $*_{to} = 248 \mu\text{m}$ . Similarly to the experiments, the sample is loaded step-by-step, and strains are extracted both in the loaded and unloaded state. In the FEM models, material properties are defined according to the stress-strain relations presented in Fig. 41a.

#### 4.3.1 Numerically predicted strain fields compared with the experiments

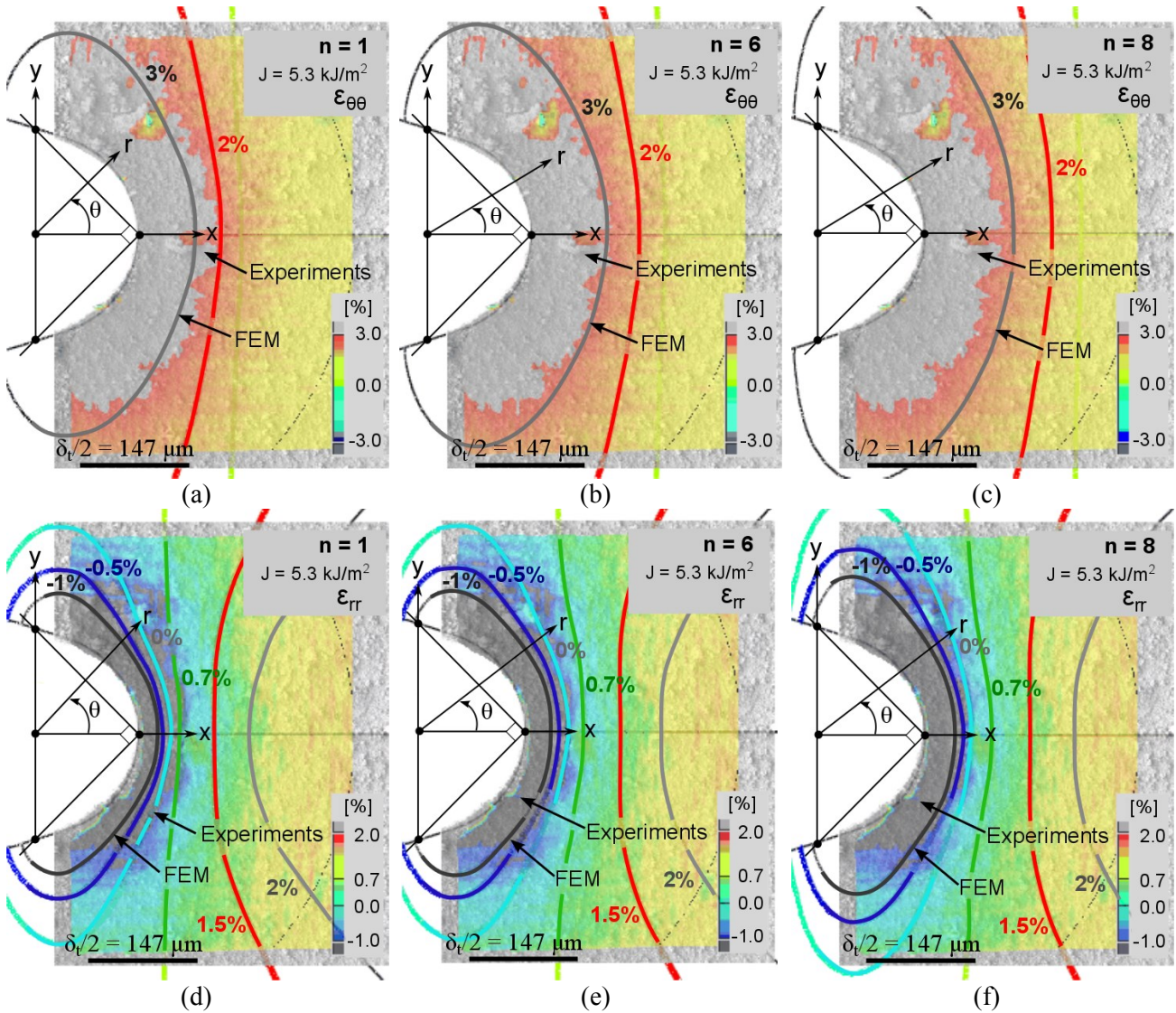


Fig. 44 Overlapped experimental and numerical strain contour plots for  $\epsilon_{\theta\theta}$  (a-c) and  $\epsilon_{rr}$  (d-f) in the loaded state with  $J = 5.3 \text{ kJ/m}^2$ ; the FEM models present the materials with  $n = 1$  (a,d),  $n = 6$  (b,e), and  $n = 8$  (c,f)

Fig. 44 shows the strain contour plots determined experimentally and numerically at  $J = 5.3 \text{ kJ/m}^2$ . The strain contour plots are overlapped by matching the circular path at the normalized distance  $r/\delta_t = 1.5$  between experimental and numerical images. At the loading state  $J = 5.3 \text{ kJ/m}^2$ , micro-cracks can be observed at their infancy and are assumed to have a negligible effect on the experimentally gained strain fields surrounding the notch. The FEM results are given for the linear-elastic material (Fig. 44a,d) and hardening materials with  $n = 6$  (Fig. 44b,e) and  $n = 8$  (Fig. 44c,f). In overall, it seems that the numerically estimated  $\varepsilon_{\theta\theta}$  variations around the notch are in a good agreement with the experiments as shown in Fig. 44a-c. The best agreement is found employing the material model with  $n = 6$  (Fig. 44b). In Table 4 it can be seen that there are small deviations between different test samples; however, in some cases it appears that the material model with  $n = 6$  is slightly overestimating the experiments at  $J = 5.3 \text{ kJ/m}^2$ . Increasing the load to  $J = 11.7 \text{ kJ/m}^2$ , the material models with larger  $n$  values are found to fit the experiments (Table 4). At higher load levels, the strain fields could be distorted by micro-cracks evolving from the notch edge and/or displacements along the  $z$ -axis (subsection 4.5).

**Table 4 Material models fitting the experiments in the loaded and unloaded state\***

Sample Nr.	$J = 5.3 \text{ kJ/m}^2$		$J = 11.7 \text{ kJ/m}^2$		unloaded after $J = 5.3 \text{ kJ/m}^2$	unloaded after $J = 11.7 \text{ kJ/m}^2$	
	$\varepsilon_{yy}$	$\varepsilon_{\theta\theta}$	$\varepsilon_{yy}$	$\varepsilon_{\theta\theta}$	$\varepsilon_e$	$\varepsilon_{\theta\theta}$	$\varepsilon_e$
1	$n \approx 6$	$n = 6$	$6 < n < 8$	$6 < n < 8$	$6 < n < 7$	$n = 8$	$n = 7$
2	$1 < n < 6$	$1 < n < 6$	$n \approx 6$	$6 < n < 7$	$n = 6$	$7 < n < 8$	$6 < n < 7$
3	$n = 6$	$n = 6$	$7 < n < 8$	$7 < n < 8$	$n = 7$	$n = 8$	$n = 7$
4	$1 < n < 6$	$1 < n < 6$	$6 < n < 7$	$6 < n < 7$	$n \approx 6$	$7 < n < 8$	$6 < n < 7$

\*Results are attained comparing the experimental strain contour plots for  $\varepsilon_{\theta\theta}$ ,  $\varepsilon_{yy}$ , and  $\varepsilon_e$  with numerically predicted, see Fig. 44 and Fig. 46

In a similar way, the experimental  $\varepsilon_{rr}$  values are compared with the FEM results within the strain range of -1% to 2% (Fig. 44d-f). The shape of the strain fields is found to be comparable between the experiments and numerical results. Nevertheless, there are noteworthy deviations comparing the strain variations with a distance from the notch. For example, experimentally, the strain range from -1% to 0.7% occupies a significantly larger area around the notch than it is numerically estimated for the material models with  $n = [1; 8]$ . Moreover, the numerical models predict that the strains will exceed 2% at the normalized distances  $r/\delta_t > 1$  for  $n = 1$  and  $r/\delta_t > 1.25$  for  $n = 8$ . Experimentally, such large values of  $\varepsilon_{rr}$  at  $r/\delta_t > 1$  are not measured. If the experimentally measured strain region having values below -1% is compared with the numerical results, then the best agreement seems to be with the material model with  $n = 8$  (Fig. 44f).



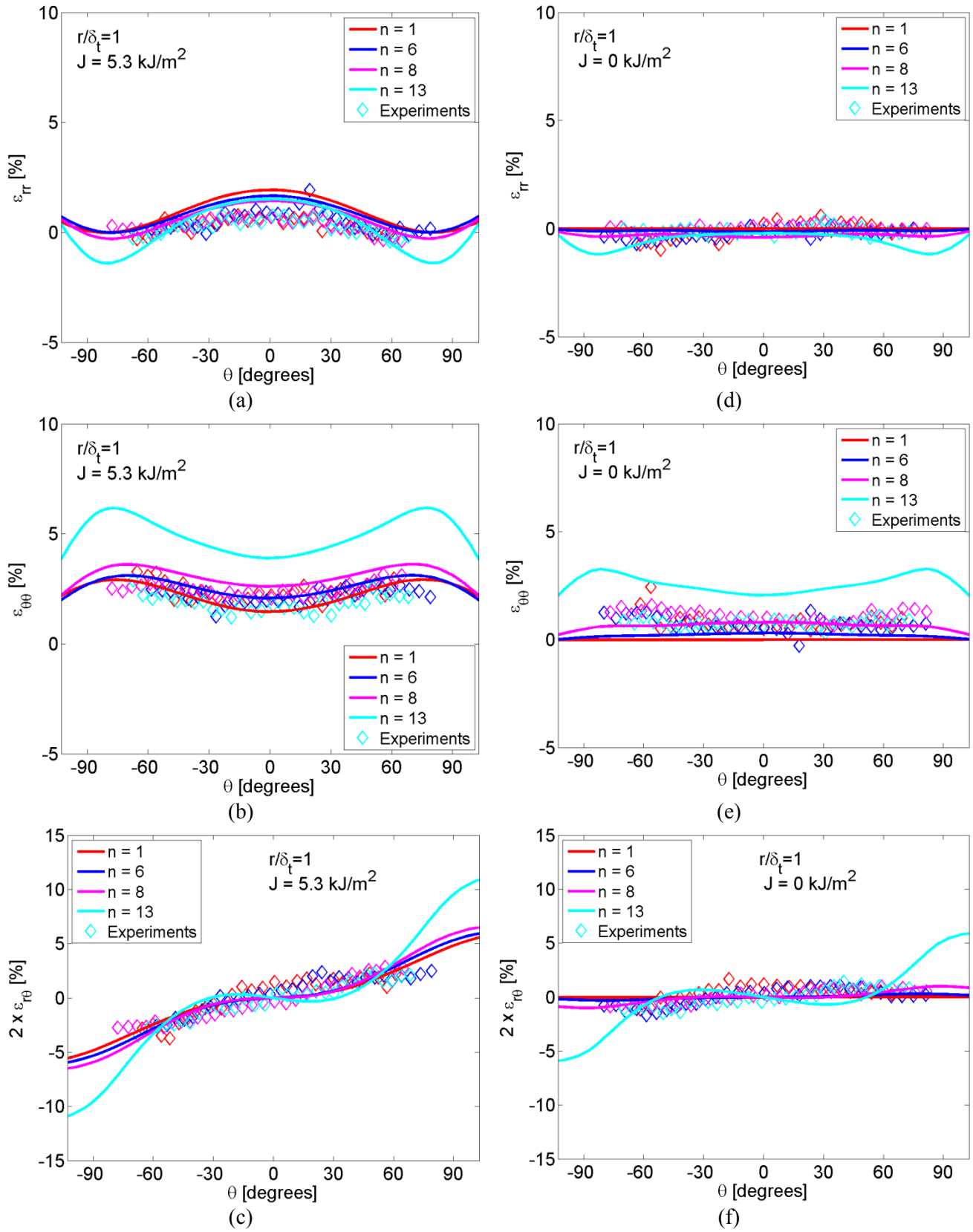
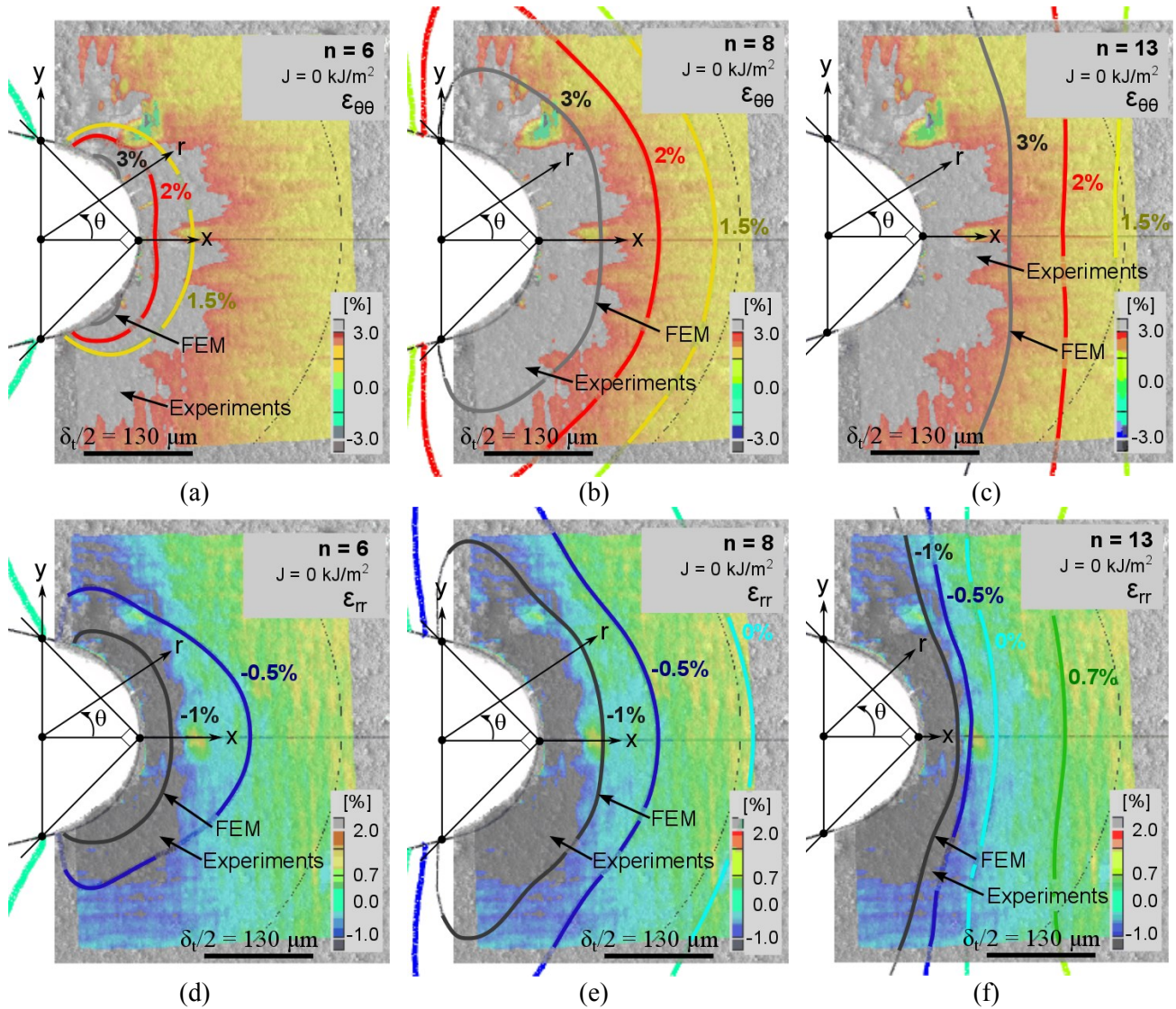


Fig. 45 Strain fields in the loaded (a-c) and unloaded (d-f) state

More detailed comparison of the strain fields is shown in Fig. 45 by extracting the strains along the circular path drawn around the notch at the normalized distance  $r/r_t = 1.0$  for the materials having  $n$  within the range of 1-13. Results in the loaded state with  $J = 5.3 \text{ kJ/m}^2$  are shown in Fig. 45a-c and afterwards in the unloaded state in Fig. 45d-f. Empty markers in Fig. 45 present the experimental results. Results in Fig. 45b show that the mean value of the experimentally measured  $\varepsilon_{\theta\theta}$  under loading fits better to the material model with  $n = 6$ . The experimental values of  $\varepsilon_{r\theta}$  are undistinguishable between the material models having  $n$  within the range of 1-8, as shown in Fig. 45c. And, Fig. 45a shows that the experimental values of the strain component  $\varepsilon_{rr}$  are somewhat lower than predicted numerically. Furthermore, comparing the strain fields in the unloaded state, it appears that the material model with  $n = 13$  predicts the largest permanent strains and is overestimating the experimental measurements. Significantly lower non-zero permanent strains are predicted for the material with  $n = 8$ , which gives the best agreement with the experiments for the strain component  $\varepsilon_{\theta\theta}$  (Fig. 45e) and  $\varepsilon_{r\theta}$  (Fig. 45f). The permanent values of  $\varepsilon_{rr}$  measured experimentally can be related to the material models with  $n$  in the range of 1-8.

Additionally, in Fig. 46 the numerically and experimentally attained contour plots of the permanent strains are overlapped in the unloaded state after loading with  $J = 11.7 \text{ kJ/m}^2$ . Numerical results are presented for the material models with  $n = 6$  (Fig. 46a,d),  $n = 8$  (Fig. 46b,e), and  $n = 13$  (Fig. 46c,f). For the strain components  $\varepsilon_{\theta\theta}$  (Fig. 46a-c), the material model with  $n = 6$  is highly underestimating the experimental permanent strains. Agreement improves increasing  $n$  to 8 (Fig. 46b), whereas the material model with  $n = 13$  overestimates the permanent  $\varepsilon_{\theta\theta}$  values (Fig. 46c). Similar results are attained for other test samples from the Test Series 2 and are given in Table 4. In Fig. 46d-e for the strain component  $\varepsilon_{rr}$ , the experimental permanent values below -1% would be comparable with the material model having  $n$  within the range of 6-8. Nevertheless, the deviations between the experiments and numerical results improve with the distance from the notch. For instance, the strain range with  $\varepsilon < 0\%$  is numerically predicted much larger for the materials with  $n = 6$  and  $n = 8$  than it is experimentally measured.



**Fig. 46** Overlapped experimental and numerical strain contour plots for  $\epsilon_{\theta\theta}$  (a-c) and  $\epsilon_{rr}$  (d-f) in the unloaded state after loading with  $J = 11.7 \text{ kJ/m}^2$ ; the FEM models present the materials with  $n = 6$  (a,d),  $n = 8$  (b,e), and  $n = 13$  (c,f)

Additionally, in Fig. 47 the strains as a function of the normalized distance,  $r/\ast_t$ , from the notch tip along the line path drawn at  $\theta = 0^\circ$  are given both in the loaded (Fig. 47a,b) and unloaded state (Fig. 47c,d). Likewise in the experiments, the numerically attained  $\epsilon_{\theta\theta}$  shows the largest values at the notch tip (Fig. 47a) and  $\epsilon_{rr}$  is negative (Fig. 47b). For  $\epsilon_{\theta\theta}$ , the experiments and FEM predictions seem to agree if the material model has  $n$  within the range of 6-8 at the distances  $r/\ast_t > 0.8$  (Fig. 47a). Closer to the notch ( $r/\ast_t < 0.8$ ) the experiments are somewhat disturbed. In the unloaded state, the experiments indicate small permanent values of  $\epsilon_{\theta\theta}$  and can be fitted with the material with  $n = 8$  (Fig. 47c). The deviations between the FEM and experimental results are observed for the strain component  $\epsilon_{rr}$ . Even though, the  $\epsilon_{rr}$  variations with  $r/\ast_t$  show similar tendency (Fig. 47b), the FEM models predict higher strains than those measured experimentally at the

distances  $r/r_t > 0.8$ . In the unloaded state, both the experiments and FEM results show small permanent values of  $\varepsilon_{rr}$  (Fig. 47d).

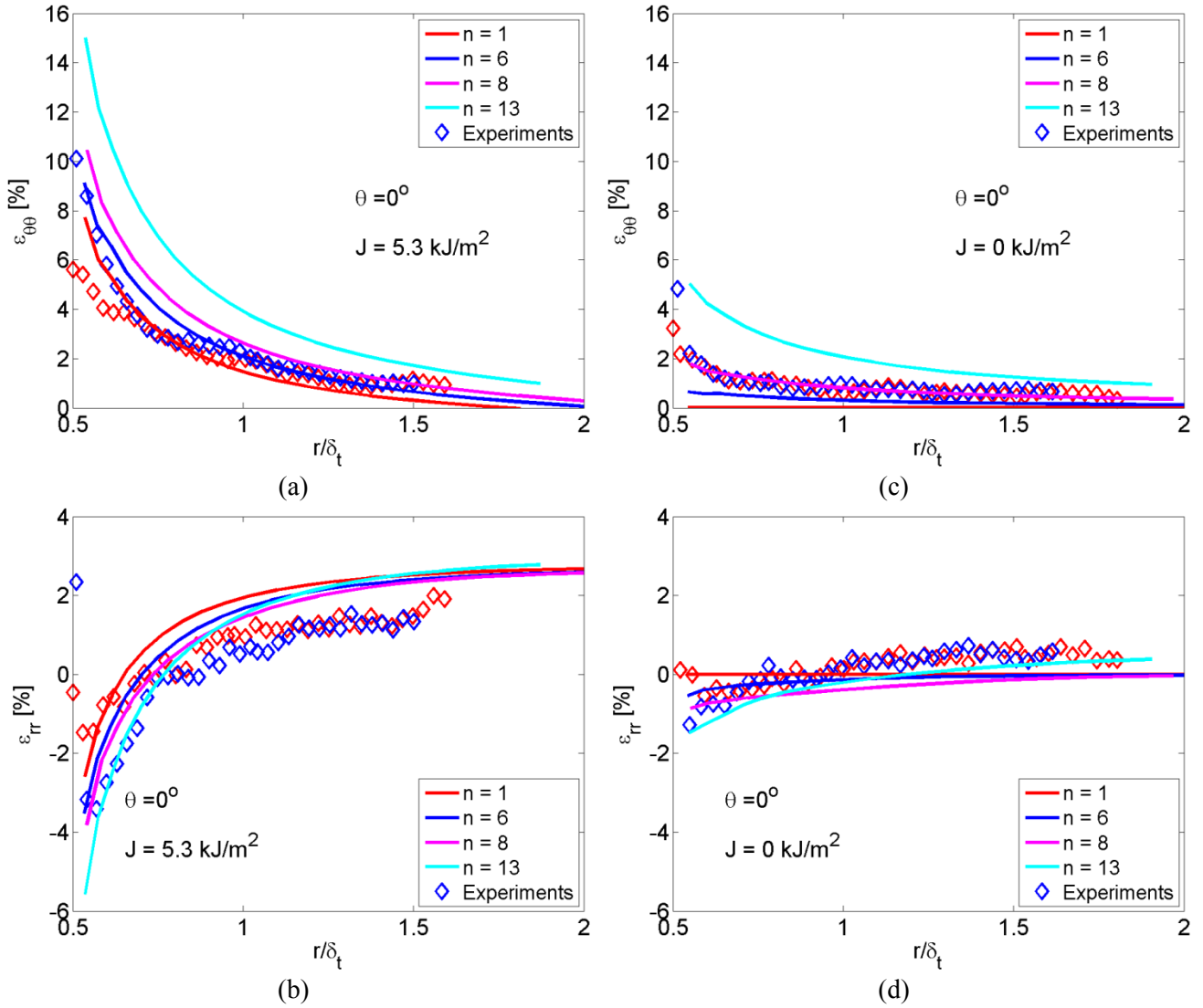


Fig. 47 Strain variations with a distance from the notch tip ( $r/r_t = 0.5$ ) in the loaded state with  $J = 5.3 \text{ kJ/m}^2$  (a,b) and afterwards in the unloaded state (c,d)

#### 4.3.2 Strain field variations in the presence of a micro-crack

##### Experimental observations

Before failure took place, the micro-cracks in the polymer material evolving from the notch edge are observed as shown in Fig. 48b,e. Mostly, the material micro-cracks are observed to be inclined respectively to the  $x$ -axis with an angle around  $30^\circ$ . Up to the failure initiation, the material micro-cracks were extending with an applied moment, but became still with the formation of the central crack at the tip of the notch. For instance, in Fig. 48b an inclined micro-crack at the notch tip can be seen, which initiated at  $J \approx 2.4 \text{ kJ/m}^2$ , but further cracking was suppressed by the growth of the central crack.

In addition, after polishing, most of the test samples were having a rather smooth surface as shown in Fig. 48a,d. After the DCB test, removing the speckles from the test surface using ultrasound a net of fine cracks on the test sample surface became visible (Fig. 48b,c,e,f). For instance, in Fig. 48b,c around the severely damaged notch multiple fine cracks extending even beyond the central crack are shown. According to Bradley [91], these are the micro-cracks in the gold coating caused by high strain.

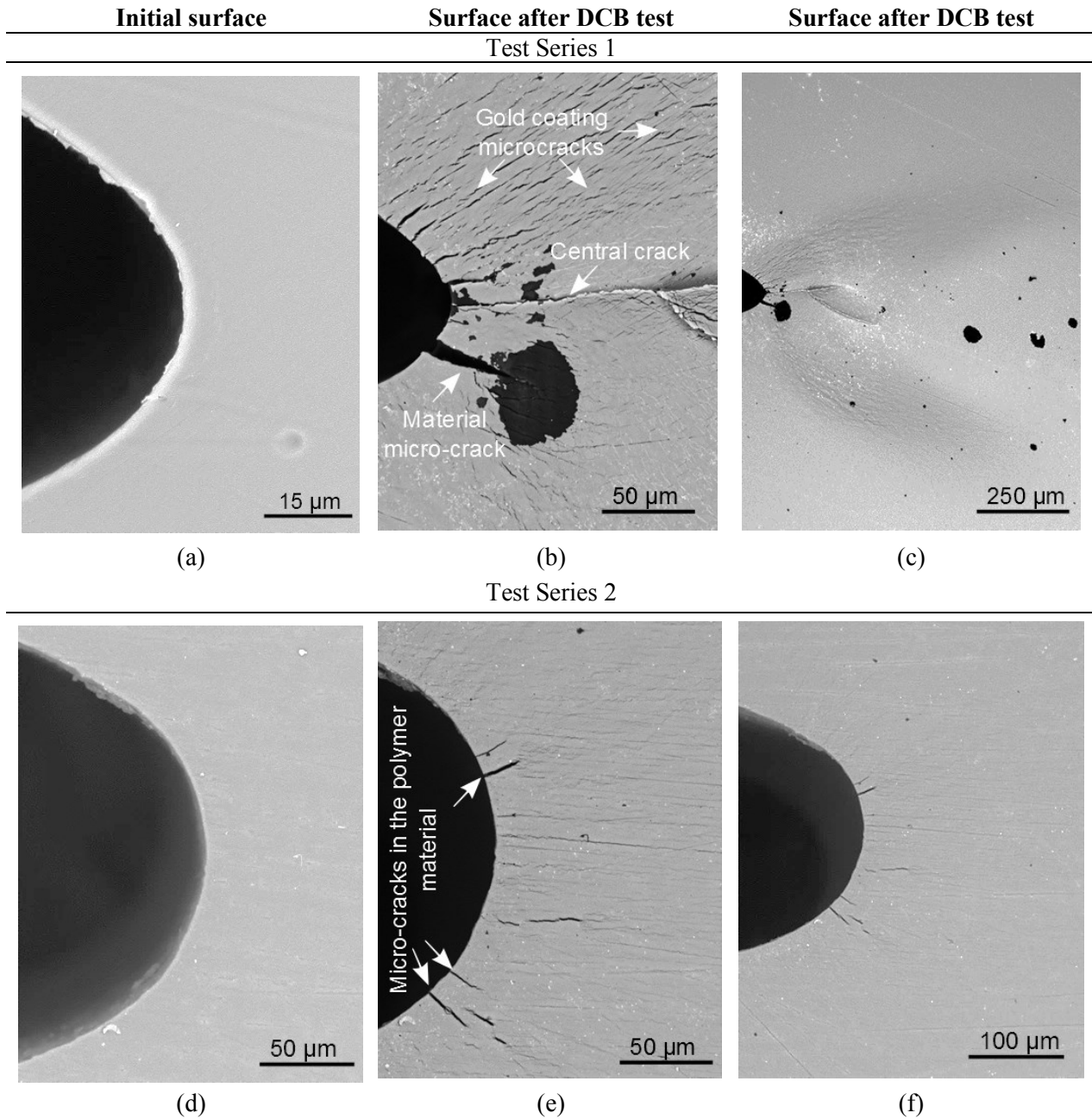


Fig. 48 The surface around the notch before the DCB test (a, d) and after the test (b, c, e, f) (surfaces without speckles)



### Numerical study

In order to see, how the side micro-cracks in the polymer material could possibly affect the strain fields in front of the notch, a simulation model with a partition (representing a micro-crack) at the side of the notch is created. The partition is 30  $\mu\text{m}$  long and inclined at  $30^\circ$  with respect to the  $x$ -axis. The corresponding contour plots of  $\varepsilon_{\theta\theta}$  for the model with and without micro-crack are presented in Fig. 49 loading with  $J = 11.7 \text{ kJ/m}^2$ .

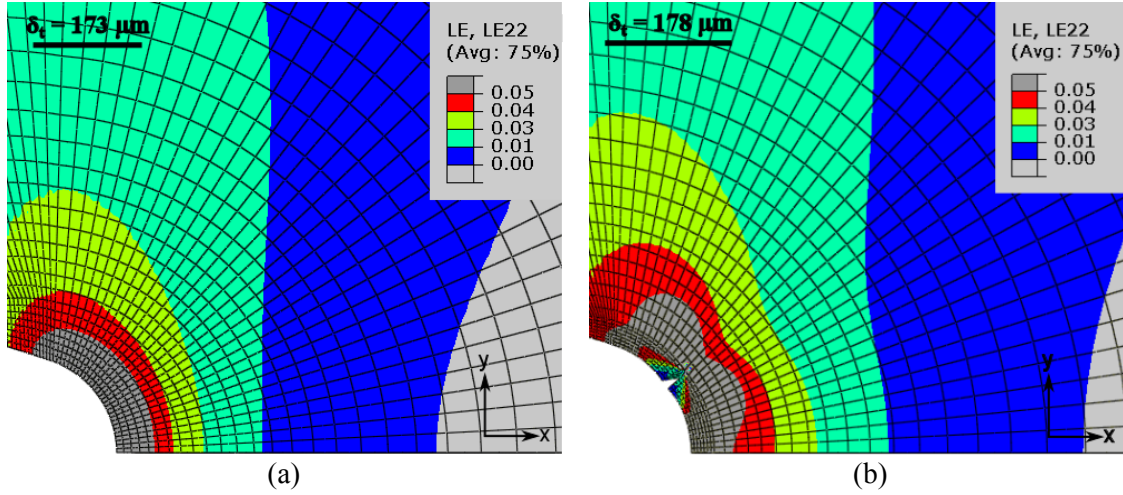


Fig. 49 FEM models with (a) and without (b) micro-crack

Similarly as above, the strain variations with an angle around the notch are compared between the FEM models with and without micro-crack and are given in Fig. 50. Results are presented for the normalized distances  $0.7 \leq r/*_t \leq 1.0$  for the material with  $n = 6$ . At the loaded state with  $J = 11.7 \text{ kJ/m}^2$ , the strain variations appear to be significantly affected close to the notch tip (Fig. 50a-c). At  $r/*_t = 0.7$  the maximum numerical values of  $\varepsilon_{rr}$  and  $\varepsilon_{\theta\theta}$  tend to increase about 1.5 times. Moreover, the angle, at which the maximum numerical values of the strain components appear, is displaced. For instance, Fig. 50b shows that at  $r/*_t = 0.8$  the maximum strain value of  $\varepsilon_{\theta\theta}$  appears at  $\theta \approx 70^\circ$  for un-cracked sample and at  $\theta = 50^\circ$  for the cracked sample. The disturbances caused by the micro-cracks are significantly reduced with a larger distance from the notch tip, however, small deviations can be still observed at  $r/*_t = 1.0$ . Therefore, according to the FEM results even though micro-crack is only 30  $\mu\text{m}$  long, it can still affect the strain fields as far as 175  $\mu\text{m}$  away from the notch tip ( $*_t = 350 \mu\text{m}$ ). The presence of the micro-crack is also affecting the permanent strains in the unloaded state, particularly, at the distances  $r/*_t < 0.8$  as shown in Fig. 50d-e. At  $r/*_t = 0.7$  the permanent strains of  $\varepsilon_{rr}$  will be slightly increased and  $\varepsilon_{\theta\theta}$  slightly decreased at  $\theta = 0^\circ$ , whereas  $\varepsilon_{r\theta}$  will have more curved distribution around the notch.

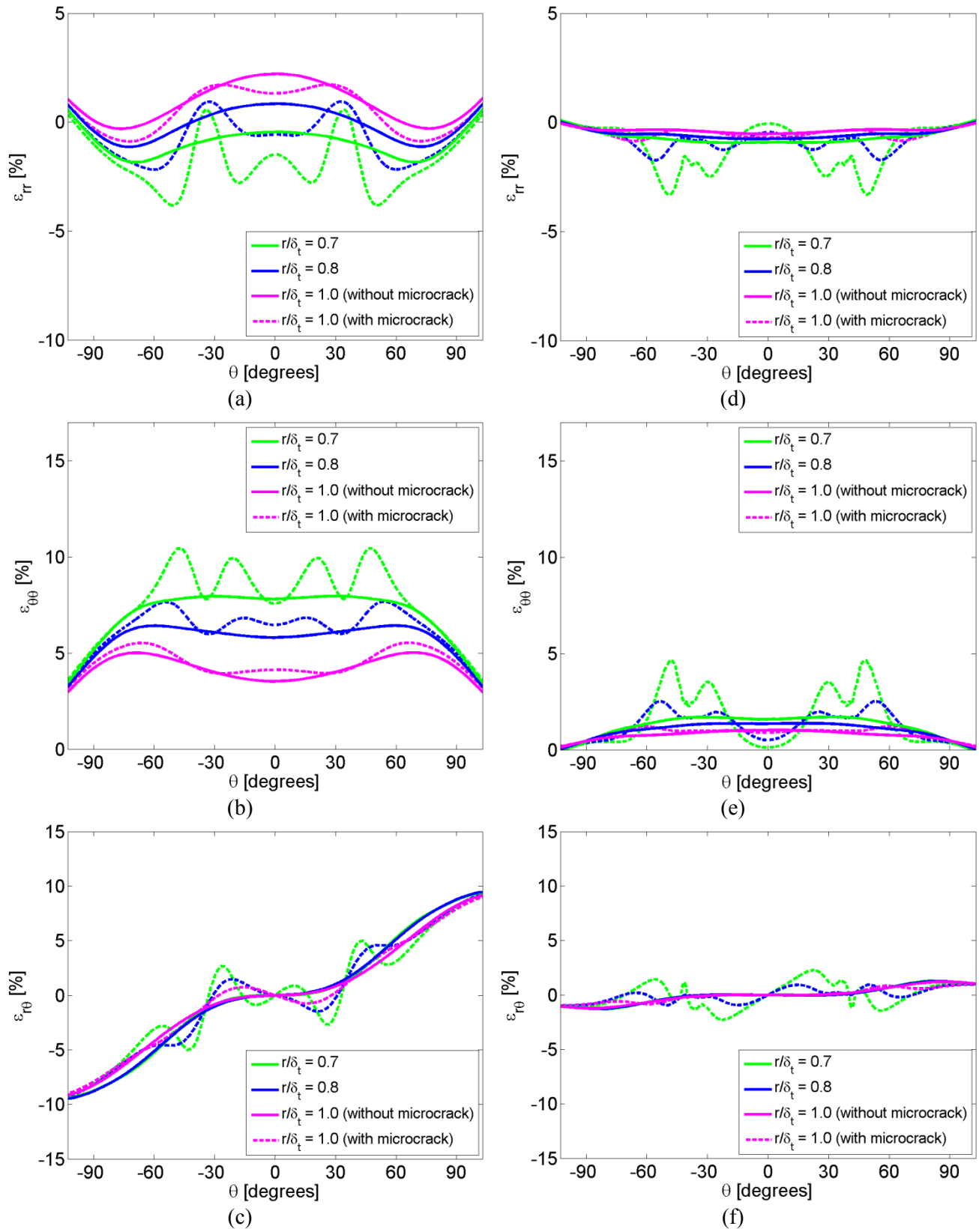
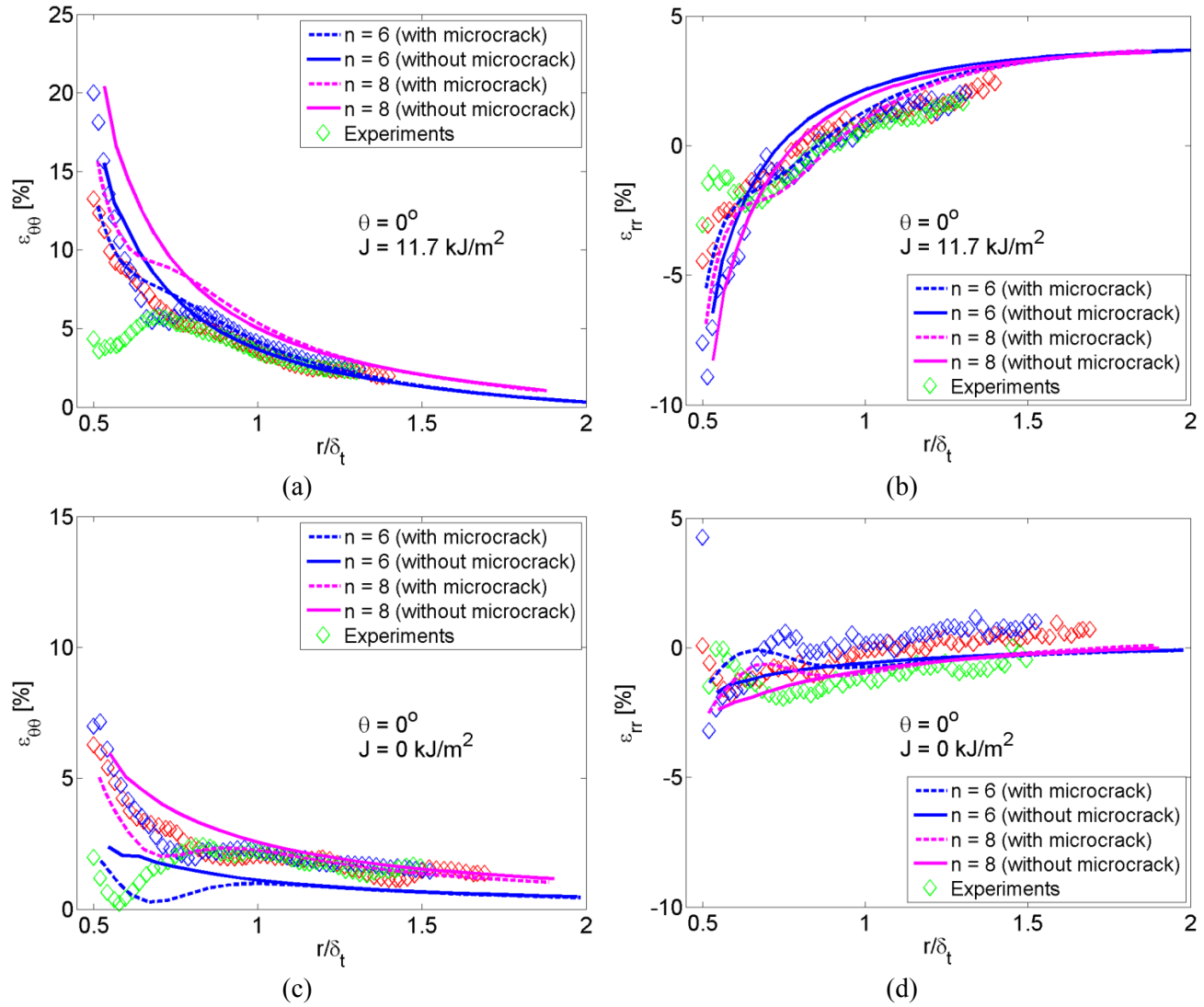


Fig. 50 FEM models with and without micro-crack are compared when loaded with  $J = 11.7 \text{ kJ/m}^2$  (a-c) and afterwards unloaded (d-f)

The strain variations along the line path drawn from the notch tip at  $\theta = 0^\circ$  are compared between the experiments and FEM models with and without micro-crack. Fig. 51a,c shows  $\varepsilon_{rr}$  and  $\varepsilon_{\theta\theta}$  variations in the loaded state with  $J = 11.7 \text{ kJ/m}^2$ , and Fig. 51b,d presents the permanent values of  $\varepsilon_{rr}$  and  $\varepsilon_{\theta\theta}$  in the unloaded state. The results from the FEM model with the micro-crack are presented by a dashed line and from the model without micro-crack by a solid line, whereas empty markers are for the experimental data. Comparing the FEM results attained from the models with and without micro-crack given in Fig. 51a, it appears that the presence of the micro-cracks has minor effect on the  $\varepsilon_{\theta\theta}$  values at the distances  $0.6 < r/\delta_t < 1.25$  for  $\theta = 0^\circ$ . But close to the notch edge ( $r/\delta_t < 0.6$ ),  $\varepsilon_{\theta\theta}$  will decline in the presence of the micro-crack. Fig. 51b shows that the strain component  $\varepsilon_{rr}$  tends to decrease in the presence of the micro-crack at the distances  $0.6 < r/\delta_t < 1.25$  and slightly increase close to the notch edge, i.e.  $r/\delta_t \approx 0.5$ . In the FEM model with the micro-crack, the strain  $\varepsilon_{rr}$  reduction at the distances  $r/\delta_t > 0.7$  gives better agreement to the experiments.



**Fig. 51** The strain variations with a distance from the notch tip ( $r/\delta_t = 0.5$ ) in the loaded state with  $J = 11.7 \text{ kJ/m}^2$  (a,b) and afterwards in the unloaded state (c,d)



Additionally, the permanent strains after loading with  $J = 11.7 \text{ kJ/m}^2$  are given in Fig. 51c,d. Both experiments and FEM results show more profound permanent values for the strain component  $\varepsilon_{\theta\theta}$  (Fig. 51c). From the numerical results, it appears that in the presence of the micro-crack the permanent strains of  $\varepsilon_{\theta\theta}$  will decrease close to the notch tip at  $r/\delta_t < 1.0$  with the lowest strain drop at  $r/\delta_t \approx 0.6$ . Experimentally, a small drop of the permanent strains of  $\varepsilon_{\theta\theta}$  close to the notch ( $r/\delta_t \approx 0.7$ ) is also observed. From the results in Fig. 51b, it appears that the experiments fit better to the material model with  $n = 8$ . Further, Fig. 51d shows small permanent strain values of  $\varepsilon_{rr}$  attained from the experiments and numerical results. The discrepancy of experimental  $\varepsilon_{rr}$  values in the unloaded state is quite large and cannot be related to any FEM model.

#### 4.3.3 Effective plastic strain

Above comparing the experimentally measured strains with the FEM results for different material models in the unloaded state, it appeared that the permanent strain fields of the epoxy resin could be fitted to the material with  $n = 8$ . Alternatively, in Fig. 52 the effective plastic strain,  $\varepsilon_e^p$ , is compared between the experiments and numerical predictions. Strains are extracted from the line path at  $\theta = 0^\circ$ . After loading with  $J = 5.3 \text{ kJ/m}^2$  (Fig. 52a), numerically, small variations of  $\varepsilon_e^p$  are observed between the materials with  $n = 6$  and  $n = 8$ , i.e. the discrepancy of the experiments fell in-between these two material models. More pronounced differences of  $\varepsilon_e^p$  are apparent after loading with  $J = 11.7 \text{ kJ/m}^2$  (Fig. 52b). For material with  $n = 8$ , the  $\varepsilon_e^p$  values are approaching 25%, which significantly exceed the experimental measurements. At the same time, it appears that the  $\varepsilon_e^p$  values will significantly drop in the presence of the micro-crack. Close to the notch, the experiments seem to fit the material model with  $n = 6$ . In addition, comparing the experimental strain contour plots with the numerically estimated similarly as in Fig. 44 and Fig. 46, the match is found with the material models with  $n = [6; 7]$ .

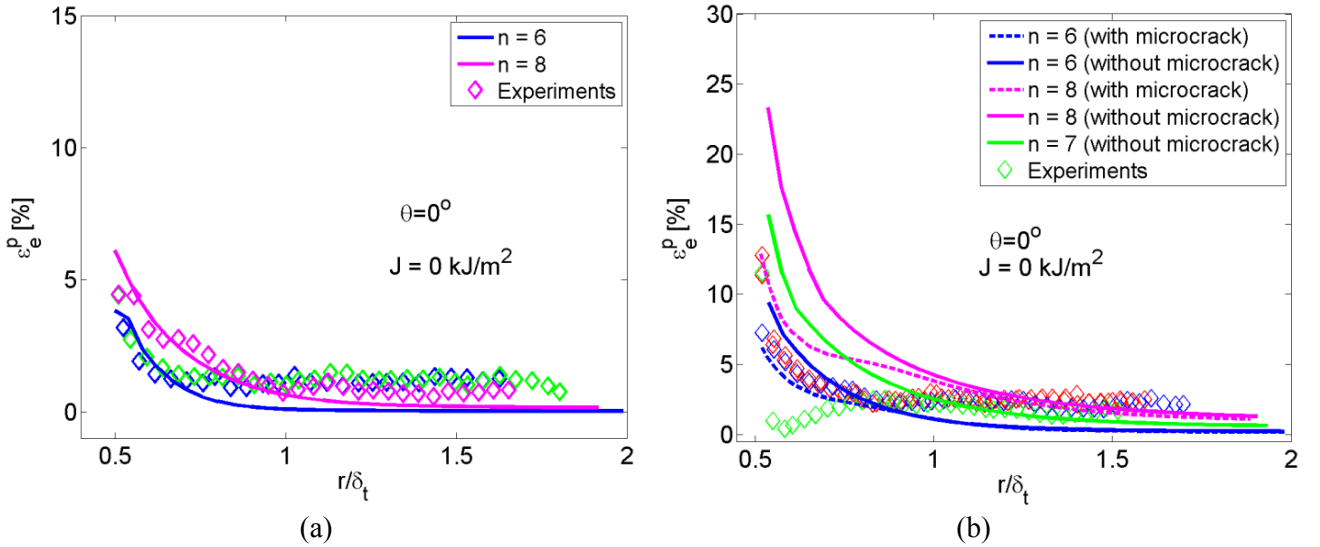


Fig. 52 The effective plastic strain extracted from the line path at  $\theta = 0^\circ$

Both in Fig. 52a and Fig. 52b, it can be seen that the experimental  $\varepsilon_e^p$  values are non-zero away from the notch edge and are constant at the distances  $r/r_t > 1$ ; whereas numerical models predict that the strains will decline with a larger distance from the notch tip. This could be explained with the measurement errors (subsection 4.5). Evaluating the DIC measurements, it is found the strain component  $\varepsilon_e^p$  is sensitive both to in-plane and out-plane-displacements. For the out-of-plane displacements of 300  $\mu\text{m}$ , the error was estimated around 1%.

#### 4.3.4 Notch opening displacement for materials with different hardening exponent

Below the experimentally and numerically measured notch opening displacement is compared. For the numerical results,  $\delta_t$  and  $\delta_{to}$  are defined in the same way as in the experiments. In Fig. 53 the normalized notch opening displacement,  $\delta_t/\delta_{to}$ , is plotted as a function of the normalized  $J$ ,  $J/\sigma_o \delta_{to}$ . Numerical results show that  $\delta_t/\delta_{to}$  increases with  $n$ , i.e. linear-elastic material has the lowest and perfectly-plastic ( $n = 13$ ) material has the highest slope. For the materials with  $n \leq 8$  at moderate loads,  $J/\sigma_o \delta_{to} < 0.9$ , the  $\delta_t/\delta_{to}$  values are very much alike, but are more distinct at  $J/\sigma_o \delta_{to} \approx 1.5$ . Additionally, the presence of 30  $\mu\text{m}$  long microcrack evolving at the side of the notch edge increases only slightly the values of  $\delta_t/\delta_{to}$  (empty markers in Fig. 53). Considering the numerical values of  $\delta_t/\delta_{to}$ , the experiments are found to fit to the power law hardening material with  $n \approx 6$ .

In addition, according to the numerical analysis, the loading beams are yielding at higher loads. Yielding is not observed at  $J = 5.3 \text{ kJ/m}^2$  for materials with  $n < 8$ , whereas at  $J = 11.7 \text{ kJ/m}^2$  the plastic strains of 1%, 2.3%, and 4.5% are measured for the materials with  $n = 6$ ,  $n = 7$ , and  $n = 8$ , respectively.

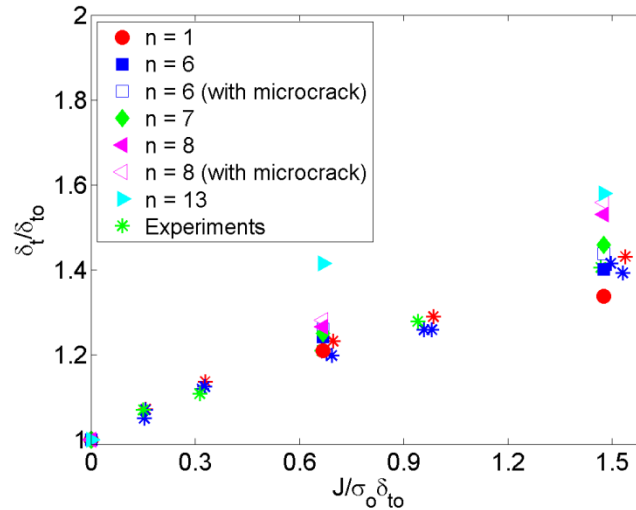


Fig. 53 Normalized  $\delta_t$  as a function of normalized  $J$

#### 4.3.5 Implementation of the Drucker-Prager yield criterion

The linear Drucker-Prager yield criterion is employed to see how the strain fields around the notch could be possibly affected by the pressure sensitivity of the epoxy resin. The pressure sensitivity parameters are the same as used in the macro-scale study (subsection 3.2.2). The strains close to the surface are found to be unaffected, whereas small deviations of around 3-5% are obtained extracting the strains in the middle of the test sample, where the sample is expected to experience the tri-axial stress state.

#### 4.3.6 Summary

1. Analytically, it is estimated that the epoxy resin fits the power law hardening material with  $n \approx 6$  (subsection 4.1).
2. Constructing the stress-strain curves from the strain measurements in the loaded and unloaded state, the epoxy resin is found to fit the material models with  $n = [5; 6]$  (Fig. 43), including uncertainties.
3. Numerically, comparing the strain contour plots for  $\varepsilon_{\theta\theta}$  in the loaded state with  $J = 5.3 \text{ kJ/m}^2$ , it appears that the epoxy resin fits the material models with  $n$  slightly below 6 (Fig. 44, Table 1). At higher loads, better agreement is found with the material models with  $n = [6; 8]$  (Table 4, Fig. 47).
4. Numerically, it is estimated that the permanent values of  $\varepsilon_{\theta\theta}$  in the unloaded state after loading with  $J = 5.3 \text{ kJ/m}^2$  and  $J = 11.7 \text{ kJ/m}^2$  are matching the material model with  $n = 8$  (Fig. 45, Fig. 47, Fig. 51, Fig. 46). On the other hand, the effective plastic strain is matching the material model with  $n = [6; 7]$  (Table 4).
5. Considering the opening displacement values (Fig. 53), the experiments seem to have a good agreement with the material model with  $n \approx 6$ .

#### 4.3.7 Failure strains and stresses

Failure strains and stresses are extracted from the FEM models considering that the epoxy resin can be fitted to the power law hardening material with  $n \approx 6$ . Loading with  $J = 11.7 \text{ kJ/m}^2$ , the maximum values of  $\varepsilon_{\theta\theta}$  and  $\varepsilon_e$  at the notch edge close to the surface will approach 18% and the effective stress is predicted of 216 MPa. In the middle of the test sample, the FEM models predict that  $\varepsilon_{\theta\theta}$  and  $\varepsilon_e$  will reach 28%, and the effective stress is expected to be as high as 250 MPa.

#### 4.3.8 Cohesive strength

The cohesive law, briefly described in subsection 2.3, is used to extract the failure stress,  $\hat{\sigma}_n$ , from the experiments. For this purpose, the test sample from the Test Series 1 is taken and given in Fig. 54. Fig. 54 shows that the crack has initiated at  $J = 2.4 \text{ kJ/m}^2$  with  $\delta_n^* = 15 \mu\text{m}$  (Fig. 54a), which continued to grow at  $J = 4.9 \text{ kJ/m}^2$  with  $\delta_n^* = 50 \mu\text{m}$  (Fig. 54b), and opening increased further up to  $\delta_n^* = 172 \mu\text{m}$  (Fig. 54c) at  $J = 7.2 \text{ kJ/m}^2$ . From Eq. 2.10, the stress at failure initiation is attained of 160 MPa. Nevertheless, results could be less accurate as the failure process given in Fig. 54 seems to be affected by a loading history. Before

failure actually took place, the test sample was loaded up to  $J = 4.9 \text{ kJ/m}^2$ , afterwards unloaded and then loaded again up to  $J = 2.4 \text{ kJ/m}^2$  where the crack occurred. It is suggested that some kind of microscopic processes have started at  $J = 4.9 \text{ kJ/m}^2$ , which promoted the failure initiation during re-loading at lower load levels.

Summarizing the results of the test sample failure, in average, the initiation of the central crack is observed at  $J = 4.9 \text{ kJ/m}^2$ , whereas complete failure is measured at  $J = 8.5 \pm 0.4 \text{ kJ/m}^2$  for the Test Series 1. Samples from the Test Series 2 are not tested up to failure due to restricted displacement of the fixture.

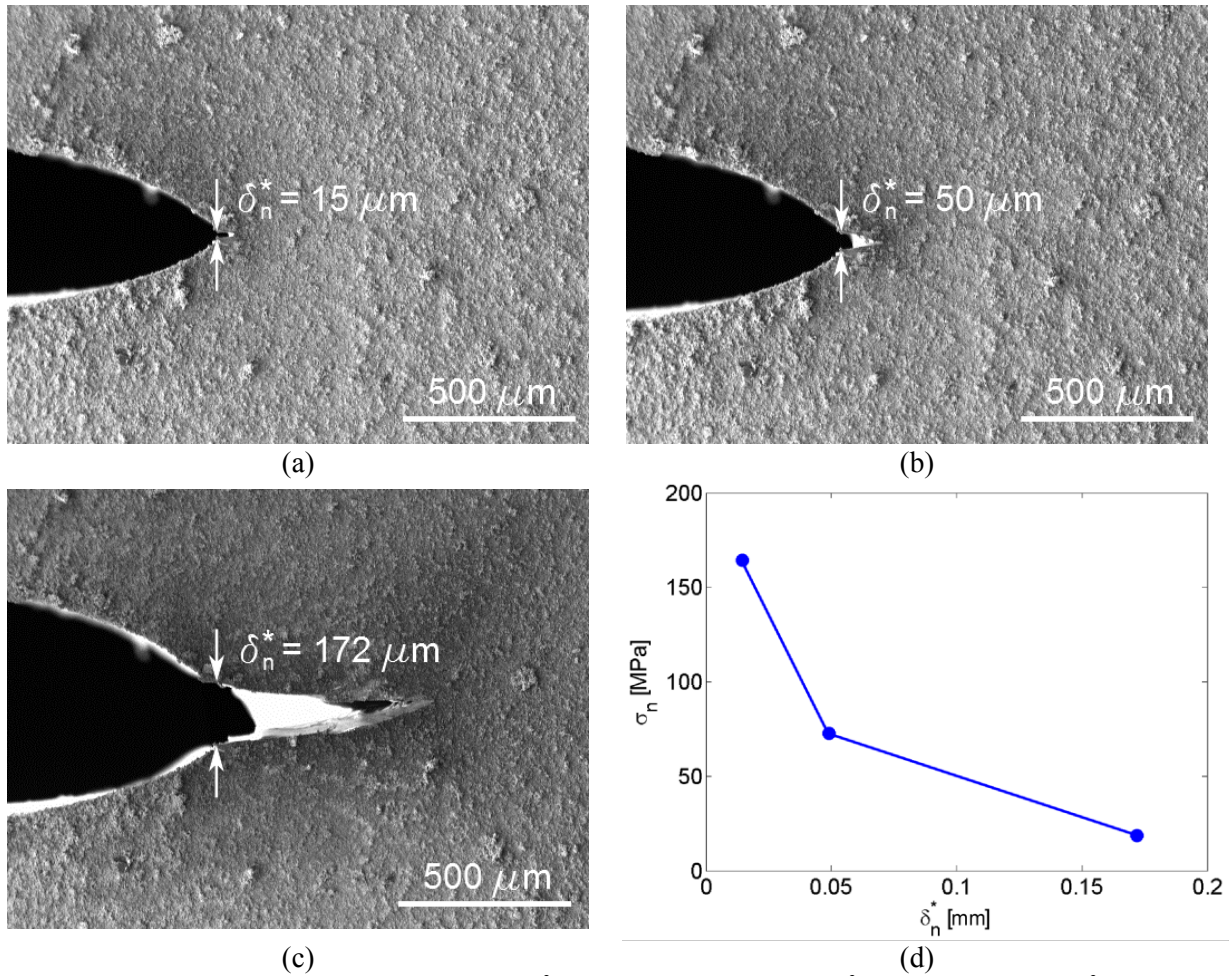


**Fig. 54** The central crack initiation at  $J = 2.4 \text{ kJ/m}^2$  (a), growth at  $J = 4.9 \text{ kJ/m}^2$  (b), and  $J = 7.2 \text{ kJ/m}^2$  (c) for the sample with the initial notch width of  $90 \mu\text{m}$  (the surface has speckles); in addition, the stresses in front of the crack as a function of the opening displacement are given for the same sample (d)



## 4.4 Strain field characterization [P3]

### 4.4.1 Overview of strain field distribution

The strain field contour plots both in Cartesian and cylindrical coordinate system are shown in Fig. 55 for the Test Series 2 at loading  $J = 5.3 \text{ kJ/m}^2$ . It can be seen that the strain  $\varepsilon_{rr}$  and  $\varepsilon_{\theta\theta}$  (Fig. 55d,a), as well as  $\varepsilon_{yy}$  and  $\varepsilon_{xx}$  (Fig. 55e,b) spreads symmetrically about  $y = 0$ , whereas  $\varepsilon_{r\theta}$  and  $\varepsilon_{xy}$  (Fig. 55f,c) asymmetrically around the notch. The values of the strain components  $\varepsilon_{yy}$  and  $\varepsilon_{\theta\theta}$  are highest at the tip and decline with increasing a distance from the notch. Contrary, the strain components  $\varepsilon_{rr}$  and  $\varepsilon_{xx}$  have its lowest value in front of the notch and becomes positive with increasing the distance from the notch tip. The strain components  $\varepsilon_{r\theta}$  and  $\varepsilon_{xy}$  are dominating around the notch sides as shown in Fig. 55f,c. Similar contour plots are obtained for the Test Series 1.

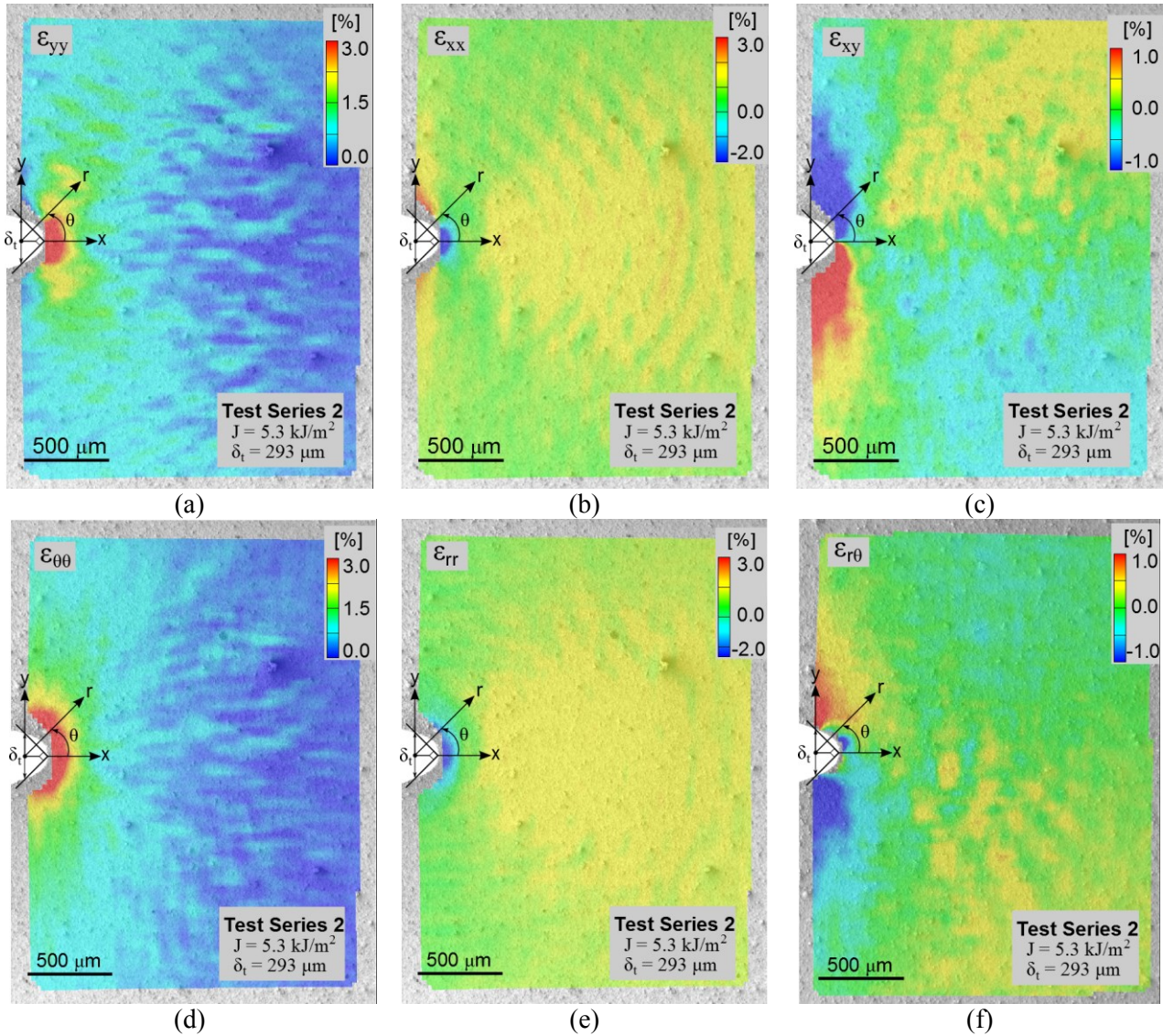
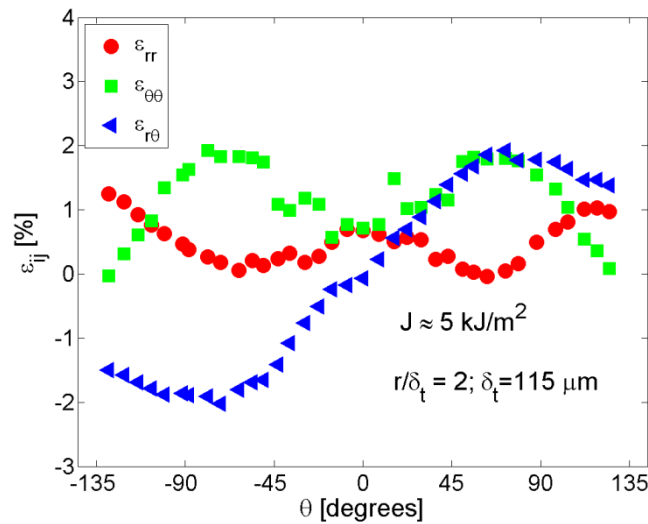


Fig. 55 The strain contour plots for the Test Series 2 in Cartesian (a-d) and cylindrical (d-f) coordinate system

#### 4.4.2 Strain variations with an angle around the notch

The variations of the strain components  $\varepsilon_{rr}$ ,  $\varepsilon_{\theta\theta}$ , and  $\varepsilon_{r\theta}$  with an angle around the notch at the normalized distance  $r/\delta_t = 2$  are given Fig. 56, where  $r$  is the radius from the notch centre and  $\delta_t$  is the notch opening displacement (see subsection 4.1.6). From Fig. 56 it can be seen that the angle of the  $\varepsilon_{\theta\theta}$  maximum tends to be similar to the angle of the  $\varepsilon_{rr}$  minimum (and vice versa). The angle, at which these peak values appear, is found to change with a distance. For instance, for the Test Series 1 the angle of the peak value of the strain components  $\varepsilon_{\theta\theta}$  and  $\varepsilon_{rr}$  varies from  $\theta \approx \pm 30^\circ$  at the distance  $r/\delta_t = 0.8$  to  $\theta \approx \pm 90^\circ$  for  $r/\delta_t = 4.0$ . Similar, but less profound strain variations are also observed for the Test Series 2. The peak values of  $\varepsilon_{\theta\theta}$  and  $\varepsilon_{rr}$  are found at  $\theta \approx \pm 45^\circ$  at the normalized distance  $r/\delta_t = 0.8$  and approach  $\theta \approx \pm 90^\circ$  at  $r/\delta_t = 3.0$ . Similarly to  $\varepsilon_{\theta\theta}$  and  $\varepsilon_{rr}$ , the angle of the maximum and minimum value of  $\varepsilon_{r\theta}$  changes with increasing the distance from the notch, i.e. at  $r/\delta_t = 0.7$  the strain peaks are observed at  $\theta \approx \pm 20^\circ$  and  $\theta \approx \pm 100^\circ$  at  $r/\delta_t = 4$ .



**Fig. 56** The strain variations with an angle around the notch at  $r/\delta_t = 2$  (Test Series 1)

#### 4.4.3 Strain fields compared between notches with different notch width

The Test Series 1 and Test Series 2 samples are having different initial notch width,  $\delta_{i0}$ , as shown in Fig. 27. According to McMeeking's [45] numerical study, the stress and strain fields are independent of the notch size if all length parameters are normalized with the notch width. In order to compare the strain fields between the Test Series 1 and Test Series 2, first, the loadings, which give the same stress in front of the notch for both Test Series, are determined. According to McMeeking [45], the stress in front of the notch depends on the ratio  $\delta_{i0}/\delta_t$ . Therefore, he suggested that there is unique relationship between the normalized displacement ( $\delta_{i0}/\delta_t$ ) and normalized applied load ( $J/\sigma_o \epsilon_o$ ) (see Eq. 2.7), which is similar to the relationship between  $\delta_t$  and  $J$  (Eq. 2.8) for initially sharp cracks. Following McMeeking's approach [45], in Fig. 57 the normalized  $J$  and  $\delta_t$  are presented for the Test Series 1 (filled markers) and Test Series 2 (empty markers). Results show that data points from both Test Series tend to lay on the same curve with a steepness of 0.3,

therefore the relation between the normalized displacement and load can be considered as independent of  $\delta_{to}$ . Further, data points, which agree between different Test Series, are assumed to have an equivalent stress state in front of the notch. Respectively, the loadings, which give the similar stress concentration at the notch for both Test Series, are divided into three Load Sets:

1. Load Set 1 ( $J/\sigma_o * \sigma_o \approx 0.45$ ),  $J = 1.1 \text{ kJ/m}^2$  (Test Series 1) and  $J = 2.5 \text{ kJ/m}^2$  (Test Series 2);
2. Load Set 2 ( $J/\sigma_o * \sigma_o \approx 0.75$ ),  $J = 2.4 \text{ kJ/m}^2$  (Test Series 1) and  $J = 5.3 \text{ kJ/m}^2$  (Test Series 2);
3. Load Set 3 ( $J/\sigma_o * \sigma_o \approx 1.60$ ),  $J = 4.9 \text{ kJ/m}^2$  (Test Series 1) and  $J = 11.7 \text{ kJ/m}^2$  (Test Series 2).

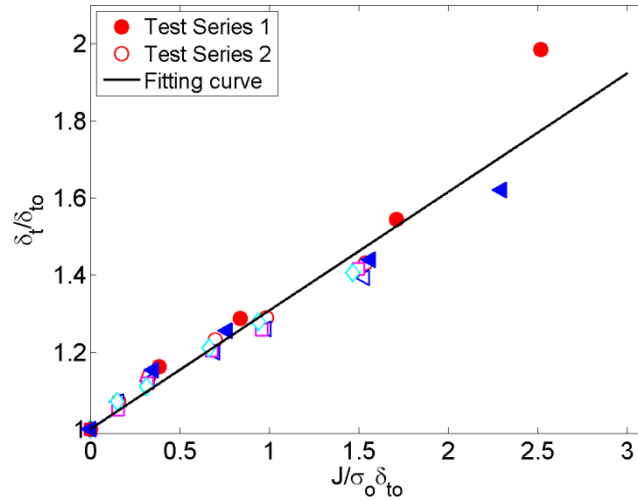


**Fig. 57 The normalized notch opening displacement shown as a function of the normalized  $J$  for the Test Series 1 and Test Series 2**

Second, at each load step it is assumed that the strain fields will match if the length parameters are normalized with  $\delta_t$ . In Fig. 58 the strain contour plots corresponding to the Load Set 2 are presented for the Test Series 1 and Test Series 2. In order to illustrate the comparable length scales, boxes with the edge length equal to  $\delta_t$  are drawn from the notch tip. One can see that the size of the box is considerably larger for the Test Series 2 and has to be squeezed in order to compare with the strains in the box of the Test Series 1. In the normalized coordinate system the boxes for the Test Series 1 and Test Series 2 are equal as in both cases the length of the box edge is  $\delta_t$ .



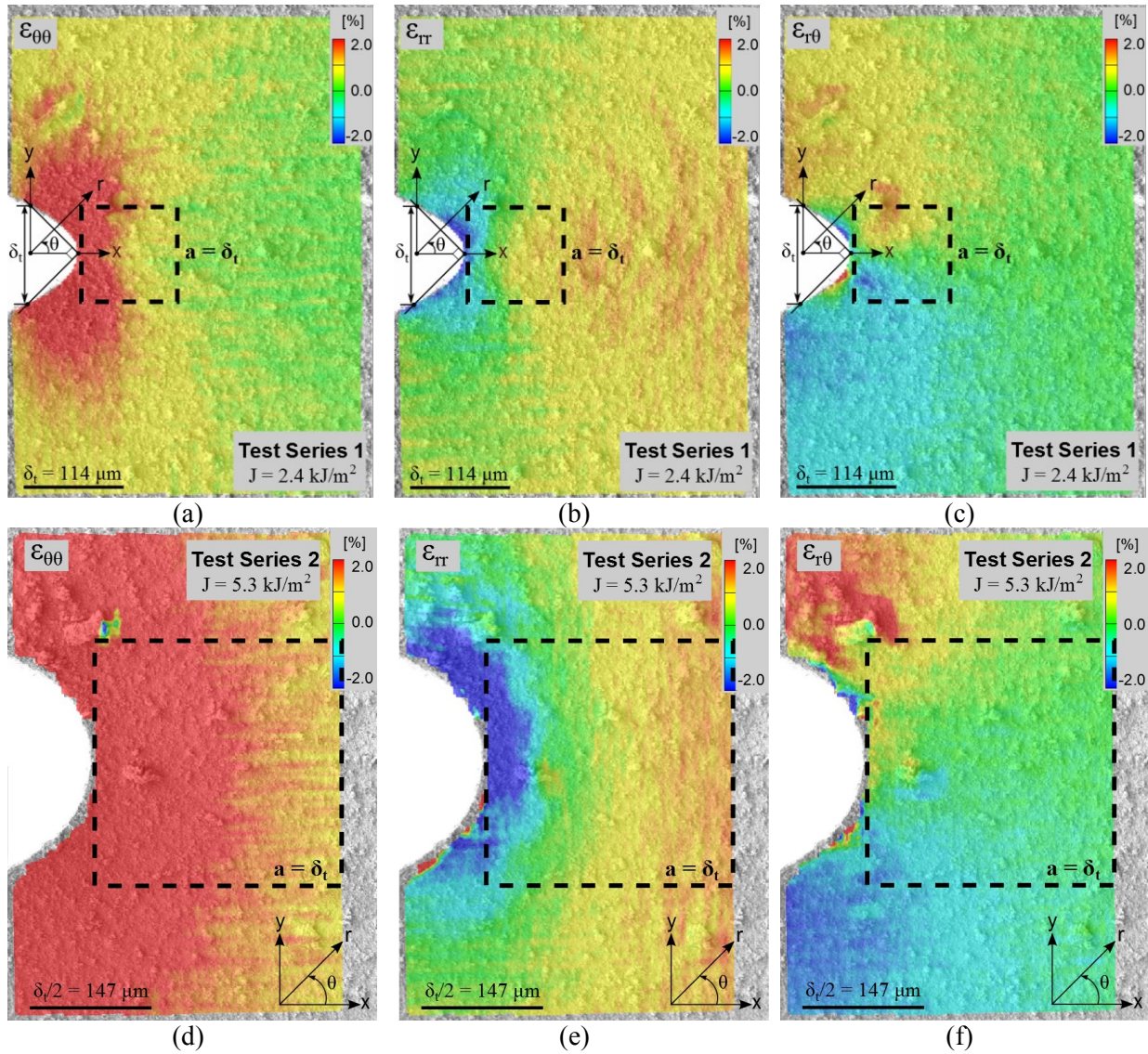


**Fig. 58** The strain contour plots for the Test Series 1 at  $J = 2.4 \text{ kJ/m}^2$  (a-c) and Test Series 2 at  $J = 5.3 \text{ kJ/m}^2$  (d-e) (boxes with a side length of  $\delta_t$  indicate the comparable length scale between the Test Series at the Load Set 2)

More detailed comparison of the strain fields is done by extracting the strains from circular paths in the vicinity of the notch. At moderate loadings, these strain variations with an angle around the notch agree closely between the Test Series. For instance, in Fig. 59a-c the strain fields of  $\epsilon_{rr}$ ,  $\epsilon_{\theta\theta}$ , and  $\epsilon_{r\theta}$  at the Load Set 2 give rather good match, disagreement is below 1% for  $\epsilon_{\theta\theta}$  at the normalized distance  $\delta_t/\delta_{t0} = 1$ . In Fig. 59a-c filled and empty markers present the Test Series 1 ( $\delta_{t0}=95 \text{ }\mu\text{m}$ ) and Test Series 2 ( $\delta_{t0}=234 \text{ }\mu\text{m}$ ), respectively.



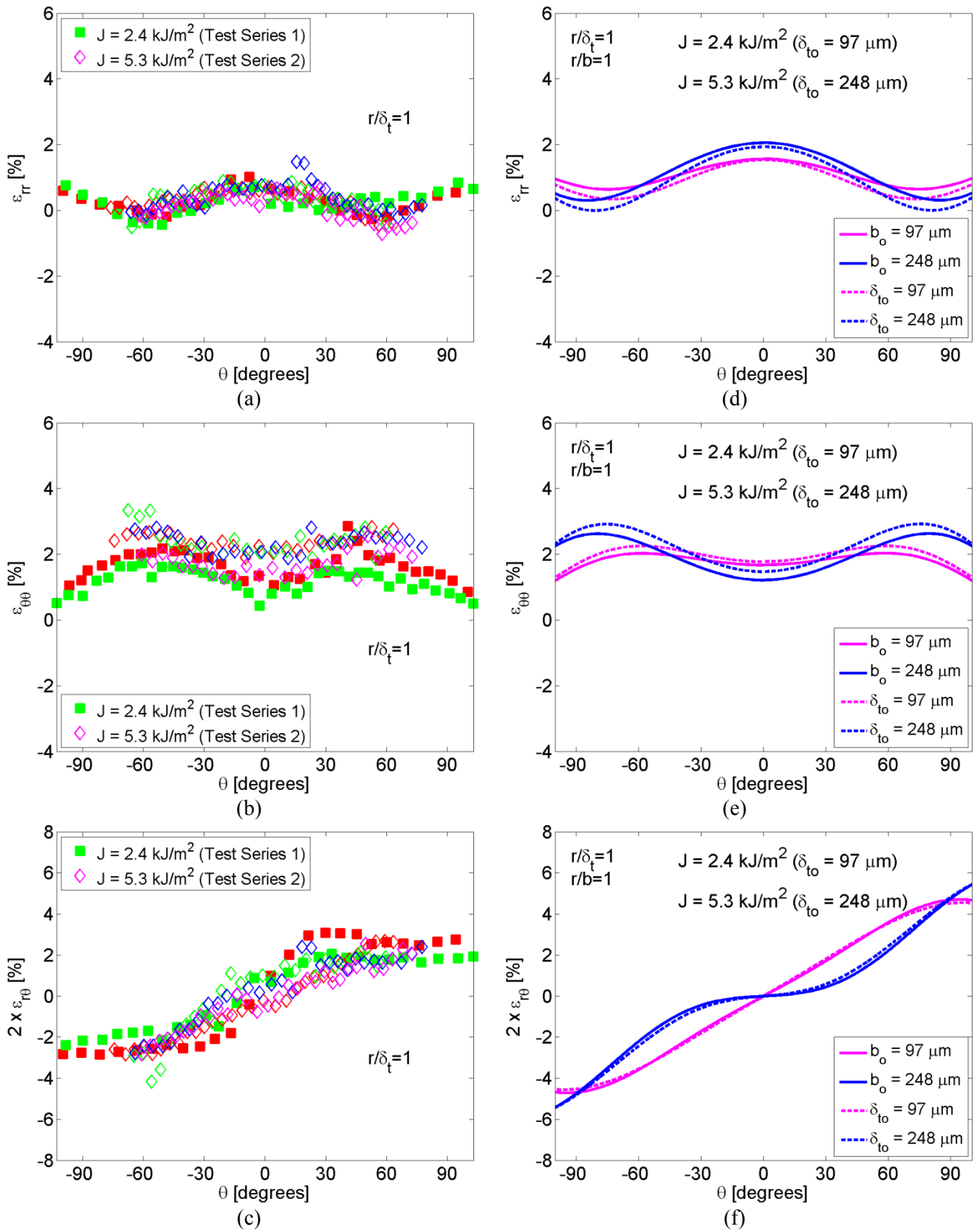


**Fig. 59** The variations of  $\epsilon_{rr}$  (a),  $\epsilon_{\theta\theta}$  (b), and  $\epsilon_{r\theta}$  (c) with an angle around the notch at  $r/\delta_t = 1$  within the Load Set 2; similar strain field discrepancies between different notches are predicted numerically (d-f) for linear-elastic material

In addition, the numerically attained strain fields for the notches with  $\delta_{to} = 97 \mu\text{m}$  and  $\delta_{to} = 248 \mu\text{m}$  for linear-elastic material are shown in Fig. 59d-f. Similarly to the experiments, the numerically attained strain fields show some dissimilarity between different notches. Thus, it seems that the strain fields are affected by the notch geometry at the normalized distance  $\delta_t/\delta_{to} = 1$ . Moreover, in Fig. 59d-f the numerical results show small differences in the choice of the normalization parameter, i.e. discrepancies of the strains around different notches remain independently of the normalization parameter. McMeeking in his numerical study [45] used  $b$  as the normalization parameter (solid line), whereas in this study  $\delta_t$  is used (dashed line), see also subsection 2.2.

#### 4.5 Error estimation of the experimental strain measurements [P3]

Fig. 60 shows that the test sample surface is undergoing brightness and contrast changes during the test. The lightning variations are evaluated increasing the brightness of still image by 10%, 20%, and 30%. The strain measurements are attained to be unaffected by the brightness, and negligible increase of standard deviation (STD) of approximately 0.05% is measured. Furthermore, contrast changes are related to the displacements in the  $z$ -axis direction (out-of-plane), which depend on the applied moment, and are estimated in the range of 100-300  $\mu\text{m}$ . In order to evaluate the effect of the displacement along the  $z$ -axis, out-of-plane rigid body displacement tests are performed. The non-zero strains are measured for all strain components along the principal axes, moreover, the most sensitive is found to be the effective strain,  $\varepsilon_e$ . For the strain components  $\varepsilon_{\theta\theta}$  and  $\varepsilon_{rr}$ , artificial strains are not exceeding 0.5%, and  $\varepsilon_{\theta r}$  is found to be insensitive to the  $z$ -axis displacements. Results are summarized in Table 5.

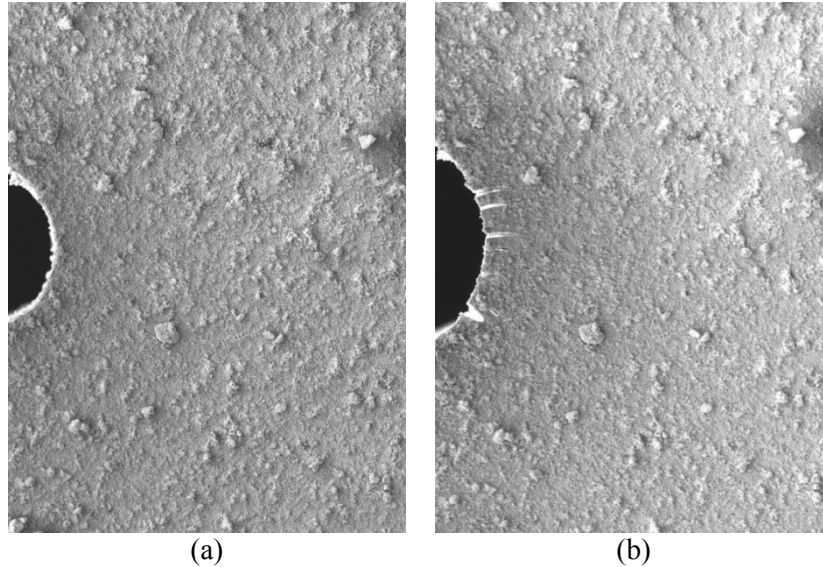


Fig. 60 Initial (a) and deformed image at  $J = 11.7 \text{ kJ/m}^2$  (b) with speckles

In addition, to evaluate possible errors due to distortions discussed in subsection 2.5, the in-plane rigid body displacement tests are performed. During the DCB test, displacements along the  $y$ -axis are measured up to 30

$\mu\text{m}$  and  $150\ \mu\text{m}$  for the results acquired at magnification x500 and x100, respectively. Similar displacements are used to perform the in-plane displacement tests. Both in Cartesian and cylindrical coordinate system for the strain components along the principal axes, the average strain is approaching zero and the STD variations are observed in the range of 0.1-0.25% as shown in Table 5. The only non-zero values are measured for  $\varepsilon_e$ , which seems to be the most sensitive strain component to any displacements.

**Table 5 Strains variations in the rigid body in-plane and out-of-plane displacement test**

Displacement [ $\mu\text{m}$ ]	$f$ [pixels <sup>2</sup> ]	$p$ [pixels]	$M_G$	$\varepsilon_e$ [%]	$\varepsilon_{\theta\theta}$ [%]	$\varepsilon_{rr}$ [%]	$\varepsilon_{r\theta}$ [%]
$\Delta x = 25$	60 x 60	5	x 500	$0.17 \pm 0.08$	$0.00 \pm 0.11$	$0.00 \pm 0.10$	$0.00 \pm 0.07$
$\Delta x = 25$	45 x 45	3	x 500	$0.31 \pm 0.15$	$0.00 \pm 0.23$	$0.00 \pm 0.20$	$0.00 \pm 0.15$
$\Delta x = 100$	60 x 60	5	x 100		$0.00 \pm 0.11$	$0.00 \pm 0.11$	$0.00 \pm 0.08$
$\Delta z = 100$	60 x 60	5	x 500	$0.35 \pm 0.16$	$-0.15 \pm 0.14$	$-0.14 \pm 0.14$	$-0.01 \pm 0.10$
$\Delta z = 200$	60 x 60	5	x 500	$0.61 \pm 0.26$	$-0.26 \pm 0.22$	$-0.27 \pm 0.21$	$-0.02 \pm 0.15$
$\Delta z = 300$	60 x 60	5	x 500	$1.02 \pm 0.50$	$-0.37 \pm 0.44$	$-0.42 \pm 0.44$	$-0.01 \pm 0.31$

#### *The DIC measurement parameters*

In this study, the images of the test sample surface are divided into facets with a length of 45-60 pixels (facet size,  $f$ ) and a distance between the centre points of the adjacent facets is set to 3-5 pixels (facet step,  $p$ ). The facet size affects the displacement spatial resolution,  $f/M_T$ , and, in this study, it is within the range of  $13\ \mu\text{m}$  to  $177\ \mu\text{m}$  as shown in Table 6. According to the literature [53,92], the facet size should contain at least 9-10 speckles (three speckles along each side of the facet). Practically, the minimum theoretical face size, which gives the highest spatial resolution, was impossible due to high noise level and decorrelation. Even though with larger facets the spatial resolution is reduced, the accuracy and the noise reduction is improved [92].

**Table 6 Parameters related to the DIC method**

Magnification	$l$ [ $\mu\text{m}^2$ ]	$M_T$ [pixel/ $\mu\text{m}$ ]	$f/M_T$ ( $f = 60$ pixels) [ $\mu\text{m}$ ]	$f/M_T$ ( $f = 45$ pixels) [ $\mu\text{m}$ ]	Pixel length [ $\mu\text{m}$ ]	min $d_p$ [ $\mu\text{m}$ ]	min $f$ [ $\mu\text{m}$ ]
x100	3000 x 2250	0.34	176.5	132.4	3.0	9.0	27.0
x500	600 x 450	1.71	35.1	26.3	0.6	1.8	5.4
x1000	300 x 225	3.41	17.6	13.2	0.3	0.9	2.7

Furthermore, the facet step is mainly responsible for how densely the facets are packed. More densely packed facet array will give more measurement points within the measurement area. At the same time, too much densely packed array can lead to higher measurement error as the area shared between adjacent facets is increased. Experimentally, the strain variations are evaluated at different degrees of overlap from 50% to 93%. With increasing overlap, the noise level tends to increase, whereas the mean strain values remain unaffected (far from the notch tip). In this study, the overlap between the adjacent facets is within the range of 92-93%.

Relatively far from the notch, neither the facet size nor the facet step is affecting the measurements, i.e. only the noise variations are observed. On the other hand, close to the notch edge, the strains are found to vary with the facet size and step. First, reducing the facet step and size the strain variations around the notch

become more distinct (more profound strain peaks). Second, at the distances up to 20  $\mu\text{m}$  from the notch tip, the strain values are increased setting smaller facet size and step. In this study, the facet size and step is chosen as a compromise between sufficiently high spatial resolution, sufficient number of measurement points, fast computation time and low noise level.

### *The effect of magnification*

Strains acquired at different magnifications are showing some discrepancies, i.e. the strains attained from the images captured at magnification x500 and x1000 agree, and are slightly in a disagreement with the strains gained from the images recorded at magnification x100. The disagreement is particularly evident for the Test Series 1 as illustrated in Fig. 61. Fig. 61 shows that the strain fields acquired from the images recorded at magnification x100 are more uniform in front of the notch and have slightly larger numerical values. Discrepancies are related to a higher spatial resolution with a larger magnification. In Fig. 61, the strain values are extracted setting  $f = 135 \mu\text{m}$ ,  $f = 75 \mu\text{m}$ , and  $f = 21 \mu\text{m}$  for magnifications x100, x500, and x1000, respectively. In the strain field analysis, the images recorded at the magnification x500 are preferred, which is a compromise between sufficiently large field of view and high spatial resolution.

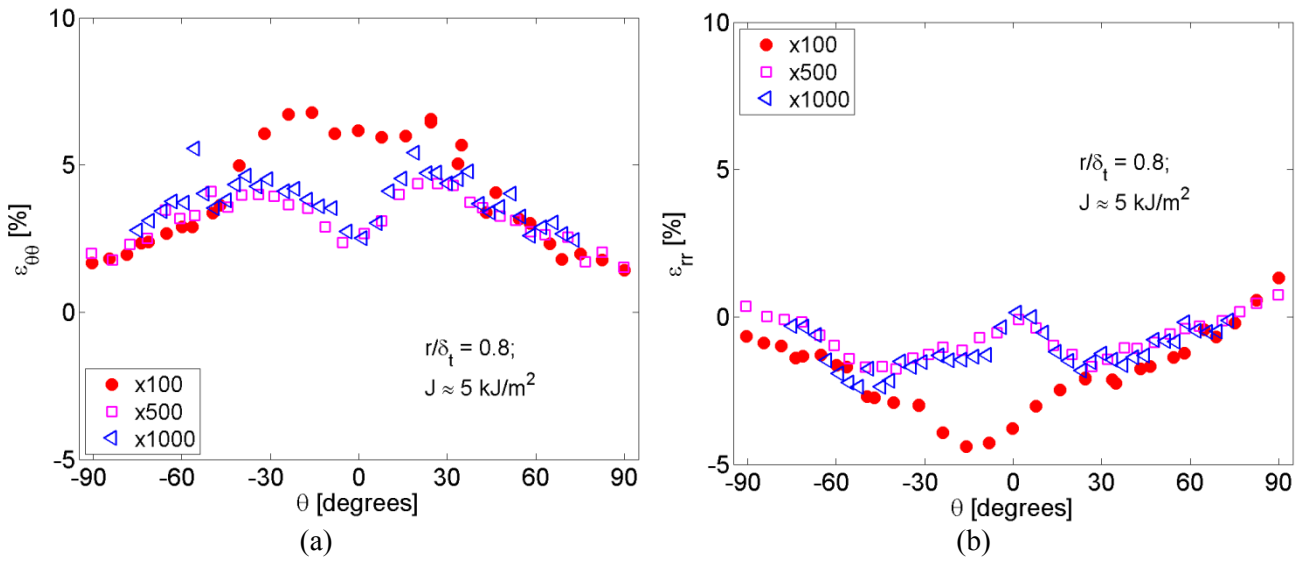


**Fig. 61** The strains  $\varepsilon_{\theta\theta}$  (a) and  $\varepsilon_{rr}$  (b) obtained from the images recorded at various magnifications for the Test Series 1

## 5 Discussion

### *Micro-scale tests*

During the micro-scale tests, the failure strain reached 20% for the strain component  $\varepsilon_{\theta\theta}$ . From the experimental tests, the stresses in front of the notch are unknown. Therefore, analytical, experimental, and numerical approaches were employed to extract the failure stress and the micro-scale stress-strain relationship.

### *Analytical approach*

Analytically, the concept of the strain energy density,  $W$ , was used to determine the stress-strain relationship and failure stress,  $\hat{\sigma}_n$ , at the micro-scale. Results show that if the strain around the notch is assumed to be uniform and equal to the maximum strain of 20%, epoxy resin fits the material with  $n \approx 6$ . Whereas considering non-uniform strain distribution around the notch edge, epoxy resin shows better agreement with the material with  $n < 4$ . This analytical approach was verified by the experimentally obtained permanent strains,  $\varepsilon^p$ . According to Fig. 41, for material with  $n = 4$ , the  $\varepsilon^p$  values are expected to be approximately 3%, whereas experimentally the maximum values of  $\varepsilon^p$  exceeded 10%. Thus, the assumption that the strain is uniform around the notch and equal to 20% agrees better with the experiments.

In general, the limitation of the analytical approach is that the actual strain measurements are restricted to the surface, while the strain distribution through the thickness remains unknown. When the  $W$  values are extracted from the stress-strain curves, the limiting strain values are taken from the measurements on the test sample surface. At the same time,  $\bar{W}$  acquired from the relationship between  $J$  and  $\ast_i$  represents the strain energy density around the notch averaged through the thickness. Numerically, the  $W$  values averaged through the thickness are found to be approximately 1.57 times larger than  $W$  obtained on the surface for the materials with  $n = 6$  and  $n = 8$ . Considering the discrepancies between  $W$  measured on the surface and  $W$  averaged through the thickness, and non-uniform strain distribution in the  $x$ - $y$  plane, epoxy resin can be fitted to the material with  $n \approx 6$ .

### *Experimental approach*

Moreover, the strains in the loaded and unloaded state were used to construct stress-strain curves. Results show that the stress-strain curves constructed are comparable with the stress-strain relationship of the power law hardening material with  $n \approx 5$ . However, these curves appear displaced along the  $\varepsilon$  axis with respect to the stress-strain relationships of the power law hardening materials. One possible reason for this is the out-of-plane displacement, which creates positive artificial strain. Consequently, the strains measured with the DIC technique are higher than the actual strains in the test sample. Furthermore, out-of-plane displacements are expected to have a small impact on the estimated stresses. For instance, assuming that the strain measurements in the unloaded state are free of errors, and that an error of 1% is present in the loaded state,

then the stresses would be overestimated by approximately 30 MPa (Eq. 4.6). These values are rather small compared to the failure stress of 300 MPa. Nevertheless, the estimated stresses could be also affected by non-linear unloading. According to the reference [90], non-linear unloading could cause a stiffness reduction during unloading of as much as 1.5 times. This would reduce the estimated failure stress to 200 MPa (Eq. 4.6). Considering all the uncertainties, it is assumed that epoxy resin can be fitted to power law hardening material with  $n = [5; 6]$  with corresponding failure stresses within the range of 200-300 MPa.

#### *Numerical approach*

In the numerical approach, the strain fields measured experimentally were matched with the numerically predicted strain fields for power law hardening materials with various  $n$  values. Results show that, for the strain component  $\varepsilon_{\theta\theta}$  in the loaded state, both extracting strains from the line paths around the notch and along the notch front, as well as overlapping strain contour plots, the experiments fit the FEM model with  $n \approx 6$ . In the unloaded state, however, better agreement is found with the material model with  $n = 8$ . Why there is this discrepancy between the loaded and unloaded states is unclear. Both experimentally and numerically, unloading was done by removing the load, i.e.  $J = 0 \text{ kJ/m}^2$ , and reverse loading, which could affect the permanent strain values, was not applied. Moreover, the FEM model with  $n = 8$  overestimates the experimentally measured opening displacement at the onset of failure, the strain fields in the loaded state, and the effective plastic strain,  $\varepsilon_e^p$ , values. If we compare  $\sigma_t/\sigma_o$  and  $\varepsilon_e^p$  extracted from the experiments and the numerical models, better agreement is found if the material has  $n \approx 6$ .

Considering analytical, experimental, and numerical results, it seems that epoxy resin can be fitted to the material model with  $n \approx 6$ . Therefore,  $\hat{\sigma}_n$  is predicted to be approximately 250 MPa (the maximum stress around the notch measured numerically).

#### *Uncertainties of the micro-scale measurements*

The uncertainty of the micro-scale measurements could be related to displacements along the  $z$ -axis (as briefly mentioned above) and the presence of micro-cracks. When the distance between the test sample and detector in the ESEM varies, the distance between particles in the recorded image also changes. If the distance is decreased, the particles in the image will appear further apart from one another, giving positive artificial strain, and vice versa if the distance is increased. In the micro-scale tests, the distance between the test sample surface and the detector was observed to decrease. The precise displacements are unknown, but studying the focus changes between the initial and the deformed image, it was estimated that the displacements are in the range of 100-300  $\mu\text{m}$  depending on the load applied. According to rigid body out-of-plane displacement tests, a displacement of 300  $\mu\text{m}$  will raise the strains,  $\varepsilon_{\theta\theta}$  and  $\varepsilon_{rr}$ , by approximately 0.4%, and by approximately 1% for  $\varepsilon_e$ . On the other hand, it could be suggested that the sample contracts locally around the notch edge. Assuming that the strain along the  $y$ -axis is 20% and  $\nu = 0.4$ , the strain in the thickness direction can be estimated as 8%. This would give displacements along the  $z$ -axis of 160  $\mu\text{m}$ .

According to the out-of-plane test, a displacement of 200  $\mu\text{m}$  will create an artificial strain of -0.27% for  $\varepsilon_{rr}$ . Because contraction would create displacements in the opposite direction, the effect of the sample movements along the z-axis should be reduced close to the notch. In general, the artificial strain values seem to be rather small compared to the maximum strains measured experimentally. Moreover, according to the FEM results, the presence of the inclined micro-crack changes strain values around the notch. For instance, the micro-crack reduces the numerical values of  $\varepsilon_{\theta\theta}$  and  $\varepsilon_{rr}$  at the notch tip where the maximum strains were measured. In the FEM model, the micro-crack is created as a partition through the thickness; but this was not certainly the case in the experiments, where some of the micro-cracks could be just surface openings, i.e. the depth of the micro-cracks was much smaller than the sample thickness. As a result, the numerical values of the strain components could be retained at the notch edge.

#### *Macro-scale tests*

The matrix in polymer/fibre composites is subjected to various stress states, which affect its mechanical behaviour. Two plasticity laws, based on the von Mises yield criterion ( $J_2$ -flow theory) and the Drucker-Prager yield criterion were used to predict the behaviour of the epoxy resin in tension, compression, and shear. The application of numerical and analytical methods showed that the  $J_2$ -flow theory predicts the epoxy resin response equally well in shear and tension, when initial properties are defined in tension. This is useful because the tensile test is generally the easiest and most common way of characterizing materials. The  $J_2$ -flow theory was therefore found to be appropriate for polymer/fibre composite models, when damage is governed by the matrix properties in tension and/or shear. On the other hand, the  $J_2$ -flow theory was unable to predict the compressive properties of the epoxy resin. According to the von Mises yield criterion, the material should have the same strength in compression and tension, but the experimental data show otherwise.

In experiments, the strength in compression was measured to be approximately 1.2 times greater than in tension (true values). Possible causes for this are the intrinsic properties of the material, greater material susceptibility to micro-cracking in tension than in compression, and friction at the interface between the test sample and the compression plate that increases the stresses in compression. Numerically, the friction was found to have only a small impact on the yield stresses, i.e. the factor by which the stresses were increased was not sufficient to explain the variations in stress between compression and tension. However, the premature failure due to micro-cracks in tension could be significant. The cracks were observed to evolve from the edges of the samples tested in tension. Differences were also observed between the effective stress-strain relationships in shear and compression, which ideally should agree according to the von Mises yield criterion. The higher stresses in compression could be due to the pressure sensitivity of epoxy resin, as reported by Li et al. [66]. In view of the differences, the pressure dependent Drucker-Prager yield criterion was used as the second material model for predicting epoxy resin behaviour under different loadings.

Numerical results showed that the Drucker-Prager yield criterion predicts equally well the behaviour of epoxy resin in shear, tension, and compression (with the initial properties defined in tension). Thereby, if the polymer/fibre composite failure is due to the matrix response in compression, then the Drucker-Prager yield criterion is suggested.

#### *Measurement errors of strain gauge devices*

Strain gauge devices are often employed to measure the strain of polymer/fibre composites. In experiments, the measurements obtained using a strain gauge were observed to differ from those gained using alternative devices on the same test samples. A numerical study was therefore conducted to investigate, and results showed that the strain gauge measurement errors increased with more compliant materials. However, use of thin samples and short strain gauges affected measurements even on moderately stiff materials with  $E = 10$  GPa. To sum up the results, the main parameters affecting the measurement accuracy of strain gauge devices are the test sample stiffness and thickness, and the strain gauge length. The use of thick specimens can significantly improve the accuracy of the measurements. Nonetheless, errors cannot be completely eliminated for compliant test samples because the effect of thickness is limited to some critical value, after which further increase in thickness has no impact on the strain gauge measurements. This can be explained by a transition from a global to only local reinforcement effect. The critical thickness was found to depend on the strain gauge length. This means that the optimal test sample thickness can be determined for any given strain gauge to minimize measurement errors. When the strain gauge is bonded on test samples with a thickness above the critical, the strain gauge measurement accuracy depends mainly on the strain gauge length and the test sample stiffness. The shorter strain gauges were found to give greater errors, because they are more affected by uneven strain distribution in the gauge, which is caused by the strain transition between materials with mismatching stiffness. The impact of these strain discrepancies can be reduced by improving strain gauge design to move the edges between materials with different stiffness further away from the gauge section.



## 6 Conclusions

The mechanical behaviour of epoxy resin was found to depend on the length scale, i.e. failure strains and strength vary at macro- and micro-scale. Macroscopically, the failure strain is within the range of 5-6%, and its failure strength is 72-86 MPa. Microscopically, strains were measured as high as 20% at the notch edge on the test sample surface. With the application of analytical and numerical approaches, the epoxy resin was found to fit the power law hardening material with the hardening exponent of approximately 6. The corresponding failure stresses were estimated to be about 250 MPa. The macroscopic stress-strain relationship was found to be inadequate for implementation in micro-mechanical models, because it lacks information on material deformation above the strain of 5%. Furthermore, the assumption that epoxy resin is nearly elastic is contradicted by the experimental measurements.

The macro-mechanical behaviour of epoxy resin under simple loadings can be predicted using two plasticity laws based on the von Mises and Drucker-Prager yield criteria. The von Mises yield criterion was found to estimate the behaviour of epoxy resin in shear accurately if the initial properties are defined in tension. Models based on the von Mises yield criterion are therefore assumed to be sufficient for numerical models of polymer/fibre composites if the failure is dominated by the matrix properties in shear and tension. If the failure of the polymer/fibre composite is expected due to the matrix response in compression, the Drucker-Prager yield criterion is suggested. Numerically, it was found that the Drucker-Prager yield criterion predicts equally well the behaviour of the epoxy resin in shear, tension, and compression (when the initial properties are defined in tension).

Moreover, the strain gauge measurement errors were studied, when these devices are applied on materials with stiffness in the range of 1-200 GPa. Results showed that the strain measurements are still biased, even for moderately stiff ( $E \approx 10$  GPa) and thin test samples, if short strain gauges are attached. The strain measurement errors become negligible, however, if moderately stiff test samples are sufficiently thick and long strain gauges are used. For more compliant materials with  $E < 10$  GPa, biased strain measurements cannot be avoided by using thick test samples and long strain gauges so the gauge factor provided by manufacturers needs to be corrected. Alternatively, the enhanced strain gauge design presented can reduce measurement errors.

## References

- [1] B.F. Sørensen, J.W. Holmes, P. Brøndsted, K. Branner, Blade materials, testing methods and structural design, in: *Wind Power Gener. Wind Turbine Des.*, WIT press, 2010: pp. 417–466.
- [2] P. Brøndsted, H. Lilholt, A. Lystrup, COMPOSITE MATERIALS FOR WIND POWER TURBINE BLADES, *Annu. Rev. Mater. Res.* 35 (2005) 505–538.
- [3] C.R. Schultheisz, A.M. Waas, Compressive failure of composites, Part I: Testing and micromechanical theories, *Prog. Aerosp. Sci.* 32 (1996) 1–42.
- [4] B. Budiansky, N.A. Fleck, Compressive Kinking of Fiber Composites: A Topical Review, *Appl. Mech. Rev.* 47 (1994) S246.
- [5] S. Kyriakides, R. Arseculeratne, E.J. Perry, K.M. Liechti, On the compressive failure of fiber reinforced composites, *Int. J. Solids Struct.* 32 (1995) 689–738.
- [6] L.P. Canal, J. Segurado, J. LLorca, Failure surface of epoxy-modified fiber-reinforced composites under transverse tension and out-of-plane shear, *Int. J. Solids Struct.* 46 (2009) 2265–2274.
- [7] L.E. Asp, L.A. Berglund, R. Talreja, Prediction of matrix-initiated transverse failure in polymer composites, *Compos. Sci. Technol.* 56 (1996) 1089–1097.
- [8] L.P. Canal, C. González, J.M. Molina-Aldareguía, J. Segurado, J. LLorca, Application of digital image correlation at the microscale in fiber-reinforced composites, *Compos. Part A Appl. Sci. Manuf.* 43 (2012) 1630–1638.
- [9] E. Correa, V. Mantič, F. París, A micromechanical view of inter-fibre failure of composite materials under compression transverse to the fibres, *Compos. Sci. Technol.* 68 (2008) 2010–2021.
- [10] J. Kim, Y. Mai, High strength, high fracture toughness fibre composites with interface control—a review, *Compos. Sci. Technol.* (1991).
- [11] L.E. Asp, L.A. Berglund, P. Gudmundson, Effects of a composite-like stress state on the fracture of epoxies, *Compos. Sci. Technol.* 53 (1995) 27–37.
- [12] B. Fiedler, M. Hojo, S. Ochiai, K. Schulte, M. Ando, Failure behavior of an epoxy matrix under different kinds of static loading, *Compos. Sci. Technol.* 61 (2001) 1615–1624.
- [13] R. Quinson, J. Perez, M. Rink, A. Pavan, Yield criteria for amorphous glassy polymers, *J. Mater. Sci.* 32 (1997) 1371–1379.
- [14] S. Rabinowitz, I.M. Ward, J.S.C. Parry, The effect of hydrostatic pressure on the shear yield behaviour of polymers, *J. Mater. Sci.* 5 (1970) 29–39.
- [15] I.M. Ward, Review: The yield behaviour of polymers, *J. Mater. Sci.* 6 (1971) 1397–1417.
- [16] P.B. Bowden, J.A. Jukes, The plastic flow of isotropic polymers, *J. Mater. Sci.* 7 (1972) 52–63.
- [17] P. Bardia, R. Narasimhan, Characterisation of pressure-sensitive yielding in polymers, *Strain.* 42 (2006) 187–196.
- [18] D. Li, A.F. Yee, I.-W. Chen, S.-C. Chang, K. Takahashi, Fracture behaviour of unmodified and rubber-modified epoxies under hydrostatic pressure, *J. Mater. Sci.* 29 (1994) 2205–2215.
- [19] T.L. Anderson, *Fracture Mechanics: Fundamentals and Applications*, 1995.
- [20] M.F. Ashby, H. Shercliff, D. Cebon, *Materials: engineering, science, processing and design*, Butterworth-Heinemann, 2013.
- [21] T. Hobbiebrunken, B. Fiedler, M. Hojo, M. Tanaka, Experimental determination of the true epoxy resin strength using micro-scaled specimens, *Compos. Part A Appl. Sci. Manuf.* 38 (2007) 814–818.
- [22] A.A. Griffith, The Phenomena of Rupture and Flow in Solids, *Philos. Trans. R. Soc. A Math. Phys.*

Eng. Sci. 221 (1921) 163–198.

- [23] J. Goodier, Concentration of stress around spherical and cylindrical inclusions and flaws, *J. Appl. Mech.* 55 (1933) 39–44.
- [24] K.J. Hemker, W.N. Sharpe, Microscale Characterization of Mechanical Properties, *Annu. Rev. Mater. Res.* 37 (2007) 93–126.
- [25] M.R. Wisnom, Size effects in the testing of fibre-composite materials, *Compos. Sci. Technol.* 59 (1999) 1937–1957.
- [26] E.M. Odom, D. Adams, Specimen size effect during tensile testing of an unreinforced polymer, *J. Mater. Sci.* 27 (1992) 1767–1771.
- [27] N.A. Fleck, G.M. Muller, M.F. Ashby, J.W. Hutchinson, Strain gradient plasticity: Theory and experiment, *Acta Metall. Mater.* 42 (1994) 475–487.
- [28] N. Fleck, J. Hutchinson, A phenomenological theory for strain gradient effects in plasticity, *J. Mech. Phys. Solids.* 41 (1993) 1825–1857.
- [29] J. Tjernlund, E. Kristofergamstedt, P. Gudmundson, Length-scale effects on damage development in tensile loading of glass-sphere filled epoxy, *Int. J. Solids Struct.* 43 (2006) 7337–7357.
- [30] A. Chong, H.K. Lam, David C.C. (Department of Mechanical Engineering, Hong Kong University of Science and Technology, Strain gradient plasticity effect in indentation hardness of polymers, *J. Mater. Res.* 14 (1999) 4103–4110.
- [31] Z.C. Xia, J.W. Hutchinson, Crack tip fields in strain gradient plasticity, *J. Mech. Phys. Solids.* 44 (1996) 1621–1648.
- [32] L.P. Mikkelsen, S. Goutianos, Suppressed plastic deformation at blunt crack-tips due to strain gradient effects, *Int. J. Solids Struct.* 46 (2009) 4430–4436.
- [33] D.C.C. Lam, A. Chong, Indentation model and strain gradient plasticity law for glassy polymers, *J. Mater. Res.* 14 (1999) 3784–3788.
- [34] D.A. Vajari, C. González, J. LLorca, B.N. Legarth, A numerical study of the influence of microvoids in the transverse mechanical response of unidirectional composites, *Compos. Sci. Technol.* 97 (2014) 46–54.
- [35] J.W. Hutchinson, Plastic stress and strain fields at a crack tip, *J. Mech. Phys. Solids.* 16 (1968) 337–342.
- [36] J.R. Rice, G.F. Rosengren, Plane strain deformation near a crack tip in a power-law hardening material, *J. Mech. Phys. Solids.* 16 (1968) 1–12.
- [37] V. Tvergaard, PLASTICITY AND CREEP IN STRUCTURAL MATERIALS, Technical University of Denmark, 2001.
- [38] W.-F. Chen, D.-J. Han, Stress-Strain Relations for Work-Hardening Materials, in: *Plast. Struct. Eng.*, J.Ross Publishing, 2007: pp. 232–292.
- [39] J.W. Hutchinson, Fundamentals of the phenomenological theory of nonlinear fracture mechanics, *J. Appl. Mech.* 50 (1983) 1042–1051.
- [40] C.F. Shih, M.D. German, Requirements for a one parameter characterization of crack tip fields by the HRR singularity, *Int. J. Fract.* 17 (1981) 27–43.
- [41] R. McMeeking, D. Parks, Elastic-Plastic Fracture, ASTM International, 100 Barr Harbor Drive, PO Box C700, West Conshohocken, PA 19428-2959, 1979.
- [42] J.D. Landes, J.A. Begly, Test results from J-integral studies: an attempt to establish a JIc testing procedure, in: *Fract. Anal.*, American Society for Testing and Materials Philadelphia, PA, 1974: pp.

170–186.

- [43] J. Rice, A path independent integral and the approximate analysis of strain concentration by notches and cracks, 35 (1967) 379–386.
- [44] W. Ramberg, W.R. Osgood, Description of stress-strain curves by three parameters, Natl. Advis. Comm. Aeronaut. (1943).
- [45] R.M. McMeeking, Finite deformation analysis of crack-tip opening in elastic-plastic materials and implications for fracture, J. Mech. Phys. Solids. 25 (1977) 357–381.
- [46] C.F. Shih, Relationships between the J-integral and the crack opening displacement for stationary and extending cracks, J. Mech. Phys. Solids. 29 (1981) 305–326.
- [47] B.F. Sørensen, Cohesive laws for assessment of materials failure: Theory, experimental methods and application, Risø DTU, 2010.
- [48] A. Hillerborg, M. Modéer, P.-E. Petersson, Analysis of crack formation and crack growth in concrete by means of fracture mechanics and finite elements, Cem. Concr. Res. 6 (1976) 773–781.
- [49] A. Hillerborg, Application of the fictitious crack model to different types of materials, Int. J. Fract. 51 (1991) 95–102.
- [50] W.-F. Chen, D.-J. Han, Yield Criteria Independent of Hydrostatic Pressure, in: Plast. Struct. Eng., 2007: pp. 72–83.
- [51] Systemes Dassault, Abaqus Analysis User's Guide, ABAQUS Inc., Dassault Syst. Fr. (2013).
- [52] W.-F. Chen, D.-J. Han, Failure Criterion for Pressure-Dependent Materials, in: Plast. Struct. Eng., 2007: pp. 84–98.
- [53] M.A. Sutton, J.J. Orteu, H.W. Schreier, Image Correlation for Shape, Motion and Deformation Measurements- Basic Concepts, Theory and Applications, 2009.
- [54] B. Pan, K. Qian, H. Xie, A. Asundi, Two-dimensional digital image correlation for in-plane displacement and strain measurement: a review, Meas. Sci. Technol. 20 (2009).
- [55] G.O.M. Techniques, ARAMIS user manual, ARAMIS 4M v5. 4.1, Gesellschaft Für Opt. Messtechnik. (2005).
- [56] W.N. Sharpe, Springer Handbook of Experimental Solid Mechanics, 2008.
- [57] T.A. Berfield, J.K. Patel, R.G. Shimmin, P. V. Braun, J. Lambros, N.R. Sottos, Micro- and Nanoscale Deformation Measurement of Surface and Internal Planes via Digital Image Correlation, Exp. Mech. 47 (2007) 51–62.
- [58] F. Lagattu, F. Bridier, P. Villechaise, J. Brillaud, In-plane strain measurements on a microscopic scale by coupling digital image correlation and an in situ SEM technique, Mater. Charact. 56 (2006) 10–18.
- [59] M.A. Sutton, N. Li, D. Garcia, N. Cornille, J.J. Orteu, S.R. McNeill, et al., Metrology in a scanning electron microscope: theoretical developments and experimental validation, Meas. Sci. Technol. 17 (2006) 2613–2622.
- [60] H. Wang, H. Xie, Y. Ju, Q. Duan, Error analysis of digital speckle correlation method under scanning electron microscope, Exp. Tech. 30 (2006) 42–45.
- [61] ASTM D5379 / D5379M, Standard Test Method for Shear Properties of Composite Materials by the V-Notched Beam Method, West Conshohocken, PA, 2012.
- [62] ASTM D695, Standard Test Method of Compressive Properties of Rigid Plastics, West Conshohocken, 2002. [www.astm.org](http://www.astm.org).
- [63] ISO 527-1, Plastics-determination of tensile properties-Part 1, 2012.

- [64] M. Jerabek, Z. Major, R.W. Lang, Uniaxial compression testing of polymeric materials, *Polym. Test.* 29 (2010) 302–309.
- [65] D.C. Drucker, Plasticity theory strength-differential(SD) phenomenon, and volume expansion in metals and plastics, *Metall. Trans.* 4 (1973) 667–673.
- [66] D. Li, A.F. Yee, I. W. Chen, S.C. Chang, K. Takashi, Fracture behaviour of unmodified and rubber-modified epoxies under hydrostatic pressure, *J. Mater. Sci.* 29 (1994) 2205–2215.
- [67] P. Stehlin, Strain distribution in and around strain gauges, *J. Strain Anal. Eng.* 7 (1972) 228–235.
- [68] M. Beatty, Numerical analysis of the reinforcement effect of a strain gage applied to a soft material, *Int. J. Eng. Sci.* (1979).
- [69] A. Ajovalasit, L. D’Acquisto, S. Fragapane, B. Zuccarello, Stiffness and Reinforcement Effect of Electrical Resistance Strain Gauges, *Strain.* 43 (2007) 299–305.
- [70] A. Ajovalasit, Advances in Strain Gauge Measurement on Composite Materials, *Strain.* 47 (2011) 313–325.
- [71] J. Swan, Resistance strain gauges on thermoplastics, *Strain.* (1973) 56–59.
- [72] E.G. Little, D. Tocher, P.O. Donnell, Strain gauge reinforcement of plastics, *Strain.* (1990).
- [73] C. Perry, Strain gauge measurements on plastics and composites, *Strain.* (1987).
- [74] E. Voet, G. Luyckx, W. De Waele, J. Degrieck, Multi-axial strain transfer from laminated CFRP composites to embedded Bragg sensor: II. Experimental validation, *Smart Mater. Struct.* 19 (2010).
- [75] W. Li, C. Cheng, Y. Lo, Investigation of strain transmission of surface-bonded FBGs used as strain sensors, *Sensors Actuators A Phys.* 149 (2009) 201–207.
- [76] K. Hoffmann, *An Introduction to Measurements using Strain Gages*, HBM, 1989.
- [77] R.B. Watson, Bonded Electrical Resistance Strain Gages, in: W.N. Sharpe (Ed.), *Handb. Exp. Solid Mech.*, Springer, 2008: pp. 283–333.
- [78] A. Ajovalasit, B. Zuccarello, Local Reinforcement Effect of a Strain Gauge Installation on Low Modulus Materials, *J. Strain Anal. Eng. Des.* 40 (2005) 643–653.
- [79] HBM Strain Gauge Catalog, (n.d.). <http://www.hbm.com/fileadmin/mediapool/hbmdoc/technical/s1265.pdf> (accessed June 5, 2012).
- [80] M. Stockmann, *Micromechanische Analyse der Wirkungsmechanismen elektrischer Dehnungsmessstreifen*, Technischen Universität Chemnitz, 2000.
- [81] L. Mikkelsen, S. Zike, A Strain Gauge, EP14180022.72014., 2014.
- [82] B.F. Sørensen, A. Horsewell, O. Jørgensen, A.N. Kumar, P. Engbæk, Fracture resistance measurement method for in situ observation of crack mechanisms, *J. Am. Ceram. Soc.* 81 (1998) 661–669.
- [83] A.J. Kinloch, J.G. Williams, Crack blunting mechanisms in polymers, *J. Mater. Sci.* 15 (1980) 987–996.
- [84] S. Goutianos, H.L. Frandsen, B.F. Sørensen, Fracture properties of nickel-based anodes for solid oxide fuel cells, *J. Eur. Ceram. Soc.* 30 (2010) 3173–3179.
- [85] E.H. Smith, Photoelasticity, in: *Mech. Eng. Ref. B.*, 12th ed., Butterworth-Heinemann, 1994: pp. 8/16–8/18.
- [86] Beckman Coulter, Laser diffraction particle size analyzer, (n.d.). <https://www.beckmancoulter.com/wsrportal/wsr/industrial/products/laser-diffraction-particle-size-analyzers> (accessed April 28, 2015).

- [87] Airbrush BossDye-132, (n.d.). <http://www.co-import.dk/16350228>.
- [88] ZEISS, Environmental scanning electron microscope, (n.d.). [http://www.zeiss.com/microscopy/en\\_de/products/scanning-electron-microscopes/evo-materials.html](http://www.zeiss.com/microscopy/en_de/products/scanning-electron-microscopes/evo-materials.html).
- [89] F.P. Beer, R.E. Johnston, Transformations of stress and strain, in: Mech. Mater., McGraw-Hill Book Company, 1992: pp. 339–400.
- [90] X. Shen, Z. Xia, F. Ellyin, Cyclic deformation behavior of an epoxy polymer. Part I: experimental investigation, Polym. Eng. Sci. 44 (2004) 2240–2246.
- [91] W.L. BRADLEY, Chapter 5 - Relationship of Matrix Toughness to Interlaminar Fracture Toughness, in: Appl. Fract. Mech. to Compos. Mater., 1989: pp. 159–187.
- [92] M. Sjö Dahl, Accuracy in electronic speckle photography., Appl. Opt. 36 (1997) 2875–2885.

## Publication [P1]

Mechanical material characterization of an epoxy  
regarding hydrostatic pressure sensitivity

# Mechanical characterization of an epoxy resin matrix and its relation to hydrostatic pressure sensitive and insensitive material models

Sanita Zike, Lars P. Mikkelsen

*Composites and Materials Mechanics Section, Department of Wind Energy, Technical University of Denmark, Risø Campus, 4000 Roskilde, Denmark*

## Abstract

A rather ductile epoxy polymer, *Airstone 760E*, typically used as a matrix material for the composite material in wind turbine blades is experimentally tested during uniaxial tension, shear loading, and uniaxial compression. It has been found that the shear properties can be estimated from the uniaxial tension using a classical  $J_2$ -flow theory based on a von Mises yield surface. An approach often used in the literature but rarely validated due to the ease of performing uniaxial tension. Nevertheless, the compression behavior is found in the present case to be underestimated with approximately 20%, an underestimation which can be covered using a pressure dependent Drucker-Prager based plasticity law.

**Keywords:** epoxy resin, mechanical properties, material models of polymer/fibre composites, Drucker-Prager yield criterion, von Mises yield criterion

## 1 Introduction

A design of polymer/fibre composite structures typically implies that load will be carried by much stronger and stiffer fibres; however, a lot of micro-mechanical processes actually depend on the matrix properties and fibre-matrix interface. This is relevant loading both parallel and transverse to the fibres. For instance, when composite structures are loaded in line with the fibres in compression, strength is influenced by fibre resistance to buckling and kinking [1–3]. Strength in compression therefore depends on how well the fibres are supported by the matrix. The fibre resistance to buckling and kinking will improve with higher shear stiffness and strength of the matrix. When composites structures are loaded transverse to the fibres whether in tension or compression, the main failure modes are related to fibre/matrix debonding, matrix yielding, and cavitation (in tension) of the matrix [4–8]. Although, composite failure in the transverse loading is dominated by the matrix properties, the strains to failure are profoundly lower than those of pure polymers [9]. According to Asp et al. [9], the foremost reason is the multi-axial stress state in the matrix caused by the fibre confinement. Furthermore, voids, flaws, and incomplete adhesion at the matrix-fibre interface would limit the composite behaviour with the transverse loading even more. The effect of the multi-axial stress state is explained with a pressure sensitivity of the matrix.

Polymer materials, in general, are considered pressure sensitive [10–14], i.e. the yield strength of a polymer material improves under hydrostatic pressure. Under moderate pressures, the polymer can experience both



higher yield strength and strain, e.g. brittle polymers can become ductile [12,15]. Moderate pressures suppress crazing and post-pone cracking, allowing the material to approach stresses needed for yielding [15]. The yield strength continues to increase with external pressure, because the molecular movements responsible for shear deformation are restricted in polymer. With high pressure, the stress required to induce shear deformation becomes greater than the stress needed for fracture [11], and the transition from ductile to brittle behaviour can occur [12]. Thus, the failure strain decreases.

Indirectly the pressure-dependent yielding can be deduced from uniaxial compression and uniaxial tension [14,16], where the stresses under compression surpass the stresses in tension. However, different yield strength in uniaxial tension and uniaxial compression can be also due to other factors. For instance, the residual stresses or Bauschinger effect [17] originating from manufacturing or multiple loading steps like tension-compression can cause differences. Moreover, the yield strength variations are explained with a larger material susceptibility to micro-crack and void [12,17] initiation, nucleation, and growth in tension than in compression.

Concluding, the role of the matrix is not negligible and affects the performance of the whole polymer/fibre composite structure. In order to understand the failure mechanisms within composites, numerical and analytical tools are often applied. The mechanical properties of the matrix material used predicting the mechanical properties of composites are frequently extracted from uniaxial tensile tests even though that e.g. the compressive failure of uniaxial composites are highly dependent on the shear properties. Based on an extensive experimental study of a specific epoxy polymer used in wind turbine industry, the validation of this approach is investigated.

In the paper, first, the mechanical properties of the epoxy resin under simple loadings as uniaxial tension, uniaxial compression, and shear, are given. In the experiments, due to the fact that strain gauges significantly will underestimate the applied strains [21], the tests have been performed using a combination of strain gauges, clip-on extensometers, and digital image correlation method. Furthermore, the uncertainties of the compression and shear test are assessed. In compression, the variations of the stress-strain relationship due to the friction at the interface between the test sample and compression plate are evaluated. In shear, the non-uniform strain distribution on the test sample surface is addressed as it affects the final results. Finally, two plasticity laws, based on the pressure dependent Drucker-Prager and the pressure independent von Mises yield criterion, are related to the experimental measurements.

## **2 Experimental measurements**

### *2.1 Material*

Commercially available epoxy *Airstone 760E* is mixed with a hardener *Airstone (TM) 766H* maintaining the ratio 3:1. The liquid mixture is degassed in a vacuum chamber reaching a vacuum of 98%. Afterwards, the epoxy is poured into a mould and cured for 5 hours at 50°C then cooled up to the room temperature and post-cured for 3 hours at 80°C. The final step of the manufacturing involves the test sample machining. The test

samples for shear and tension are cut out utilizing the CNC milling machine *ISEL GFV 102/72-SW*, and a diamond cutting blade is used to cut out the compression test samples. For the shear test samples, additional surface preparation is done in order to employ the digital image correlation method (DIC). First, a white background is painted on one of the test sample's surfaces, afterwards a black paint is sprayed creating randomly distributed speckles.

## 2.2 The tensile test

According to the standard [20] samples of a dumb-bell shape with dimensions of the gauge section of  $70 \times 10 \times 4.2 \text{ mm}^3$  are tested in tension as shown in Fig. 1a. The tests (also in shear and compression) are carried out utilizing the universal testing machine *Instron 88R1362* with a 50 kN load cell (SN: UK 230), and strains are measured applying the clip-on extensometers with a gauge section of 50 mm.

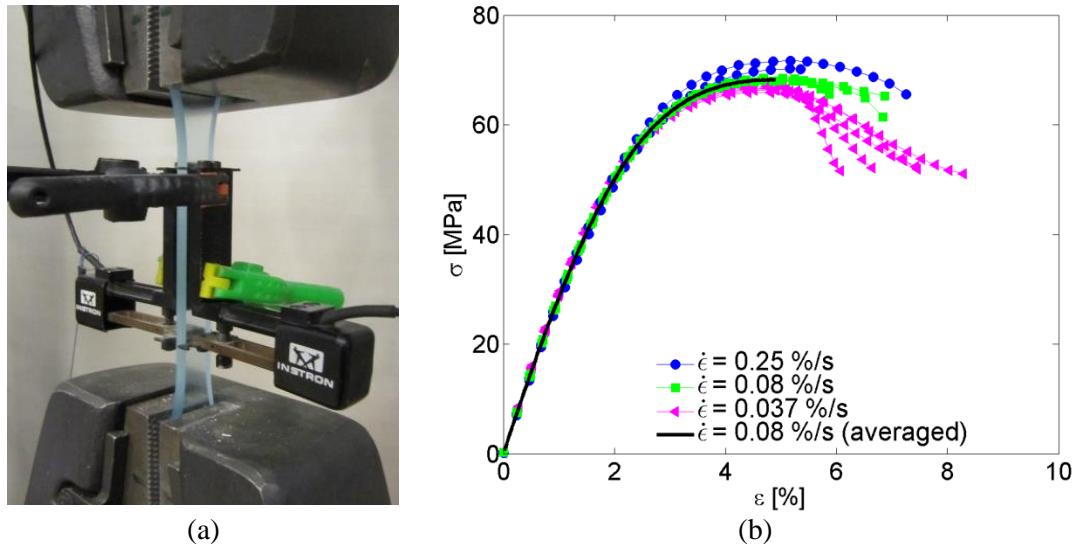


**Fig. 1 The tensile test set-up (a), and the stress-strain relations attained under different strain rates (b) (nominal values are presented)**

During the tensile test, the samples are subjected to three different displacement rates, which give constant strain rates,  $\dot{\varepsilon}$ , of 0.037%/s, 0.08%/s, and 0.25%/s. The corresponding stress-strain relations under different strain rates are given in Fig. 1b. Results show that the test samples subjected to lower strain rates undergo more gradual failure, whereas increasing  $\dot{\varepsilon}$  the failure becomes more abrupt. With higher  $\dot{\varepsilon}$ , the ultimate stress,  $\sigma_u$ , and the strain corresponding to the ultimate stress,  $\varepsilon_u$ , increases. Nevertheless, the variations of  $\sigma_u$  and  $\varepsilon_u$  with  $\dot{\varepsilon}$  are rather small (see also Table 1). Attained results show that the nominal values of  $\sigma_u$  are within the range of 67-71 MPa,  $\varepsilon_u$  is approximately 5%, and material stiffness,  $E$ , is around 3 GPa within the strain range  $\varepsilon = [0.0005; 0.0025]$  [20].

**Table 1 The mechanical properties of the epoxy resin in tension, shear, and compression**

	$G$ [GPa]	$\tau_u$ [MPa]	$\gamma_u$ [%]
<b>Shear<sup>a</sup></b>			
$A = 3 \times 3 \text{ mm}^2$	$0.97^b \pm 0.03$	$42.9 \pm 0.4$	$8.6 \pm 0.3$
$A = 0.6 \times 0.6 \text{ mm}^2$	$0.95^b \pm 0.03$	$42.9 \pm 0.4$	$10.0 \pm 1.0$
	$E$ [GPa]	$\sigma_u$ [MPa]	$\varepsilon_u$ [%]
<b>Compression<sup>b</sup></b>			
$E$	$3.43 \pm 0.08$	$92.0 \pm 2.0$	$6.0 \pm 0.1$
<b>Tension<sup>b</sup></b>			
$\dot{\varepsilon} = 0.037\%/s$	$3.04 \pm 0.02$	$66.8 \pm 0.5$	$4.8 \pm 0.1$
$\dot{\varepsilon} = 0.08\%/s$	$3.01 \pm 0.03$	$68.4 \pm 0.4$	$4.9 \pm 0.1$
$\dot{\varepsilon} = 0.25\%/s$	$2.98 \pm 0.06$	$71.2 \pm 0.8$	$5.2 \pm 0.1$

<sup>a</sup>  $G$  is measured for  $\gamma = [0.005; 0.0075]$  due to the small number of data and sharp transition in the stress-strain curve steepness in the range of  $\gamma$  defined by the test standard [19]

<sup>b</sup> Nominal values are presented

### 2.3 The shear test

In accordance to the test standard [19], ten samples with dimensions of  $76 \times 20 \times 4 \text{ mm}^3$  and with a distance of 12 mm between the notch tips are tested in shear utilizing the Iosipescu fixture (see Fig. 2a). Three samples are used to evaluate twist. The shear strain is measured employing the DIC method available through the software ARAMIS [22]. For the DIC analysis, the images with dimensions of  $3232 \times 2432 \text{ pixels}^2$  are captured with digital photo camera *Nikon D200*. Performing baseline tests [23], the equipment and environmental conditions, e.g. light vibrations, are not found to affect the DIC measurements. Strains are acquired setting the facet size to 30 pixels and facet step to 15 pixels [24].

During the shear test, the test samples are subjected to a constant displacement rate of 2 mm/min, which gives  $\dot{\varepsilon}$  within the range of 0.05-0.5%/s. The strain rate is found to vary with an amount of deformation, i.e. for  $\gamma < 1\%$  the strain rate is approximately 0.053%/s and increases to 0.49%/s for  $\gamma = [7\%; 9\%]$ . The ultimate shear stress,  $\tau_u$ , is measured of 43 MPa with the corresponding shear strains,  $\gamma_u$ , in the range of 8.5-10%, and the shear modulus,  $G$ , is attained in the range of 0.95-0.97 GPa for  $\gamma = [0.005; 0.0075]$  (see also Table 1). The corresponding stress-strain relations in shear are presented in Fig. 2b.

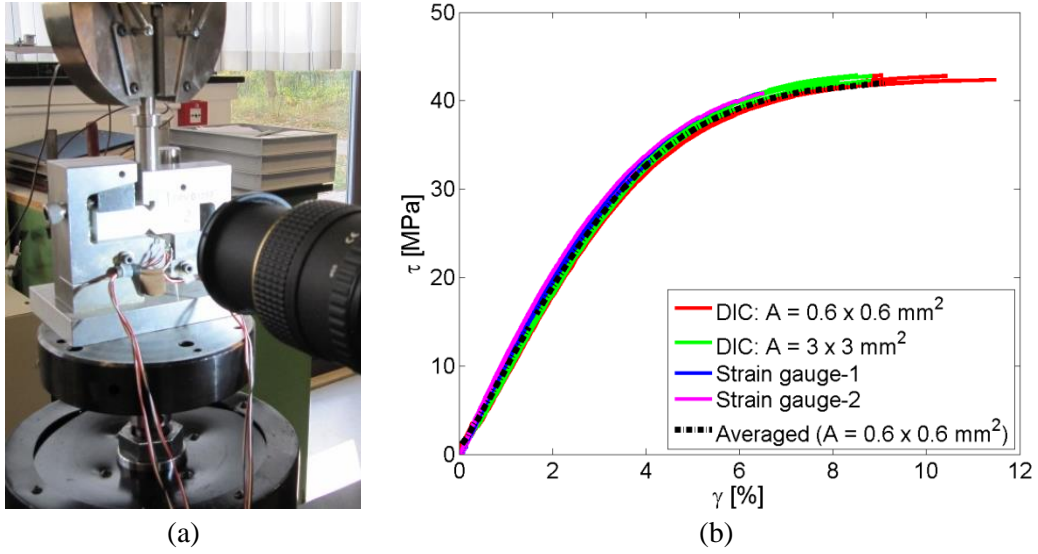
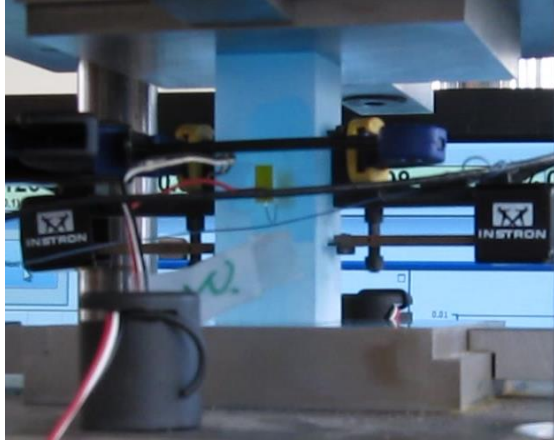


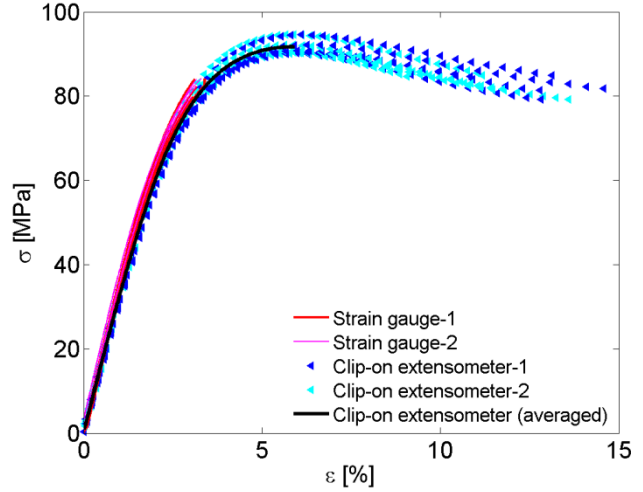
**Fig. 2** The shear test set-up (a), and the stress-strain relations in shear up to  $\tau_u$  (b)

#### 2.4 The compression test

Seven prismatic test samples are manufactured with a cross-section of  $25 \times 25 \text{ mm}^2$  and height of 60 mm [18]. During the test, the test samples are compressed between two steel plates (Fig. 3a) with a constant displacement rate of 0.6 mm/min. Results show that, similarly to the shear test,  $\dot{\epsilon}$  varies with sample deformation, i.e. for  $\epsilon < 2.5\%$  the strain rate is around 0.07%/s, and it reaches 0.12 %/s for  $\epsilon = [8\%; 12\%]$ . In the elastic region,  $\dot{\epsilon}$  is comparable between tension, shear, and compression. In the compression test, strains are measured on all four faces of the prismatic samples employing the strain gauge devices and clip-on extensometers (a gauge length is 25 mm) as shown in Fig. 3a. The acquired stress-strain relations from all four faces are shown in Fig. 3b, including the average curve attained from the clip-on extensometer measurements. In compression, the material reached the nominal strength,  $\sigma_u$ , of  $92 \pm 2 \text{ MPa}$ ,  $\epsilon_u = 6.0 \pm 0.1\%$ , and  $E = 3.43 \pm 0.8 \text{ GPa}$  for  $\epsilon = [0.05\%; 0.25\%]$ . After reaching  $\sigma_u$ , the test samples continued to deform up to very high strain values exceeding 30% along with an extensive face deformation in the form of barrelling. The tests were stopped manually, when  $\epsilon$  reached 30%. None of the samples therefore were tested up to failure.



(a)



(b)

**Fig. 3** The compression test set-up (a), and the stress-strain relations attained from the strain measurements on all four faces (b) (nominal values are shown)

### 3 Validity of experimental measurements

#### 3.1 The shear test

##### Twisting

The primary difficulty to perform an accurate shear test is force eccentricity, i.e. twisting [19]. The main causes of twisting for isotropic materials can be listed as a low tolerance to twist of the testing samples (e.g. too thin sample), an out-of-tolerance fixture, and improperly installed test sample in the fixture. The standard [19] recommends that twist is evaluated, and that the measurements from one surface of the test samples are applicable, if twist is not exceeding 3%. Experimentally, twist is evaluated applying the strain gauge couples ( $\pm 45^\circ$ ; *HBM 1-XY21-1.5/350*) on the front and back surface for three different test samples. The stress-strain curves attained from the strain gauges applied on the opposite faces are shown in Fig. 2b. Afterwards,  $G$  is extracted from the front and back surface,  $G_a$  and  $G_b$ , and substituted into  $|(G_a - G_b)/(G_a + G_b)| \times 100$  [19]. Experimentally, minor twist of 1.5-4% is measured. Consequently, in a further analysis, the shear strain is measured only on one surface of the test sample.

##### Non-uniform shear strain distribution

Performing measurements with the DIC method, the final stress-strain curve in shear is observed to depend on the measurement area,  $A$ , over which the strain is averaged. In Fig. 2b two stress-strain curves are compared with  $A = 0.6 \times 0.6 \text{ mm}^2$  and  $A = 3.0 \times 3.0 \text{ mm}^2$ . The latter agrees with the measurement area covered by the strain gauge devices commonly used in the shear tests utilizing the Iosipescu fixture. From Fig. 2b it can be seen that, using smaller  $A$ , higher average strain and lower  $G$  can be obtained, see also Table 1. These observations are attributed to a non-uniform strain distribution on the test sample surface as shown in Fig. 4. In Fig. 4a the shear strains extracted from several line paths, similar to those shown in Fig. 4b, are presented. Results indicate that the strains are rather uniform for the line paths along the  $y$ -axis connecting the tips of the notches (red curve in Fig. 4). Two strain maximums, however, can be distinguished close to the notch tips and

the minimum in the centre. More pronounced non-uniformity can be seen in the transverse direction, along the  $x$ -axis (blue curve in Fig. 4).

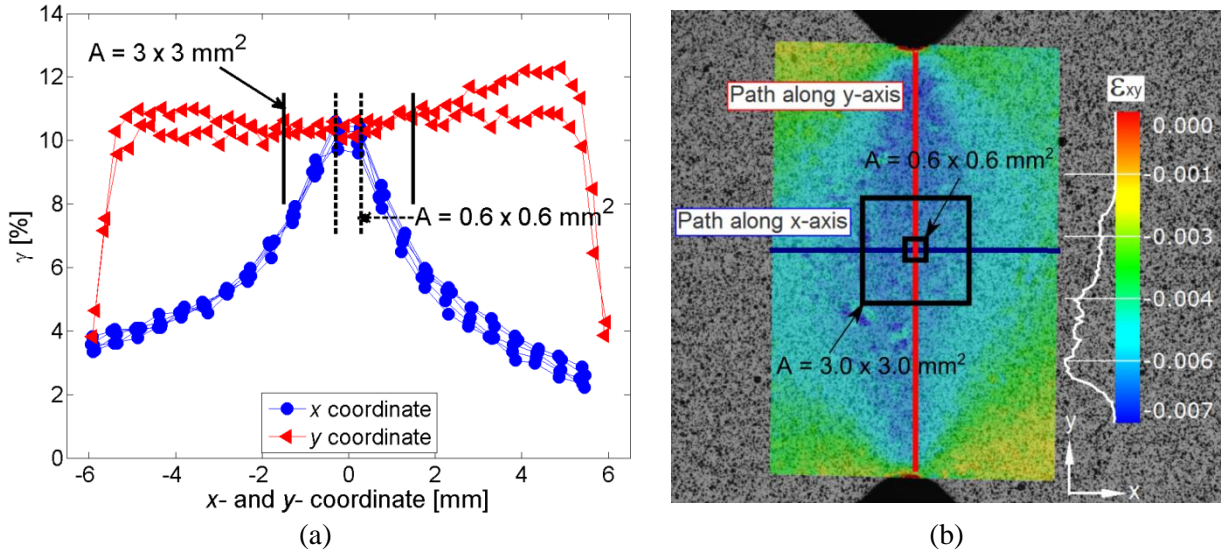


**Fig. 4** The shear strain variations along the  $x$ - and  $y$ - axis (a) with corresponding contour plots shown in (b)

The non-uniformities along the  $x$ -axis are observed to depend on the applied load, i.e. increasing the load the maximum strains along the  $x$ -axis are confined to a narrower region as shown in Fig. 5b. For instance, let's consider that  $A = 3.0 \times 3.0 \text{ mm}^2$ . From Fig. 5 it can be seen that if  $\gamma < \gamma_u$  then the difference between the maximum and minimum strain is below 1% (*Point-1*), and the strain distribution can be considered as rather uniform. At *Point-2*, where  $\gamma \approx \gamma_u$ , the difference is about 3%, and even larger variations of 7% are observed at *Point-3*, where  $\gamma > \gamma_u$ . Consequently, more profoundly the choice of the measurement area is affecting the stress-strain relations beyond  $\tau_u$ . Fig. 5a shows that reducing the measurement area from  $A = 3 \times 3 \text{ mm}^2$  to  $A = 0.6 \times 0.6 \text{ mm}^2$ , the averaged shear strain at complete failure will increase from 30% to 70%. Even though these are very high strains, the DIC software seems to be able to follow the test sample deformation as decorrelation was not observed. Additionally, the strain rate is found to be independent of the measurement area.

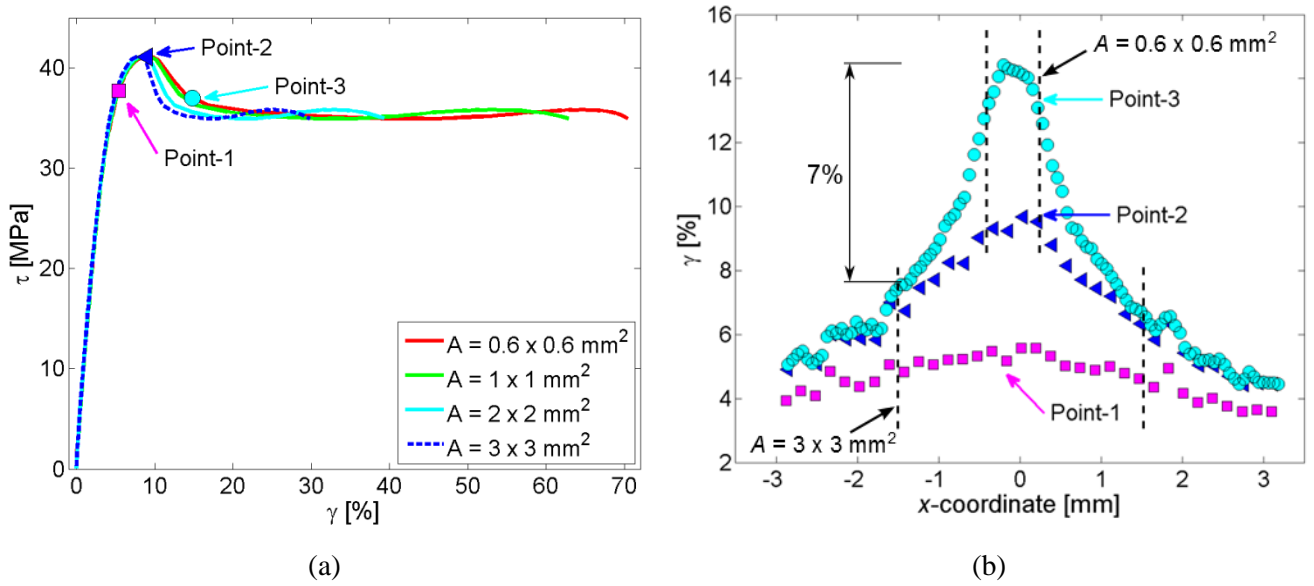


**Fig. 5** The stress-strain curves in shear up to complete failure varying with the measurement area over which the strain is averaged (a), and the shear strain distribution along the  $x$ -axis at various loading steps (b), see also Fig. 4

### 3.2 The compression test

#### Load eccentricity

Load eccentricity during the compression test is evaluated applying the strain measurement devices on all four faces as shown in Fig. 3a. The strain is measured both with the strain gauges *HBM LY11-3/350* with a gauge length, over which the strain is measured, of 3 mm and clip-on extensometers with a gauge length of 25 mm. Results are indicating that the load has been applied evenly as  $E$  acquired from the measurement devices on the opposite faces shows small differences, i.e. 8% and 12% for the strain gauges and clip-on extensometers within the strain range of 0.25%-0.65%, respectively. From Fig. 3b it can be seen that the deviations between the strains measured on the opposite faces increase with a larger deformation, and, in the region around the strength limit,  $\sigma_u$ , the results are expected to be affected by the barrelling of the test samples.

#### Friction

After approaching  $\sigma_u$ , the test samples were undergoing non-uniform deformation in the form of barrelling caused by friction [18,25]. The friction between the test sample surface and compression plate restricts deformation of the test sample faces. As a result, the test samples are non-uniformly deformed through a volume. In order to evaluate the effect of the friction on the stress-strain relation in compression, numerical tools are employed. In the FEM model, 1/8th part of the actual test sample with a symmetry along the  $x$ -,  $y$ -, and  $z$ - axis is considered. Compressive loading is generated applying the displacements on the face. Two FEM models can be distinguished depending on the applied boundary conditions on the loading face. In the first model, the loading face is pinned allowing only a movement in the loading direction (model with constrained loading face). In the second model, the loading face has all degrees of freedom (model with unconstrained loading face). Numerically, the strains are extracted from the loading face displacements. Small differences far in the plastic strain region were observed, when the strains were attained from the side faces in the way to



mimic the clip-on extensometers. In the numerical model, the averaged experimental stress-strain relation in compression is used to define material properties.

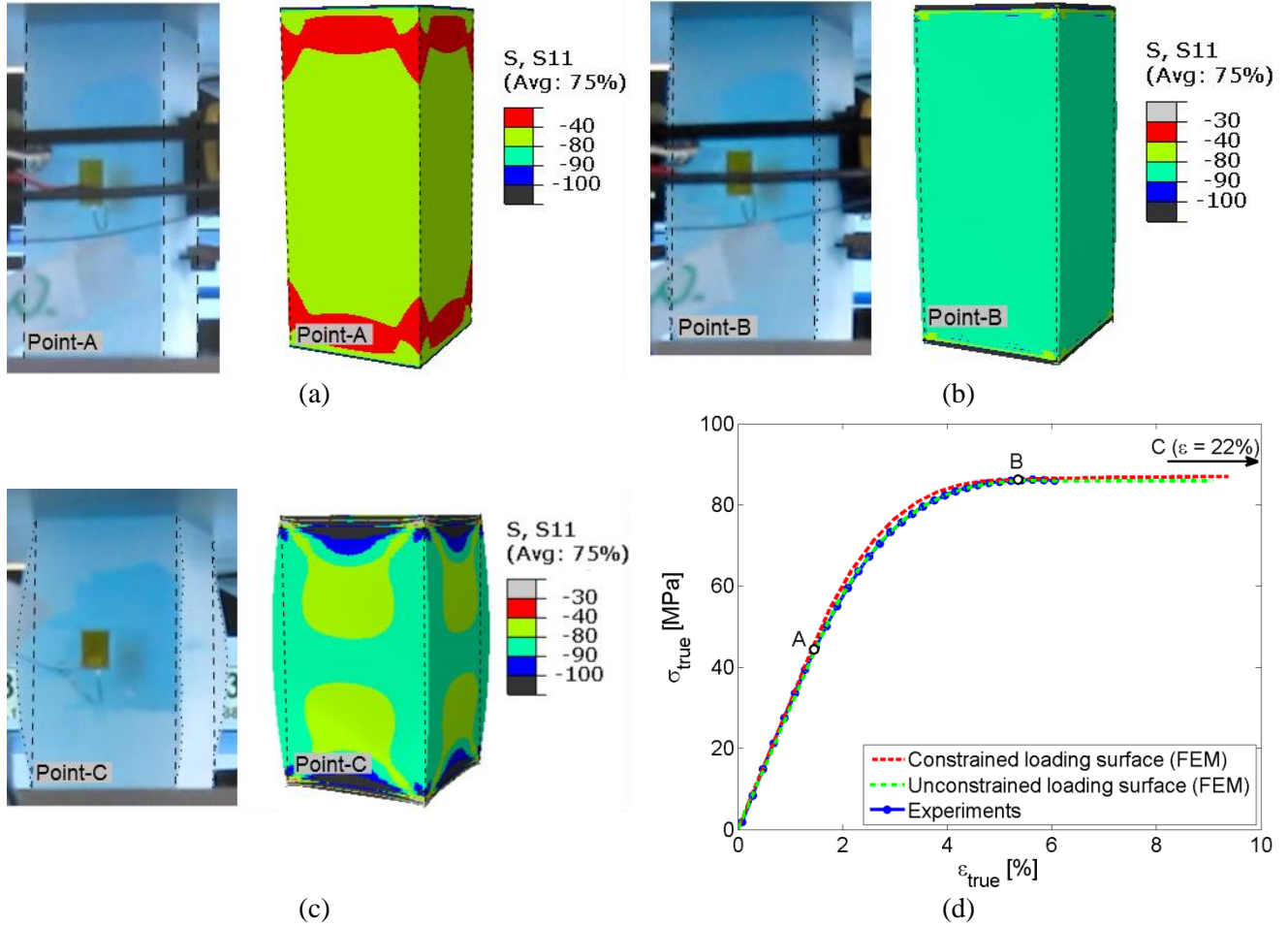


**Fig. 6** The test sample deformation in compression compared between the experiments and numerical results in elastic region (a), at  $\sigma_u$  (b), and at  $\varepsilon = 22\%$ ; the corresponding stress-strain curves are shown in (d)

Fig. 6 shows the test sample deformation in compression observed both experimentally and numerically. Three characteristic deformation regions are distinguished and denoted as point **A**, **B**, and **C**, see Fig. 6d. The point **A** (Fig. 6a) corresponds to the elastic region, point **B** (Fig. 6b) shows the material deformation at  $\sigma_u$ , and **C** (Fig. 6c) is related to the extensive deformation region at  $\varepsilon = 22\%$ . Visual observations of the deformed test sample shape indicate that at the point **A** the side edge deflection is not present (Fig. 6a); at the point **B** (Fig. 6b) the side edge inclination is very small; whereas at the point **C** (Fig. 6a) an extensive barrelling is visible. From Fig. 6a-c it can be seen that the FEM model with constrained loading surface shows good agreement with the experiments. In the FEM model without constrained loading face, uniform material deformation at different loading steps is predicted.

Even though, the shape of the deformed test samples highly differs in compression with the constrained and unconstrained loading face, actual variations in the stress-strain relation are minor as shown in Fig. 6d. Small variations can be observed throughout the yielding region up to  $\sigma_u$ , where the constraint raises the yield stresses. Nonetheless, the differences are smaller than the discrepancy of the experimental results. Similar

observations have been reported by other authors comparing experimentally the stress-strain behaviour between the test samples with and without additional PTFE tape at the contact surface [25].

### 3.3 The strain measurement variations with an applied device (application of strain gauge devices)

Numerically, Zike and Mikkelsen [21] have shown that the measurements of the strain gauge device are affected by the stiffness mismatch between the strain gauge and more compliant test sample, although the metallic part of the strain gauge device is only 5  $\mu\text{m}$  thick. Partly, this is explained by the reinforcement effect. Below the attached strain gauge, the deformation of more compliant test sample is constrained, which results in smaller measured strains. The reinforcement effect decreases using thicker samples, however, it cannot be completely eliminated as the strain in the gauge, over which the strain is averaged, is also reduced by strain distortions around the edges separating materials with mismatching stiffness. The latter becomes even more profound employing the strain gauge devices with a shorter gauge section. Similarly in this study, experimental results show that the strains acquired from the strain gauge devices are somewhat smaller than those gained from the clip-on extensometers and DIC. For instance, from Fig. 2b and Fig. 3b it can be seen that steeper stress-strain curves are attained using the strain gauge devices. In shear, results show that  $G = 1.04 \pm 0.04$  GPa and  $G = 0.97 \pm 0.03$  GPa in the strain range  $\gamma = [0.5\%; 0.75\%]$  using the strain gauges and DIC, respectively. Thus,  $G$  is about 7% greater, when the strain gauges are applied. Similarly in compression  $E$  is increased by approximately 10% using the strain gauge devices. It is acquired that  $E = 3.79 \pm 0.09$  GPa and  $E = 3.43 \pm 0.08$  GPa in the strain range  $\varepsilon = [0.05\%; 0.25\%]$  applying the strain gauges and clip-on extensometers, respectively.

## 4 Material models

Experimentally, the strength in compression of the epoxy resin was measured higher than in tension. This is explained with a pressure sensitivity of the polymer. Consequently, plasticity laws based on the pressure independent von Mises and pressure dependent Drucker-Prager yield criteria are examined applying the finite element code ABAQUS. A 3D model, as shown in Fig. 7, is used to simulate tension, compression, and shear. For tension, the loading displacement is applied on the face with the nodes 1,2,3,4 (face-1) along the  $x$ -axis. To avoid the movements in a space and to allow contraction, the opposite face (nodes: 5,6,7,8) is constrained along the  $x$ -axis, i.e.  $x = 0$ , the side face (nodes: 1,4,5,8) and the bottom face (nodes:1,2,7,8) is constrained along the  $z$ -axis and  $y$ -axis, respectively. In compression, the numerical model has the same boundary conditions except that the loading displacement has a reverse direction. For shear, the front face (nodes: 1,2,3,4) is subjected to the displacement along the  $y$ -axis and is constrained along the  $x$ -axis, i.e.  $x = 0$  and  $y \neq 0$ . The opposite face (nodes: 5,6,7,8) is constrained along the  $x$ - and  $y$ - axis, and the node 8 is constrained along the  $z$ -axis in order to avoid the model movements in a space.

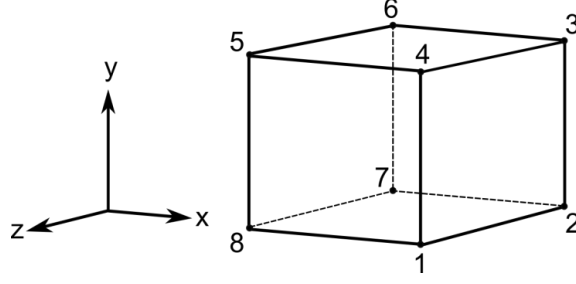


**Fig. 7 Nodes of the 3D one element model**

Numerical models are homogenous solids with an 8-node linear brick element. Material is defined as elastic-plastic deforming perfectly plastic after the maximum stress. Up to  $\sigma_u$  material is characterized according to the experimental results in tension under the strain rate 0.083%/s. Poisson's ratio is set to 0.4 and  $E = 2.85$  GPa gained from the strain range  $\varepsilon = [0; 0.0112]$ . The numerically attained stress-strain relations under different loading are compared to the averaged experimental stress-strain curves, which are averaged after strain in compression and tension and after stress in shear.

#### 4.1 $J_2$ flow theory

In the  $J_2$ -flow theory the shapes of the initial and subsequent yield surfaces agree with the Mises yield surfaces [26]. According to the pressure independent von Mises criterion, yield will occur as the elastic shear strain-energy density reaches a critical value [27]. And, the yield surface can be described with the expression

$$F = \sigma_e - \sigma_o, \quad (1)$$

where  $F$  is the plastic flow potential,  $\sigma_o$  is the yield stress in tension and the effective stress,  $\sigma_e$ , as a function of the second deviatoric stress invariant,  $J_2$ , is given as [27]

$$\sigma_e = \sqrt{3J_2}. \quad (2)$$

From Eq. 2 follows that  $\sigma_e = \sigma_t = \sigma_c = \tau\sqrt{3}$ , where  $\sigma_t$ ,  $\sigma_c$ , and  $\tau$  is the stress in uniaxial tension, uniaxial compression, and shear, respectively. The corresponding effective strain is given as [27]

$$\varepsilon_e = \sqrt{4/3 J'_2}, \quad (3)$$

where  $J'_2$  is the second deviatoric strain invariant. According to Eq. 3, for the constant volume  $\varepsilon_e = \varepsilon_t = \varepsilon_c = \gamma/\sqrt{3}$ , where  $\varepsilon_t$ ,  $\varepsilon_c$ , and  $\gamma$  is the strain in uniaxial tension, uniaxial compression, and shear, respectively. The experimentally attained effective stress-strain relations from Eq. 2 and Eq. 3 are shown in Fig. 8. It can be seen that there is a negligible difference between the effective stress-strain relation in tension and shear. But both relations are profoundly different from the effective stress-strain relation in compression. From this analytical approach appears that Eq. 2 and Eq. 3 are improper for the epoxy resin. Ideally, the effective stress-strain relations under different loading should overlap.

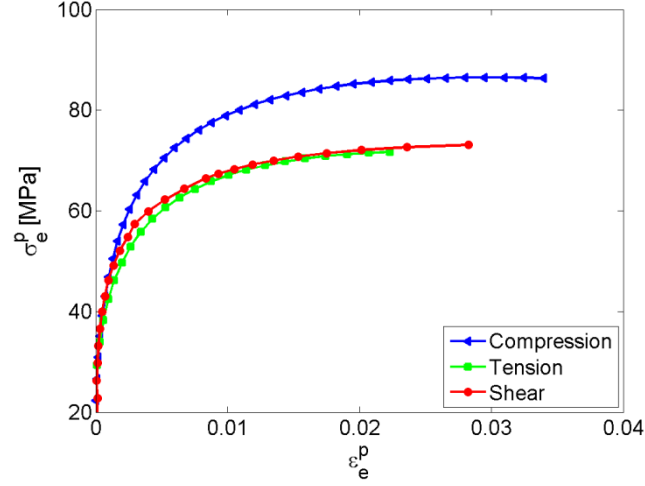


**Fig. 8 The effective plastic stress-strain curve in compression, tension, and shear (experiments)**

#### 4.2 Material model based on the Drucker-Prager yield criterion

The flow rule in the Drucker-Prager material model is similar to the one given by the von Mises yield criterion except it includes additional term characterizing the flow dependency on the hydrostatic pressure. Therefore, the flow is given as [28]

$$F = \sigma_e - \sigma_o - \mu\sigma_m, \quad (4)$$

where  $\sigma_m = 1/3\sigma_{ii}$  is a hydrostatic component of the stress and  $\mu$  is the pressure sensitivity parameter.

In this study, the extended linear Drucker-Prager criterion is used. It assumes that the yield stress will increase linearly with an applied pressure. According to the reference [29], the flow rule in the extended linear Drucker-Prager model is given as

$$F = t - p \tan \beta - d. \quad (5)$$

In Eq. 5 the parameter  $t$  is given as  $t = \frac{1}{2}q \left[ 1 + \frac{1}{K} - \left( 1 - \frac{1}{K} \right) \left( \frac{r}{q} \right)^3 \right]$ , where  $q$  is equal to  $\sigma_e$  as  $q = \sqrt{3 \cdot J_2}$ , and  $r$  depends on the third deviatoric stress invariant,  $J_3$ , i.e.  $r^3 = \frac{27}{2}J_3$  [29]. Moreover,  $K$  is the ratio between the yield stress in tri-axial compression and tri-axial tension. If the yield stress in tri-axial tension and tri-axial compression is equal, i.e.  $K = 1$ , then  $t = q = \sigma_e$ . Furthermore, in Eq. 5 the hydrostatic pressure is denoted as  $p$ , i.e.  $p = -\sigma_m$ ,  $d$  is cohesion, and  $\tan \beta$  can be related to  $\mu$  given in Eq. 4, where  $\beta$  is the friction angle.

Due to the lack of tri-axial data, the parameters given in Eq. 5 are found by matching the linear extended Drucker-Prager yield criterion with the Mohr-Coulomb criterion [29,30]. Matching is done by expressing the flow rules for both criteria in tri-axial compression, and following expressions are used to extract parameters [29]

$$K = \frac{3 - \sin \phi}{3 + \sin \phi} \text{ and} \quad (6)$$

$$\tan \beta = \frac{6 \sin \phi}{3 - \sin \phi}, \quad (7)$$

where  $\phi$  is an angle of internal friction in the Mohr-Coulomb criterion ( $\phi \neq \beta$ ). In the Mohr-Coulomb criterion the failure strength in tension is given as  $\sigma_t = 2c \cos \phi / (1 + \sin \phi)$  and in compression as  $\sigma_c = 2c \cos \phi / (1 - \sin \phi)$  [28], where  $c$  is cohesion ( $c \neq d$ ). Relating the failure strength in tension and compression, i.e.  $\lambda_{ct} = \sigma_c / \sigma_t$ , parameter  $\phi$  can be directly derived from  $\sigma_c$  and  $\sigma_t$  as follows

$$\sin \phi = \frac{\lambda_{ct} - 1}{\lambda_{ct} + 1}. \quad (8)$$

Using Eq.8, the relations given in Eq. 6 and Eq. 7 can be expressed as

$$K = \frac{\lambda_{ct} + 2}{2\lambda_{ct} + 1} \text{ and} \quad (9)$$

$$\tan \beta = \frac{3(\lambda_{ct} - 1)}{\lambda_{ct} + 2}. \quad (10)$$

For example, if the strength in compression and tension is equal, i.e.  $\lambda_{ct} = 1$ , then  $\tan \beta = 0$  (Eq. 10) and  $K = 1$  (Eq. 9). Moreover, the flow rule given in Eq. 5 becomes equal to the von Mises criterion given in Eq. 1. Experimentally,  $\lambda_{ct}$  is attained of 1.2, respectively  $\phi = 5.3^\circ$  according to Eq. 8. Using  $\phi = 5.3^\circ$  or  $\lambda_{ct} = 1.2$ , the parameter  $K = 0.94$  (Eq. 9) and  $\beta = 11^\circ$  (Eq. 10). Knowing the parameters  $K$  and  $\beta$ , the material cohesion,  $d$ , is determined of 80 MPa (Eq. 5).

Besides the input parameters  $K$  and  $\beta$ , which are derived from the expression given above, the dilatational angle,  $\psi$ , has to be provided. In the case of an associated flow rule, when the plastic flow develops along the normal to the yield surface,  $\psi = \beta$  while for a non-associated flow  $\psi \neq \beta$  [28,29]. In this study, the parameter  $\psi$  is set to zero as the volume changes in the yielding or post-yielding deformation regimes have been reported to be minor for polymer materials [30], thus the tested epoxy resin is considered as a non-dilatational.

#### 4.3 Numerical results

In Fig. 9 the numerical and experimental results are compared in tension, compression, and shear. Fig. 9a shows that employing  $J_2$ -flow theory the numerical results agree with the experiments in shear and tension; however, the stress-strain relation in compression is underestimated. Opposite to the  $J_2$ -flow theory, the plasticity model based on the Drucker-Prager criterion equally well predicts the stress-strain relations in tension, shear, and compression as it is shown in Fig. 9b. Nonetheless, some differences can be observed as the FEM model slightly underestimates the stresses in the yield initiation region under the compressive loading. Studying the validity of the compression test, it is found that the friction at the interface between the test sample and compression plate raises the yield stresses. In this FEM model, the constraint of the loading face was not included. Thus, in Fig. 9b the discrepancy between the experiments and numerical results is related to slightly higher yield stresses in the experiments due to the friction.

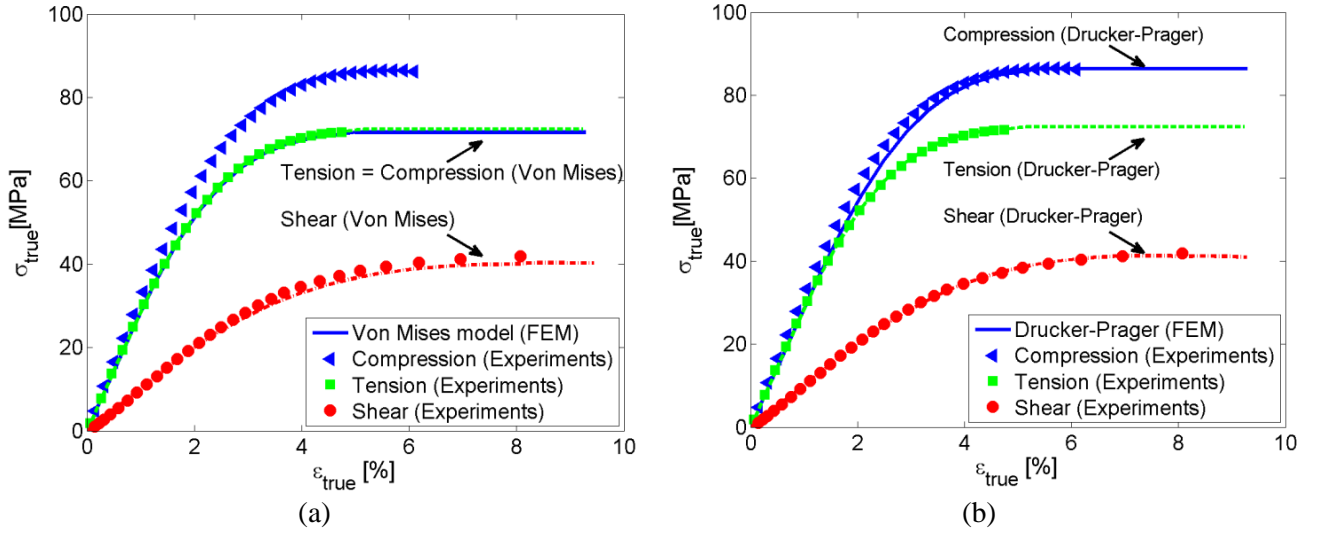


**Fig. 9** Numerically attained stress-strain relations under different loadings employing the material models based on the von Mises yield criterion (a) and the linear extended Drucker-Prager yield criterion (b)

## 5 Discussion

Employing numerical and analytical methods, it was attained that the  $J_2$ -flow theory predicts the epoxy resin response equally well in shear and tension, when initial properties are defined in tension. This is useful because the tensile test is generally the easiest and most common way of characterizing materials. The  $J_2$ -flow theory was therefore found to be appropriate for polymer/fibre composite models, when damage is governed by the matrix properties in tension and/or shear. On the other hand, the  $J_2$ -flow theory was unable to predict the compressive properties of the epoxy resin. According to the von Mises yield criterion, the material should have the same strength in compression and tension, but the experimental data show otherwise.

In experiments, the strength in compression was measured to be approximately 1.2 times greater than in tension (true values). Similar differences were also observed throughout the yielding region comparing stresses in compression and tension for the same plastic strain, i.e.  $\lambda_{ct}$  was obtained from 1.1 to 1.2 at  $\sigma_u$ . The strength variations are not necessarily due to the intrinsic properties of the material. For instance, the higher strength in compression can be due to residual stresses or due to larger susceptibility to micro-cracking in tension than in compression, also the friction at the interface between the test sample and compression plate can raise the stresses in compression. Numerically, the friction was found to have only a small impact on the yield stresses, i.e. the factor by which the stresses were increased was not sufficient to explain the variations in stress between compression and tension. However, the premature failure due to micro-cracks in tension could be significant. The cracks were observed to evolve from the edges of the samples tested in tension. At the same time, the effect of the micro-cracks could be less critical as the epoxy resin was possessing rather ductile behaviour. For example, in compression and tension  $\varepsilon_u$  reached 5% and 6%, respectively, and even larger strains were measured at complete failure. Moreover, differences were also observed between the effective stress-strain relationships in shear and compression, which ideally should agree according to the von Mises yield criterion. The higher stresses in compression could be due to the pressure sensitivity of epoxy resin, as

reported by Li et al. [65]. In view of the differences, the pressure dependent Drucker-Prager yield criterion was used as the second material model for predicting epoxy resin behaviour under different loadings. Numerical results showed that the Drucker-Prager yield criterion predicts equally well the behaviour of epoxy resin in shear, tension, and compression (with the initial properties defined in tension). Thereby, if the polymer/fibre composite failure is due to the matrix response in compression, then the Drucker-Prager yield criterion is suggested. For the Drucker-Prager model, the friction angle is obtained of  $11^\circ$ , which falls within the common range for polymer materials, i.e.  $0^\circ$ - $20^\circ$  [10,13]. In overall, the ratio between strength in compression and tension,  $\lambda_{ct} = 1.2$ , is found to be low as the typical values are reported within the range of 1.2-1.5 [30].

## 6 Conclusions

According to our study, the  $J_2$ -flow theory is sufficient in mechanical models of polymer/fibre composites if the failure is dominated by the matrix in tension and/or shear, whereas alternative material models as the Drucker-Prager yield criterion have to be implemented if the behaviour in compression is relevant.

Generalizing the experimental results, the epoxy resin appeared as rather ductile having  $\varepsilon_u$  of 5-6% with the corresponding true strength within the range of 72-86MPa in tension and compression; in shear  $\gamma_u$  was measured within the range of 8.6-10% and  $\tau_u = 43$  MPa. Varying the strain rate from 0.053%/s to 0.23%/s, a negligible impact on the epoxy resin behaviour in tension was observed. The evaluation of the compression and shear test validity showed that the stress-strain relation in compression is only slightly perturbed by the friction at the interface between the test sample and loading plate, whereas the resultant stress-strain relation in shear depends on the area over which the strain is averaged. Choosing the area between notches of  $3 \times 3$  mm<sup>2</sup>, which agrees with the area covered by the gauge section of the strain gauges, smaller values of  $G$  and  $\gamma_u$  were attained.

## Acknowledgements

This research was supported by the Danish Centre for Composite Structures and Materials for Wind Turbines (DCCSM), grant no. 09-067212, from the Danish Strategic Research Council (DSF).

## References

- [1] C.R. Schultheisz, A.M. Waas, Compressive failure of composites, Part I: Testing and micromechanical theories, *Prog. Aerosp. Sci.* 32 (1996) 1–42.
- [2] B. Budiansky, N.A. Fleck, Compressive Kinking of Fiber Composites: A Topical Review, *Appl. Mech. Rev.* 47 (1994) S246.
- [3] S. Kyriakides, R. Arseculeratne, E.J. Perry, K.M. Liechti, On the compressive failure of fiber reinforced composites, *Int. J. Solids Struct.* 32 (1995) 689–738.
- [4] L.P. Canal, J. Segurado, J. LLorca, Failure surface of epoxy-modified fiber-reinforced composites under transverse tension and out-of-plane shear, *Int. J. Solids Struct.* 46 (2009) 2265–2274.



- [5] L.E. Asp, L.A. Berglund, R. Talreja, Prediction of matrix-initiated transverse failure in polymer composites, *Compos. Sci. Technol.* 56 (1996) 1089–1097.
- [6] L.P. Canal, C. González, J.M. Molina-Aldareguía, J. Segurado, J. LLorca, Application of digital image correlation at the microscale in fiber-reinforced composites, *Compos. Part A Appl. Sci. Manuf.* 43 (2012) 1630–1638.
- [7] E. Correa, V. Mantič, F. París, A micromechanical view of inter-fibre failure of composite materials under compression transverse to the fibres, *Compos. Sci. Technol.* 68 (2008) 2010–2021.
- [8] J. Kim, Y. Mai, High strength, high fracture toughness fibre composites with interface control—a review, *Compos. Sci. Technol.* (1991).
- [9] L.E. Asp, L.A. Berglund, P. Gudmundson, Effects of a composite-like stress state on the fracture of epoxies, *Compos. Sci. Technol.* 53 (1995) 27–37.
- [10] R. Quinson, J. Perez, M. Rink, A. Pavan, Yield criteria for amorphous glassy polymers, *J. Mater. Sci.* 32 (1997) 1371–1379.
- [11] S. Rabinowitz, I.M. Ward, J.S.C. Parry, The effect of hydrostatic pressure on the shear yield behaviour of polymers, *J. Mater. Sci.* 5 (1970) 29–39.
- [12] I.M. Ward, Review: The yield behaviour of polymers, *J. Mater. Sci.* 6 (1971) 1397–1417.
- [13] P.B. Bowden, J.A. Jukes, The plastic flow of isotropic polymers, *J. Mater. Sci.* 7 (1972) 52–63.
- [14] P. Bardia, R. Narasimhan, Characterisation of pressure-sensitive yielding in polymers, *Strain.* 42 (2006) 187–196.
- [15] D. Li, A.F. Yee, I.-W. Chen, S.-C. Chang, K. Takahashi, Fracture behaviour of unmodified and rubber-modified epoxies under hydrostatic pressure, *J. Mater. Sci.* 29 (1994) 2205–2215.
- [16] B. Fiedler, M. Hojo, S. Ochiai, K. Schulte, M. Ando, Failure behavior of an epoxy matrix under different kinds of static loading, *Compos. Sci. Technol.* 61 (2001) 1615–1624.
- [17] D.C. Drucker, Plasticity theory strength-differential(SD) phenomenon, and volume expansion in metals and plastics, *Metall. Trans.* 4 (1973) 667–673.
- [18] ASTM D695, Standard Test Method of Compressive Properties of Rigid Plastics, West Conshohocken, 2002.
- [19] ASTM D5379 / D5379M, Standard Test Method for Shear Properties of Composite Materials by the V-Notched Beam Method, West Conshohocken, PA, 2012.
- [20] ISO 527-1, Plastics-determination of tensile properties-Part 1, 2012.
- [21] S. Zike, L.P. Mikkelsen, Correction of Gauge Factor for Strain Gauges Used in Polymer Composite Testing, *Exp. Mech.* 54 (2014) 393–403.
- [22] GOM, ARAMIS software, (n.d.). <http://www.gom.com/3d-software/aramis-software.html>.
- [23] B. Pan, K. Qian, H. Xie, A. Asundi, Two-dimensional digital image correlation for in-plane displacement and strain measurement: a review, *Meas. Sci. Technol.* 20 (2009) 062001.
- [24] G.O.M. Techniques, ARAMIS user manual, ARAMIS 4M v5. 4.1, Gesellschaft Für Opt. Messtechnik. (2005).

- [25] M. Jerabek, Z. Major, R.W. Lang, Uniaxial compression testing of polymeric materials, *Polym. Test.* 29 (2010) 302–309.
- [26] V. Tvergaard, Plasticity and creep in structural materials, Technical University of Denmark, 2001.
- [27] W.-F. Chen, D.-J. Han, Yield Criteria Independent of Hydrostatic Pressure, in: *Plast. Struct. Eng.*, 2007: pp. 72–83.
- [28] W.-F. Chen, D.-J. Han, Failure Criterion for Pressure-Dependent Materials, in: *Plast. Struct. Eng.*, 2007: pp. 84–98.
- [29] Systemes Dassault, Abaqus Analysis User's Guide, ABAQUS Inc., Dassault Syst. Fr. (2013).
- [30] M.Y.M. Chiang, H. Chai, Plastic deformation analysis of cracked adhesive bonds loaded in shear, *Int. J. Solids Struct.* 31 (1994) 2477–2490.
- [31] D. Li, A.F. Yee, I. W. Chen, S.C. Chang, K. Takashi, Fracture behaviour of unmodified and rubber-modified epoxies under hydrostatic pressure, *J. Mater. Sci.* 29 (1994) 2205–2215.

Publication [P2]

# Correction of Gauge Factor for Strain Gauges Used in Polymer Composite Testing

# Correction of Gauge Factor for Strain Gauges Used in Polymer Composite Testing

S. Zike · L.P. Mikkelsen

Received: 10 December 2012 / Accepted: 23 September 2013 / Published online: 9 October 2013  
© Society for Experimental Mechanics 2013

**Abstract** Strain gauges are used together with the corresponding gauge factor to relate the relative electrical resistance change of the strain gauge with the strain of the underlying material. The gauge factor is found from a calibration on a stiff material - steel. Nevertheless, the gauge factor depends on the stiffness of the calibration material and ideally the calibration should be done on a similar material as tested. In practice, the gauge factor found by the strain gauge manufacturer is often used. The paper documents that even for moderately stiff materials such as glass-fibre composites a significant error is found on the strain measurements obtained by the strain gauges. This is documented both experimentally and numerically. A stiffness, also test sample and strain gauge geometry dependent correction coefficient of the gauge factor is proposed. A correction coefficient covers material stiffnesses ranging from 1 GPa to 200 GPa.

**Keywords** Strain gauge · Strain measurements · Polymer material testing · Composites · Material characterization

## Notations

$A$	parameter used for correction coefficient determination for the global reinforcement effect;
$B$	width;
$C$	correction coefficient;
$C_0$	permanent correction coefficient (depends on the strain gauge length);
$E$	Young's modulus;
$E^*_{sg}$	reduced Young's modulus of the strain gauge, which depends on the strain gauge stiffness and geometrical dimensions [10];
$GF_{act}$	actual gauge factor;
$GF_{cal}$	gauge factor provided by manufacturer (determined on a stiff calibration specimen);
$L$	length;
$t$	thickness;
$t_{cr}$	critical thickness showing transition from a global to only a local reinforcement effect;
$\Delta R/R_0$	relative change of resistivity;
$\epsilon$	strain;
$\epsilon_{ave}$	average strain experienced by specimen.

## Subscripts

$ext + SG$	values determined with clip on extensometer, when specimen is simultaneously bonded to strain gauge;
$gauge$	gauge, i.e., measuring grid, properties;
$loop$	end-loops of strain gauge (Fig. 1);
$PI$	polyimide (carrier film) properties;
$ref$	reference values obtained by an extensometer for specimens with or without attached strain gauge;

S. Zike (✉) · L.P. Mikkelsen  
Composites and Materials Mechanics Section, Department  
of Wind Energy, Technical University of Denmark,  
Risø Campus, 4000 Roskilde, Denmark  
e-mail: zike@dtu.dk

L.P. Mikkelsen  
e-mail: lapm@dtu.dk



<i>sg</i>	used to indicate strain gauge measurements and properties of homogenized strain gauge;
<i>spec</i>	properties of unreinforced test specimen (also relates to input values in simulation model).

## Introduction

Strain gauges are commonly used strain measurement devices constructed from thin metallic grid, which is enclosed between polymer films (see Fig. 1). The working principle of the strain gauge incorporates the change of electrical resistance in the metal part linearly with its deformation [1]. Correlation between these two variables is expressed as the gauge factor [2], its determination is in more detail discussed later in subsection “[Correction coefficient determination](#)”. During experimental testing the change of electrical resistance in the strain gauge is measured and converted into the strain values using the gauge factor.

This study is initiated by experimental observations, during which different elastic modulus values were obtained for identical polymer matrix based composite. The difference observed comparing the strain measurement from the strain gauge with the clip on extensometer. Deviations suspected to be caused by the stiffness mismatch between the

strain gauge, which includes a thin metal grid, and the test sample, which is more compliant. Therefore the strain gauge induces strain reduction in the more compliant test sample [3] and promote strain distortions around the edges, where strains are transmitted from the test sample to the gauge [4, 5]. These phenomena are attributed to the effect known as the “reinforcement effect” [6]. As a result of the reinforcement effect, strain gauges measure lower strains compared with the strains experienced locally by the test sample in the absence of the strain gauge. This can lead to significant errors in determination of strain and elastic modulus. In spite of this, the standards often recommend the use of a strain gauge as an optional strain measurement device during mechanical testing of polymer and polymer matrix composite materials [7–9]. In addition to this, strain gauges are used to a great extent as strain identification sensors in composite structures.

One of the earliest studies regarding the strain gauge reinforcement effect are given by Stehlin [4]. Stehlin has modelled stress and strain distortions in the test sample, strain gauge and adhesive. This has been further applied by Beatty’s and Chewning’s [5] to conduct numerical analysis of strain gauge geometrical parameters such as thickness and length. These authors have provided an approximate expression to predict the local reinforcement effect, when strains are modified locally around an attached strain gauge and are found to be independent of specimen geometry. The expression indicates that reinforcement increases with stiffer and thicker strain gauges, whereas it decreases with longer strain gauges and stiffer specimens [5]. On the basis of these studies, a more detailed discussion regarding correction of strain gauge measurements has been presented by Ajovalasit et al. [10–12]. First of all, the correction of the gauge factor obtained by conventional strain gauge calibration methods can be done [10] by correction coefficients derived from mathematical expressions. For that Ajovalasit et al. have provided improved mathematical expression based on deductions of Beatty and Cheawning [5]. Another approach involves strain gauge calibration on materials more compliant than the test samples [11]. The above mentioned studies were focussed on the local reinforcement effect estimation. Thus in the analytical and numerical models the specimen has been considered as a thick and semi-infinite plate having the same width as the strain gauge. The two dimensional problem has been considered for three dimensional calculations, in which the strain gauge and specimen have been defined as linear-elastic materials.

A similar approach has been used for the global reinforcement effect by Swan [13] and Little et al. [14]. Now the strain fields are not only localized by attachment of the stiff strain gauge material but also depends on the geometry of the test samples. Swan [13] deduced an approximate expression to predict the global reinforcement effect, which

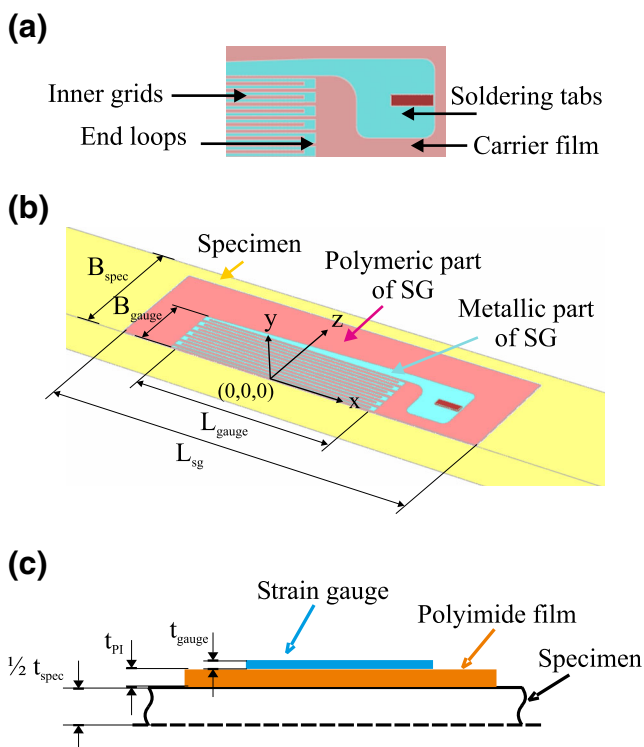


**Fig. 1** Representation of strain gauge grid pattern (a), the 3D (b) and the 2D (c) simulation model

has been found to be proportional to the stiffness ratio of the strain gauge and the test sample as well as the thickness ratio. Moreover, Little et al. [14] observed that the reinforcement effect is affected not only by the specimen geometry, but also by the loading mode e.g. bending or tension.

Similar to strain gauges, fibre Bragg grating sensors have shown a reinforcement effect [15, 16]. Li et al. [16] has obtained a higher amount of reinforcement for fibre Bragg grating sensors, even though the elastic modulus of glass is much lower than that of the metal incorporated in strain gauge manufacturing. This was found to be due to the larger dimensions of glass fibres used for Bragg grating sensors.

In conclusion, the reinforcement effect was identified already in early studies of strain gauge implementation, where approximative mathematical expressions were presented in order to predict the strain gauge measurement errors coming from the local and global reinforcement effects. In the previous studies a simplified model of the strain gauge has been used homogenizing all parts of the strain gauge into one element. Therefore, the importance of the actual strain gauge pattern design has not been sufficiently discussed and error prediction has found to be limited. In addition, previous studies have been confined to elastic materials. Some research has been done to analyse gauge factor variations due to the plastic deformation of the metallic grid incorporated in the strain gauges [17–19]. Nevertheless, changes of the reinforcement effect due to plastic deformation both of the specimen and the strain gauge material has not previously been studied.

The purpose of the present study is to derive correction methods for the strain gauge experimental measurements, when a strain gauge is applied on specimens with elastic modulus in the range of 1–200 GPa and various geometrical dimensions. The finite element methods (FEM) are used to create detailed two (2D) and three (3D) dimensional models, in order to conduct a parametric study to assess the effect of specimen and strain gauge geometry with respect to the stiffness, both with the local and the global reinforcement effect. The 3D study of the strain gauge geometry is based on commercially available Y series strain gauges provided by the *Hottinger Baldwin Messtechnik GmbH* (HBM) company, but the results will not be limited to this. The study considers both elastic and plastic deformation in the strain gauge as well as in the test sample.

## Methods

### Simulation model

The commercial finite element code ABAQUS is used to create 2D and 3D numerical models of the experimental material set-up. This setup consists of a test sample with

attached back-to-back strain gauges, which is subjected to tensile loading.

### Parts

The test sample is modelled with a stiffness from 1 GPa to 200 GPa. The purpose is to cover the range of materials used for polymer matrix based composites and also to compare their response to metals. The thickness of the test sample is varied from 1 mm to 30 mm, so that both the global and the local reinforcement effect by the strain gauge is presented.

The detailed strain gauge pattern is included in the 3D model obtained from the micrographs (Fig. 1 (a), (b)) captured with a photo camera *Canon G9*. The width of the inner grids is set to 0.08 mm and the space between grids is 0.1 mm, which corresponds to the strain gauge type *LY11-10/350*. In the 2D plane stress simulation model, the strain gauge part is simplified as a uniform foil with half the thickness of gauge. This is due to merging the inner grids and the empty space between grids. Even though the 2D model is simplified, however similar to the 3D model, the distinction of the end loops, gauge and soldering tab area (Fig. 1 (a), (c)) is retained. For all strain gauge models the length of the end-loops is set to 3 % of the corresponding gauge length; a value, which corresponds quite well with the commercially available *HBM* strain gauges. The distinction of different strain gauge parts, what is done in this analysis, is contrary to previous studies [4, 5, 10–12], where a homogenised strain gauge model was preferred by merging all parts of the strain gauge including carrier film.

In order to exclude the effect of strain transition through carrier film and adhesive, a numerical calibration is conducted. The manufacturers provided gauge factor already includes these distortions, because it is obtained, while the commercial prototype of the strain gauge is glued on a steel surface [11]. Therefore numerical calibration involves determination of strain distortions applying different type of strain gauges, shown in Fig. 1, on a 200 GPa stiff and significantly thick material. The observed strain discrepancy of approximately 1 % is thus extracted from all the numerical results.

### Material formulation

The metallic wire and the polymeric carrier film in the HBM Y series strain gauge is made of constantan and polyimide, respectively. The corresponding material properties are taken from Stockmann studies [20]. The polyimide carrier film is modelled as a linear-elastic material with  $E = 3.1$  GPa and  $\nu = 0.41$ . The constantan is modelled as an elastic-plastic material with the elastic properties as  $E = 180$  GPa

and  $\nu = 0.3$ , and the plastic deformation is described with Ludwik's equation:

$$\sigma = \sigma_y \left[ 1 + a(\phi)^n \right], \quad (1)$$

where the yield stress  $\sigma_y = 400$  MPa, hardening parameters  $a = 4$  and  $n = 0.45$  and  $\phi$  is the plastic deformation.

### Constraints and elements

All material interfaces are modelled as perfectly bonded materials, thus are given as a tie constraint with no requirements of matching FE-meshes in the numerical procedure. A half model using 4 node isoparametric quadrilateral plane stress elements in the 2D representation, and a quarter of the model using 8 node isoparametric brick elements in the 3D representation of the test set-up is modelled using symmetric boundary conditions. The prescribed displacement boundary condition is used to mimic the tensile deformation.

### Experimental testing

Validation of the simulation is done by performing tensile tests of a neat polymer and polymer matrix based glass fibre reinforced composites using a range of stiffness as  $E \in [1; 37]$  GPa and thickness as  $t_{spec} \in [1.5, 20]$  mm). The corresponding experiments are performed on a universal testing machine *Instron 88R1362* with a 5 kN (SN: UK 802) or a 100 kN (SN: UK 1028) load cell. Specimens with and without strain gauges *LY11-10/350* are tested using reference measurement methods with a laser extensometer ('Fiedler Optoelektronik GmbH', *PS-E50-0160-AH*) and a clip on extensometer (*Instron 2620-601*,  $\pm 5/50$  mm). Therefore two reference strain values of the test sample are presented. The first set of strain values is gained from the clip on extensometers mounting them on the samples with attached back-to-back strain gauges. The second set of strain values is measured by the laser extensometer, which is applied on the unreinforced test sample (the strain gauges are not attached to the test sample).

### Correction coefficient determination

A correction coefficient,  $C$ , see equation (5), is defined in order to evaluate the error of strain gauge measurements and to provide gauge factor adjustment values [10]. The gauge factor,  $GF$ , of the strain gauge is defined as the ratio between the electrical resistance change and the deformation in the gauge:

$$GF = \frac{\Delta R/R_0}{\epsilon_{gauge}}, \quad (2)$$

where  $\Delta R/R_0$  is the relative change of resistivity and  $\epsilon_{gauge}$  is the strain in the gauge. Manufacturers provided strain gauges are calibrated on sufficiently large and stiff materials such as steel [11]. If the strain gauges are applied on compliant materials, new calibrations are needed, because the strain fields are changed due to the stiffness difference between the strain gauge and the specimen material. Additional calibration can be avoided by correcting manufacturers' provided gauge factors as follows:

$$GF_{act} = \frac{GF_{cal}}{C}, \quad (3)$$

where  $GF_{act}$  is the actual gauge factor and  $GF_{cal}$  is the calibrated gauge factor provided by the strain gauge manufacturers. From equations (2) and (3) the strain gauge measurement error can be deduced as follows:

$$C = \frac{GF_{cal}}{GF_{act}} = \frac{\Delta R/R_0}{\epsilon_{sg}} \frac{\epsilon_{ave}}{\Delta R/R_0} = \frac{\epsilon_{ave}}{\epsilon_{sg}}, \quad (4)$$

where  $\epsilon_{ave}$  and  $\epsilon_{sg}$  are the strains experienced by the specimen and the strain gauge, respectively. The correction coefficient can also be expressed as the ratio of elastic modulus determined by the strain gauge ( $E_{sg}$ ) and actual elastic modulus of material ( $E_{spec}$ ):

$$C = \frac{\epsilon_{ave}}{\epsilon_{sg}} = \frac{\epsilon_{ave}\sigma}{\epsilon_{sg}\sigma} = \frac{E_{sg}}{E_{spec}}. \quad (5)$$

## Results

The finite element model is first used to investigate the strain gauge caused strain disturbances in the test samples. This is followed by a parametric study to obtain the most significant strain gauge and test sample properties, which affect the correction coefficient of the gauge factor. The parametric study includes an analysis of the material stiffness, the strain gauge and the test sample geometrical properties, and the elastic-plastic material behaviour. Numerical results are compared to experimentally determined correction coefficients.

### Strain gauge introduced strain disturbances

The accuracy of the strain gauge measurements depends on the amount of the reinforcement effect, which is caused by the stiffness discrepancy between the specimen and the strain gauge material. As shown in Fig. 2 as well as discussed by Little et al. [14] the reinforcement effect includes the strain reduction in the specimen and the strain distortions around the edges. The reinforcement effect can be split up into a local and a global part. The global part describes the phenomenon, where strains are modified through the

whole thickness with the attached strain gauge. The influence of the global reinforcement increases by reducing the specimen thickness and increasing the strain gauge geometrical dimensions, for more details see subsection “Correction coefficient influenced by specimen geometry” and “Correction coefficient influenced by strain gauge geometrical properties”. By contrast, in the local part, strains are considered to change only close to the attached strain gauge and the effect of the test sample thickness can be eliminated.

In Fig. 2(a), the contour plots of the logarithmic axial strain component,  $\epsilon_{11}$ , in a 3D model from the XY, XZ and XYZ planes are presented for the local reinforcement. The total region of distorted strains is approximately double the gauge length for a 1 GPa stiff specimen attached to the strain gauge type LY11-10/350. The contour plots reveal both a strain reduction below the gauge and a non-uniform strain distribution along the strain gauge width (z axis) and length (x axis) directions.

In the length direction, the strain distortions are mainly caused by the strain transition between materials with mismatching stiffness. These strain transition points are also illustrated in Fig. 2(b), where the normalized strain distribution along the specimen surface and inside the gauge is presented. Normalized strains are obtained dividing strains

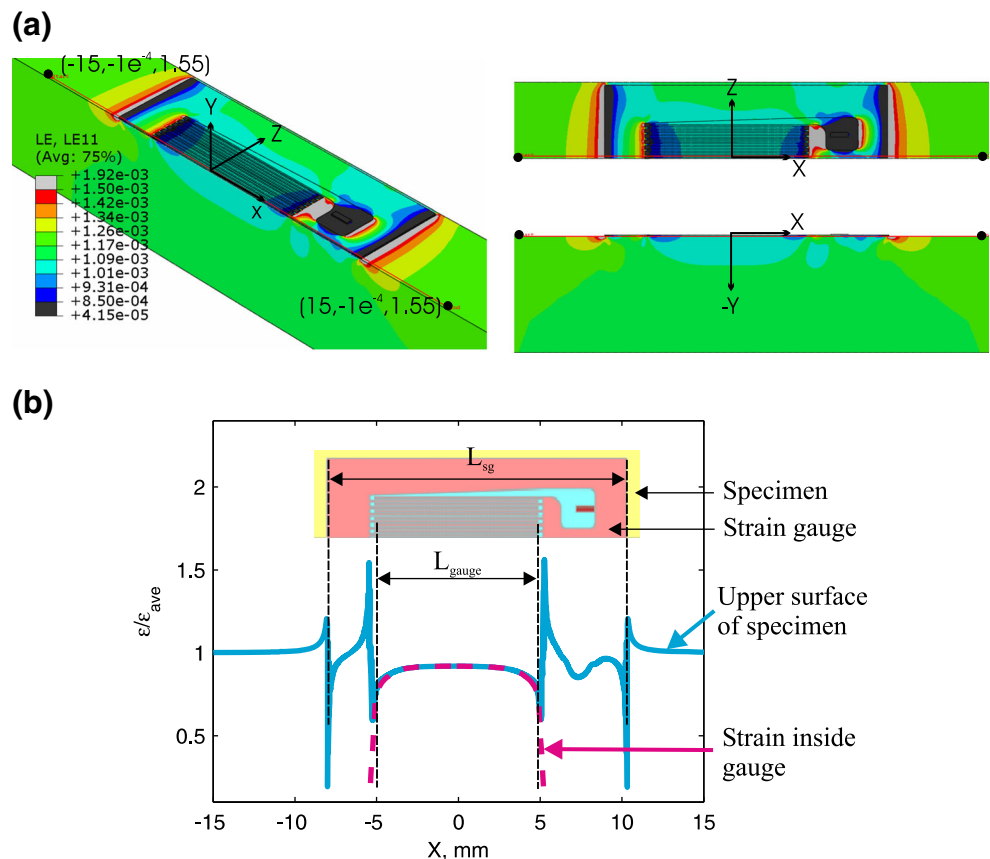
at the surface of the specimen by the average strain experienced over the whole specimen. Sharp peaks of the normalized strains are related to the edges where strains are transferred between the metal and carrier film, also the carrier film and the test sample. Peaks indicate very large and very low strain existence along the edges. Due to the strain distortions along the edges, inside the gauge the normalized strains tend to decrease close to the end-loops, which respectively affects the strain measurement accuracy of strain gauge devices.

In the width direction, in Fig. 2(a), which corresponds to the z axis, the strain field variations are smaller and depend more on the strain gauge pattern features. For example, it is observed that the strain drop in the gauge ends tends to be smaller when moving to the side edges of the test sample. Also the soldering tabs are found to lower the strain disturbances around the end-loops.

Correction coefficient influenced by the elastic modulus of specimen

Figure 3 shows the correction coefficient obtained by the 2D and the 3D simulation models for the test samples with different elastic moduli attached to the strain gauge

**Fig. 2** Strain fields in the 3D model at  $\epsilon_{ave} = 0.35\%$  (a) and normalized strain distribution along the specimen surface and inside the gauge obtained by the 3D model at  $\epsilon_{ave} = 0.012\%$ . Strain path for specimen is between points  $(-15, -10^{-3}, 1.55)$  and  $(15, -10^{-3}, 1.55)$ , and for the gauge including the end-loops between  $(-5.3, 4.8 \times 10^{-2}, 1.55)$  and  $(5.3, 4.8 \times 10^{-2}, 1.55)$  (b)





*LY11-10/350*. The 3D model predicts that the correction coefficient can be as high as 1.3 for the 1 GPa specimen, i.e., the strain gauge measurement error is 30 %. This is reduced by increasing the specimen stiffness, hence a 10 GPa stiff specimen has a correction coefficient around 1.04, i.e., a 4 % measurement error. A further increase of the test sample stiffness reduces the correction coefficient down to 1 %, therefore no error is expected for the test sample with  $E_{spec} = 200$  GPa.

Along with the numerical results, in Fig. 3, experimental data are presented for an unreinforced polymer material test sample with  $t_{spec} = 4$  mm and an attached strain gauge with  $L_{gauge} = 10$  mm. Experimentally the elastic modulus is acquired using two different reference strain measurement methods,  $E_{ref}$ . The first experimental data point, noted as *Laser*, is obtained measuring strains with a laser extensometer for the test sample without attached strain gauges. Hence the elastic moduli for unreinforced test samples is noted as  $E_{spec}$ . The second data point, noted as *Extensometer*, is gained from the test samples with attached back-to-back strain gauges simultaneously with clip on extensometers, which are used to measure the actual strains in the test sample. Experimental results shown in Fig. 3 indicate that the correction coefficient ( $E_{spec} = 2.15 \pm 0.01$  GPa and  $E_{ext+sg} = 2.22 \pm 0.01$  GPa) is changed from 1.17 to 1.12, and thus is decreased by 5 %, implementing the second reference strain measurement method,  $E_{ext+sg}$ . Further in this paper, for most of the experimental results the correction coefficient is derived with the second method due to conveniences in experimental testing. This is underestimating the correction coefficient which is needed for actual test sample stiffness determination.

Furthermore, numerically the effect of the reference strain measurement method on the correction coefficient

with the test samples stiffness is presented. The results obtained are shown in Fig. 3. Estimated values in 3D and 2D reveal that the difference between correction coefficients are 7.5 % and 10 %, respectively, for the specimen with an elastic modulus of 1 GPa. The deviation is gradually declining for stiffer test samples.

#### Correction coefficient influenced by strain gauge geometrical properties

Evaluation of the gauge thickness and length is presented for the strain gauges listed in Table 1. The correction coefficient rises linearly up to 3 % by increasing the gauge thickness from 3.8 to 5.0  $\mu\text{m}$ , if  $t_{spec} = 30$  mm and  $E_{spec} = 1$  GPa. The larger correction coefficient changes are observed changing the gauge length from 1.5 mm to 10 mm. For example, in Fig. 4 the 2D model results show that the correction coefficient increases up to 1.52, i.e., the strain gauge measurement error is 52 %, if  $t_{spec} = 30$  mm,  $E_{spec} = 1$  GPa and  $L_{gauge} = 1.5$  mm. Furthermore, the error is gradually reduced to 14 % for longer strain gauges with  $L_{gauge} = 10$  mm.

In addition, the numerical results are compared with the analytical model derived for the local reinforcement effect by Ajovalasit et al. [10, 11] as follows:

$$C_{Ajovalasit} = \frac{\epsilon_{ave}}{\epsilon_{sg}} = 1 + \frac{E_{sg}^*}{E_{spec}}, \quad (6)$$

where  $E_{sg}^*$  is the reduced Young's modulus of the homogenized strain gauge, which characterizes the strain gauge sensitivity to the reinforcement effect and depends on the strain gauge stiffness, thickness and length [10]. The reduced Young's modulus for the strain gauges with  $L_{gauge} = 3$  mm and  $L_{gauge} = 10$  mm is given by Ajovalasit et al. [11] as 265 MPa and 175 MPa, respectively. Comparisons indicate deviations around 2.7 % for the strain gauges with  $L_{gauge} = 10$  mm and increase up to 10 % reducing the gauge length to 3 mm.

Further study revealed that the correction coefficient dependency on the strain gauge length is related to the strain distortions inside the gauge. In Fig. 2(b) results show that the strain distribution in the gauge sections has a curved shape with higher strains in the middle section, which tend

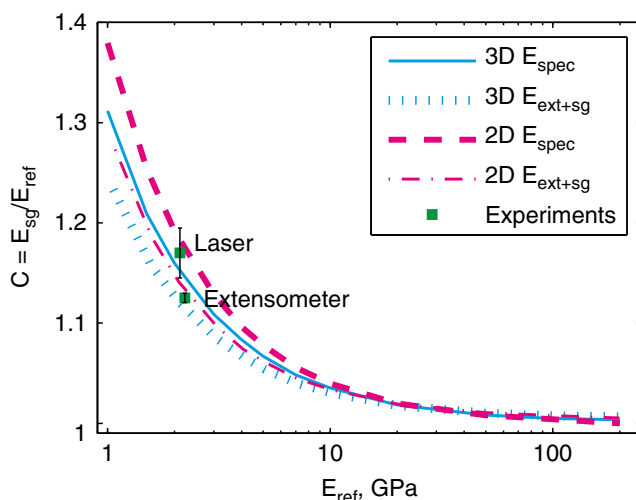


**Fig. 3** Comparison between the 2D and the 3D models introducing different reference values ( $L_{gauge} = 10$  mm,  $t_{spec} = 4$  mm)

**Table 1** Geometrical dimensions of HBM strain gauges (*LY11-L<sub>gauge</sub>/350*) [1]

$L_{gauge}$ (mm)	$B_{gauge}$ (mm)	$t_{gauge}$ ( $\mu\text{m}$ )	$L_{PI}$ (mm)	$t_{PI}$ ( $\mu\text{m}$ )
1.5	1.2	5.0	5.7	45.0
3.0	1.5	5.0	8.5	45.0
6.0	2.9	5.0	13.0	45.0
10.0	5.0	5.0	18.5	45.0

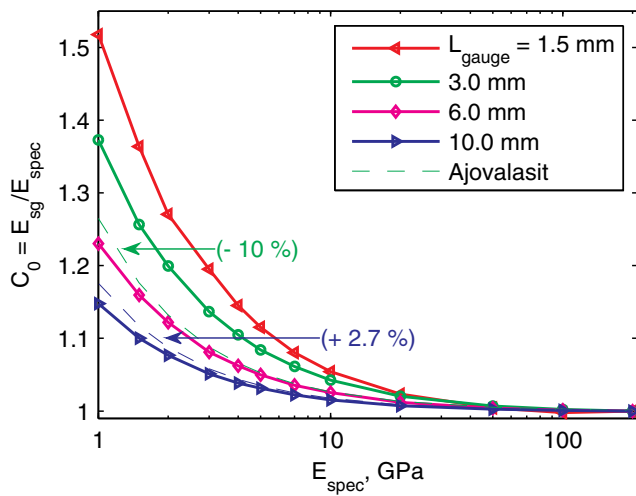


**Fig. 4** The 2D simulation results presenting correction coefficient variations with strain gauge length ( $t_{spec} = 30$  mm)

to approach the actual strain values of the test sample, and lower strains at the ends of the gauge. Analysing the strain distortions in the test samples, which are attached to the strain gauges with different lengths, it is observed that for shorter strain gauges the strains close to the ends reduce an average strain of the gauge more significantly. The reason is that for the shorter strain gauges the middle part of the gauge, which is unaffected by the edges, is narrower than is observed for the longer strain gauges. Therefore increasing the length of the strain gauge, the section of the gauge, which is unaffected by the edge effects, increases and contribute to higher accuracy of strain gauge measurements.

#### Correction coefficient influenced by specimen geometry

In the following subsection, the reinforcement effect sensitivity to the specimen dimensions such as width [10] and thickness [14] is discussed.

In Fig. 5(a), the 2D model results present the correction coefficient variations with the elastic modulus and the thickness of test sample, which is attached to the strain gauges with a gauge length 10 mm. Data obtained reveal a high sensitivity of the correction coefficient to the test sample thickness. Results show that for a 30 mm thick sample the correction coefficient is around 1.15 and it increases up to 2.18, i.e., obtaining 118 % of the strain gauge measurement error, when the test sample thickness is reduced to 1 mm. From Fig. 5(a) it is seen that the effect of the test sample thickness is larger for more compliant test samples. However, the reinforcement can still be significantly large even for relatively stiff, but thin test samples. For instance, the correction coefficient is as high as 1.15, which corresponds to a 15 % measurement error, if the elastic modulus

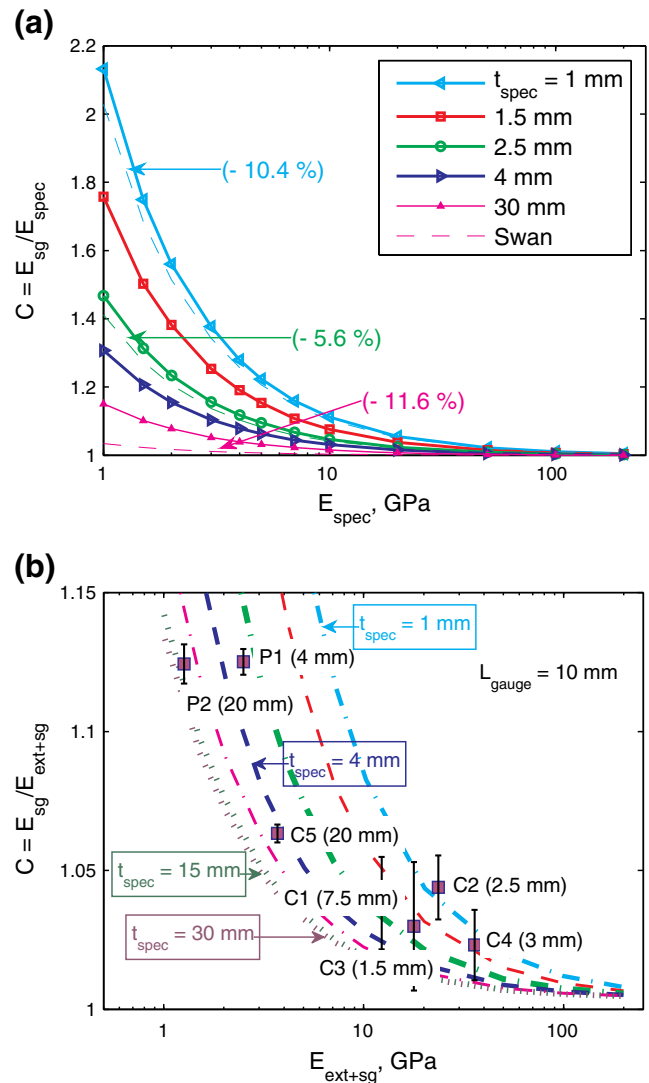


**Fig. 5** The 2D model results presenting the correction coefficient variations with the specimen thickness and elastic modulus, if  $L_{gauge} = 10$  mm

and thickness of the test sample is 10 GPa and 1 mm, respectively.

Additionally, in Fig. 5(b) a comparison between numerical and experimental results is given. The experimental data are shown for the test samples with different thicknesses and material stiffnesses, which are attached to the strain gauges with a gauge length 10 mm. The largest correction coefficient values are obtained for the neat polymer materials noted as *P1* and *P2*, which are also the most compliant materials used in this study. In addition, these experimental results demonstrate the influence of the test sample thickness, i.e., even though *P2* is softer than *P1* it has the same correction coefficient value due to the thicker test sample. Further the correction coefficient descend for multi-axial glass fibre and polymer

matrix composites, noted as *C1*, *C2*, *C3*, *C4* and *C5*, which are around ten times stiffer than the neat polymer material test samples. From Fig. 5(b) it is seen that the correlation between the experimental correction coefficient and the test sample material stiffness follows the same tendency as it is numerically predicted. Nevertheless, the effect of the test sample thickness is not captured for composite materials. The authors suggest this is due to the substantially inhomogeneous structure of composites.

Numerical results are also verified with the analytical model proposed by Swan [13]. This model is intended for the correction coefficient determination, if a global reinforcement effect is present, and it can be calculated as follows:

$$C_{Swan} = 1 + \frac{2E_{sg}t_{sg}}{E_{spec}t_{spec}}, \quad (7)$$

with  $E_{sg}$  and  $t_{sg}$  as the elastic modulus and the thickness of an homogenized strain gauge, respectively. The elastic modulus of an homogenized strain gauge is taken from Ajovalasit et al. study [11]. Results, presented in Fig. 5(a), show that the analytically determined correction coefficients deviate from the numerical results by 5 % to 12 % depending on the test sample thickness.

Furthermore, the study shows that the impact of the test sample thickness on the correction coefficient determination is limited. In Fig. 6, the 2D predictions indicate the presence of a transition point at certain critical thickness,  $t_{cr}$ , after which the correction coefficient tends to saturate and retain permanent value,  $C_0$ . The critical thickness is attributed to the transition between the local and the global reinforcement by the strain gauge. The difference between these two reinforcement effects are described in subsection “Strain gauge introduced strain disturbances”.

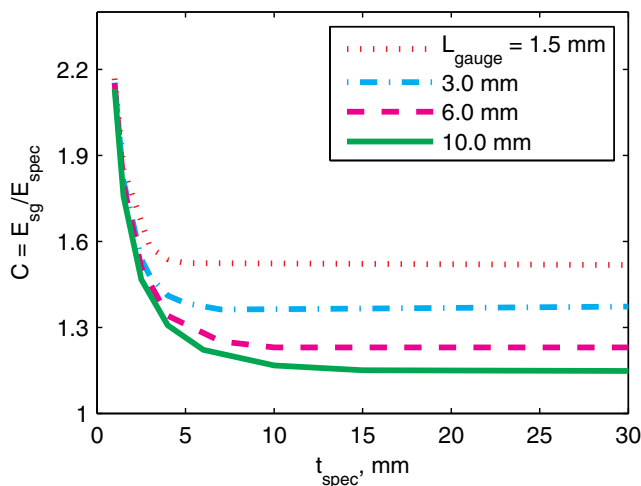


**Fig. 6** The 2D model results presenting the effect of the specimen thickness on the correction coefficient applying different length strain gauges, if  $E_{spec} = 1$  GPa

The critical thickness obtained is found to be dependent on the strain gauge length, i.e., implementing shorter strain gauges the critical thickness is reduced.

In addition, the effect of the specimen width is evaluated by a 3D model, where  $t_{spec} = 10$  mm and  $E_{spec} = 1$  GPa. Increasing the specimen width from 10 mm to 20 mm the correction coefficient is reduced from 1.141 to 1.127, thus it is 2.5 % lower. The simulation results obtained agree well with the similar study done by Ajovalasit and Zuccarello [10], who also found that the width effect is negligible, when the width ratio of the specimen and strain gauge ( $B_{spec}/B_{sg}$ ) exceeds 3.

#### Correction coefficient influenced by plastic deformation

The elastic-plastic material definition of the test sample is included to evaluate the correction coefficient changes at deformation levels exceeding the elastic region. In Fig. 7 the experimentally and in 2D correction coefficient obtained is presented for the specimen with dimensions 85 x 10 x 4 mm<sup>3</sup> and  $E = 2.1$  GPa mounted on the strain gauge LY11-10/350. The correction coefficient is determined from the ratio of the strain measured by the extensometer and strain gauge according to equation (4).

The experimental results, shown in Fig. 7, indicate non-uniform correction coefficient values in the strain region of 0.05 % - 0.25 %, which is used for elastic modulus determination of polymers accordingly to the standard ISO 527-1 [7]. The observed non-uniformity of the experimentally determined correction coefficient is not known. Comparing averaged experimental correction coefficient values with numerical results the difference is below 5 %, which is considered as small.

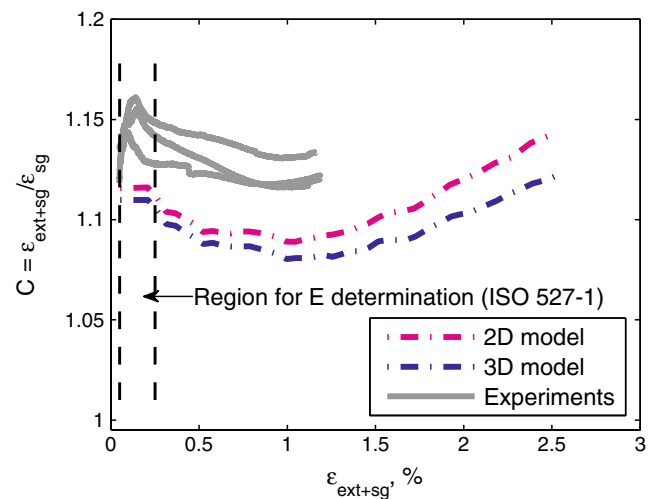


**Fig. 7** Correction coefficient changes with plastic deformation ( $t_{spec} = 4$  mm;  $L_{gauge} = 10$  mm and  $E_{spec} = 2.3$  GPa)

Beyond this deformation region the correction coefficient descends both for experimental and 2D results. In the 2D model, the correction coefficient starts to decrease at a strain of 0.24 %, whereas for some of the experimental results it is observed with even smaller values. The change of the correction coefficient is attributed to initiation of plastic deformation in constantan, which is the main component of the metallic parts in the strain gauge [2]. Continuing to deform the test sample above 1 % strain, the correction coefficient values again begin to rise. The ascending part is explained with more pronounced stiffness reduction by the test sample material during plastic deformation than it is in constantan.

### Discussion on correction coefficient determination

Results revealed that the strain gauge measurement precision significantly alters with specimen stiffness and is considerably influenced by test sample and strain gauge geometry. The specimen thickness and the gauge length are found to be the most crucial geometrical dimensions. Generalizing results, the largest strain gauge measurement errors are expected for short strain gauges bonded to thin and compliant specimens.

In subsection “Correction coefficient influenced by specimen geometry”, it is shown that the correction coefficient gradually decreases for thicker specimens, however the effect of thickness is limited. The numerical results predict that an increase of test sample thickness improves the strain gauge measurement precision only up to some critical value, i.e.,  $t_{cr}$  - critical thickness. Further the enlargement of thickness has no impact on strain gauge measurements, and it is explained with a transition from a global to only local reinforcement effect. The critical thickness is dependent on strain gauge length and independent of specimen stiffness. Hence for each type of strain gauge the optimal test sample thickness can be determined to minimize the gauge measurement errors. In addition, if the optimal thickness is known then the effect of test sample thinning can be sufficiently well predicted by mathematical model provided by Swan [13]. The drawback of this model is that it does not provide any information about the transition between local and global reinforcement, and the optimal geometry of a specimen.

Furthermore, when the strain gauge is bonded on the test samples with a thickness above the critical one, the global reinforcement, i.e., strain distortions through the whole thickness, can be neglected. Therefore for thick test samples the reinforcement by the strain gauge is localized and the effect of the specimen geometry can be excluded. In the local reinforcement the strain gauge measurement accuracy depends mainly on the strain gauge geometry and the

test sample stiffness. In subsection “Correction coefficient influenced by specimen geometry”, the 2D results demonstrate the importance of strain gauge geometry. The strain gauge length is found as a dominating parameter affecting the measurement accuracy of commercially available strain gauges used in this study. The correction coefficient needed to adjust the strain gauge measurements is larger implementing shorter strain gauges, even though longer strain gauges contributed to a larger volume of total strain field disturbances. This phenomenon is explained with uneven strain distribution in the gauge, which is caused by the strain transition between materials with mismatching stiffness. For more details see subsection “Strain gauge introduced strain disturbances” and “Correction coefficient influenced by strain gauge geometrical properties”.

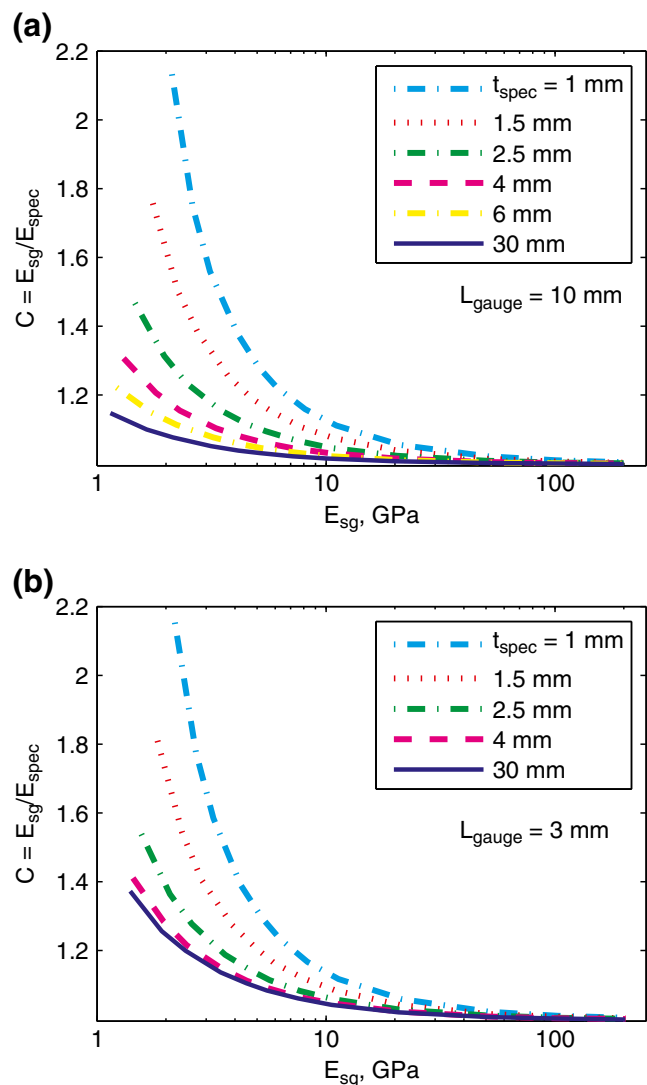


**Fig. 8** Curves for strain gauge measurement correction, when  $L_{gauge} = 10$  mm (a) and 3 mm (b)

In subsection “Correction coefficient influenced by plastic deformation”, it is shown that plastically deforming the test sample the correction coefficient tends to decrease due to the plastic deformation of constantan. Nevertheless, it is expected that the resultant correction coefficient depends on the competition between plastic deformation of specimen and constantan. More pronounced stiffness reduction by the test sample will lead to an increase of the correction coefficient, and it will descent with larger stiffness reduction by constantan.

### Practical determination of correction coefficient

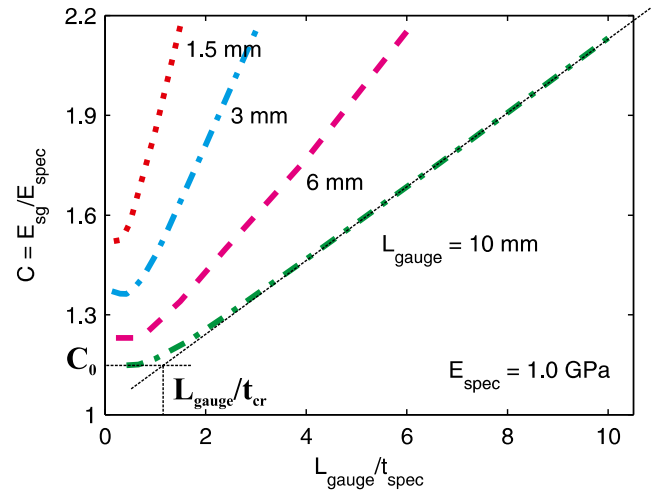
The results reveal that the strain gauge measurement precision significantly depends on the specimen thickness, strain gauge length and amount of total deformation. Experimentally obtained strain gauge measurements can be modified by the correction coefficient considering the effect of these critical parameters. Otherwise calibration of the strain gauge on the specific test sample has to be performed. This study is focused on the adjustment of experimental results using numerically obtained correction coefficients accounting for the dominating local or global reinforcement effect.

In Fig. 8 the correction coefficient variations with elastic modulus determined by the strain gauge are presented for different specimen thicknesses. Therefore, the actual specimen's elastic modulus can be extracted using experimentally obtained strain gauge measurements and applying equation (5). The correction coefficient values are presented for specimens with attached strain gauges of type LY11-10/350 (Fig. 8(a)) and LY11-3/350 (Fig. 8(b)).

Figure 9 summarizes the results shown in Fig. 6 for the strain gauges with different lengths mounted on a 1 GPa stiff test sample. From this, a bi-linear correlation between the correction coefficient and the aspect ratio of the gauge length and the specimen thickness can be observed. A bi-linear correlation indicates a transition between locally and globally dominating reinforcement. Therefore above the critical thickness, i.e., lower values of  $L_{gauge}/t_{spec}$ , the correction coefficient is constant and indicates the local reinforcement dominating region. Decreasing the specimen thickness, i.e., increasing the values of  $L_{gauge}/t_{spec}$ , the correction coefficient tends to increase linearly and this is attributed to the global reinforcement dominating region. Depending on the current reinforcement effect the correction coefficient can be expressed as follows:

$$C = \begin{cases} C_0 + AL_{gauge} \frac{t_{cr} - t_{spec}}{t_{cr} t_{spec}}, & t_{spec} < t_{cr} \\ C_0, & t_{spec} > t_{cr} \end{cases} \quad (8)$$

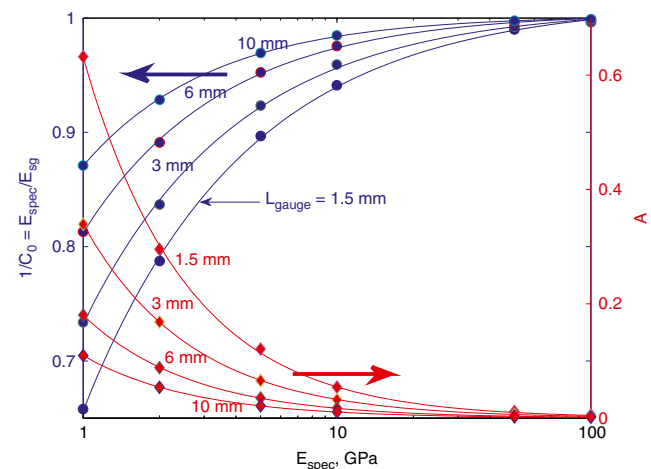
By fitting a linear relation between the correction coefficient and  $L_{gauge}/t_{spec}$  for thinner specimens, a parameter A



**Fig. 9** The effect of specimen thickness and grid length on correction coefficient

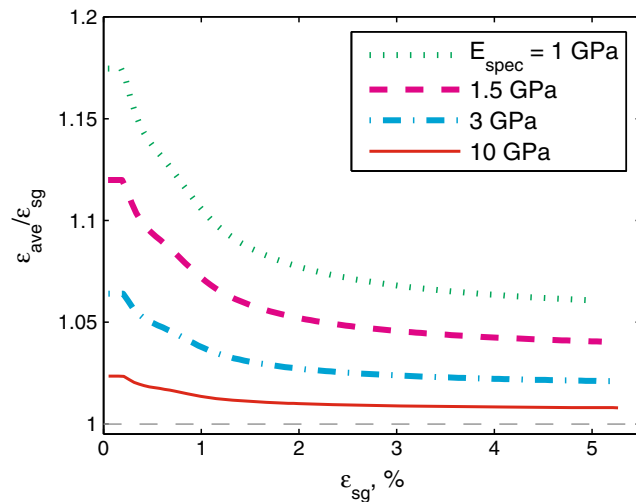
is extracted. In Fig. 10, conversion of the parameter A and the permanent correction coefficient with the test sample elastic modulus is demonstrated. It is found that the parameter A and the permanent correction coefficient both depend on the gauge length and elastic modulus of the specimen - tending to reduce with stiffer specimens. The critical thickness is found to be independent of the elastic modulus of the specimen, thus the critical thickness is estimated to be 3.3, 4.4, 6.5 and 9.5 mm for strain gauges with gauge lengths 1.5, 3.0, 6.0 and 10.0 mm, respectively.

Figure 11 presents the 2D model prediction of the correction coefficient variations for strains up to 5 % by including only the elastic-plastic material properties of the strain gauge metallic part. Simulation results are presented for the specimens with elastic modulus 1, 1.5, 3 and 10 GPa.



**Fig. 10** Variations of parameters A and  $C_0$  with material stiffness for strain gauges with different length ( $L_{gauge} = 1.5, 3.0, 6.0$  and  $10.0$  mm)





**Fig. 11** The correction coefficient variation with large strains ( $t_{spec} = 30$  mm;  $L_{gauge} = 10$  mm)

The outcome demonstrates that the effect of the reinforcement will tend to decrease due to the plastic deformation of the constantan wire and softer materials will be more prone to the correction coefficient reduction. Nevertheless, the final  $C$  depends also on the specimen stiffness reduction as is shown in Fig. 7, where the correction coefficient increases due to the larger stiffness reduction by the specimen. Thus Fig. 11 allows one to determine the correction coefficient for a gauge factor, if the amount of specimen stiffness reduction with plastic deformation is known.

## Conclusions

Results reveal that even for moderately stiff test materials sufficiently high correction coefficient values have to be used if short strain gauges are attached on thin test samples. Therefore the strain gauge length and the test sample thickness are found as the most significant geometrical dimensions. Depending on the correlation of these two parameters the dominating reinforcement effect by the strain gauge is divided into global and local ones. For each of the reinforcement effects different correction coefficient determination methods are applied. The transition between the global and only the local reinforcement effect is characterized with a *critical thickness*, above which only the local reinforcement effect exists. The *critical thickness* depends solely on the strain gauge length, thus can be used to optimize the test sample thickness.

In addition, it is observed that the correction coefficient tends to decrease due to plastic deformation of the strain gauge metallic part – constantan. Nevertheless, the resul-

tant correction coefficient depends also on the test sample material deformation.

**Acknowledgments** This research was supported by the Danish Centre for Composite Structure and Materials for Wind Turbines (DCCSM), grant no. 09-067212, from the Danish Strategic Research Council (DSF).

## References

1. HBM. Strain Gauge Catalog, [www.hbm.com](http://www.hbm.com)
2. Hoffmann K (1989) An Introduction to Measurements using Strain Gages
3. Perry CC (1984) The resistance strain gage revisited. *Exp Mech* 24(4):286–299
4. Stehlin P (1972) Strain distribution in and around strain gauges. *The Journal of Strain Analysis for Engineering* 7(3):228–235
5. Beatty MF, Chewning SW (1979) Numerical analysis of the reinforcement effect of a strain gage applied to a soft material. *International Journal of Engineering Science* 17(7):907–915
6. Watson RB (2008) Bonded electrical resistance strain gages. In: Sharpe WN (ed) *Springer handbook of experimental solid mechanics*, chapter 12. Springer, New York, pp 283–333
7. ISO 527-1: Plastics - Determination of tensile properties - Part 1: General principles, 1993
8. ISO 527-1: Plastics - Determination of tensile properties - Part 5: Test conditions for unidirectional fibre-reinforced plastic composites, 2009.
9. ASTM D5379/D5379M-12: Standard Test Method for Shear Properties of Composite Materials by the V-Notched Beam Method, 2012
10. Ajovalasit A, Zuccarello B (2005) Local reinforcement effect of a strain gauge installation on low modulus materials. *The Journal of Strain Analysis for Engineering Design* 40(7):643–653
11. Ajovalasit A, D'Acquisto L, Fragapane S, Zuccarello B (2007) Stiffness and Reinforcement Effect of Electrical Resistance Strain Gauges. *Strain* 43(4):299–305
12. Ajovalasit A (2011) Advances in Strain Gauge Measurement on Composite Materials. *Strain* 47(4):313–325
13. Swan JW (1973) Resistance strain gauges on thermoplastics. *Strain* 9(2):56–59
14. Little EG, Tocher D, O'Donnell P (1990) Strain gauge reinforcement of plastics. *Strain* 26(3):91–98
15. Luyckx G, Voet E, De Waele W, Degrieck J (2010) Multi-axial strain transfer from laminated CFRP composites to embedded Bragg sensor: I. Parametric study. *Smart Materials and Structures* 19(10):105017
16. Li W, Cheng C, Lo Y (2009) Investigation of strain transmission of surface-bonded FBGs used as strain sensors. *Sensors and Actuators A: Physical* 149(2):201–207
17. Ajovalasit A (2012) The Measurement of Large Strains Using Electrical Resistance Strain Gages. *Experimental Techniques* 36(3):77–82
18. Krempl E (1968) Evaluation of high-elongation foil strain gages for measuring cyclic plastic strains. *Exp Mech* 8(8):19N–26N
19. Rees DWA (1986) The sensitivity of Strain Gauges when Used in the Plastic Range. *International Journal of Plasticity* 2(3): 295–309
20. Stockmann M (2000) *Micromechanische Analyse der Wirkungsmechanismen elektrischer Dehnungsmessstreifen*. PhD thesis, Technischen Universität Chemnitz

Publication [P3]

Experimental determination of the micro-  
scale strength and stress-strain relation  
for an epoxy resin

# Experimental determination of the micro-scale strength and stress-strain relation of an epoxy resin

Sanita Zike, Bent F. Sørensen, Lars P. Mikkelsen

*Composites and Materials Mechanics Section, Department of Wind Energy, Technical University of Denmark, Risø Campus, 4000 Roskilde, Denmark*

## Abstract

Constitutive laws (stress-strain and cohesive laws) to be used in micro-mechanical models cannot be fully obtained from macro-scale measurements. A method is developed for determining the stress-strain law and a peak cohesive traction value appropriate for micro-mechanical models. Experimentally, test samples made of an epoxy polymer used in fibre composite materials for wind turbine blades with notches having finite root radius were subjected to double cantilever beam tests in an environmental scanning electron microscope. The recorded images were used to measure strains around the notch with a 2D digital image correlation method. Furthermore, the experimentally measured strains around the notch edge were related to stresses in a compliance with an HRR theory. The hardening exponent (also the failure strength) of a power law hardening material was obtained by the use of the J-integral, estimating the strain energy density at failure.

During the micro-scale measurements, the strain in front of the notch reached 20% before the failure initiation, which significantly exceeds the failure strains measured at the macro length scale (5-6%). The epoxy polymer was found to have a hardening exponent within the range of 5 to 6 and a corresponding microscopic failure stress in the range of 220-300 MPa. In addition, our experimental study shows that the strain fields between the notches with different notch root radii are comparable, if all length parameters are normalized with the notch opening displacement.

**Keywords:** micro-scale test, micro-mechanical models, *in-situ* testing, polymer/fibre composites, epoxy matrix

## 1 Introduction

Polymer/fibre composite materials are often used in structural load carrying components. In the wind energy industry, the polymer/fibre composites are particularly important due to their high stiffness, low density, and good fatigue performance [1,2]. The fibres are usually designed to carry the main load of the composite structure. Some of the microscopic processes, however, are greatly dependent on the matrix behaviour, e.g. loading transverse to the fibres. At the micro-scale, the failure of the matrix initiates from a flaw in the matrix or at a fibre/matrix interface leading to the fibre-matrix debonding and fibre cracking. These micro-scale events result in a macro-scale failure, e.g. delamination between plies, reducing performance of the composite structure [3]. For this reason, micro-mechanical models are often used to study the effect of micro-scale material properties and microscopic defects on the microscopic damage evolution.



In this paper, we aim to determine the matrix material properties (stress-strain and traction separation laws) to be used in micro-mechanical models for the simulation of progressive damage evolution in composite materials. First, in order to characterize micro-mechanical behaviour of matrix, its properties have to be determined at the relevant length scale. The macroscopic stress-strain law and tensile strength of a material is not sufficient for use in micro-mechanical modelling. Consider a simple uniaxial tensile testing of a material, shown in Fig. 1a, that fails by brittle fracture, i.e. from pre-existing flaws. At the macro-scale, we consider the material as well as stress and strain fields to be uniform, i.e. the same at any point within the gauge section. Model wise, the macroscopic failure stress would be determined simply as the force at failure,  $F_u$ , divided by the cross-section area,  $A$ , i.e. the average failure stress  $\tilde{\sigma} = F_u/A$ . Likewise, the macroscopic failure strain  $\tilde{\epsilon}_u$  will be determined from the macroscopic deformation, e.g. the elongation  $\Delta L$  measured by an extensometer with a certain initial gauge length,  $L_o$ ,  $\tilde{\epsilon}_u = \Delta L/L_o$ . A strain gauge will also give the strain averaged over its gauge length. These strength values are appropriate for modelling structures at the macro-scale.

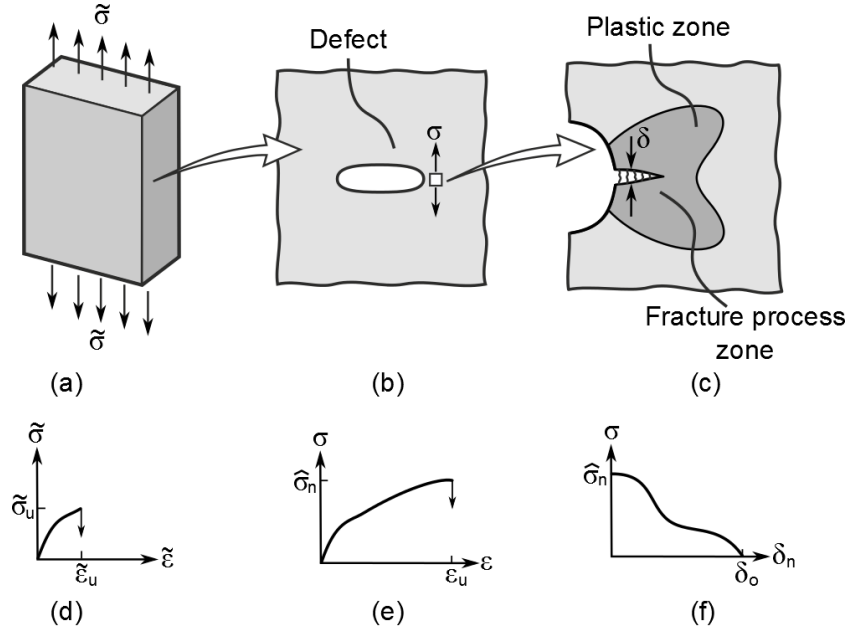


**Fig. 1 Failure at macro- (a, d) and micro- scale (b, c, e, f)**

On the micro-scale, however, the situation is very different. Here we will consider the material as heterogeneous, such as a composite consisting of discrete fibres in a matrix material that contains micro-scale defects (Fig. 1b). The stress and strain fields will be non-uniform, depending on micro-scale features. Failure will initiate from a pre-existing flaw. A pre-existing flaw, e.g. a pore (e.g. an air bubble) in a polymer material, will create a local stress concentration and multi-axial stress state at the vicinity of the pore (Fig. 1b) and a plastic zone can form around the fracture process zone (Fig. 1c), represented by a non-linear stress strain law. A fracture process zone will form when the stress at a pore reaches the micro-scale strength, denoted as  $\hat{\sigma}_n$ . The fracture process zone will develop into a micro-crack that will eventually grow into a macro-crack that will propagate across the entire cross-section of the specimen leading to macro-scale failure. At the instance when the fracture process zone begins to form, and the micro-scale stress at the pore is equal to  $\sigma = \hat{\sigma}_n$ , the associated strain is equal to the micro-scale failure strain,  $\epsilon_u$  (Fig. 1d). Once a fracture process

zone has formed, its mechanical behaviour can be represented by a cohesive law (traction-separation law) as shown in Fig. 1f, i.e.  $\sigma_n = \sigma_n(\delta_n^*)$ , where  $\delta_n^*$  is the normal opening of the formed crack faces within the fracture process zone.

The micro-scale strength,  $\hat{\sigma}_n$ , and the associated failure strain,  $\varepsilon_u$ , will be higher (Fig. 1d) than the associated macroscopic properties (Fig. 1e),  $\hat{\sigma}_n > \tilde{\sigma}_u$  and  $\varepsilon_u > \tilde{\varepsilon}_u$ . It is the micro-scale failure strength and failure strain that should be used in micro-mechanical models. The macroscopic strength and failure strain are not sufficient as the micro-scale stress-strain relationship beyond  $\tilde{\sigma}_u$  and  $\tilde{\varepsilon}_u$  is not available from macro-scale measurements.

In case we wish to make a micro-mechanical model of the experiment described above, it is obvious that we cannot use  $\tilde{\sigma}_u$  as a local stress criterion for failure at the micro-scale. We need to know the local micro-scale strength  $\hat{\sigma}_n$ , and we must know the micro-scale stress-strain law in the entire strain range,  $0 < \varepsilon < \varepsilon_u$ . Therefore, in the present study, we aim to develop an approach to determine the micro-scale stress-strain law in the strain range beyond that obtainable from a traditional macroscopic tensile test,  $\tilde{\varepsilon}_u < \varepsilon < \varepsilon_u$ , and determine the micro-scale strength  $\hat{\sigma}_n$ .

In this study, in order to obtain the micro-mechanical properties of the epoxy resin used in polymer/fibre composites, the test samples with the finite notch root radii are made to mimic the stress state around a void. The test samples are subjected to double cantilever beam (DCB) tests in a vacuum chamber of an environmental scanning electron microscope (ESEM). From the images captured in the ESEM, the strains around deformed notches are measured with the 2D digital image correlation (DIC) method using the commercial software ARAMIS [4]. To attain the microscopic stress-strain relation and micro-scale strength, the strain energy density around the notch is related to different power law hardening material models. Analytical approach is verified by constructing the stress-strain curve from the experimental strain measurements in the loaded and unloaded state (permanent strains). In addition, the paper includes the analysis of the characteristic strain fields around the notches recorded at high magnification. The strain fields between the notches with initially different root radii are compared normalizing all length parameters with the notch opening displacement following McMeeking's numerical study [5].

## 2 Theory

### 2.1 Non-linear fracture mechanics and concept of the strain energy density

In order to characterize mechanical behaviour of the epoxy resin around the notches with finite root radii, the theory of non-linear fracture mechanics is used. The non-linear fracture mechanics, established by Hutchinson, Rice, and Rosengren (HRR) [6,7], provide a unique measure of the crack tip fields for elastic-plastic materials within the context of the small strain deformation theory. The stress intensity around the crack tip under monotonic loading is described with a path-independent line integral  $J$ . The path-independence of the J-integral indicates that it can be determined around any contour encircling the tip of the crack,  $\Gamma$ , in a counter clockwise direction as shown in Fig. 2 [8]. Along  $\Gamma$  the J-integral can be determined as

$$J = \int_{\Gamma} W dx_2 - T_i \frac{\partial u}{\partial x_1} ds, \quad (1)$$

where  $T_i$  is the traction vector acting on the contour  $\Gamma$ ,  $u$  is the displacement vector,  $s$  is the arc length along  $\Gamma$ ,  $x_1 = x$ , and  $x_2 = y$ . The strain energy density,  $W$ , is a function of stress,  $\sigma$ , and strain,  $\varepsilon$ , increment

$$W = \int_0^\varepsilon \sigma_{ij} d\varepsilon_{ij}. \quad (2)$$

If  $\Gamma$  is taken around the notch edge ( $\Gamma = \Gamma_{tip}$ ) as the blue dashed line in Fig. 2, then there is no traction acting on the contour, i.e.  $T_i = 0$ . According to Eq. 1, now  $J$  is only a function of  $W$  and is given as [9]

$$J = \int_{\Gamma_{tip}} W dx_2, \quad (3)$$

where  $dx_2 = r \cos \theta d\theta$ ,  $r = \delta_t/2$ ,  $\delta_t$  is the notch opening displacement,  $r$  is the distance from the notch centre, and  $\theta$  is an angle, see also Fig. 2. According to Eq. 3, integrating around the notch, i.e. from  $-\pi/2$  to  $\pi/2$ , follows that the mean strain energy density,  $\bar{W}$ , around the notch is

$$\bar{W} = J/\delta_t. \quad (4)$$

From Eq. 2 and Eq. 4, it can be seen that  $W$  can be determined with two independent approaches. These two approaches are applied here to relate the micro-mechanical behaviour of the epoxy resin with a power law hardening material. First,  $\bar{W}$  around the notch is determined considering the path independence of the J-integral [9], i.e. the J-integral evaluated around the notch is the same as around the external boundaries. Next,  $W$  (Eq. 2) is extracted from the stress-strain relationships of power law hardening materials with various hardening exponents,  $n$  ( $W$  denotes the area below the stress-strain curve). The stress-strain relationships are obtained fitting the macroscopic stress-strain curve of the epoxy resin in tension to Ramberg-Osgood relation [10]

$$\frac{\varepsilon}{\varepsilon_o} = \frac{\sigma}{\sigma_o} + \alpha \left( \frac{\sigma}{\sigma_o} \right)^n, \quad (5)$$

where  $\sigma_o$  is the yield stress,  $\varepsilon_o = \sigma_o/E$  is the elastic strain,  $E$  is the elastic modulus, and  $\alpha$  is a parameter. The experimental strain measurements around the notch are used to define the strain limit of the stress-strain curves. Finally, the hardening exponent of the micro-scale stress-strain relationship and failure stress of epoxy resin are found by matching  $\bar{W}$  (Eq. 4) with  $W$  (Eq. 2).

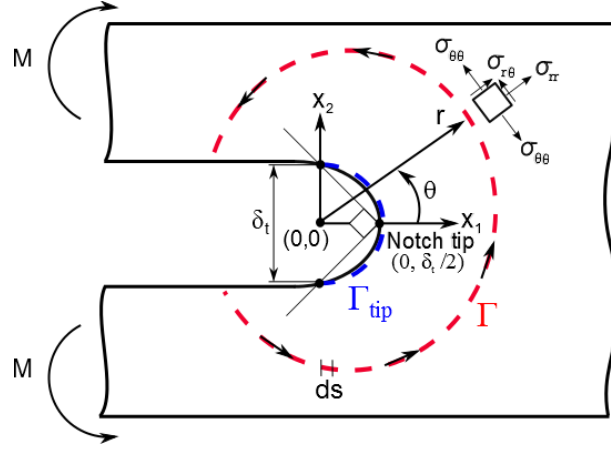


Fig. 2 Contours used for the J-integral determination

## 2.2 Permanent strains

Permanent strains are used to verify the analytical approach given above. We assume that during unloading elastic deformation is completely removed, and the steepness of the unloading curve agrees with the steepness of the stress-strain relation during loading in the elastic region as shown in Fig. 3. Moreover, we expect that during re-loading the epoxy resin will yield when the stresses at previous loading are reached. These assumptions are used to construct the stress-strain relation, i.e. knowing the strain values in loaded,  $\varepsilon$ , and unloaded state,  $\varepsilon^p$ , the stress,  $\sigma$ , is found from

$$\sigma = E(\varepsilon - \varepsilon^p). \quad (6)$$

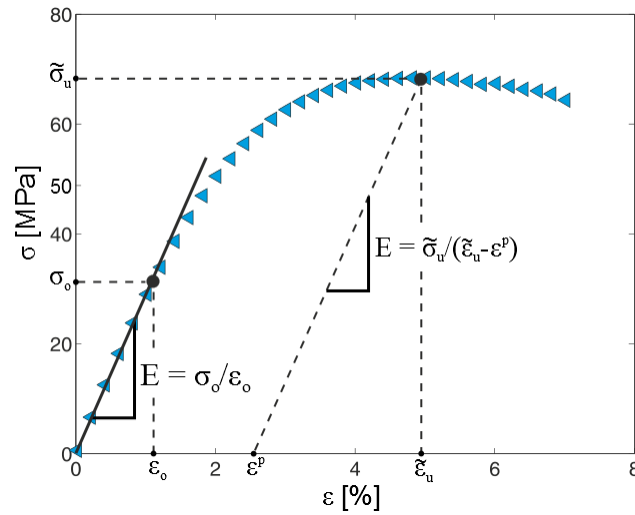


Fig. 3 The averaged macroscopic stress-strain curve in tension of epoxy resin

## 2.3 Cohesive law

In addition, the cohesive law is used to find the failure strength. According to this theory [11,12], the failure initiates not at the real crack tip, but in the fracture process zone where microscopic failure processes (e.g. void formation, micro-cracks, etc.) take place. The length of fictitious crack therefore is the sum of the actual

crack length and fracture process zone. As the material strength in tension,  $\sigma_t$ , is reached in the fracture process zone, the material between the actual and fictitious crack tip will start to weaken, and the actual crack will start to propagate. The work done during the separation can be evaluated by means of J-integral, i.e. the J-integral evaluated around the crack tip equals the crack tip fracture energy,  $G$  [13]. And,  $J$  during crack propagation,  $J_R$ , is expressed as

$$J_R = \int_0^{\delta_n^*} \sigma(\delta_n^*) d\delta_n^* + J_o, \quad (7)$$

where  $J_o$  denotes the crack initiation and  $\delta_n^*$  is the opening of newly developed crack, see Fig. 1c,f.

#### 2.4 Strain field characterization

The experimentally measured strain fields are characterized considering that the strains around the crack tip in the HRR theory within the  $J$  dominance region are given as

$$\varepsilon_{ij} = \alpha \varepsilon_o \left( \frac{J}{\alpha \sigma_o \varepsilon_o I_n r} \right)^{\frac{n}{n+1}} \bar{\varepsilon}_{ij}(\theta, n), \quad (8)$$

where the dimensionless function  $\bar{\varepsilon}_{ij}(\theta, n)$  and normalizing constant  $I_n$  is dependent on the crack loading mode, on  $n$ , and on whether plane strain or plane stress state prevails [8]. The dimensionless function  $\bar{\varepsilon}_{ij}(\theta, n)$  is independent of  $J$  and  $r$  and dependent on  $n$  in the  $J$  dominance region [8]. Therefore, the strain variations around the crack can be described with two components. The first component refers to the strain magnitude and the second component,  $\bar{\varepsilon}_{ij}(\theta, n)$ , shows the strain variations with an angle around the crack.

Moreover, in accordance to the numerical study by McMeeking [5], the stresses and strains around the notch can be describe in the same way as around smoothly blunting initially sharp cracks if all length parameters are normalized with the current notch width. The same assumptions are employed here, i.e. we assume that in the normalized coordinate system the strain fields around the notch with smaller and larger notch root radii, which are made of the same material, will agree. The strain fields between different notches are compared considering that the stress in front of the notch depends on the ratio between the current notch opening displacement,  $\delta_t$ , and initial notch width,  $\delta_{to}$ , [5]

$$\delta_t / \delta_{to} = d_n J / \sigma_o \delta_{to}, \quad (9)$$

where  $d_n$  is a parameter. Likewise, the crack tip opening,  $\delta_t^*$ , varies linearly with  $J$  for the initially sharp cracks according to the HRR theory

$$\delta_t^* = d_n (\alpha \varepsilon_o, n) J / \sigma_o, \quad (10)$$

where the parameter  $d_n$  is ranging approximately from 0.3 for  $n = 3$  to 0.8 for large  $n$  values with  $\alpha = 1$  [8,14].

### 3 Material and methods

#### 3.1. The macro-mechanical properties of an epoxy resin

The macro-mechanical properties of the polymer used in the present study, *Airstone 760E* epoxy, are briefly described below. According to the reference [15], the material possesses certain ductility as the macro-scale failure strain,  $\tilde{\epsilon}_u$ , reaches 5% in tension and 6% in compression. The corresponding maximum stress,  $\tilde{\sigma}_u$ , is measured to be 72 MPa in tension and 86 MPa in compression. Defining the yield at the point where the relationship between the tensile stress and strain deviates from the linearity, the yield stress,  $\sigma_o$ , is obtained of 32 MPa, the elastic strain,  $\epsilon_o$ , of 1.12%, and the elastic modulus,  $E = \sigma_o/\epsilon_o$ , of 2.85 GPa. For more details, regarding the macroscopic properties of the epoxy polymer see the study by Zike and Mikkelsen [15]. In addition, the averaged macroscopic tensile curve is shown in Fig. 3.

#### 3.2. The test sample design

The DCB sample design is based on the previously conducted numerical parameter study [16]. In this study, the dimensions of the test sample were optimized in order to enable loading up to the onset of fracture within the fixture limitations [17]. It was considered that the sample should be loaded in pure bending; the rear end of the test sample should be stress free; the deflection of the loading beams must not exceed the fixture limits; and buckling of the sample must not occur. The design was done for a sample with a sharp tip.

#### 3.3. The test sample preparation

##### 3.3.1. Manufacturing (Test Series 1 and Test Series 2)

An epoxy resin *Airstone 760E* is mixed with a hardener *Airstone (TM) 766H* maintaining ratio 3:1. Further, the mixture is degassed in a vacuum chamber up to the vacuum of 98%, what takes approximately 5 minutes. After degassing, the liquid epoxy is poured into the mould consisting of two glass plates positioned parallel to each another with a distance equal to the specimen width as shown in Fig. 4b. In order to ensure that the liquid resin stays in the mould, a rubber pipe (red line in Fig. 4) between two glass plates is wrapped around three side edges. Clamping holders are used to fix the mould. Further, in order to create notches with different radii, a sharp paper knife razor wrapped with an ETFE (ethylene tetrafluoroethylene) film with thickness of 12.7  $\mu\text{m}$  and PTFE (polytetrafluoroethylene) adhesive tape with thickness of 80  $\mu\text{m}$  is placed into an uncured epoxy. As a result, the test samples have an initial notch width of approximately 95  $\mu\text{m}$  and 245  $\mu\text{m}$ , denoted as Test Series 1 and Test Series 2, respectively. The epoxy is cured at 50°C for 5 hours. After cooling up to the room temperature, it is post-cured at 80°C for 3 hours.

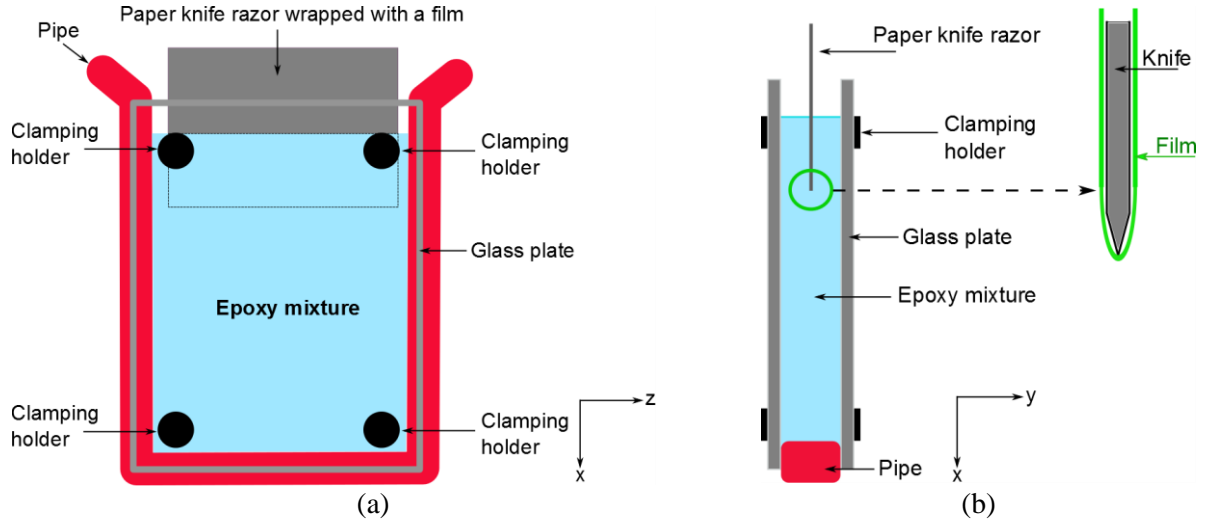


Fig. 4 The procedure of the test sample manufacturing shown in  $x$ - $z$  plane (a) and  $x$ - $y$  plane (b)

### 3.3.2. Machining

After post-curing, the paper knife razor is removed and the block of epoxy is cut into samples with thickness of approximately 2.5 mm. Furthermore, holes with a radius of 1 mm are drilled at the end of the beams to create a “hook” for fixing the test sample within the DCB fixture [17]. In order to remove cutting defects and deep scratches around the notch, water cooled grinding of the front and back surface of the test samples is done utilizing a machine *Struers LabPol 25*. Sandpapers with a grit of 1000 and 4000 are used to grind off approximately 0.4 mm and 0.1 mm, respectively, including the front and back surface. Additional polishing is done with a diamond paste with monocrystalline diameter of 1  $\mu\text{m}$  using a silk cloth to remove grinding scratches on the surface to be used for strain measurements. In total, the polishing time was about 5 to 10 minutes. After machining, the test samples are heated in an oven at 80°C for one hour to remove residual stresses around the notches. The final test sample dimensions are given in Fig. 5.

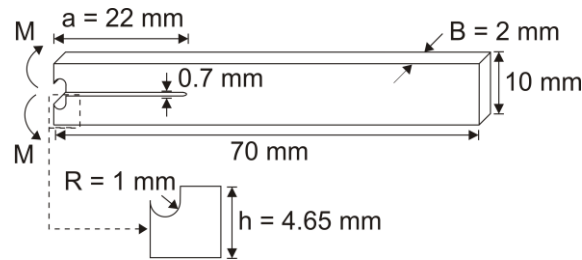


Fig. 5 The test sample dimensions

### 3.3.3. Speckle sputtering

Additional test sample surface preparation is done in order to utilize the digital image correlation (DIC) method for the strain measurements. First, a gold layer with thickness of 15 nm is sputtered onto the surface to be imaged. This is done to evaluate a surface smoothness before and after the test, since the speckle particles can be easily removed by immersing samples in ethanol and applying ultrasound. In addition, gold layer gives a higher contrast for ESEM images later used for the digital image correlation method analysis. Next, speckles on the test sample surface are created by spraying solutions containing Ti- and Fe- oxide particles. The

solutions are created by dissolving 1 w% of Ti- and 5 w% of Fe- oxide particles in ethanol separately and stirred for approximately 2 hours with a magnetic mixer and mechanically with zirconia balls, respectively. The mean diameter of TiO<sub>2</sub> and FeO particles is 0.5 µm and 1.1 µm, respectively, and the total range of particle size is from 0.05 to 3 µm according to the measurements by a laser diffraction particle size analyser *Beckman Coulter LS 13 320* [18]. The spraying is done with an airbrush *BossDye-132* with a nozzle size of 0.3 mm [19].

### 3.4. The DCB test procedure

Micro-scale tests are performed with the DCB fixture specially designed by Sørensen et al. [17] for *in-situ* observations of failure mechanisms in an environmental scanning electron microscope (ESEM) *ZEISS EVO 60* [20]. The loading fixture is equipped with a load cell with a capacity of 75 N (corresponding to a maximum moment of 6 Nm) and high precision linear displacement transducer *LDI 8/1* for load and opening measurements, respectively. The tests are performed step by step including *loading-hold-unloading-hold* procedure as shown in Fig. 6. In this study, results are presented for five steps separated by an applied moment values: 0.40 Nm, 0.56 Nm, 0.80 Nm, 0.96 Nm, and 1.20 Nm. At each step, the test samples are loaded and unloaded with a rate within the range of 0.9-1.2 Nm/min. The reason for conducting the *unloading* and *hold* is to study permanent strains and to capture images at different magnifications, respectively. Moreover, during *hold* of approximately 4 min, the fixture displacement is fixed, and load drop up to 15% is observed. The highest load drop occurred for higher applied moments and is attributed to visco-elastic or visco-plastic deformation of the epoxy polymer. In a result analysis, the load drop is neglected.

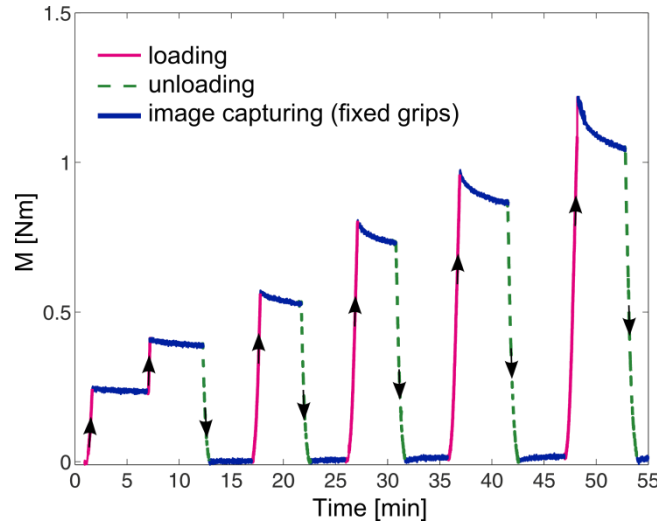


Fig. 6 A typical loading curve during the DCB test showing the applied moment versus time

In this study, the  $J$  integral is considered as a loading parameter. Assuming that the material is macroscopically linear-elastic, the relation between  $J$  and applied moment,  $M$ , for double cantilever beam test samples in plane stress is [21]

$$J = \frac{12M^2}{B^2h^3E}, \quad (11)$$



where  $B$  and  $h$  are the test sample dimensions presented in Fig. 4b and  $\nu$  is Poisson's ratio taken as 0.4 (see also subsection 3.1). Fig. 7 shows that the actual test samples are having small variations of the beam width close to the notch tip. For instance, the beam width is increasing from  $h = 4.65$  mm to  $h = 4.95$  mm and to  $h = 4.88$  for the Test Series 1 and Test Series 2, respectively. Numerically [22],  $J$  around the notch was found to decrease due to the non-uniformities of the beam width. Therefore, in this study, the numerically estimated  $J$  values around the notch for linear-elastic material under different applied moments are used and are given in Table 1. The loading beams are expected to deform elastically during the experiments.

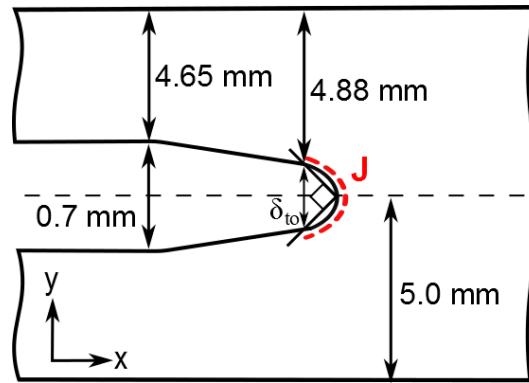


Fig. 7 The sketch of the actual notch (Test Series 2)

Table 1 The numerically estimated  $J$  values under different applied moments

$M$ [Nm]	$J$ [kJ/m <sup>2</sup> ]	
	Test Series 1	Test Series 2
1.20	12.7	11.7
0.96	7.2	7.5
0.80	4.9	5.3
0.56	2.4	2.5
0.40	1.1	1.2

### 3.5. Image capturing

Inside the ESEM images are captured under high vacuum of  $6 \times 10^{-7}$  mbar using secondary electrons. The acceleration voltage is set to 8 kV, and the working distance is within the range of 12-14 mm. During each *hold*, images are captured at different magnifications as x100, x500, and x1000, i.e. magnification is altered during the test. This was possible as the microscope software allows setting magnification with a decimal precision of 0.001. Moreover, in order to use images for the digital image correlation (DIC) analysis, it is important that the same view around the notch is maintained between different steps. Thus, a specific point as a rigid particle on the surface for each magnification level is found and used to centre the image after each alteration of the magnification. The recording resolution,  $N$ , of the captured images is  $1024 \times 768$  pixels<sup>2</sup>, further the field of view,  $l$ , and the magnification factor,  $M_T = N/l$ , are listed in Table 2.

### 3.6. DIC method

From the images captured in the ESEM, the strains of the deformed test sample are measured with the 2D DIC method [23,24] using the commercial software ARAMIS v6.3.0 [4]. In this study, the images of the test sample surface are divided into facets with a length of 45-60 pixels (facet size,  $f$ ) and a distance between the

centre points of the adjacent facets is set to 3-5 pixels (facet step,  $p$ ). The facet size affects the displacement spatial resolution,  $f/M_T$ , and, in this study, it is within the range of 13  $\mu\text{m}$  to 177  $\mu\text{m}$  as shown in Table 2.

**Table 2 Parameters used to evaluate the DIC method**

Magnification	$l$ [ $\mu\text{m}^2$ ]	$M_T$ [pixel/ $\mu\text{m}$ ]	$f/M_T$ ( $f = 60$ pixels) [ $\mu\text{m}$ ]	$f/M_T$ ( $f = 45$ pixels) [ $\mu\text{m}$ ]	Pixel length [ $\mu\text{m}$ ]
x100	3000 x 2250	0.34	176.5	132.4	3.0
x500	600 x 450	1.71	35.1	26.3	0.6
x1000	300 x 225	3.41	17.6	13.2	0.3

During the DCB test, the test sample surfaces were undergoing brightness and contrast changes. Contrast changes are related to the displacements in the  $z$ -axis direction (out-of-plane), which depend on the applied moment, and are estimated in the range of 100-300  $\mu\text{m}$ . The out-of-plane displacements are found to create artificial strain up to 0.42% for the strain components  $\varepsilon_{\theta\theta}$  and  $\varepsilon_{rr}$ , and up to 1% for  $\varepsilon_e$ . The brightness, in-plane displacements, and imaging related distortions [25] are found to have a minor effect on the strain measurements, for more details see *Appendix*.

### 3.7. The strain transformation

Strains obtained from the ARAMIS software are measured in the Cartesian ( $x$ - $y$ - $z$ ) coordinate system. As stress and strain fields around cracks and notches are commonly characterized in the polar coordinate system, a strain transformation is done as follows [26]

$$\varepsilon_{rr} = \varepsilon_{xx} \cos^2 \theta + \varepsilon_{yy} \sin^2 \theta + \varepsilon_{xy} \sin 2\theta, \quad (12)$$

$$\varepsilon_{\theta\theta} = \varepsilon_{xx} \sin^2 \theta + \varepsilon_{yy} \cos^2 \theta - \varepsilon_{xy} \sin 2\theta, \quad (13)$$

$$\varepsilon_{r\theta} = \sin \theta \cos \theta (\varepsilon_{yy} - \varepsilon_{xx}) + \varepsilon_{xy} \cos 2\theta, \quad (14)$$

where  $\theta = \tan^{-1}(y/x)$  and  $x, y$  are point coordinates in the deformed state, when the centre point (0,0) is set to  $\delta_r/2$  from the notch tip (see Fig. 2). Following the reference [8], the notch opening displacement,  $\delta_r$ , is used as the opening distance between the intercept of two  $45^\circ$  lines drawn back from the tip in the deformed state as shown in Fig. 2. Similar approach is used to measure the initial notch width in the un-deformed state denoted as  $\delta_{to}$ . Moreover, Eq. 12-14 are used to create a user defined visualization in the DIC software for the strain contour presentation. In this study, the effective von Mises strain,  $\varepsilon_e$ , which is a combination of different strain components,  $\varepsilon_{ij}$ , is as well included and given as

$$\varepsilon_e = \sqrt{\frac{2}{3} \varepsilon_{ij} \varepsilon_{ij}}. \quad (15)$$

## 4 Results

### 4.1 Determination of the micro-scale stress-strain relation and failure stress

#### 4.1.1 Strain energy density

The test sample without an extensive amount of micro-cracks around the notch edge at the loading step close to failure is chosen and shown in Fig. 8a. The test sample is loaded with  $J = 11.7 \text{ kJ/m}^2$ , and has the notch

opening displacement,  $\delta_t$ , of 346  $\mu\text{m}$ . From Eq. 4, it is attained that  $\bar{W} = 33.8 \text{ MJ/m}^3$ . Furthermore, the failure strain is measured around the same notch. These values are later used to set the strain limit of the stress-strain curves used to extract  $W$  values according to Eq. 2. In order to avoid that the strain measurements around the notch are distorted by larger particles or micro-cracks, the strains are extracted both along circular and line paths drawn in the front of the notch as shown in Fig. 8. The circular paths have a normalized radius  $r/\delta_t = 0.52$  and  $r/\delta_t = 0.55$ , respectively the distance from the notch edge is approximately 7  $\mu\text{m}$  and 17  $\mu\text{m}$ . The acquired strain-angle curve in Fig. 8b shows two regions of missing data points, which are due to two largest material micro-cracks at  $\theta \approx \pm 30^\circ$ . Insignificant scatter is considered for  $\theta < -40^\circ$  and just in the front of the notch tip (Fig. 8b). Fig. 8b shows results along circular paths with the extreme values of  $\varepsilon_{rr}$  and  $\varepsilon_{\theta\theta}$  at  $\theta = 0^\circ$  as -13% and 17%, respectively. Slightly larger absolute strain values are attained from the line paths starting just at the notch edge without incline as it is shown in Fig. 8c, where the extreme values of  $\varepsilon_{rr}$  and  $\varepsilon_{\theta\theta}$  reach -15% and 20%, respectively. The extreme value of  $\varepsilon_{\theta\theta}$  obtained from the inclined line paths are from 10 to 15% at  $\theta \approx \pm 15^\circ$  (Fig. 8c). Results indicate that the actual strain distribution around the notch is non-uniform and can be fitted to relation  $\varepsilon_u \cos^2 \theta + 0.5 \varepsilon_u \sin^2 \theta$  (Fig. 8b). This gives the mean strain,  $\bar{\varepsilon}$ , of 15% for  $\varepsilon_u = 20\%$ .

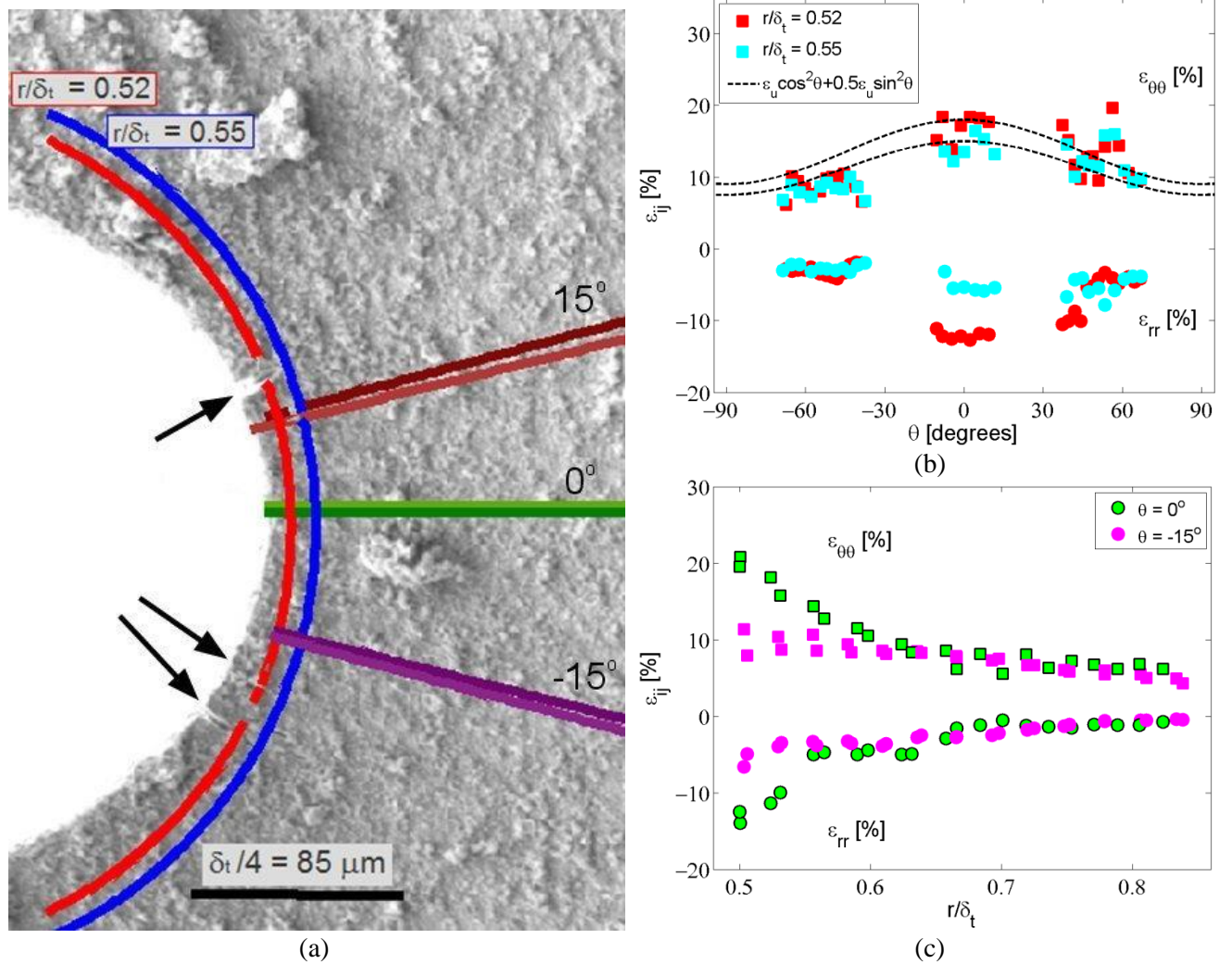
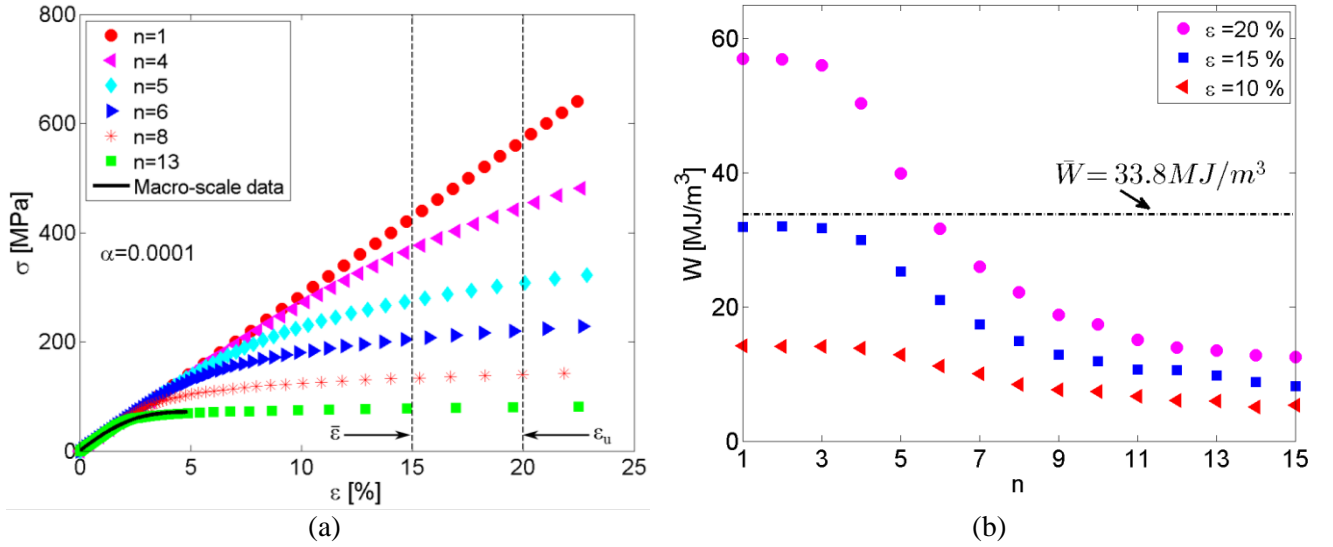


Fig. 8 The notch loaded with  $J = 11.7 \text{ kJ/m}^2$  (a) and the corresponding strains along circular (b) and line paths (c)

Now,  $W$  is determined according to Eq. 2 from the stress-strain curves presented in Fig. 9a, which are acquired fitting the macro-scale stress strain curve of the epoxy resin in tension (Fig. 3) to the Ramberg-Osgood relation given in Eq. 5. The calculated  $W$  values for the stress-strain relations with the strain limits of 15% and 20% as a function of  $n$  are shown in Fig. 9b. In addition,  $\bar{W}$  is given as black dotted line. The power law exponent,  $n$ , is found at the point where  $W$  agrees with  $\bar{W}$ . First, assuming that the strain around the notch is uniform and equal to the maximum strain of 20%, gives that  $n = 6$ , and  $\hat{\sigma}_u$  is approximately 220 MPa. Second, considering a non-uniform strain distribution, thus taking the limiting strain value of 15%, the material behaviour can be characterized as nearly elastic with  $n < 4$  and  $\hat{\sigma}_u$  within the range of 450-580 MPa at  $\varepsilon = 20\%$ .



**Fig. 9** The stress-strain relations with  $n$  within the range of 1-13 for  $\alpha = 0.0001$  (a), and the strain energy density as a function of  $n$  for strain limits of 10%, 15%, and 20% (b)

In the similar way, the  $n$  values are estimated for lower loading steps, i.e. applied  $J < 11.7 \text{ kJ/m}^2$ , and are given in Table 3. At applied  $J = 7.5 \text{ kJ/m}^2$ ,  $n$  is gained around 5, which is comparable with the results presented above. For even lower loadings, however, the match between  $\bar{W}$ , i.e. strain energy around the notch, and  $W$  extracted from the stress-strain curves is not found. In addition, uncertainty of the strain measurements of approximately 1 % is not found to affect results significantly.

**Table 3** Extracted  $n$  values for different applied  $J$  (Test Series 2)

$J_{app}$ [kJ/m <sup>2</sup> ]	$J_{loc}$ [kJ/m <sup>2</sup> ]	$\delta_t$ [μm]	$\bar{W}$ [MJ/m <sup>3</sup> ]	Uniform $\varepsilon$ ( $\varepsilon = \varepsilon_{max}$ )		Non-uniform $\varepsilon$ ( $\varepsilon = \bar{\varepsilon}$ )	
				$\varepsilon_{\theta\theta}$ [%]	$n$	$\varepsilon_{\theta\theta}$ [%]	$n$
12.7	11.7	346	33.8	$20 \pm 1$	6	15	$< 4$
8.1	7.5	308	24.4	$15 \pm 1$	5	11	no fit
5.6	5.3	294	18.0	$10 \pm 0.5$	no fit	7.5	no fit

#### 4.1.2 Permanent strains

An independent check can be made on the stress-strain curves retrieved above by means of the measured permanent strains,  $\varepsilon^p$ . During the DCB tests, the samples are loaded up to certain  $J$  and afterwards unloaded to  $J = 0 \text{ kJ/m}^2$ . Results show that  $\varepsilon^p$  measured in the unloaded state changes almost linearly with  $\varepsilon$  in the loaded state. Moreover,  $\varepsilon^p$  is approximately half of  $\varepsilon$  in the loaded state for the strain components  $\varepsilon_e$  and  $\varepsilon_{\theta\theta}$ , e.g. for  $\varepsilon_e$

= 20% the experimentally measured  $\varepsilon_e^p$  slightly exceeds 10%. From Fig. 9a it can be seen that such large  $\varepsilon^p$  are not expected for the material models with  $n < 4$  as  $\varepsilon^p < 3\%$  for  $\varepsilon = 20\%$ . Thus, these material models are assumed to be inappropriate to characterize the micro-mechanical behaviour of the epoxy resin. And, the first approximation, where the strain is considered to be uniform around the notch and equal to the maximum strain of 20%, fits with the experiments better.

Furthermore, the experimental  $\varepsilon_e$  and  $\varepsilon_e^p$  values are used to construct the stress-strain curve. The strain values are collected from the line paths drawn in front of the notch at  $\theta = 0^\circ$ . For the measurement points with the same index number in the loaded and unloaded state, Eq. 6 is used to extract the stress. Obtained results are shown in Fig. 10 for two loading steps, i.e. for the test samples first loaded up to  $J = 5.3 \text{ kJ/m}^2$  and afterwards unloaded then loaded up to  $J = 11.7 \text{ kJ/m}^2$  and afterwards unloaded. Additionally, the stress-strain curves with  $n = 1$ ,  $n = 5$ ,  $n = 6$ , and  $n = 13$ , also given in Fig. 9a, are included. In Fig. 10 it can be seen that the constructed stress-strain curves are displaced along the  $\varepsilon_e$  axis respectively to the Ramberg-Osgood relations. Moreover, the constructed stress-strain relations acquired from different loading steps are not overlapping (red and green markers in Fig. 10). The reason could be artificial strain created by the out-of-plane displacements (see *Appendix*). For the strain component  $\varepsilon_e$ , the artificial strain of 1% is measured for the displacements along the  $z$ -axis of 300  $\mu\text{m}$ . Moreover, the estimated stresses can be expected slightly overestimated. For instance, assuming that the permanent strains are unaffected by out-of-plane displacements, then the difference between  $\varepsilon_e$  and  $\varepsilon^p$  will increase by 1%. According to Eq. 6, additional strain of 1% will rise the estimated stress by 30 MPa for  $E = 3 \text{ GPa}$ . Including the uncertainties, the epoxy resin seems to be matching with the material models having  $n = [5; 6]$ . Similar stress-strain curve is constructed for the strain component  $\varepsilon_{\theta\theta}$ .

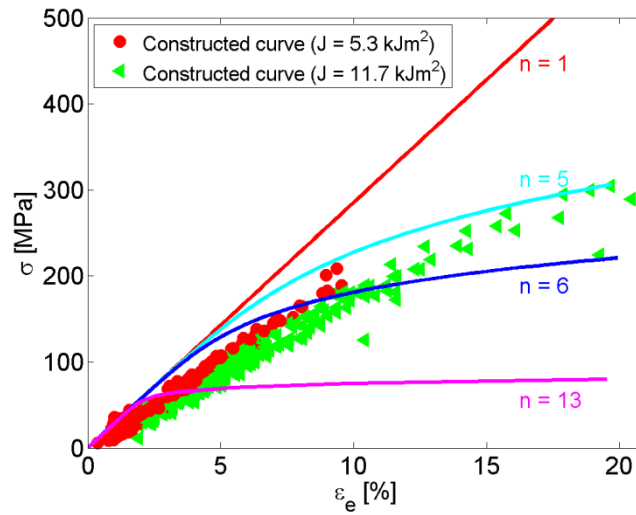


**Fig. 10** The stress-strain curve constructed from the strains in the loaded and unloaded state (Eq. 6)

#### 4.1.3 Cohesive law

Alternatively, the micro-scale failure stress is extracted employing the cohesive law. Summarizing the experimental observations, the test sample failure occurred with the central crack initiation as shown in Fig. 11a. In average, the initiation of the central crack is observed at  $J = 4.9 \text{ kJ/m}^2$ , whereas complete failure is

measured at  $J = 8.5 \pm 0.4 \text{ kJ/m}^2$  for the Test Series 1. Samples from the Test Series 2 are not tested up to failure due to restricted displacement of the fixture. For the sample from the Test Series 1 shown in Fig. 11, the crack has initiated at  $J = 2.4 \text{ kJ/m}^2$  with  $\delta_n^* = 15 \mu\text{m}$  (Fig. 11a), which continued to grow at  $J = 4.9 \text{ kJ/m}^2$  with  $\delta_n^* = 50 \mu\text{m}$  (Fig. 11b), and opening increased further up to  $\delta_n^* = 172 \mu\text{m}$  (Fig. 11c) at  $J = 7.2 \text{ kJ/m}^2$ . Using the cohesive law given in Eq. 7, the failure stress,  $\hat{\sigma}_n$ , is attained of 160 MPa (at the initiation point  $J_R = 0 \text{ kJ/m}^2$  in Eq. 7). It has to be admitted that the failure process given in Fig. 11 seems to be affected by a loading history. Before failure actually took place, the test sample was loaded up to  $J = 4.9 \text{ kJ/m}^2$ , afterwards unloaded and then loaded again up to  $J = 2.4 \text{ kJ/m}^2$  where the crack occurred. It is suggested that some kind of microscopic processes have started at  $J = 4.9 \text{ kJ/m}^2$ , which promoted the failure initiation during re-loading at lower load.

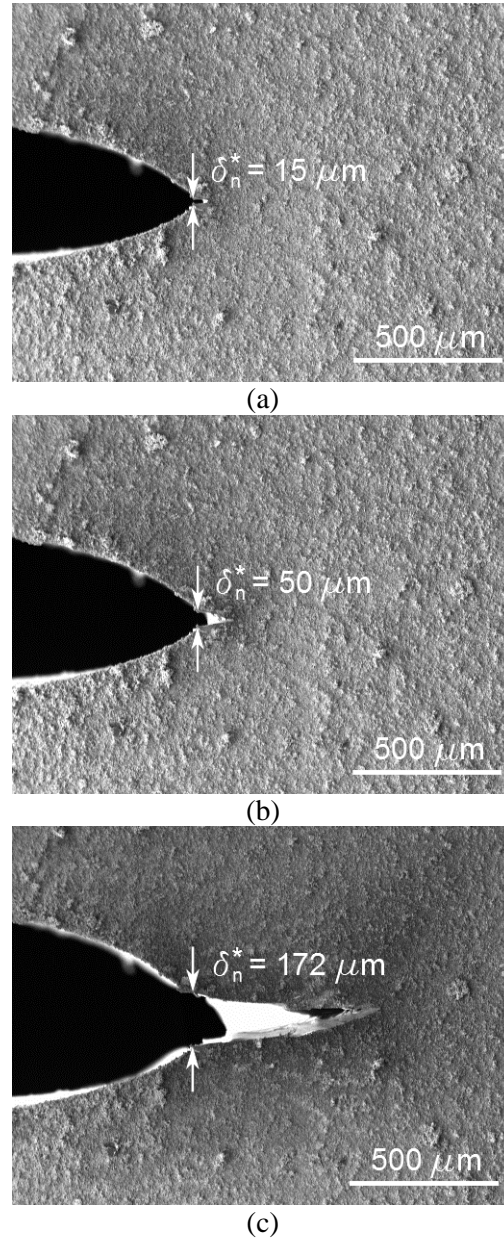


**Fig. 11** The central crack initiation at  $J = 2.4 \text{ kJ/m}^2$  (a), growth at  $J = 4.9 \text{ kJ/m}^2$  (b), and  $J = 7.2 \text{ kJ/m}^2$  (c) for the sample from the Test Series 1 (the surface has speckles)

#### 4.2 Strain fields compared between notches with different notch root radius

Strain fields are compared between the Test series 1 and Test series 2 having an average initial notch width,  $\delta_{to}$ , of 95  $\mu\text{m}$  and 245  $\mu\text{m}$ , respectively. First, similar stress states in front of the notch for both Test Series are determined. According to McMeeking [5], the stress in front of the notch depends on the ratio between the current and initial notch width,  $\delta_t/\delta_{to}$ , which changes linearly with normalized  $J$ ,  $J/\sigma_o\delta_{to}$  (Eq. 9). Following McMeeking's approach, in Fig. 12 the normalized  $J$  integral versus normalized  $\delta_t$  are presented for the Test Series 1 (filled markers) and Test Series 2 (open markers). Results show that for both Test Series  $\delta_t/\delta_{to}$  varies linearly with  $J/\sigma_o\delta_{to}$  and tend to lie on the same curve ( $d_n = 0.3$ ), which indicates that the relation between the normalized displacement and load can be considered as independent of  $\delta_{to}$ . Data points having the same  $\delta_t/\delta_{to}$  and  $J/\sigma_o\delta_{to}$  values between both Test Series are expected to have the same stress around the notch. Thus, according to the results illustrated in Fig. 12, the applied loads giving similar stress state in front of the notch for the Tests Series 1 and Test series 2 are divided into following Load Sets:

1. Load Set 1 ( $J/\sigma_o\delta_o \approx 0.45$ ):  $J = 1.1 \text{ kJ/m}^2$  (Test Series 1) and  $J = 2.5 \text{ kJ/m}^2$  (Test Series 2);
2. Load Set 2 ( $J/\sigma_o\delta_o \approx 0.75$ ):  $J = 2.4 \text{ kJ/m}^2$  (Test Series 1) and  $J = 5.3 \text{ kJ/m}^2$  (Test Series 2);
3. Load Set 3 ( $J/\sigma_o\delta_o \approx 1.6$ ):  $J = 4.9 \text{ kJ/m}^2$  (Test Series 1) and  $J = 11.7 \text{ kJ/m}^2$  (Test Series 2).

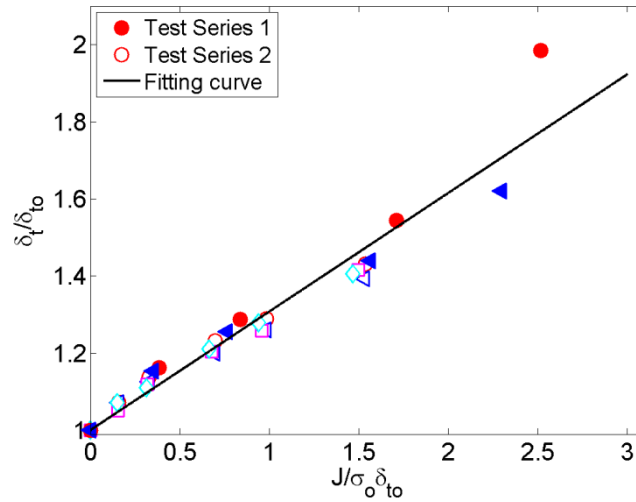


**Fig. 12 The normalized notch opening displacement shown as a function of the normalized  $J$**

Furthermore, within each Load Set the strain fields of the two Test Series are expected to match if the length parameters are normalized with  $\delta_t$  [5]. For instance, in Fig. 13 ( $\blacktriangle$  – sample in Fig. 12) and Fig. 14 ( $\blacktriangleleft$  – sample in Fig. 12) the strain contour plots corresponding to the Load Set 2 are presented for the Test Series 1 and Test Series 2, respectively. In order to illustrate the comparable length scales, the boxes with the edge length equal to  $\delta_t$  are drawn in front of the notch in not normalized coordinate system. One can see that the size of the box is considerably larger for the Test Series 2 and has to be squeezed, in order to compare with the strains in the box of the Test Series 1. In the normalized coordinate system, the boxes for the Test Series 1 and Test Series 2 are equal as in both cases the length of the box edge is  $\delta_t$ .



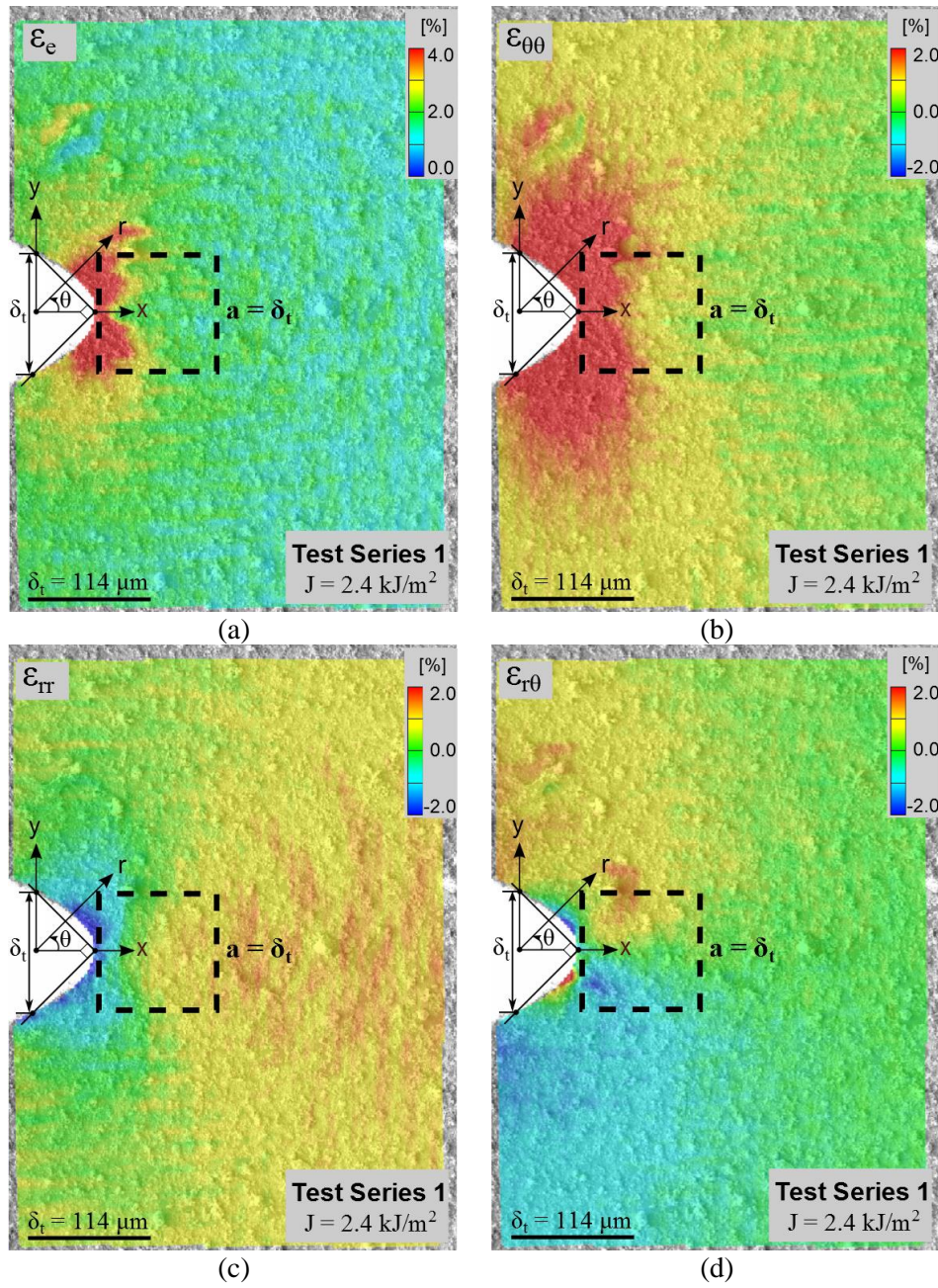
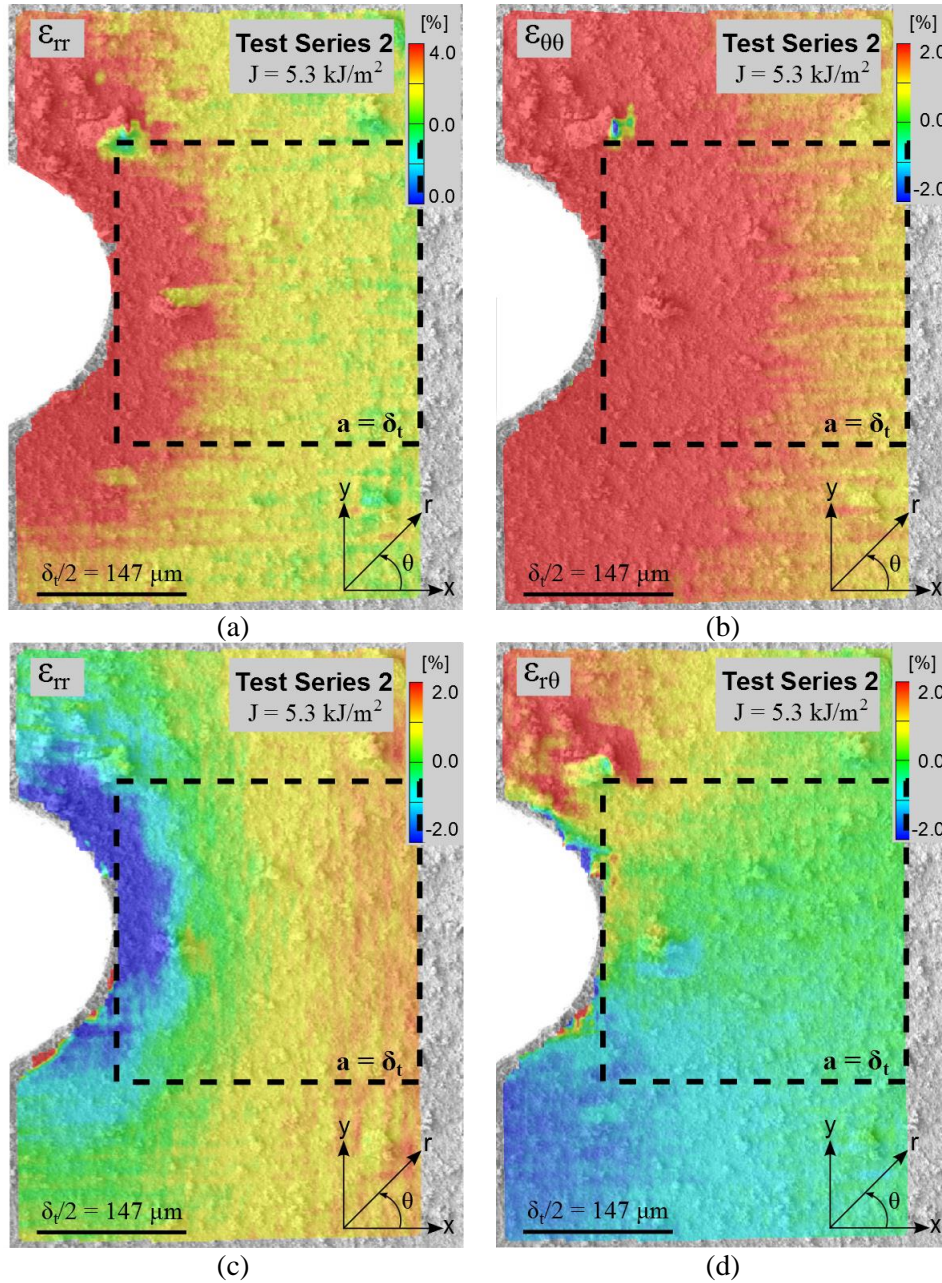


Fig. 13 The strain contour plots for the Test Series 1 at  $J = 2.4 \text{ kJ/m}^2$  (boxes indicate the comparable length scale with the Test Series 2, see Fig. 14)





**Fig. 14** The strain contour plots for the Test Series 2 at  $J = 5.3 \text{ kJ/m}^2$  (boxes indicate the comparable length scale with the Test Series 1, see Fig. 13; the point of origin is out of view)

More detailed strain fields are compared by extracting the strains from circular paths in the vicinity of the notch. Fig. 15 shows the strain variations along a circular path with a normalized radius from the notch centre  $r/\delta_t = 1$  for both Test Series at Load Set 2, i.e. applied  $J = 2.4 \text{ kJ/m}^2$  for the Test Series 1 and  $J = 5.3 \text{ kJ/m}^2$  for the Test Series 2. Presented data are not averaged, and instead the strain values are given for the individual samples. Filled markers correspond to the Test Series 1 and open markers to the Test Series 2, whereas colour indicates the sample within the Test Series. In Fig. 15b small deviations of 1% are observed comparing  $\epsilon_{\theta\theta}$  between both Test Series. Slightly larger variations are attained for  $\epsilon_e$ , whereas a good match is found for  $\epsilon_{rr}$ . In general, the strain fields seem to be comparable between the Test Series at moderate loads (Load Set 1 and Load Set 2), and deviations improve with greater  $J$  values (Load Set 3). Some of the dissimilarities can be listed as

- 1) The values of  $\varepsilon_{\theta\theta}$  and  $\varepsilon_e$  appear smaller for the Test Series 1 than for the Test Series 2 within the same Load Sets and at the same normalized distance (Fig. 15b,d);
- 2) The strain peaks of  $\varepsilon_{\theta\theta}$  are less profound for the Test Series 2 as the strain drop at  $\theta \approx 0^\circ$  is larger for the Test Series 1 (Fig. 15b);
- 3) The angle corresponding to the maximum value of  $\varepsilon_{\theta\theta}$  is larger for the Test Series 2, e.g. the maximum strain peak appears at  $\theta \approx 55^\circ$  and  $\theta \approx 45^\circ$  for the Test Series 2 and Test Series 1, respectively;
- 4) The strain variations of  $\varepsilon_{r\theta}$  are somewhat more disturbed in the range of  $\theta \approx \pm 30^\circ$  at  $r/\delta_t = 1$  for the Test Series 2 (Fig. 15c). Disturbances are significantly reduced for both Test Series with a larger distance from the notch ( $r/\delta_t > 1$ ).

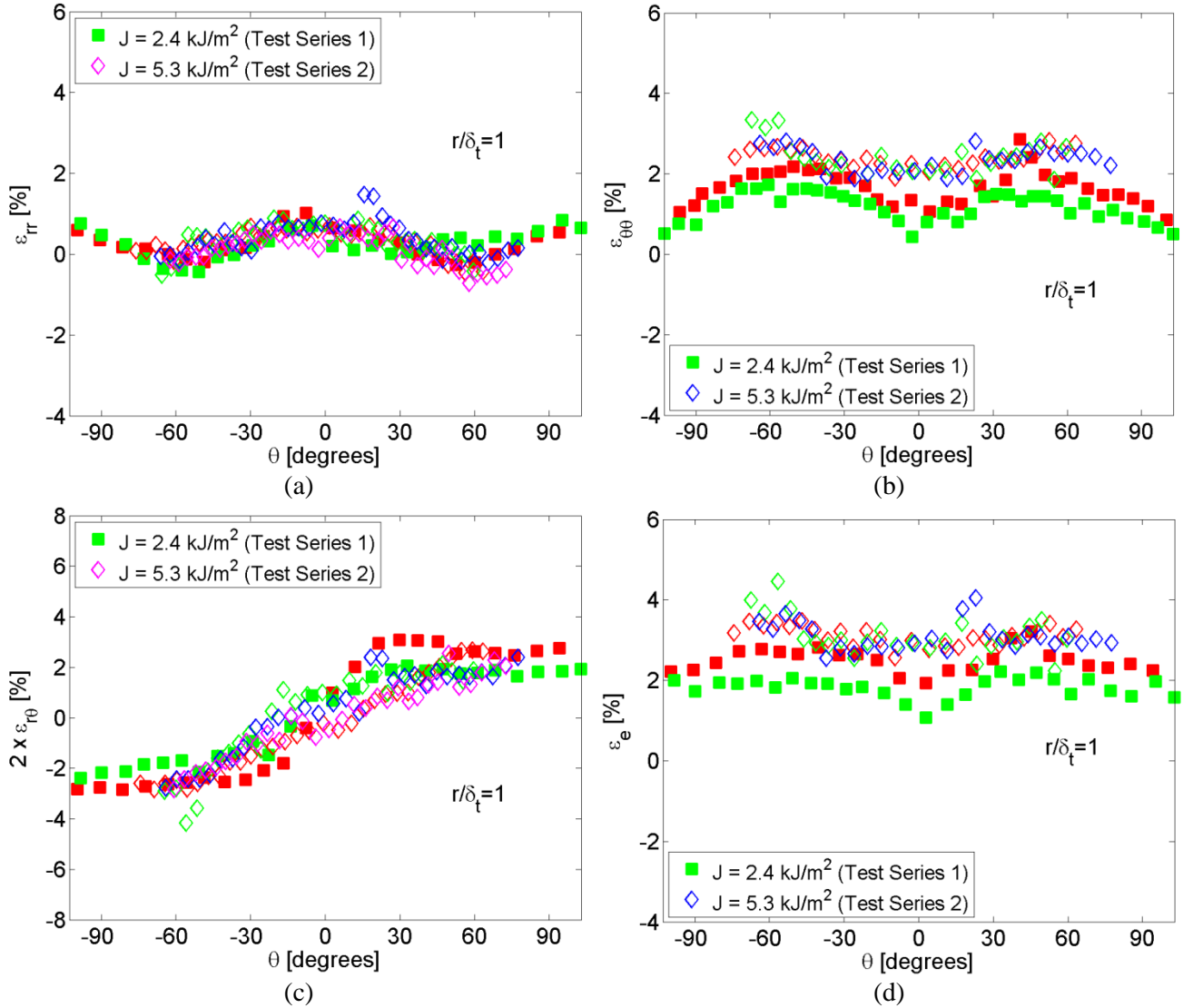


**Fig. 15** The strain component  $\varepsilon_{rr}$  (a),  $\varepsilon_{\theta\theta}$  (b),  $\varepsilon_{r\theta}$  (c), and  $\varepsilon_e$  (d) variations with an angle around the notch at  $r/\delta_t = 1$  within the Load Set 2

### 4.3 Strain field characterization

#### 4.3.1 Global strain fields

The contour plots of the strain fields around the deformed notches for the Test Series 1 are given in Fig. 16a-c and Test Series 2 in Fig. 16d-f at  $J \approx 5 \text{ kJ/m}^2$  recorded at magnification  $\times 100$ . The strain distribution is similar



for both Test Series with positive  $\varepsilon_{\theta\theta}$  (Fig. 16a,d) and negative  $\varepsilon_{rr}$  (Fig. 16b,e) in the front of the notch tip. The value of the strain component  $\varepsilon_{\theta\theta}$  is highest at the tip and decline with increasing a distance from the notch, whereas the strain component  $\varepsilon_{rr}$  has its lowest value (negative) in front of the notch and becomes positive with increasing the distance from the notch tip. In addition, a compressive region of  $\varepsilon_{rr}$  diminishes with an initiation of the central crack, similar to that shown in Fig. 11. The strain component  $\varepsilon_{r\theta}$  is dominating around the notch edge sides (Fig. 16c,f) and is asymmetric around the notch. Whereas the strains,  $\varepsilon_{rr}$  and  $\varepsilon_{\theta\theta}$ , both spread symmetrically about  $y = 0$ . Such symmetries are anticipated for the symmetric test samples loaded symmetrically. The  $\varepsilon_e$  values vary similarly to  $\varepsilon_{\theta\theta}$  (Fig. 13a and Fig. 14a). Observing the strain variations around the notch at larger magnification of x500 for the Test Series 1 (Fig. 13), the distribution of  $\varepsilon_e$ ,  $\varepsilon_{\theta\theta}$ , and  $\varepsilon_{rr}$  appears to have a butterfly shape, which is hidden at the magnification x100. The dissimilarity between the strain measurements attained from the images recorded at lower and higher magnification seems to be due to different spatial resolution (subsection 3.6 and *Appendix*).

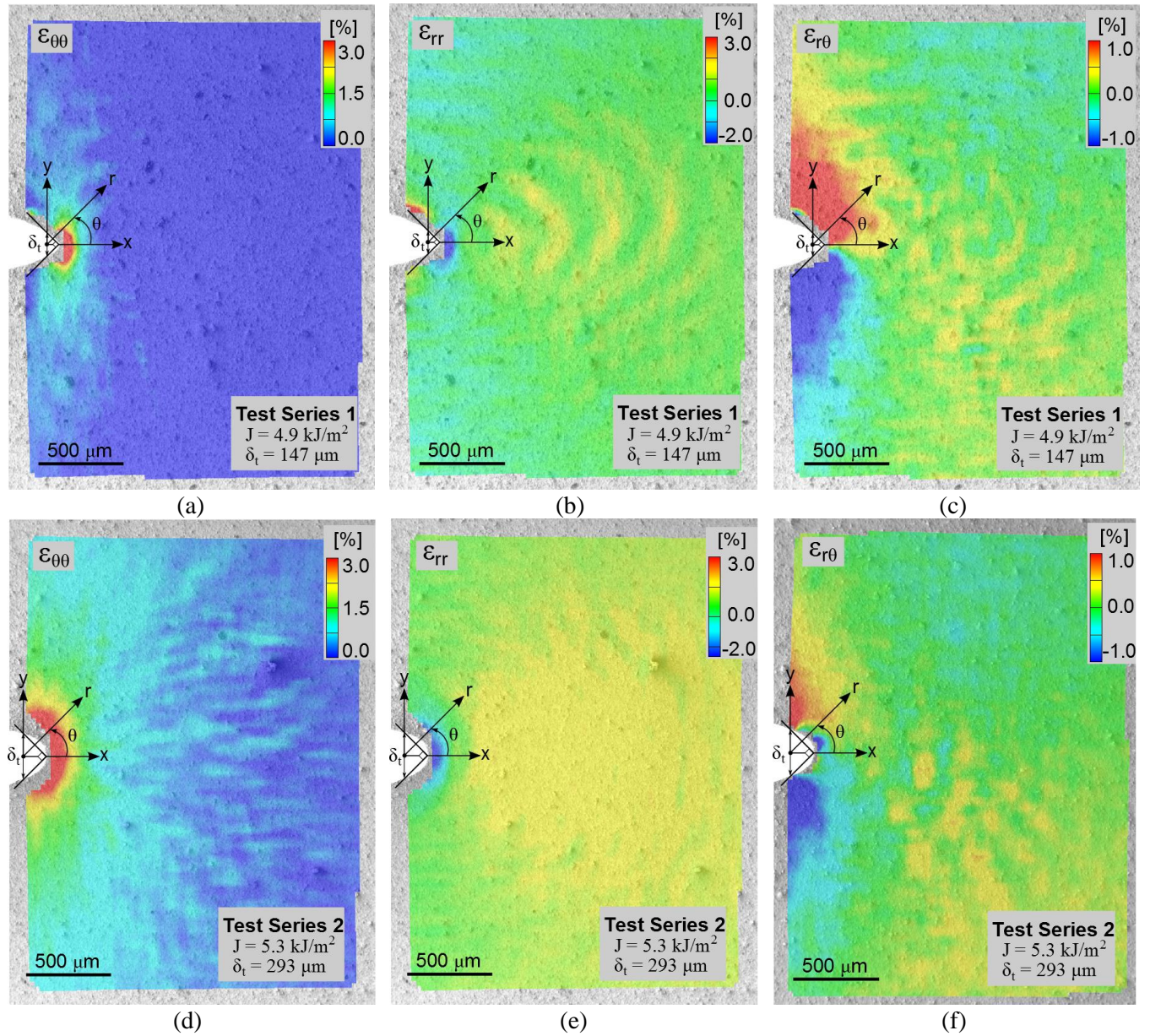


**Fig. 16** The strain contour plots for the Test Series 1 (a-c) and Test Series 2 (d-e) captured at magnification x100

#### 4.3.2 The strain variations with an angle around the notch at different normalized distances

The  $\varepsilon_{\theta\theta}$  variations with an angle around the notch at different normalized distances  $r/\delta_t$  for the sample from the Test Series 1 with  $\delta_t = 104 \mu\text{m}$  for  $J = 1.1 \text{ kJ/m}^2$  are presented in Fig. 17a. Data are acquired from a circular path drawn around the notch using images recorded at magnification x500. Results are presented for small applied  $J$  to avoid the effect of the material micro-cracks evolving from the notch edge at higher loads. At the distance  $r/\delta_t = 0.8$ , it is seen that starting from  $\theta = -90^\circ$ ,  $\varepsilon_{\theta\theta}$  increases with  $\theta$  until a maximum is attained at  $\theta \approx -30^\circ$ . After the maximum, the strain component  $\varepsilon_{\theta\theta}$  declines and reaches minimum at  $\theta = 0^\circ$ . The strain  $\varepsilon_{\theta\theta}$  appears to be symmetric about  $\theta = 0^\circ$ , since the second maximum is reached at  $\theta \approx 30^\circ$ . Results show that the angle of the maximum  $\varepsilon_{\theta\theta}$  value varies from  $\theta \approx \pm 30^\circ$  at the distance  $r/\delta_t = 0.8$  to  $\theta \approx \pm 60^\circ$  at  $r/\delta_t = 1.5$  (Fig. 17b) and  $\theta \approx \pm 90^\circ$  for  $r/\delta_t = 4.0$ . Similar but less profound strain variations are also observed for the Test Series 2, i.e. the  $\varepsilon_{\theta\theta}$  maximums are found at  $\theta \approx \pm 45^\circ$  at the normalized distance  $r/\delta_t = 0.8$  and approach  $\theta \approx \pm 90^\circ$  at  $r/\delta_t = 3.0$ .

Furthermore, the strain variations around the notch for all three strain components, i.e.  $\varepsilon_{rr}$ ,  $\varepsilon_{\theta\theta}$ , and  $\varepsilon_{r\theta}$ , for  $J \approx 5 \text{ kJ/m}^2$  at the normalized distance  $r/\delta_t = 2$  are shown in Fig. 17b. Data are attained at magnification x100. As it was apparent from the contour plots in Fig. 16,  $\varepsilon_{rr}$  and  $\varepsilon_{\theta\theta}$  are symmetric and  $\varepsilon_{r\theta}$  asymmetric about  $\theta = 0^\circ$ . Moreover, from Fig. 17b follows that the angle of the  $\varepsilon_{\theta\theta}$  maximum tends to agree with the  $\varepsilon_{rr}$  minimum and vice versa. Thus, the angle of the minimum  $\varepsilon_{rr}$  value varies similarly to the maximum  $\varepsilon_{\theta\theta}$  value with various distances from the notch. In addition, likewise to  $\varepsilon_{rr}$  and  $\varepsilon_{\theta\theta}$ , the angle of the maximum and minimum value of  $\varepsilon_{r\theta}$  changes with increasing the distance from the notch, i.e. at  $r/\delta_t = 0.7$  the strain peaks are observed at  $\theta = \pm 20^\circ$  and at  $r/\delta_t = 4$  the angle increases up to  $\theta = \pm 100^\circ$ . In Fig. 17b  $\varepsilon_{rr}$  and  $\varepsilon_{\theta\theta}$  overlap at  $\theta = 0^\circ$  what is coincidence as they neither agree for smaller nor larger normalized distances, e.g. the strain  $\varepsilon_{rr}$  opposite to  $\varepsilon_{\theta\theta}$  increases for  $r/\delta_t > 2.0$  at  $\theta = 0^\circ$ .

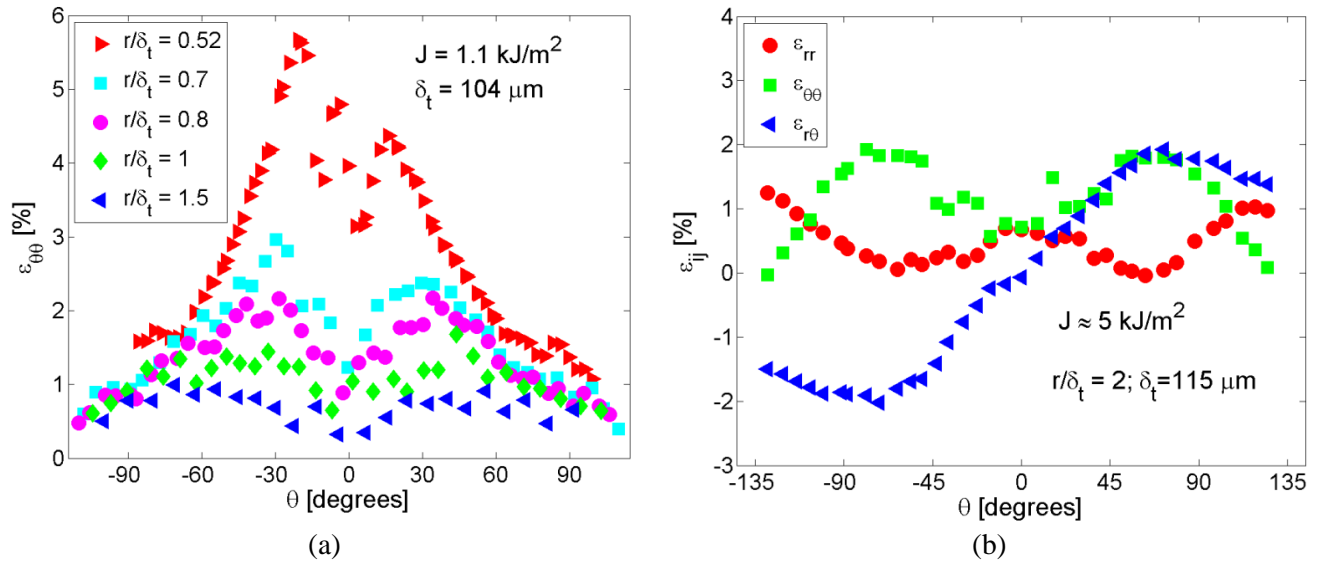


**Fig. 17** The  $\varepsilon_{\theta\theta}$  variations with an angle around the notch for various distances  $r/\delta_t$  from the notch tip (a); the variations of all strain components with an angle around the notch at  $r/\delta_t = 2$  (b) (results are presented for the Test Series 1)

Moreover, the strain variations along the radial position  $r/\delta_t$  at the fixed angle with an applied  $J$  are acquired by drawing line paths both parallel ( $\theta = 0^\circ$ ) and inclined ( $\theta = 30^\circ$ ) to the  $x$ -axis. Fig. 18 shows  $\varepsilon_{\theta\theta}$  and  $\varepsilon_{rr}$  as a function of the normalized distance  $r/\delta_t$  for  $J$  within the range of 1.2-11.7 kJ/m<sup>2</sup>. At the normalized distance  $r/\delta_t < 1$ , the variations of  $\varepsilon_{\theta\theta}$  become more distinct with an applied load approaching the strain values of 15-20% (Fig. 18a,b). Slightly different observations are done for  $\varepsilon_{rr}$  presented in Fig. 18c,d. The strain component  $\varepsilon_{rr}$  along the path  $\theta = 0^\circ$  lies close to zero except in the vicinity of the notch edge, i.e. at the notch edge,  $r/\delta_t = 0.5$ ,  $\varepsilon_{rr}$  is lower than -10%.

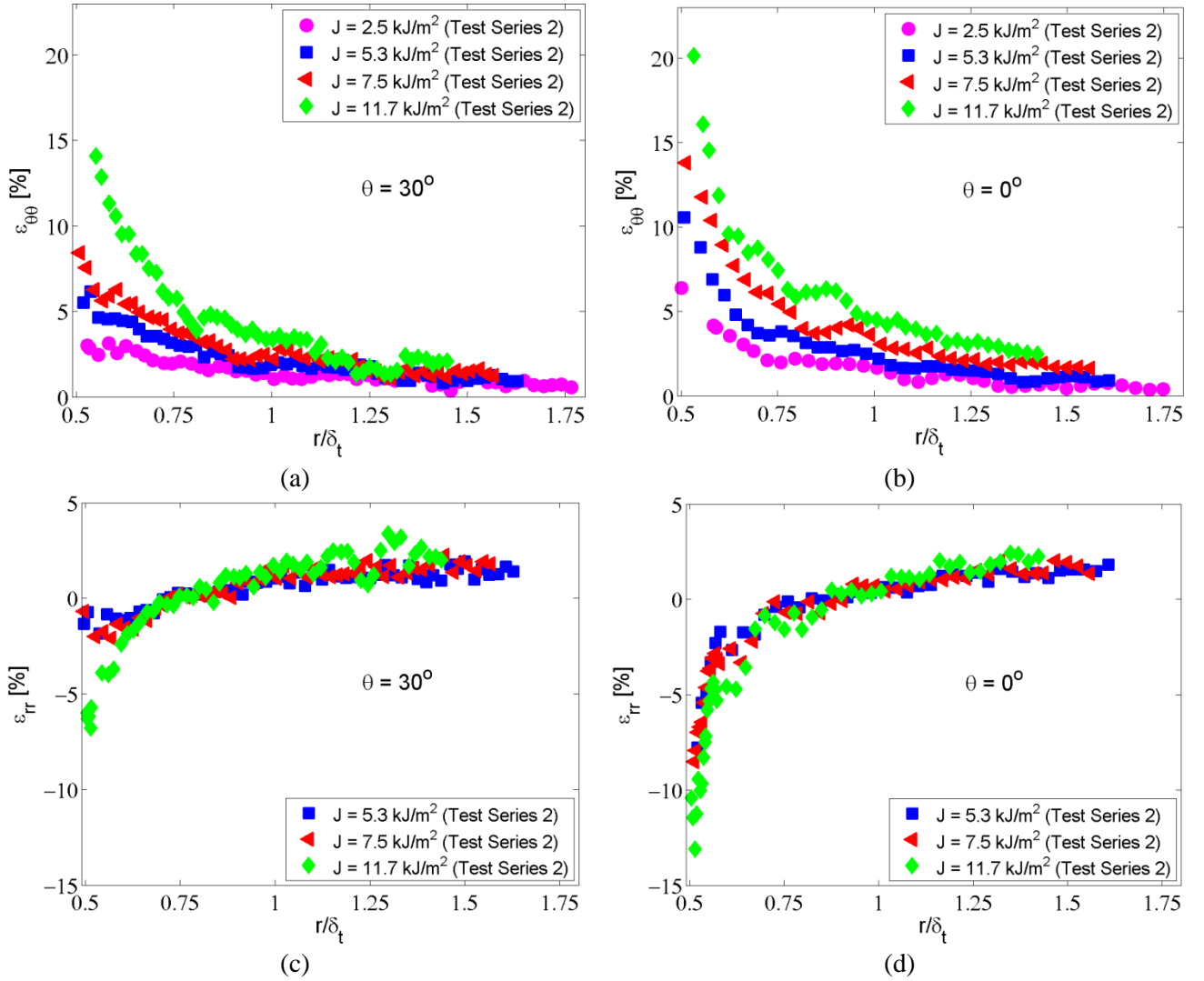


**Fig. 18** The strains along the line paths for  $\varepsilon_{\theta\theta}$  at  $\theta = 30^\circ$  (a) and  $\theta = 0^\circ$  (b), as well for  $\varepsilon_{rr}$  at  $\theta = 30^\circ$  (c) and  $\theta = 0^\circ$  (d)

#### 4.4 Overview of plastic deformation, damage initiation, and crack formation

A general overview of principal features of plastic deformation, damage initiation and failure are given below. Performing the DCB test without speckles a few small fine cracks both parallel and inclined respectively to the  $x$ -axis are observed in the front of the notch at relatively low applied  $J$  ( $J < 2.4$  kJ/m<sup>2</sup>). The density of these micro-cracks increases with larger applied load. Accordingly to Bradley [27], the formation of these fine micro-cracks is related to the gold coating cracking caused by increasing deformation in the material below the coating. For instance, in Fig. 19 multiple fine cracks next to the severely damaged notch with a central



crack are shown at two different magnifications. From the image captured at lower magnification (Fig. 19b), it is apparent that the net of fine cracks continues even beyond the central crack indicating the size of the region of non-linear material deformation [27]. In Fig. 19 the test samples were initially tested with speckles, which were afterwards removed with ultrasound, thus the dark and white spots visible in Fig. 19 are related to the peeled off gold coating and remaining of speckles, respectively.

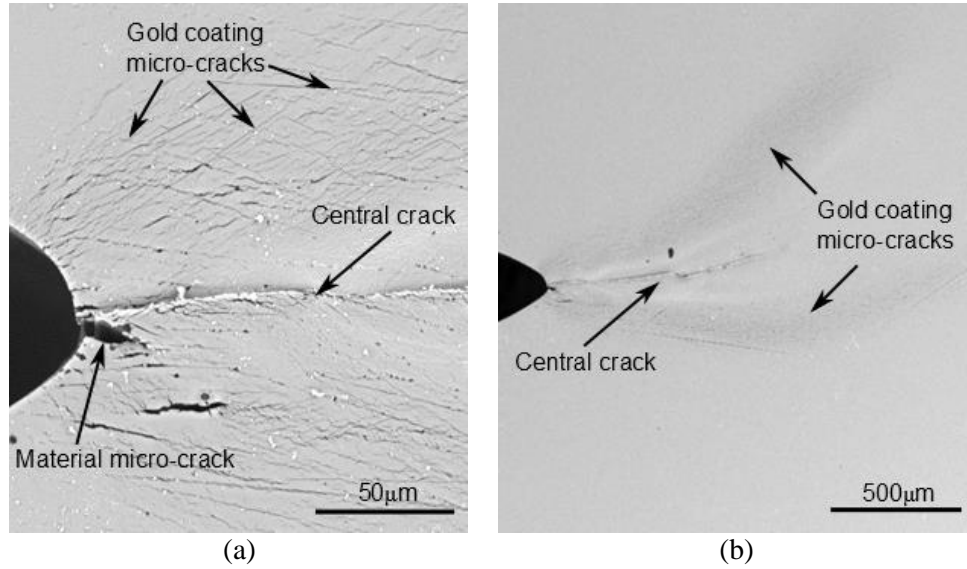


**Fig. 19 The damaged surface around the notch for the sample from the Test Series 1 in the unloaded state after applied  $J = 7.2 \text{ kJ/m}^2$  at magnification x1000 (a) and x100 (b) (the surface without speckles)**

For applied  $J > 2.4 \text{ kJ/m}^2$ , fine gold coating micro-cracks proceed to formation of micro-cracks in the polymer material evolving from the notch edge as shown in Fig. 19a. These material micro-cracks similarly to the gold coating cracks appear as surface openings both parallel and inclined respectively to the  $x$ -axis, but are deeper and wider. The micro-cracks in the polymer material appear at the sides of the notch with the mean angle of  $33 \pm 7^\circ$  respectively to the notch centre. The micro-crack length is measured up to  $60 \text{ }\mu\text{m}$ , most are around  $25 \text{ }\mu\text{m}$  with a total damage area within the range of  $50\text{-}100 \text{ }\mu\text{m}$  for the Test Series 2 at  $J = 11.7 \text{ kJ/m}^2$ . The results presented above are retrieved from the images of the damaged surface without speckles in the unloaded state. Furthermore, up to the failure initiation, the material micro-cracks extend with an applied moment, but become still with the formation of the central crack at the tip of the notch. For instance, in Fig. 19a an inclined material micro-crack close to the notch tip can be observed, which initiated at  $J \approx 2.4 \text{ kJ/m}^2$  but was suppressed by the growth of a central crack at  $J \approx 5 \text{ kJ/m}^2$ . The micro-cracks in the polymer material are not observed to promote the subsequent formation of the central crack. The appearance of the central crack is found to indicate the failure initiation of the polymer material. The samples from the Test Series 1 failed at the mean  $J = 8.5 \pm 0.4 \text{ kJ/m}^2$ , whereas samples from the Test Series 2 were not tested up to failure due to restricted displacement of the fixture.

## 5 Discussion

### *The micro-mechanical properties of the epoxy resin*

Our measurements confirm the expectations that at the micro-scale failure strain and stress are significantly larger than the failure strain and stress at the macro-scale. The micro-scale measurements show that just prior to failure initiation the strain components  $\varepsilon_{\theta\theta}$  and  $\varepsilon_{rr}$  reach 20% and -15% at the notch edge, respectively. Moreover, the micro-scale failure stress,  $\hat{\sigma}_u$ , is estimated in the range of 220-300 MPa employing analytical and empirical approaches.

Analytically, two independent methods of the strain energy density determination were used to extract the stress-strain relation and the failure stress,  $\hat{\sigma}_n$ . Results show that if the strain around the notch is assumed to be uniform and equal to the maximum strain, then the epoxy resin fits with the material model with  $n \approx [5; 6]$ , including different loading steps. Actual strain variations around the notch, however, were non-uniform. When  $W$  is extracted from the stress-strain curves for different power law hardening material models, the limiting strain values are taken from the experimental measurements on the test sample surface. At the same time,  $\bar{W}$  acquired from the relation between  $J$  and  $\delta_t$  represents the strain energy density around the notch averaged through the thickness. Even though this introduced uncertainty in the analytical approach, the results seem to be consistent with an empirical approach.

Empirically, the stress-strain relation was constructed from the strain measurements in the loaded and unloaded state (permanent strains). Results show that the constructed stress-strain curves can be related with the power law hardening material with  $n \approx 5$ , which gives  $\hat{\sigma}_u$  of 300 MPa. Results, however, seem to be biased by the out-of-plane displacements and possibly non-linear unloading. The out-of-plane displacement of 300  $\mu\text{m}$  creates artificial strain of 1% for the strain component  $\varepsilon_e$ . As a result, this would translate the constructed stress-strain curves along the  $\varepsilon_e$  axis. Moreover, the stresses can be expected to be slightly overestimated assuming that the measurements in the loaded state are more significantly affected by the out-of-plane displacements. For the measurement error of 1%, the estimated stresses would be increased by 30 MPa (Eq. 6). On the other hand, contraction close to the notch can be expected to reduce the effect of the out-of-plane displacements. Prior to failure, assuming the strain along the  $y$ -axis is 20% and  $\nu = 0.4$ , contraction could reach 160  $\mu\text{m}$ . Additionally, it has been reported [28] that the epoxy resin possesses some non-linearity during unloading. Since the stiffness tends to decline during unloading, the stresses in the constructed stress-strain curve could be overestimated. Considering uncertainties of this empirical approach, the epoxy resin is assumed to fit with the power law hardening materials having  $n = [5; 6]$ , and  $\hat{\sigma}_u$  is within the range of 220-300 MPa. Additionally, employing the cohesive law,  $\hat{\sigma}_u$  was acquired of 160 MPa. These values, however, seem to be affected by a loading history.

### *Strain field comparison between notches with various notch root radii*

At moderate loadings, the strain variations agree closely between the Test Series with an initial width of 95  $\mu\text{m}$  (Test Series 1) and 245  $\mu\text{m}$  (Test Series 2) normalizing the  $x$  and  $y$  coordinates with  $\delta_t$  [5]. Some minor

differences were observed as the strains seem to be slightly lower, the strain peaks were more profound, and the angle at which the maximum strain was measured was smaller for the Test Series 1. Moreover, discrepancies between the Test Series improved with an applied load. It is suggested that, at the normalized distance  $r/\delta_t = 1$ , the strain fields are somewhat affected by the notch geometry. This agrees with the numerical study by Zike [22], where similar discrepancies of the strain fields between the Test Series were attained for linear-elastic material. Summarizing, this approach seems to be suitable for comparing the strain fields between the test samples with different notch width at moderate loads. In a not normalized coordinate system, the strain fields appear to be greatly unlike.

#### *Characterization of the strain fields around the notch*

According to the HRR theory [6,7], the strain around the crack tip can be described as a product of two components (Eq. 8). The first component is related to the amplitude, and the second to the strain variations with an angle around the notch. The second component is expected to be unique for material if the HRR region prevails, and independent of both the distance from the crack tip,  $r$ , and applied loading  $J$ . Moreover, we assumed that the strain fields around the notch can be described in the same way as around the sharp crack if the length parameters are normalized with  $\delta_t$  [5]. In our experimental results, the strain variations with an angle were found to change with a distance from the notch centre, e.g. the maximum of  $\varepsilon_{\theta\theta}$  translates from  $\theta = \pm 30^\circ$  at  $r/\delta_t = 0.6$  to  $\theta = \pm 90^\circ$  at  $r/\delta_t = 4$ , and  $-\varepsilon_{rr} = \varepsilon_{\theta\theta}$ . Likewise, changes  $\varepsilon_{r\theta}$  reaching the largest angle of the strain maximum of  $\theta \approx 90^\circ$  at  $r/\delta_t = 4$ . At the notch edge, the strain component  $\varepsilon_{\theta\theta}$  was dominating, whereas for  $r/\delta_t > 2$  the strain components  $\varepsilon_{\theta\theta}$ ,  $\varepsilon_{rr}$ , and  $\varepsilon_{r\theta}$  showed similar amplitude. Results seem to deviate from those numerically derived by Hutchinson [29] in the agreement with the HRR theory. Discrepancies can be expected to be due to the notch geometry as it is not entirely semi-circular. Other reason can be that the evolution of the strain fields in the plastic zone is not uniquely controlled by the HRR field. This can be the case if the assumption of a small plastic zone (in comparison with specimen dimensions) is not met.

## **6 Conclusions**

Mechanical behaviour of the epoxy resin was found to depend on the length scale, i.e. failure strain and strength vary at macro- and micro- scale. Macroscopically, the failure strain of the epoxy resin has been reported in the range of 5-6%, and the failure strength in the range of 72-86 MPa. In our micro-mechanical study, the failure strain reached 20% at the notch edge with the corresponding failure stress within the range of 220-300 MPa. This gives that the strength of the epoxy resin at micro-scale is about 3 to 4 times larger than the strength at the macro-scale. Therefore, implementation of the macroscopic stress-strain relation in micro-mechanical models appears to be insufficient, and the microscopically measured stress and strain values are the one that should be used in micro-mechanical models, e.g. the peak stress of the cohesive law representing material fracture.

Furthermore, the strain fields of the test samples with dissimilar initial notch root radii were found comparable under moderate loadings. To compare the strain fields, the length parameters have to be normalized with the notch opening displacement,  $\delta_t$ , for the loadings giving the same stress in front of the notch. The equivalent



stress states can be found from the relationship between the normalized notch opening displacement,  $\delta_i/\delta_{io}$ , and normalized  $J$  integral,  $J\sigma_o/\delta_{io}$ .

## Acknowledgments

This research was supported by the Danish Centre for Composite Structure and Materials for Wind Turbines (DCCSM), grant no. 09-067212, from the Danish Strategic Research Council (DSF). The authors would like to thank Christian H. Madsen for assistance with test sample preparation and Erik Vogeley for help with the test set up.

## References

- [1] P. Brøndsted, H. Lilholt, A. Lystrup, Composite materials for wind power turbine blades, *Annu. Rev. Mater. Res.* 35 (2005) 505–538.
- [2] B.F. Sørensen, J.W. Holmes, P. Brøndsted, K. Branner, Blade materials, testing methods and structural design, in: *Wind Power Gener. Wind Turbine Des.*, WIT press, 2010: pp. 417–466.
- [3] L.E. Asp, L.A. Berglund, P. Gudmundson, Effects of a composite-like stress state on the fracture of epoxies, *Compos. Sci. Technol.* 53 (1995) 27–37.
- [4] GOM, ARAMIS software, (n.d.). <http://www.gom.com/3d-software/aramis-software.html>.
- [5] R.M. McMeeking, Finite deformation analysis of crack-tip opening in elastic-plastic materials and implications for fracture, *J. Mech. Phys. Solids.* 25 (1977) 357–381.
- [6] J.W. Hutchinson, Plastic stress and strain fields at a crack tip, *J. Mech. Phys. Solids.* 16 (1968) 337–342.
- [7] J.R. Rice, G.F. Rosengren, Plane strain deformation near a crack tip in a power-law hardening material, *J. Mech. Phys. Solids.* 16 (1968) 1–12.
- [8] J.W. Hutchinson, Fundamentals of the phenomenological theory of nonlinear fracture mechanics, *J. Appl. Mech.* 50 (1983) 1042–1051.
- [9] J. Rice, A path independent integral and the approximate analysis of strain concentration by notches and cracks, 35 (1967) 379–386.
- [10] W. Ramberg, W.R. Osgood, Description of stress-strain curves by three parameters, *Natl. Advis. Comm. Aeronaut.* (1943).
- [11] A. Hillerborg, M. Modéer, P.-E. Petersson, Analysis of crack formation and crack growth in concrete by means of fracture mechanics and finite elements, *Cem. Concr. Res.* 6 (1976) 773–781.
- [12] A. Hillerborg, Application of the fictitious crack model to different types of materials, *Int. J. Fract.* 51 (1991) 95–102.
- [13] B.F. Sørensen, Cohesive laws for assessment of materials failure: Theory, experimental methods and application, Risø DTU, 2010.
- [14] C.F. Shih, Relationships between the  $J$ -integral and the crack opening displacement for stationary and extending cracks, *J. Mech. Phys. Solids.* 29 (1981) 305–326.
- [15] S. Zike, L.P. Mikkelsen, Mechanical characterization of the epoxy polymer matrix with an application to pressure dependent material model, Unpublished. (n.d.).
- [16] S. Zike, B.F. Sørensen, L.P. Mikkelsen, DCB Test Sample Design for Micro-Mechanical Testing, in: *19th Int. Conf. Compos. Mater. (ICCM 19)*, Montreal, 2013.

- [17] B.F. Sørensen, A. Horsewell, O. Jørgensen, A.N. Kumar, P. Engbæk, Fracture resistance measurement method for in situ observation of crack mechanisms, *J. Am. Ceram. Soc.* 81 (1998) 661–669.
- [18] Beckman Coulter, Laser diffraction particle size analyzer, (n.d.). <https://www.beckmancoulter.com>.
- [19] Airbrush BossDye-132, (n.d.). <http://www.co-import.dk/16350228>.
- [20] ZEISS, Environmental scanning electron microscope, (n.d.). [http://www.zeiss.com/microscopy/en\\_de/products/scanning-electron-microscopes/evo-materials.html](http://www.zeiss.com/microscopy/en_de/products/scanning-electron-microscopes/evo-materials.html) (accessed April 28, 2015).
- [21] T.L. Anderson, *Fracture Mechanics: Fundamentals and Applications*, 1995.
- [22] S. Zike, *Micro-Scale Experiments and Models for Composite Materials with Materials Research* (Thesis), Technical University of Denmark, 2015.
- [23] M.A. Sutton, J.J. Orteu, H.W. Schreier, *Image Correlation for Shape, Motion and Deformation Measurements- Basic Concepts, Theory and Applications*, 2009.
- [24] B. Pan, K. Qian, H. Xie, A. Asundi, Two-dimensional digital image correlation for in-plane displacement and strain measurement: a review, *Meas. Sci. Technol.* 20 (2009) 062001.
- [25] M.A. Sutton, N. Li, D. Garcia, N. Cornille, J.J. Orteu, S.R. McNeill, et al., Metrology in a scanning electron microscope: theoretical developments and experimental validation, *Meas. Sci. Technol.* 17 (2006) 2613–2622.
- [26] F.P. Beer, R.E. Johnston, Transformations of stress and strain, in: *Mech. Mater.*, McGraw-Hill Book Company, 1992: pp. 339–400.
- [27] W.L. BRADLEY, Chapter 5 - Relationship of Matrix Toughness to Interlaminar Fracture Toughness, in: *Appl. Fract. Mech. to Compos. Mater.*, 1989: pp. 159–187.
- [28] H.S. Da Costa Mattos, S.D.A. Martins, Plastic behaviour of an epoxy polymer under cyclic tension, *Polym. Test.* 32 (2013) 1–8. doi:10.1016/j.polymertesting.2012.08.009.
- [29] J.W. Hutchinson, *Nonlinear Fracture Mechanics*, Technical University of Denmark, 1979.
- [30] F. Lagattu, F. Bridier, P. Villechaise, J. Brillaud, In-plane strain measurements on a microscopic scale by coupling digital image correlation and an in situ SEM technique, *Mater. Charact.* 56 (2006) 10–18.
- [31] H. Wang, H. Xie, Y. Ju, Q. Duan, Error analysis of digital speckle correlation method under scanning electron microscope, *Exp. Tech.* 30 (2006) 42–45.
- [32] M. Sjö Dahl, Accuracy in electronic speckle photography., *Appl. Opt.* 36 (1997) 2875–2885.

## List of symbols and abbreviations

$a$	notch root length (Fig. 4)
$d_n$	parameter indicating the slope of $\delta_t$ versus $J$ (Eq. 10 and Eq. 9)
$d_p$	particle diameter (subsection 3.6)
$f$	facet size (subsection 3.6)
$h$	width of the DCB test specimen beam (Fig. 4)
$n$	hardening exponent (Eq. 5)
$l$	field of view (subsection 3.6)
$p$	facet step (subsection 3.6)
$r$	radius drawn from the notch centre (Fig. 2)
$s$	arc length along contour $\Gamma$ (Eq. 1)
$u$	displacement vector (Eq. 1)
$A$	area of the cross section (section 1)
$B$	thickness of the DCB test sample (Fig. 4)
DCB	double cantilever beam (subsection 3.4)
DIC	digital image correlation (subsection 3.6)
$E$	elastic modulus (Fig. 3)
ESEM	environmental scanning electron microscope (subsection 3.5)
$F_u$	failure load at the macro-scale (section 1)
$J$	$J$ integral as a loading parameter (Eq. 11)
$L_o$	initial gauge length (section 1)
$M$	moment (subsection 3.4)
$M_T$	magnification factor (subsection 3.6)
$N$	recording resolution (subsection 3.6)
$T$	traction vector (Eq. 1)
$W$	strain energy density (subsection 2.1, Eq. 2)
$\bar{W}$	averaged $W$ around the notch (subsection 2.1, Eq. 4)
$\alpha$	material constant (Eq. 5)
$\delta_n^*$	normal opening of the crack faces (section 1, Fig. 11)
$\delta_t$	notch/crack opening displacement (Fig. 2, Eq. 10, and Eq. 9)
$\delta_{to}$	initial notch width (determined for initially un-deformed notch in the same way as $\delta_t$ )
$\varepsilon$	strain
$\varepsilon_e$	von Mises strain (subsection 3.7, Eq. 15)
$\varepsilon^p$	permanent strain (Fig. 3, Fig. 10)
$\varepsilon_{rr}$	radial strain (subsection 3.7, Eq. 12)
$\varepsilon_{r\theta}$	angular shear strain (subsection 3.7, Eq. 14)
$\varepsilon_{\theta\theta}$	angular strain (subsection 3.7, Eq. 13)
$\varepsilon_o$	elastic strain (Fig. 3)
$\varepsilon_u$	failure strain at the micro-scale (section 1)
$\tilde{\varepsilon}_u$	failure strain at the macro-scale (section 1)
$\theta$	angle
$\nu$	Poisson's ratio (Eq. 11)
$\sigma$	stress
$\hat{\sigma}_n$	failure stress at the micro-scale (section 1)
$\sigma_o$	yield stress (Fig. 3)
$\tilde{\sigma}_u$	failure stress at the macro-scale (section 1)
$\Gamma$	integration path for the J-integral, a curve/contour encircling the crack tip (Eq. 1)
$\Delta L$	elongation (section 1)

## Appendix: The accuracy of DIC measurements

The test sample surface is observed to undergo brightness and contrast changes during the DCB test. The lightning variations are evaluated increasing the brightness of still image by 10 %, 20 %, and 30 %. The strain measurements are attained to be unaffected by the brightness, and negligible increase of a standard deviation is measured, i.e.  $\varepsilon = 0.00 \pm 0.05$  %. Further, contrast changes are related to the displacements in the  $z$ -axis direction (out-of-plane), which depend on the applied moment, and are approximately 100-300  $\mu\text{m}$ . The displacements are estimated comparing focus changes between initial and deformed image. In order to evaluate the effect of the displacement along the  $z$ -axis, the out-of-plane rigid body displacement tests are performed. The non-zero strains are measured for all strain components. The most sensitive is found to be the effective strain,  $\varepsilon_e$ . For the strain components  $\varepsilon_{\theta\theta}$  and  $\varepsilon_{rr}$ , artificial strains are not exceeding 0.42 %, and minor strains are measured for  $\varepsilon_{r\theta}$ . Results for different magnifications,  $M_G$ , are summarized in Table 4.

**Table 4 Strains variations in the rigid body in-plane and out-of-plane displacement test**

Displacement [ $\mu\text{m}$ ]	$f$ [pixels <sup>2</sup> ]	$p$ [pixels]	$M_G$	$\varepsilon_e$ [%]	$\varepsilon_{\theta\theta}$ [%]	$\varepsilon_{rr}$ [%]	$\varepsilon_{r\theta}$ [%]
$\Delta x = 25$	60 x 60	5	x 500	$0.17 \pm 0.08$	$0.00 \pm 0.11$	$0.00 \pm 0.10$	$0.00 \pm 0.07$
$\Delta x = 25$	45 x 45	3	x 500	$0.31 \pm 0.15$	$0.00 \pm 0.23$	$0.00 \pm 0.20$	$0.00 \pm 0.15$
$\Delta x = 100$	60 x 60	5	x 100		$0.00 \pm 0.11$	$0.00 \pm 0.11$	$0.00 \pm 0.08$
$\Delta z = 100$	60 x 60	5	x 500	$0.35 \pm 0.16$	$-0.15 \pm 0.14$	$-0.14 \pm 0.14$	$-0.01 \pm 0.10$
$\Delta z = 200$	60 x 60	5	x 500	$0.61 \pm 0.26$	$-0.26 \pm 0.22$	$-0.27 \pm 0.21$	$-0.02 \pm 0.15$
$\Delta z = 300$	60 x 60	5	x 500	$1.02 \pm 0.50$	$-0.37 \pm 0.44$	$-0.42 \pm 0.44$	$-0.01 \pm 0.31$

In addition, to evaluate possible errors due to distortions and in-plane displacements ( $x$ - $y$  plane), the in-plane rigid body displacement tests are performed. According to the references [25,30,31], distortions are caused by electromagnetic field fluctuations, time shift between scan lines, heating, charging of the SEM stage or sample, and environmental factors (e.g. thermal fluctuations, mechanical vibrations, air currents, etc.). During the DCB test, displacements along the  $y$ -axis are measured up to 30  $\mu\text{m}$  and 150  $\mu\text{m}$  for the results acquired at magnification x500 and x100, respectively. Similar displacements are used to perform the in-plane displacement tests. Results show that the strain components are rather insensitive to in-plane displacements, and distortions are not found to affect the measurements, see also Table 4. The only non-zero values are measured for  $\varepsilon_e$ , which seems to be the most sensitive strain component to any displacements.

### *The effect of measurement parameters*

According to Sutton et al. [23], in order to have an accurate matching during DIC analysis, speckles should be sampled by a 3 by 3 pixel array. Therefore, the minimum particle diameter,  $d_p$ , should be 1.8  $\mu\text{m}$  and 9  $\mu\text{m}$  for magnification x500 and x100, respectively. The required  $d_p$  partly overlaps with the particle size used in this study as according to measurements done by laser diffraction [18] particle size is within the range of 0.05-3  $\mu\text{m}$ . Apart from the laser diffraction measurements, the microscope images show the presence of even larger particles ( $d_p > 3$   $\mu\text{m}$ ). Moreover, according to Sutton et al. [23], the facet size,  $f$ , should contain at least 9-10 speckles, i.e.  $f \geq 5.4$   $\mu\text{m}$  and  $f \geq 27$   $\mu\text{m}$  for magnification x500 and x100, respectively. Practically, the minimum theoretical face size, which gives the highest spatial resolution, was impossible due to high noise level and decorrelation. Even though, with larger facets the spatial resolution is reduced, the accuracy and the

noise reduction is improved [32]. In this study, the images of the test sample surface are divided into facets with a length of 45-60 pixels ( $f = [26 \mu\text{m}; 177 \mu\text{m}]$ , see Table 2) and a distance between the centre points of the adjacent facets is set to 3-5 pixels ( $p = [3 \mu\text{m}; 15 \mu\text{m}]$ , see Table 2). The facet step is mainly responsible for how densely the facets are packed. More densely packed facet array will give more measurement points within the measurement area. At the same time, too much densely packed array can lead to higher measurement error as the area shared between adjacent facets is increased. In this study, the overlap between the adjacent facets is within the range of 92-93 %. Relatively far from the notch, neither the facet size nor the facet step, within the range given above, is affecting the measurements, i.e. only the variations of the measurement noise are observed. Slightly different situation is near the notch edge. Smaller facet step and facet size, first, make the strain variations around the notch more distinct (more profound strain peaks); second, close to the notch tip (at the distances smaller than  $20 \mu\text{m}$  from the notch tip), the strain values rise. In this study, the facet size and facet step is chosen as a compromise between sufficiently high spatial resolution, sufficient number of measurement points, fast computation time and low noise level.

#### *The effect of magnification*

The strain measurements are observed to vary with the magnification, at which the images are recorded. The strains acquired from the images captured at magnification x500 and x1000 agree with each other, and are slightly in disagreement with the measurements gained from the images captured at magnification x100. The disagreement is particularly evident for the Test Series 1 as shown in Fig. 20. Results show that the strain peaks are less profound, and the numerical values of strain are increasing using images recorded with the magnification x100. Discrepancies are related to the differences in the spatial resolution (see Table 2). Hence, in this study, the images recorded at the magnification x500 are preferred, which are found as a compromise between sufficiently large field of view and high spatial resolution.

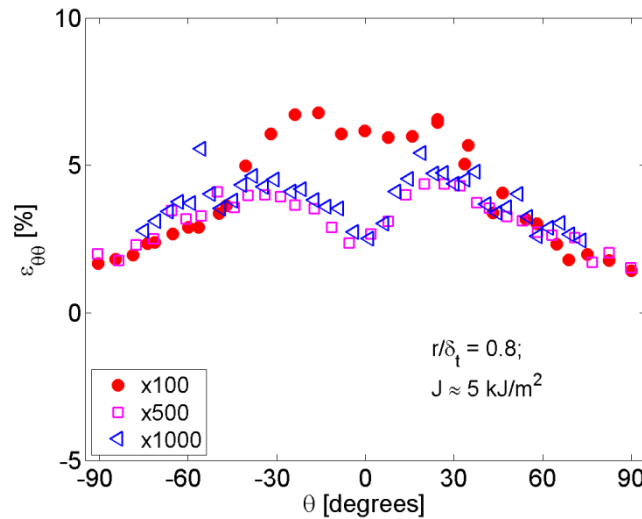


**Fig. 20 Strains obtained from the images recorded at various magnifications for the Test Series 1**

Publication [P4]

# DCB Test Sample Design for Micro-Mechanical Testing

# DCB TEST SAMPLE DESIGN FOR MICRO-MECHANICAL TESTING

S. Zike, L. P. Mikkelsen, B. F. Sørensen

Composites and Materials Mechanics Section, Department of Wind Energy, Technical University of Denmark, Risø Campus, Roskilde, Denmark

\* Corresponding author ([zike@dtu.dk](mailto:zike@dtu.dk))

**Keywords:** *DCB testing, micro-mechanical testing, polymer fracture, polymer modeling*

## 1. Introduction

Application of composite materials based on polymer matrix and inorganic fibers is continuously increasing in high performance structures such as airplanes, wind turbines etc. Further development and improvement of structural performance is highly dependent on understanding of damage initiation and damage evolution in composite materials. An overview of composite material failure affected by micro-scale processes as fracture both in matrix and fiber, fiber-matrix de-bonding, pull-out of fibers etc. is discussed by Kim and Mai [1].

Damage evolution at micro-scale can be evaluated combining micro-mechanical testing *in situ* with visual observation methods as optical and electron microscope. Some review papers regarding micro-mechanical testing are given by Hemker and Sharpe [2], and Srikar and Spearing [3]. An example of micro-mechanical testing with *in situ* visual observation methods for polymer matrix based composites is given by Schoßig et al. [4]. These authors conduct micro-tension tests for polymer/glass fiber composites in an environmental scanning electron microscope (ESEM) in order to correlate visually observed damage with the signals of acoustic emission.

A comprehensive study on fracture testing in micro-scale utilizing double cantilever beam (DCB) specimens subjected to pure bending inside ESEM is done by Sørensen et al. [5–8]. They present stable crack growth in ceramics and composite materials enabling *in-situ* observations of crack growth mechanisms and material toughness variations.

The aim of this study is to determine the optimal DCB test specimen configuration for polymer materials for micro-mechanical testing inside optical

microscope and ESEM. The optimal specimen design is found by conducting numerical parameter study with finite element method (FEM) code. For the fracture analysis the J integral is used [9], since this approach is valid to analyze an onset of crack growth of non-linear materials [10]. A parameter variation of DCB test specimens is done accordingly to requirements and restrictions listed in section 2.

## 2. DCB test requirements and restrictions

The design of DCB test specimen requires finding the balance between DCB fixture restrictions, material properties and conditions of reliable fracture parameter determination. The specimen design is done as a pre-study for experimental testing of samples made of thermoset and thermoplastic material, respectively, with properties defined in Table 1.

Experimental setup requires to operate with DCB test fixture described by Sørensen et al. [7] Fixture restricts specimen dimensions to 70 x 10 x 5 mm<sup>3</sup> as it is shown in Fig. 1. The total deflection of specimen is limited to 15 mm and the minimum crack length is  $> 12+1$  mm.

Regarding fracture parameter determination following requirement are set:

### 1. Pure bending

Pure bending is considered to be a prerequisite to ensure stable crack growth under constant test rate, what allows determination of actual material toughness properties. In the case of unstable crack growth, fracture parameters will be related to crack initiation and more sensitive to initial conditions as pre-crack sharpness. This can lead to determination of fracture parameters,



which are significantly higher than actual material fracture resistance [7], [11].

## 2. Sufficiently high J integral values

The specimen design should be such that the J integral values are high enough to induce crack growth. Polymer materials tend to exhibit tough behavior, thus relatively high J integral values can be needed. In addition, the effect of yielding around the crack tip on the J integral determination is evaluated.

## 3. Stress free rear end

A stress free rear end in the test sample is required to consider the J integral independent on the crack length. In addition, stresses at the rear end are used to evaluate the bending.

## 4. No buckling

During the DCB tests, the crack tip is experiencing tension and a field with compression exists further ahead in the uncracked part of the test sample. This study is focused on soft and relatively thin materials with thickness in range of 0.75 – 1 mm. Based on these assumptions, initially, it is expected that specimens could be prone to buckling in compression dominated area.

# 3. Methods

## 3.1 Computational model

A 3D model is created to mimic the experimental set-up for Mode I DCB fracture test described by Sørensen et al. [7] using the commercial FEM code *ABAQUS*. Fig. 2 shows the corresponding numerical model of the DCB test specimen. The specimen is divided into two parts: sample and sample holder beams, also noted as skins. Parts are defined as linear-elastic and elastic-plastic.

A crack is created by partitioning sample in the middle and nodes of partitioned area are separated by assigning seams. The J integral value is determined at the crack tip by averaging 3<sup>rd</sup>-5<sup>th</sup> contour values.

Bending moment in the model is created applying two concentrated forces ( $F$ ) pointed in opposite directions along x direction and equally applied to each skin. The force is equally distributed along the

width of the skin introducing constraints (*equation constraints*). In addition, the linear perturbation testing procedure is set to predict buckling load during the DCB test.

Boundary conditions are set to restrict skins movement in z direction, the test sample surface at the rear end in y direction and the middle point of the same surface in x direction.

A reference point with kinematic constraints is set at the upper corner of the skin beam in order to measure deflection in x axis direction. The total deflection is the sum of deflections experienced by both skin beams.

A structured mesh is used for skins and sweep mesh is used for sample with an eight node linear brick elements including reduced integration and hourglass control.

## 3.2 Parameter study

A parameter study is conducted to design the DCB test specimen for polymer material testing. The study is focused on two specific samples one made of thermoset and another from thermoplastic material with properties listed in Table 1. Therefore to satisfy in section 2 listed requirements and restrictions for the DCB test specimen, following parameters are varied:

- 1) Elastic modulus of skin ( $E_{skin}$ );
- 2) Thickness ( $t_{skin}$ ) and width ( $h_{skin}$ ) of skin;
- 3) Width of sample ( $h_{sample}$ );
- 4) Crack length ( $L_{crack}$ ).

# 4. Results

Results of the DCB test specimen design for polymer materials are summarized in the following steps:

- 1) Design of skins;
- 2) Determination of appropriate crack length;
- 3) Estimation of compression stresses at the rear end;
- 4) Evaluation of yielding around the crack tip;
- 5) Buckling analysis.

## 4.1 Design of skins

The sample holders are included in the DCB test specimen configuration to control the stress field around the crack tip, to limit the beam deflection and

rotation, and also to ensure the test sample is subjected to pure bending. Results regarding skin design are mostly focused on determining appropriate skin material stiffness, because variations of geometrical dimensions are very much limited by the available DCB test fixture [7].

#### 4.1.1 J integral determination

First the effect of skin stiffness on the J integral value is evaluated. In Fig. 3 the J integral values are shown as a function of the elastic modulus of skin material ( $E_{skin}$ ) for both samples made of thermoset and thermoplastic material. In addition, FEM results are compared with analytical J integral calculations for the DCB test specimens provided by Goutianos et al. [8], [11].

In Fig. 3 obtained results show that the J integral value is decreasing with stiffer skin material. Moreover, in certain range almost linear correlation between the J integral and the elastic modulus of skin material exist. This is true for specimens with relatively much stiffer skins than sample, whereas implementing softer skins deviation from linearity is observed. Deviation is more pronounced for the thermoset sample, which is stiffer and has initial elastic modulus 3 GPa. Similarly, deviations increase for wider and thicker samples. Numerical results are found to be in a good agreement with analytical model provided by Goutianos et al. [11].

In order to ensure that crack growth occurs, the J integral value ( $J_c$ ) for thermoset sample should be around 0.1-1 kJ/m<sup>2</sup> and for thermoplastic sample around 20 kJ/m<sup>2</sup> [12]. In Fig. 3 results indicate that for the thermoplastic sample the elastic modulus of skin material should be below 4 GPa, to obtain desired J integral values if skin dimensions are 70 x 4 x 3 mm<sup>3</sup> and applied load is 75 N. In the case of the thermoset sample, selection of skin material is less critical due to stiffer sample material and much lower J integral values, thus a skin with stiffness up to 70 GPa can be used.

#### 4.1.2 Limitations of deflection

Second the effect of skin stiffness on the total deflection is evaluated. Usage of soft skins is limited by the maximum allowable deflection (15 mm) by the DCB test fixture. Fig. 4 presents numerical results of the DCB test specimen deflection variations with product of elastic modulus and

moment of area of skins ( $I_{skin}$ ) when maximum load 75 N is applied. Results also include the effect of crack length for 6 mm wide ( $h_{sample}$ ) thermoplastic sample using 3 mm thick ( $t_{skin}$ ) and 4 mm wide ( $h_{skin}$ ) skins -  $I_{skin} = 9 \text{ mm}^4$ .

The results in Fig. 4 demonstrate that the total deflection is reduced linearly with stiffer skins, i. e. with larger product of  $I_{skin}$  and  $E_{skin}$ , and shorter crack. To satisfy the restrictions of the DCB test fixture the product of  $E_{skin}$  and  $I_{skin}$  should be at least 25 GPa·mm<sup>4</sup> and 100 GPa·mm<sup>4</sup> for 19 and 34 mm long crack ( $L_{crack}$ ), respectively. Accordingly to results in Fig. 4, the elastic modulus of skin for the thermoplastic sample should be at least 2.8 GPa and 10 GPa for  $L_{crack} = 19 \text{ mm}$  and  $L_{crack} = 34 \text{ mm}$ , respectively. The thermoset sample is much stiffer and in both cases does not exceed the deflection limitations.

#### 4.2 Crack length

In subsection 4.1., it was shown that the requirement of sufficiently high J integral value and the restrictions of deflection can be fulfilled choosing appropriate crack length. In this subsection, the J integral value variations with the crack length are discussed in order to determine the range of the crack length, which allows stable crack growth and is independent on the sample length and test fixture configuration.

In Fig. 5 the normalized J integral is shown as a function of the crack length for the specimens with different ratio of sample and skin stiffness. Initially a 1 GPa stiff, 6 mm wide and 70 mm long sample is chosen. Normalized J integral is calculated dividing numerically obtained J integral values with analytically determined using model provided by Goutianos et al. [8], [11]. The crack length is varied from 14 to 60 mm. The minimum allowable crack by the DCB test fixture is 12+1 mm.

From Fig. 5 it can be seen that the normalized J integral is constant and equal to 1 in the certain range of the crack length. This distance is enclosed by the minimum and the maximum crack length, where the normalized J integral starts to deviate from one. The minimum crack length for the specimen with the skin stiffness 1 GPa, i.e.  $E_{sample}/E_{skin} = 1$ , is found at  $L_{crack}/L_{sample} = 0.39$ , i.e. the crack length is approximately 27 mm. The total

deviation of the normalized J integral at  $L_{\text{crack}} = 14$  mm is around 5 %. The minimum crack length is not found for the specimens with relatively stiff skins as 20 GPa and 200 GPa in the prescribed crack length region.

Significantly larger deviations from 1 are observed increasing the crack length above the maximum value. The obtained maximum crack length is in the range of 35 mm to 57 mm depending on the skin material stiffness. For the specimens with 200 GPa stiff skins, the maximum crack length is obtained at shorter distance, i.e. 35 mm, whereas the length of maximum crack increases implementing softer skins. The largest maximum crack length is obtained for the specimen with 1 GPa stiff skins.

### 4.3 Compression stresses at the rear end

Compression stresses develop in a region ahead of the crack tip. It is considered that less the skins will deflect the larger area of crack free region in the test sample will be subjected to compression. Therefore, initially, it is expected that for very stiff skins as 200 GPa, the specimens will not be subjected to pure bending as the test samples are relatively soft and will not provide sufficient resistance needed to bend the skin beams.

In Fig. 6 the length of the compression zone is shown as a function of the elastic modulus of the skin material for an applied load of 15 N. The results are obtained for 4 mm wide samples using skins with dimensions  $70 \times 3 \times 3 \text{ mm}^3$ . Numerical results present that thermoplastic samples will be more compressed comparing to thermoset sample using the skins with the same stiffness. For example, implementing 10 GPa stiff skins the compression zone size for thermoplastic sample is 40 % and for thermoset sample 25 % from total crack free region. Further increasing the skin material stiffness to 200 GPa, compression zone enlarges to 70 % and 47 % from total crack free region for thermoplastic and thermoset sample, respectively. In addition, it is seen that compression region distances from the crack tip with stiffer skin material.

### 4.4 Evaluation of yielding around the crack tip

The effect of yielding around the crack tip on the J integral determination is assessed for specimens with  $E_{\text{skin}} = 3 \text{ GPa}$  and skin beam dimensions  $70 \times 3$

$\times 3 \text{ mm}^3$ . Skins in both samples ensure sufficiently high J integral value and fulfill the restrictions of deflection implementing 19 mm long crack. Evaluation is done comparing three material configurations as listed below:

- 1) *Elastic-elastic*, where the linear-elastic material properties are used both for sample and skin. The “size of plastic zone” is evaluated solely on the elastic strain contour.
- 2) *Plastic-elastic*, where the plastic yielding of the sample material is included and the skins remain elastic.
- 3) *Plastic-plastic*, where the plastic deformation of the sample and the skin material is included. Thus the effect of the test sample and the skin material yielding on the J integral assessment is evaluated.

In Fig. 7 the J integral variations with the deflection for different material formulations are presented for the thermoset sample. The results show that the yielding of the sample and the skin material does not affect the J integral determination up to  $J = 1 \text{ kJ/m}^2$  with the total deflection 2 mm. The deviations tend to increase with increasing the deflection. For instance, the difference between the J integral value obtained by the elastic-elastic and the plastic-plastic material formulation is approximately  $0.5 \text{ kJ/m}^2$  for the total deflection 3 mm. The size of plastic zone is not found to be affected by the plastic deformation of the skin and the test sample material if  $J = 1 \text{ kJ/m}^2$ . The length of the plasticity zone around the crack tip is 1.5 mm both in the direction of the crack tip and transverse to it.

A similar approach is used to evaluate the effect of yielding on the J integral determination for the thermoplastic sample. In Fig. 8 it is shown that for the thermoplastic material the J integral variations with deflection using the elastic-elastic and the plastic-plastic material formulation coincidence up to  $J = 5\text{--}7 \text{ kJ/m}^2$ . Large deviations are observed at critical J integral value -  $J = 20 \text{ kJ/m}^2$  [12]. The numerically determined plasticity zone size is 9.5 mm if  $J = 20 \text{ kJ/m}^2$  for 4 mm wide sample. A widening of the sample till 10 mm slightly increase the J integral values, nevertheless the plasticity zone is still spread along the whole width of test sample.

#### 4.5 Buckling analysis

Buckling analysis is conducted for both thermoplastic and thermoset sample in order to predict the sample buckling during DCB test. In addition, numerical results are compared with Euler beam buckling predictions.

##### 4.5.1 Euler buckling

Euler buckling stress is determined for the crack free region assuming both ends are pinned. Skin properties are not included in calculations. The Euler buckling stress is found to be 3.2 MPa if  $E_{sample} = 250$  MPa,  $t_{sample} = 0.75$  mm and width is 6 mm. The buckling stress value is increased up to 7.2 MPa if the width is reduced to 4 mm. Significantly higher buckling stress values as 38 MPa are obtained for the thermoset sample with  $E_{sample} = 3$  GPa,  $t_{sample} = 1$  mm and  $h_{sample} = 6$  mm.

##### 4.5.2 Numerically determined buckling

Numerically obtained buckling results are shown in Fig. 9 for 6 mm wide thermoplastic sample. Both the buckling load and the maximum stress at the first stable buckling mode are shown as function of the skin stiffness in the range of 1-200 GPa. Buckling threshold equals to the maximum load allowable by DCB test fixture – 75 N.

In Fig. 9 results indicate that the buckling of sandwich type DCB test specimen is significantly affected by the skin stiffness. Usage of stiffer skins leads to larger buckling loads and lower compression stresses in the crack free region. Results show that to avoid the buckling in thermoplastic sample the elastic modulus of the skins should be above 3 GPa. In Fig. 9 the Euler buckling stress is included for this sample, which is approximately 4 times lower than the numerically determined if the test sample with 2 GPa stiff skins is considered.

In the range of skin stiffness 1-200 GPa no buckling is observed neither for the thermoplastic sample with  $h_{sample} = 4$  mm nor the thermoset sample with  $h_{sample} = 4$  mm and  $h_{sample} = 6$  mm.

Additionally, in Fig. 10 the first stable buckling mode is shown for 6 mm wide thermoplastic sample with 3 GPa stiff skins. It is observed that with increasing stiffness of the skin material, the buckled area widens and tends to move away from the crack

tip, therefore if  $E_{sample} = 0.25$  GPa and  $E_{skin} = 200$  GPa buckling will occur at the end of the crack free region of test sample.

#### 5. Discussion

##### 5.1 Skin selection

Results in Fig. 3 and Fig. 4 show that the stiffness of skins highly affects the stress concentration at the crack tip and also the deflection of specimen beams. Softer skins promote higher stress localization close to the crack tip leading to higher J integral values. With increasing skin stiffness, the compression region increases, thus stresses tend to be more delocalized, and the values of the maximum compression stress and the J integral value are reduced, see Fig. 5.

In Fig. 3 for stiff skins linear relation between J integral and elastic modulus of the skins can be observed. Deviations from the linear correlation between the J integral and the skin stiffness are observed reducing the elastic modulus of skin. Deviations from linearity become more pronounced for stiffer, wider and thicker sample, thus sample properties more significantly start to affect total bending of outer beams.

Besides larger J integral values, the implementation of soft skins leads to larger deflections, which then can be reduced by shortening the crack as shown in Fig. 4. Two lengths of crack are compared showing that for thermoplastic sample the 19 mm long crack is preferable as deflection restrictions are satisfied. The thermoset sample is much stiffer and in both cases does not exceed the deflection limitations.

To satisfy both requirements of sufficiently high stresses at the crack tip and deflection restrictions, it is proposed that for thermoplastic sample with skin dimensions  $70 \times 4 \times 3$  mm<sup>3</sup>  $E_{skin}$  should be in the range of 2.8 - 4 GPa. Thus skins made of polymer materials, e.g. made of epoxy, are suggested.

##### 5.2 Crack length limitations

In Fig. 5 the effect of crack length on the J integral determination is presented. The range of optimal crack length, when J integral value is not affected by the sample dimensions and the crack tip is loaded under pure bending, is confined by minimum and maximum crack length. Inside this region, the

normalized J integral value is constant and equal to one. The deviations below the minimum crack are considered to be small comparing to the values above the maximum crack length. Furthermore, it is found that the maximum crack is shorter for specimens with stiffer skin material, and also the range of the constant J integral value is reduced. These observations are explained with more localized stresses, and thus smaller compression area in the uncracked part of sample, using soft skins, see Fig. 6.

## 5.2 Yielding at the crack tip

The plastic deformation of the test sample and the skin material is included to evaluate the effect of yielding on the J integral determination. No effect of plastic deformation on the J integral value is observed for the thermoset sample up to  $1 \text{ kJ/m}^2$ , see Fig. 7. The same J integral values are obtained using elastic and elastic-plastic material formulation both for the skin and the test sample. Thus the effect of yielding around the crack tip for thermoset sample is considered to be small.

Considerably different results are attained for the thermoplastic sample shown in Fig. 8. Defining the test sample and the skin as a linear-elastic material the critical J integral  $20 \text{ kJ/m}^2$  is achieved at total deflection 14 mm. Including the plastic deformation of the sample and the skin J integral values are reduced to half for the same deflection. The plasticity zone is found to be 9.5 mm long if  $J = 20 \text{ kJ/m}^2$  and sample width 4 mm. Moreover, widening the sample till 10 mm is not sufficient to reduce the effect of plastic deformation. In both cases, the observed plasticity zone exceeds the test sample width.

## 5.3 Buckling

Numerical results presented in Fig. 10 show the local type of buckling what is largely affected by the utilized skins. Stiffer skins tend to delocalize stresses and therefore increase required load to induce buckling. Applying skins with elastic modulus  $E_{skin} = 3 \text{ GPa}$ , what satisfies requirement of high stress concentration at the crack tip and the restrictions of deflection, numerically no buckling is expected for both thermoplastic and thermoset samples either 4 mm or 6 mm wide, see Fig. 9. In all

cases, to induce buckling externally applied load has to be larger than 75 N, what is the limit of fixture.

In addition, numerical buckling results for specimens with  $E_{skin} = 3 \text{ GPa}$  and  $E_{sample} = 250 \text{ MPa}$  are compared to Euler beam buckling stresses. In this case, Euler buckling stress values are attained to be much smaller than the numerically obtained maximum compression stress for 6 mm and 4 mm wide thermoplastic samples, respectively. Therefore, in this study, Euler beam buckling formulation is considered to be too conservative for buckling evaluation in DCB test samples.

## Conclusions

### *Thermoplastic sample*

- 1) The elastic modulus of skin should be below 4 GPa to obtain the required J integral values. Due to relatively soft skins large deflections are expected, therefore 19 mm long crack is recommended.
- 2) J integral values are strongly affected by the plastic deformation of the test sample and the skin material. The yielding is not small scale. The determined plastic zone is 9.5 mm.
- 3) Thermoplastic samples are not prone to buckling in the range of dimension limitations if epoxy based skins are chosen.
- 4) Euler beam buckling formulation is too conservative to predict buckling stresses for this study.

### *Thermoset sample*

- 1) Skin selection is less critical than for the thermoplastic sample because the critical J integral values are lower and are achieved at rather small deflections.
- 2) Deflection does not exceed DCB test fixture limitations both implementing 19 mm and 34 mm long crack.
- 3) Yielding around the crack tip is found to be small. Fracture parameter determination can be based on elastic material formulation as the effect of plastic deformation is not found. The determined plastic zone is 1.5 mm.

- 4) Buckling is not expected using skins with elastic modulus 3 GPa.

## References

- [1] J. Kim and Y. Mai, "High strength, high fracture toughness fibre composites with interface control—a review," *Composites Science and Technology*, 1991.
- [2] K. J. Hemker and W. N. Sharpe, "Microscale Characterization of Mechanical Properties," *Annual Review of Materials Research*, vol. 37, no. 1, pp. 93–126, Aug. 2007.
- [3] V. T. Srikar and S. M. Spearing, "A Critical Review of Microscale Mechanical Testing Methods Used in the Design of Microelectromechanical Systems," *Experimental Mechanics*, vol. 43, no. 3, pp. 238–247, Sep. 2003.
- [4] M. Schoßig, A. Zankel, C. Bierögel, P. Pölt, and W. Grellmann, "ESEM investigations for assessment of damage kinetics of short glass fibre reinforced thermoplastics – Results of in situ tensile tests coupled with acoustic emission analysis," vol. 71, pp. 257–265, 2011.
- [5] A. N. Kumar and B. F. Sørensen, "Fracture Resistance and Stable Crack-Growth Behavior of 8-mol%-Yttria-Stabilized Zirconia," *Journal of the American Ceramic Society*, vol. 83, no. 5, pp. 1199–1206, 2000.
- [6] B. F. Sorensen and A. Horsewell, "Crack Growth along Interfaces in Porous Ceramic Layers," *Journal of the American Ceramic Society*, vol. 84, no. 9, pp. 2051–59, 2001.
- [7] B. F. Sørensen, A. Horsewell, O. Jørgensen, A. N. Kumar, and P. Engbæk, "Fracture resistance measurement method for in situ observation of crack mechanisms," *Journal of the American Ceramic Society*, vol. 81, no. 3, pp. 661–669, 1998.
- [8] S. Goutianos, R. Arevalo, B. F. Sørensen, and T. Peijs, "Effect of Processing Conditions on Fracture Resistance and Cohesive Laws of Binderfree All-Cellulose Composites," *International Journal of Solids and Structures*, 2013.
- [9] J. Rice, "A path independent integral and the approximate analysis of strain concentration by notches and cracks," vol. 35, pp. 379–386, 1967.
- [10] N. Fleck and J. Hutchinson, "A phenomenological theory for strain gradient effects in plasticity," *Journal of the Mechanics and Physics of Solids*, vol. 41, no. 12, pp. 1825–1857, 1993.
- [11] S. Goutianos, H. L. Frandsen, and B. F. Sørensen, "Fracture properties of nickel-based anodes for solid oxide fuel cells," *Journal of the European Ceramic Society*, vol. 30, no. 15, pp. 3173–3179, Nov. 2010.
- [12] A. J. Kinloch and R. J. Young, *Fracture behaviour of polymers*. Applied Science Publishers, 1983.

## Acknowledgments

This research was supported by the Danish Centre for Composite Structure and Materials for Wind Turbines (DCCSM), grant no. 09-067212, from the Danish Strategic Research Council (DSF).

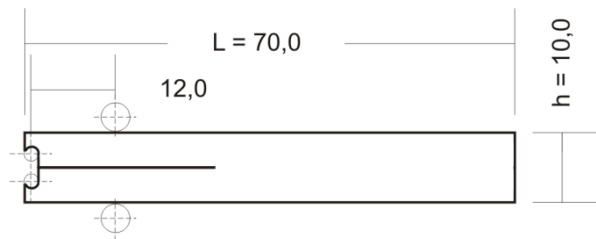


Fig. 1. The DCB test specimen dimensions

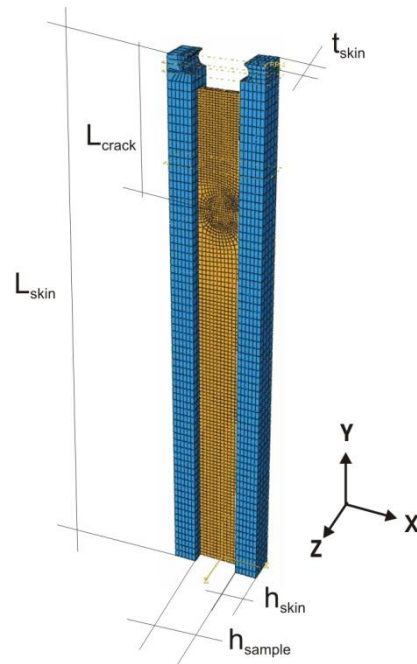


Fig. 2. DCB model used in numerical calculations

Table 1. Material properties of samples

	Thermoplastic	Thermoset
$E_{\text{sample}}$ , GPa	0.25	3
$\sigma_{\text{yield}}$ , MPa	10	26.5
$\epsilon_{\text{ultimate}}$ , %	78.5	7.8
$t_{\text{sample}}$ , mm	0.75	1
$G_{\text{IC}}$ , kJ/m <sup>2</sup> [12]	20	0.1-1

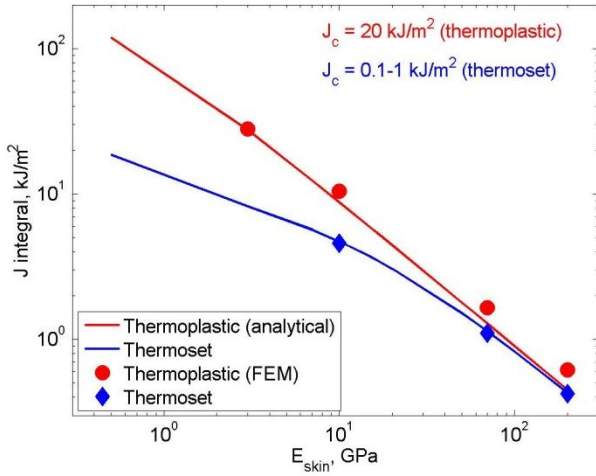


Fig. 3. Comparison between FEM and analytically [11] determined J integral variations with skin stiffness for external load 75 N

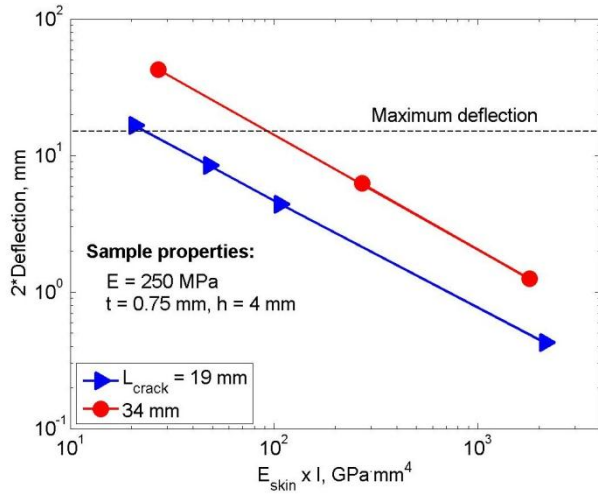


Fig. 4. Numerically obtained deflection values for the thermoplastic sample varying the crack length

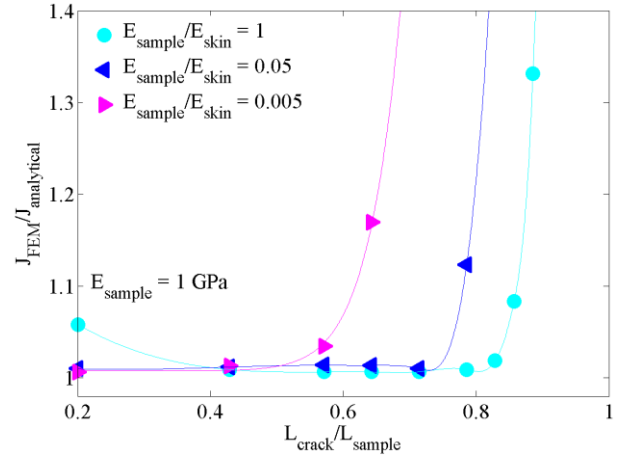


Fig. 5. Normalized J integral values versus crack length for the specimens with different skin stiffness

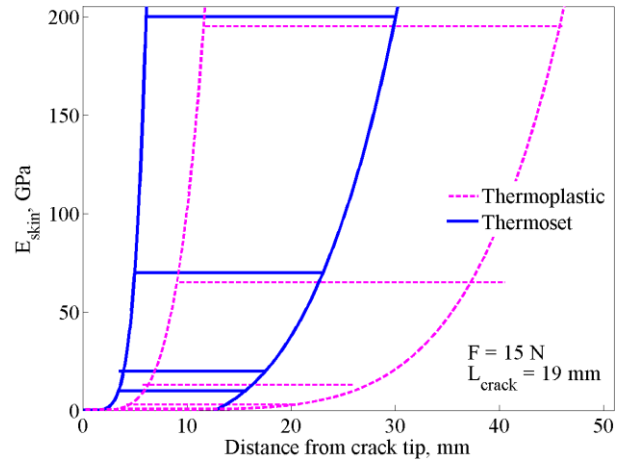


Fig. 6. The length of compressed region in the rear end of sample versus skin stiffness



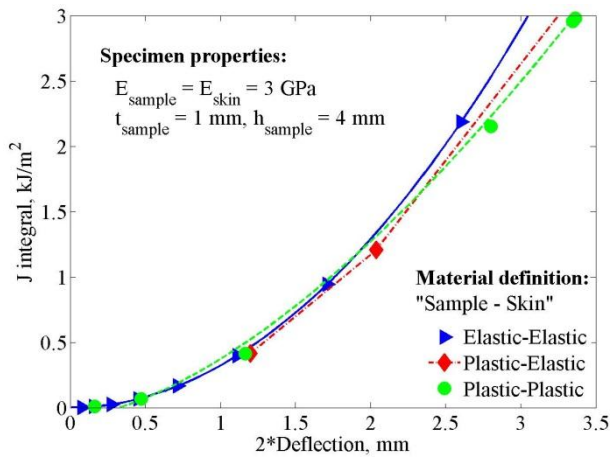


Fig. 7. J integral variations with material formulation for thermoset sample

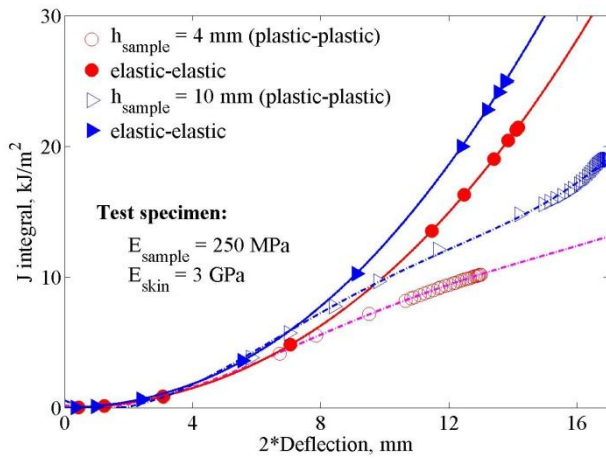


Fig. 8. J integral variations with material formulation for thermoplastic sample

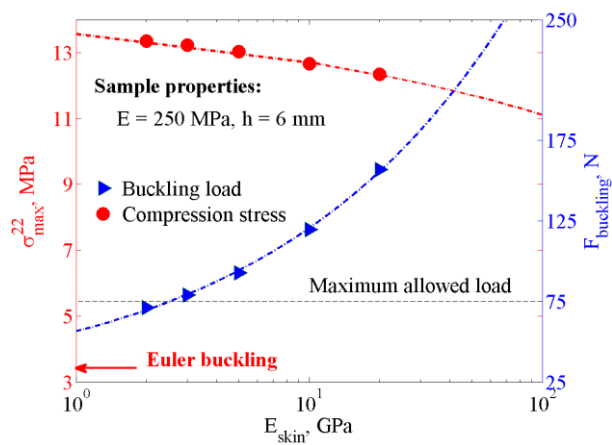


Fig. 9. Buckling results determined by FEM

**Thermoplastic sample with**  
 $h_{\text{sample}} = 6 \text{ mm}$ ,  
 $I_{\text{skin}} = 6.75 \text{ mm}^4$

$S_y, S_{22}$   
 (Avg: 75%)

13.3
10.5
8.7
6.8
5.0
3.2
1.3
-0.5
-2.3
-4.2
-6.0
-13.3

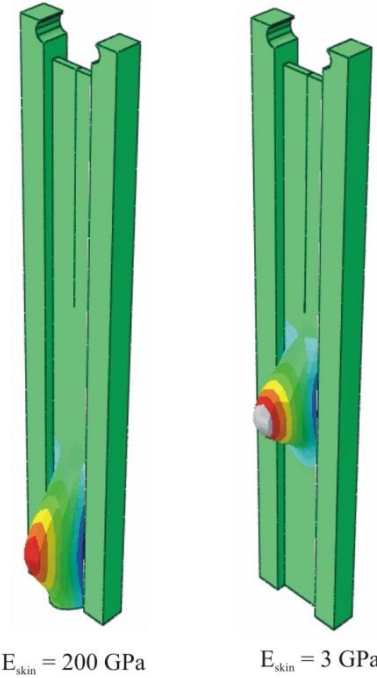


Fig. 10. Examples of stable buckling mode used for buckling result extraction